Automated Microfluidic Droplet Generation and Merging with Integrated Salt-water Electrodes for Analyte Quantification and Monitoring of Endocrine Tissue Secretion Dynamics

by

Nan Shi

A dissertation submitted to the Graduate Faculty of
Auburn University
in partial fulfillment of the
requirements for the Degree of
Doctor of Philosophy

Auburn, Alabama
August 8, 2021

Keywords: Droplet Microfluidics, Merge, White Adipose Tissue (WAT), Dynamics

Approved by

Christopher J. Easley, Chair, C. Harry Knowles Professor of Chemistry and Biochemistry
German Mills, Professor of Chemistry and Biochemistry
Wei Zhan, Associate Professor of Chemistry and Biochemistry
Ahmed M. Hamid, Assistant Professor of Chemistry and Biochemistry

Abstract

Adipose tissue, playing an important role in the global epidemic obesity and diabetes, has attracted extensive attention in recent decades. However, quantitative measurement of dynamics of nutrient uptake and metabolic process in adipose tissue has not been accomplished at high temporal resolution (< 1 min) with traditional instruments and methods. Rapid developments in tissue engineering and microfluidic techniques have begun to meet the requirements of culturing and precisely bio-analyzing adipose tissue explants or adipocytes. Specially, our lab pioneered using automatic droplet-based microfluidics to reveal the metabolic dynamics of pancreatic islets and primary murine epididymal white adipose tissue (eWAT) at a temporal resolution of just a few seconds. In addition, droplet microchips should be powerful tools which significantly enhance the sensitivity of biomolecule (such as proteins, small molecules, nucleic acids, etc) detection with less labor and cost. This dissertation mainly focuses on the evolution of our automated droplet-based secretion sampling systems and their applications to quantification of analytes and the dynamic functions of eWAT.

In Chapter 1, we introduce obesity and adipose tissue. To deepen our understanding about adipose tissue, its inner structures and functions as well as its metabolic and uptake mechanisms are discussed in this chapter. Later the methodologies for quantifying biomolecules via heterogeneous and homogeneous immunoassays are reviewed herein. The last and most

analytically important part of Chapter 1 is the detailed introduction of droplet-based microfluidics, which is viewed as an efficient tool to overcome several specific challenges in chemical and biological fields.

Chapter 2 describes the applications of our recently developed droplet microdevice which integrate salt-water electrodes, merging channels, and pneumatic valves. Firstly, the effects of frequency and magnitude of salt-water electrode voltage on droplet coalescence in this system were studied. Then, this automatic microfluidic system was proved to be a powerful platform for achieving precise serial dilution for pH regulation, and for exploring the assay responses of a homogeneous immunoassay via programmably generating and coalescing several nanoliter volume daughter droplets with a high electric field.

Chapter 3 highlights the integration of our μChopper approach with active valve-based pumps and salt-water electrodes for the first time, taking advantage of the benefits of programmable control of droplet generation and electrocoalescence. In this proof-of-concept work, we applied the device to real-time, continuous calibration of fluorescent labels, then we validated the system for continuous calibration of a homogeneous insulin immunoassay that exhibits a nonlinear response. With the significant savings in reagent use, assay cost, and user time that were incurred, this device provided a novel means to carry out economical measurements with precious reagents in a static or real-time manner.

Droplet-compatible nicking enzyme signal amplification (NESA) is discussed in Chapter 4. As we know, amplification methods enable improving detection sensitivity of biomolecules by several orders of magnitude compared to direct assays, and these benefits are combined with automation, multi-function, and high-throughput of our droplet system mentioned in Chapter 2. Herein, we developed a powerful microdevice by integrating droplet microdevice and isothermal

NESA for analyte quantification. In this droplet-compatible NESA system, the limit of detection (LOD) of DNA and anti-digoxigenin were as low as the femtomolar level. This integrated system has the potential of measuring various types of targets at low concentrations.

In Chapter 5 and 6, two droplet-based system are introduced which are applied to resolve dynamics of uptake and metabolism of eWAT, a tissue of high functional importance in the global epidemics of obesity and diabetes. Here, we cultured and sampled from *ex vivo* eWAT explants with valve-automated droplet formation, then used on-chip mergers to combine tissue eluates with assay reagents downstream. For the first time, dynamics of both nutrient absorption (free fatty acid uptake) and lipolysis (glycerol secretion) from single eWAT explants were quantified at high temporal resolution (~9 s), revealing rapid reversal of uptake after treating with isoproterenol, without significant effects on lipolysis dynamics.

The final installment, Chapter 7, summaries this dissertation and provides an outlook into future research about the development of droplet microfluidics, analyte quantification and activities of tissue/cell monitoring on the novel platform of droplet microfluidics.

Acknowledgements

First of all, I would like to express my sincere acknowledgements to my advisor, Dr. Christopher J. Easley, for his mentorship and support during my Ph.D. study in the Department of Chemistry and Biochemistry, Auburn University. He opened the research gate for me and led me to a productive path of research when I had nearly lost my interests in science, after finishing my master study. In the previous four and half years, Dr. Easley continuously told and showed me what research was and how to methodically study my analytical systems, and this really inspired me and made me love discovering the unknown world. His impressive advice ("slow down in doing your experiments and think more critically about them") will be firmly inserted into my brain.

Then I want to express my appreciation to my committee members: Dr. Wei Zhan, Dr. Ahmed Hamid, Dr. Jimmy Mills, and Dr. Pengyu Chen. Thank you very much for spending precious time serving as my committee members and university reader. Your generous guidance, suggestion and support have had significantly important effects on my research career. Many thanks also to Dr. Christopher J. Easley (Advanced Analytical Chemistry), Dr. Pengyu Chen (Nanomaterials for Biotechnology), Dr. Jimmy Mills (Chemical Kinetics), Dr. Rashad Karimov (Advanced Organic Chemistry I), Dr. Monika Raj (Advanced Biochemistry I), Dr. C. Randall Clark & Dr. Angela

Calderon (Mass Spec of Organic Compounds), and Dr. Guanqun Cao (Experimental Statistics I). I really learned a lot from these courses, and I will keep studying the related knowledge and hope to better understand them in the future. I also would like to thank Timothy Knox, manager of the Biological Research Facility for helping in mouse orders and housing.

I am also very grateful to my amazing lab mates: Dr. Xiangpeng Li, Dr. Juan Hu, Dr. Buhua Wang, Amanda Kurian, Md Moniruzzaman, Andresa Bezerra, Asanka Gedara, Md Mohibullah, Yvette Kayirangwa, Joanne Seow, Mainul Mazumder, Dr. Subramaniam Somasundaram, Dr. Niamat Khuda, Dr. Joonyul Kim, Dr. Mark Holtan, Dr. Jean Negou, Dr. Katarena Ford and Dr. Adriana Avila Flores. I am so lucky to work with such amazing people and have such happy and unforgettable days together. Here, I want to specially thank Dr. Buhua Wang and Asanka for their tutelage in electrochemistry. And I really appreciate my best friends Dr. Xiangpeng Li and Dr. Juan Hu for their continuous help in my experiments, research ideas and career suggestions from 2017 to now. Fortunately, some of us will meet in California soon. Good luck to all of you!

Finally, my greatest gratitude goes to my wife, Dr. Yuling Han, for her enduring love and selfless dedication. I now have a great, five-year story in Auburn because she encouraged me to come to the USA and try a different culture and study environment. In the past years, I mainly focused on my work, and Yuling took over all the daily chores without complaints. It is my smartest decision to marry and bring Yuling into my life. I also do want to thank my parents, parents-in-law, older sisters (Na Shi & Lingling Han), and other relatives and friends for their constant concerns and support in these years. In addition, thanks my lovely cat (Dudu) for her accompaniment and for bringing me so much warmth.

Table of Contents

List of Figures

List of Tables

Chapter 1

Introduction

In this chapter, we will review the systems that combine analyte quantification, adipose tissue engineering, and droplet microfluidics. As the introduction, the obesity and epidemiology, structure and mechanisms of adipose tissue will be discussed firstly, then we will give an overview of relevant bioanalytical methods. Lastly, the history, improvement, and applications of droplet microfluidics will be comprehensively discussed.

1.1 Obesity

1.1.1 Obesity and Its Epidemiology

Obesity is defined by excess body fat accumulation, and it presents a risk to human health as the prevalence of obesity has rapidly increased worldwide in the past several decades and reach pandemic levels now[1]. In clinical practice, obesity is assessed by the body mass index (BMI), calculated by dividing the body weight in kilograms by the square of height in meters, as categorized with the World Health Organization (WHO) classification. In the classification of Centers for Disease Control and Prevention (CDC) and the WHO, a normal BMI range is 18.5 to 24.9 kg/m^2 for adults, whereas a BMI $\geq$ 25 kg/m^2 will be viewed as overweight, and a BMI $\geq$ 30 kg/m^2 and BMI $\geq$ 40 kg/m^2 are defined as obese and severely obese, respectively[2]. The state of obesity enhances the risk of diseases, such as type 2 diabetes mellitus, fatty liver disease, cardiovascular diseases, breast cancer, and Alzheimer's disease. Additionally, reduced qualify of

life, unemployment, lower productivity, and social disadvantage caused by obesity significantly increases the economic burden [1,3].

1.1.2 Functions, Components, and Types of Adipose Tissue

Adipose tissue is an essential, complex, and highly active metabolic and endocrine organ that plays crucial roles in maintaining lipid and glucose homeostasis. On the one side, free fatty acids (FFAs) in the form of triacylglycerols (TGs) is stored in adipose tissue and this organ also handles the lipid mobilization and distribution in the body. On the other side, numerous bioactive factors secreted from adipose tissue will modulate the metabolic mechanisms of other organs. In addition, adipose also help maintaining euthermic body temperature by burning lipids[4]. Adipose tissue normally contains adipocytes, connective tissue matrix, nerve tissue, stromovascular cells, and immune cells[5].

Currently, adipose tissue can be classified by morphology into white adipose tissue (WAT), brown adipose tissue (BAT), and beige[6]. The main function of WAT composed of unilocular adipocyte is to store extra energy as TGs, but BAT consists of mitochondria-rich multilocular adipocytes focuses on transferring energy from food into heat. Compared to large amount of WAT, BAT exists in smaller depots in adults. Interestingly, newborn humans are provided with a higher proportion of BAT, but adult humans have a relatively lower amount[7]. Another type of adipose tissue called beige or brite (brown-like-in-white), which is the accumulation of brown adipocytes within the white fat depots, has been just discovered in recent years. This types of beige cells have the ability of shifting between white adipocytes and brown adipocytes and are revealed to be useful in improving glucose homeostasis (**Figure 1.1**)[8,9]. As described in **Figure 1.1**, during the pregnancy and lactation period, white adipocytes and brown adipocytes will reversibly convert

into milk producing epithelial cells and myoepithelial cells, respectively. The pink adipocytes will shift back to white and brown adipocytes after lactation[8].

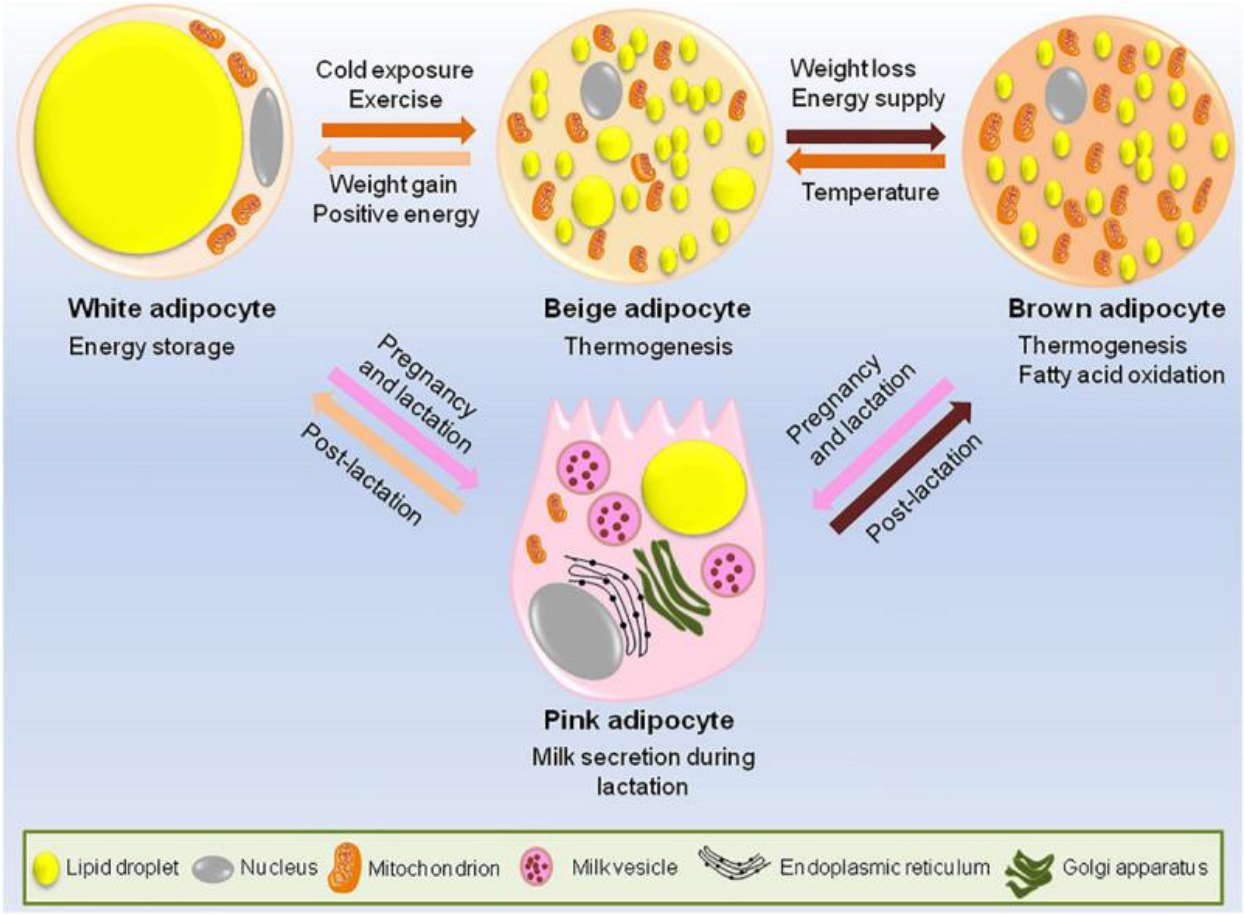

Figure 1.1 There are remarkable plastic properties in white, brown, and beige adipocytes. The figure is reprinted with permission from ref [8] ©2020, Frontiers Media S.A.

According to fat distribution in human body, adipose tissue can be divided into two types: visceral adipose tissue (VAT) and subcutaneous adipose tissue (SAT). There are many differences between SAT and VAT including anatomical, cellular, molecular, physiological, clinical and prognostic differences. Compared to SAT, there are larger amount of inflammatory and immune cells, less differentiating ability of preadipocyte, and higher percentage of large adipocytes in VAT.

In addition, VAT adipocytes are more sensitive to adrenergic stimulation, lipolysis, and insulin-resistant than SAT, as well as the VAT's capacity in free fatty acid generation and glucose uptake is relatively more prominent. However, SAT adipocytes have better performance in the absorption of free fatty acids and triglycerides[10]. Previous research indicates that accumulation of visceral abdominal adipose tissue has a higher risk to human than SAT in obesity-related disorders[11].

1.1.3 Absorption and Metabolism Mechanisms of White Adipose Tissue

The crucial roles of white adipose tissue (WAT) is storing energy and helping to regulate the endocrine system through lipogenesis and lipolysis, respectively (**Figure 1.2**). In the feeding condition, glucose and fatty acids (FA) will be absorbed into WAT and stored as the form of triacylglycerols (TGs) where FA is derived from dietary fat intake and also from endogenous de novo lipogenesis (DNL) that normally happens in liver. During the process of lipogenesis, glucose not only provides its metabolite (acetyl-CoA) as the substrate for *de novo* biosynthesis of FA, but it also activates the expression of acetyl-CoA carboxylase (ACC), the rate-limiting enzyme of lipogenesis, and stimulates the release of pancreatic insulin[12]. High circulating insulin facilitates glucose uptake in the adipocytes, activates glycolytic and lipogenic enzymes, and induces the expression of sterol regulatory element-binding protein 1 (SREBP1) which controls the gene expression required for the biosynthesis of cholesterol, FAs, TGs, and phospholipid[13,14]. Another transcriptional factor carbohydrate response element-binding protein (ChREBP) is revealed that it promotes fatty acid synthase (FAS)-activated increase of DNL in adipose tissue when the insulin level is high, and this type of protein also regulates the metabolism of lipid and glucose in adipocytes and the whole-body insulin sensitivity[15,16].

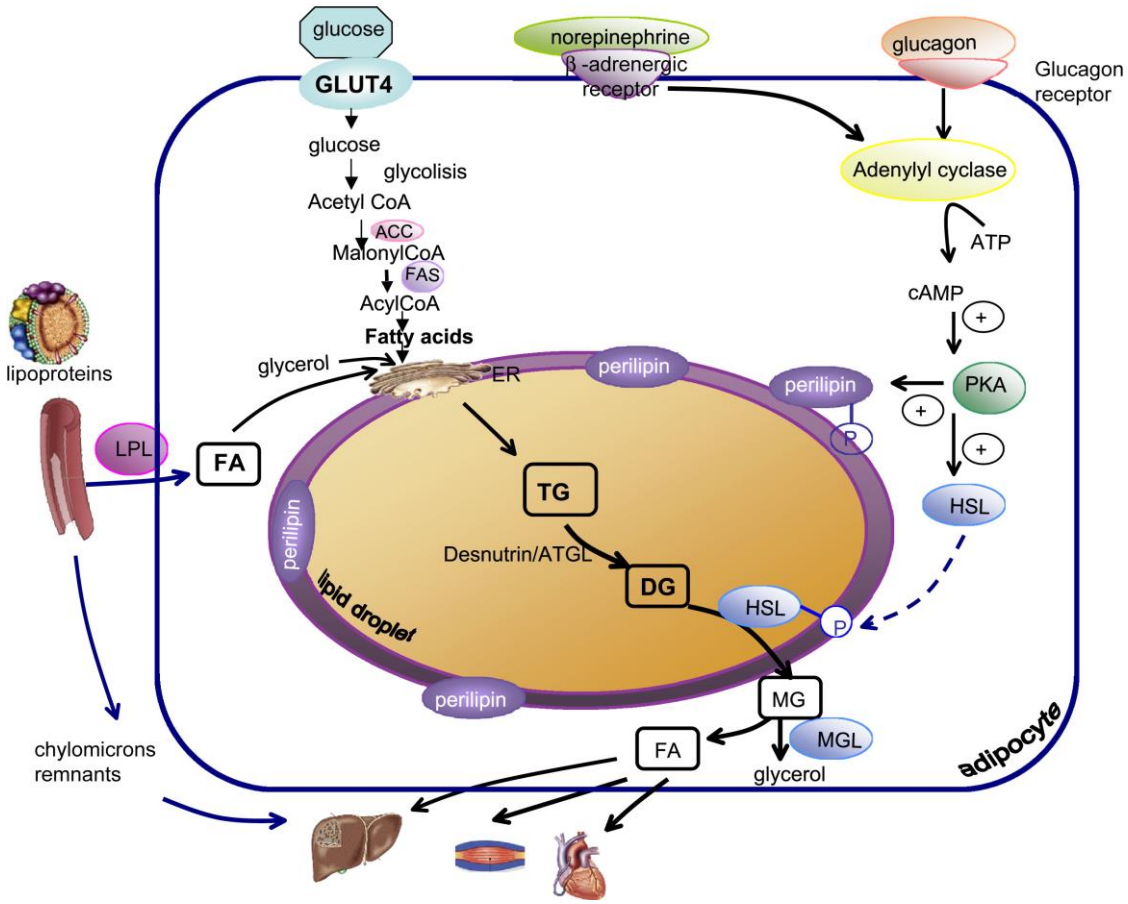

Figure 1.2 Lipid metabolism and mobilization controlled by adipose tissue.
The figure is reprinted with permission from ref [14] ©2008, Elsevier.

Opposite to lipogenesis, breakdown of TGs stored in lipid droplets to diacylglycerols (DG), monoacylglycerols (MG), and finally glycerol as well as free FAs occurs in white adipose tissue lipolysis in the fasting situation (**Figure 1.2**). Adipose triglyceride lipase (ATGL), hormone-sensitive lipase (HSL), and monoacylgalycerol lipase (MGL) are three primary lipases in the lipolysis process and respectively regulate the conversion of TGs to DGs, DGs to MGs, and MGs to glycerol and free FAs[17]. In addition, perilipins and other proteins in the surface of lipid droplets also have essential roles in lipolysis regulation, such as Caveolin-1, proteins interacting with hormone-sensitive lipase, proteins interacting with adipose triglyceride lipase, Aquaporin, and

cide-domain-containing proteins (CideN). The lipolytic pathway has been revealed to be regulated by hormones. Insulin and catecholamines are two well-known types of hormones affecting the adipose tissue lipolysis process. Additionally, heart-derived natriuretic peptides and numerous autocrine/paracrine factors also participate in the regulation of lipolysis. In addition to hormones, previous reports show that physiological characteristics (age, anatomical site, sex, genotype, and species differences) also play a part in controlling the lipolytic pathway[18].

1.1.4 Adipokines of White Adipose Tissue

Another important function of white adipose tissue is secreting a series of bioactive cytokines to regulate systemic metabolism and inflammation, and those released hormones are referred to as "adipokines"[19,20]. **Table 1** summaries a list of key adipokines from white adipose tissue and their functions[20]. Early-discovered leptin and adiponectin are key adipokines secreted form WAT which play essential roles in regulation of energy homesotasis[21]. Leptin reduces the food intake by passing the blood-brain barrier and targeting on the hypothalamus, which controls the adipose tissue mass, and the circulated concentration of leptin is proportional to the relative body fat weight[22,23]. Hansen et al. found that leptin is also produced or exists in some other organs like stomach, muscle, and intestine[24]. Adiponectin is a multimeric adipokine structure made of many ~30-kDa monomers that regulates the insulin sensitizing effect, cardiovascular protection, and anti-inflammation[25]. Resistin, named for its property of inducing insulin resistance via enhancing expression of gluconeogenic enzymes and lowering the activity of AMPK and the expression of insulin receptor substrate (IRS)-2 , is a type of peptide released from adipocytes in mice but the mRNA levels of resistin are relatively low in primary human adipocytes[26-29]. Though treatment of resistin increases the production of inflammatory cytokines (TNFα and IL6) and adhesion molecule and chemokines (ICAM1 and VCAM1), but it remains a mystery about the relation

between resistin and obesity[30]. Other hormones secreted from white adipose tissue are listed in **Table 1**.

Adipokine	Function	Regulation in the obese
TNF-α	Inflammation, antagonism of insulin signaling	Upregulated
Leptin	Appetite control through central nervous system	Upregulated
Adiponectin	Insulin sensitizer, anti-inflammatory action	Downregulated
IL-6	Variable with origin and targeted tissues	Upregulated
RBP4	Role in systemic insulin resistance	Upregulated
Resistin	Promotes insulin resistance and inflammation through macrophages	Upregulated
IL-18	General inflammation	Upregulated
CCL2	Monocyte recruitment	Upregulated
Lipocalin 2	Promotes insulin resistance and inflammation through adipocytes	Upregulated
Nampt	Monocyte chemotactic activity	Upregulated
ANGPTL2	Local and vascular inflammation	Upregulated
CXCL5	Antagonism of insulin signaling through the JAK–STAT pathway	Upregulated
SFRP5	Suppression of pro-inflammatory WNT signaling	Downregulated
Asprosin	induces hepatic glucose production	Upregulated

TNF-α tumor necrosis factor alpha, IL-6 interleukin 6, IL-18 interleukin 18, RBP4 retinol binding protein 4, CCL2 CC-chemokine ligand 2, Nampt nicotinamide phosphoribosyltransferase (also called pre-B-cell colony-enhancing factor 1, PBEF1, or visfatin), ANGPTL2 angiopoietin Like Protein 2, CXCL5 signifies one of the cytokine-like proteins with a highly conserved ELR motif preceding the N-terminal cysteine, SFRP5 secreted frizzled-related protein 5

Table 1 List of important adipokines in WAT

1.2 Quantification of Biomolecule

Biomolecules play important roles in biological research and clinic diagnosis, and many protein and nucleic acid biomolecules normally exist at pretty low concentration. Therefore, highly sensitive and accurate bioassays are crucial for the quantification of biomolecules[31]. For this purpose, various detection strategies based on electrochemistry, optical readout, and other types of bioanalytical assays have been developed over the past decades[32-37]. Often, antibodies are leveraged due to their high specificity and affinity toward analytes, and those immune-based bioassays can be divided into two main formats: heterogeneous and homogeneous. Here, we will briefly compare these two types of immunoassays and specifically introduce the amplified homogeneous assays.

1.2.1 Heterogeneous and Homogeneous Immunoassays

Immunoassays referred to as "heterogeneous" require some sort of washing or separation, and these are required to be manipulated in several steps with reactants being added and washed away or separated at different points. The classical and famous heterogeneous immunochemical technique is the enzyme-linked immunosorbent assay (ELISA), which is viewed as the gold standard of protein measurement. ELISA is a plate-based assay technique involving three principles in combination: immune reaction, enzymatic chemical reaction, and signal detection and quantification. The most traditional ELISAs are two-site, non-competitive assay where the analyte is "sandwiched" between two antibodies. The conventional sandwich-ELISA is proceeded in microliter plates where primary antibodies are immobilized on the bottom of each well and used to capture target molecules after incubation with the sample, followed by a washing step to remove the nonbinding agents, and finally a secondary antibody conjugated with enzymes is added to trigger a reaction to produce many chromophores per analyte molecule for optical detection.

ELISA has a lot of benefits in sample detection, such as highly specific, flexible, sensitive, and suitable for complex samples. However, several washing steps make ELISA time-consuming and 96-well plate setting limits the operational flexibility.

Some immunoassays can be carried out simply by mixing the all of reagents and finally making a physical measurement—without washing steps—and such assays are normally called homogeneous immunoassays. It is obvious that homogeneous assays have the advantages of reagent consumption, analysis time, portability, and disposability in comparison to heterogeneous immunoassays. However, lack of separation and purification processes often lowers the biological specificity of labelled biomolecules and limits the sensitivity of target analysis[38]. In her dissertation describing work in the Easley group, Dr. Juan Hu noted some successful homogeneous assays such as amplified luminescent proximity homogeneous immunoassay (ALPHA), homogeneous time-resolved fluorescence (HTRF), Luminex® xMAP® technology (combination of flow cytometry and sandwich immunoassays), and DNA-based homogeneous immunoassays[39,40].

1.2.2 Isothermal Amplification Methodologies

For quantification of precious biomolecules, numerous methods have been developed in the past few decades, and those techniques mainly consist of two categories: direct and amplified reactions. For direct measurement of proteins, recognition elements (antibodies and aptamers) are applied to bind to proteins due to their high selectivity and affinity, and the antibody-protein or aptamer-protein complexes are analyzed through chemical or physical signals[41,42]. However, relatively low association constants of some antibodies or aptamers limit the detection sensitivity. Therefore, for many low abundance analytes, it is crucial to develop amplification strategies for protein quantification.

Compared to direct way, amplification is more sensitive and enables detection of a small quantity of proteins and nucleic acids[43]. The polymerase chain reaction (PCR) is the most popular method for DNA amplification for detection and identification of infectious diseases, genetic disorders and other research purposes, as it rapidly generates millions to billions of copies of a specific DNA sample. However, multiple-step thermal cycling and expensive thermal control instrumentation hampers its application in some fields. Some isothermal amplification techniques have been put forward to overcome the challenges of PCR in last two decades, such as transcription mediated amplification (TMA)[44], signal mediated amplification of RNA technology (SMART)[43], strand displacement amplification (SDA)[45], rolling circle amplification (RCA)[46], loop-mediated isothermal amplification (LAMP)[47], helicase-dependent amplification (HDA)[48], recombinase polymerase amplification (RPA)[49], and nicking enzyme signal amplification (NESA)[31].

Herein, we only briefly discuss the mechanisms of RPA and NESA techniques that were used in projects in our laboratory[50]. The RPA process starts when a recombinase protein uvsX from T4-like bacteriophages binds to primers in the presence of ATP and a crowding agent to format a recombinase-primer complex. The complex then interrogates double stranded DNA seeking a homologous sequence and promotes strand invasion by the primer at the cognate site. For preventing the ejection of the inserted primer by branch migration, the displaced DNA strand is stabilized by single-stranded binding proteins. Finally, the recombinase disassembles, and a strand displacing DNA polymerase binds to the 3' end of the primer to elongate it with dNTPs. Cyclic repetition of this process results in the achievement of exponential amplification[51] as shown in **Figure 1.4**. NESA is a novel isothermal amplification tool developed in recent years. NESA assays are mainly based on nicking enzymes that can specifically recognize and nick restriction sites of a

certain sequence on one oligonucleotide strand (**Figure 1.3**). NESA assays can exponentially amplify the target nucleic acid in a quite short time with repeating cleaving the specific ssDNA[52,53].

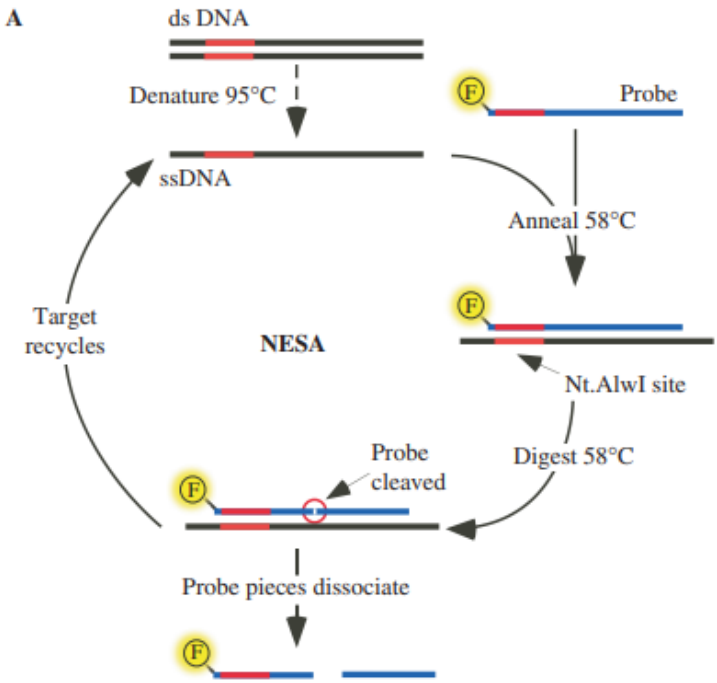

Figure 1.3 Nicking endonuclease signal amplification (NESA).

The figure is reprinted with permission from ref [52] ©2007, Oxford University Press.

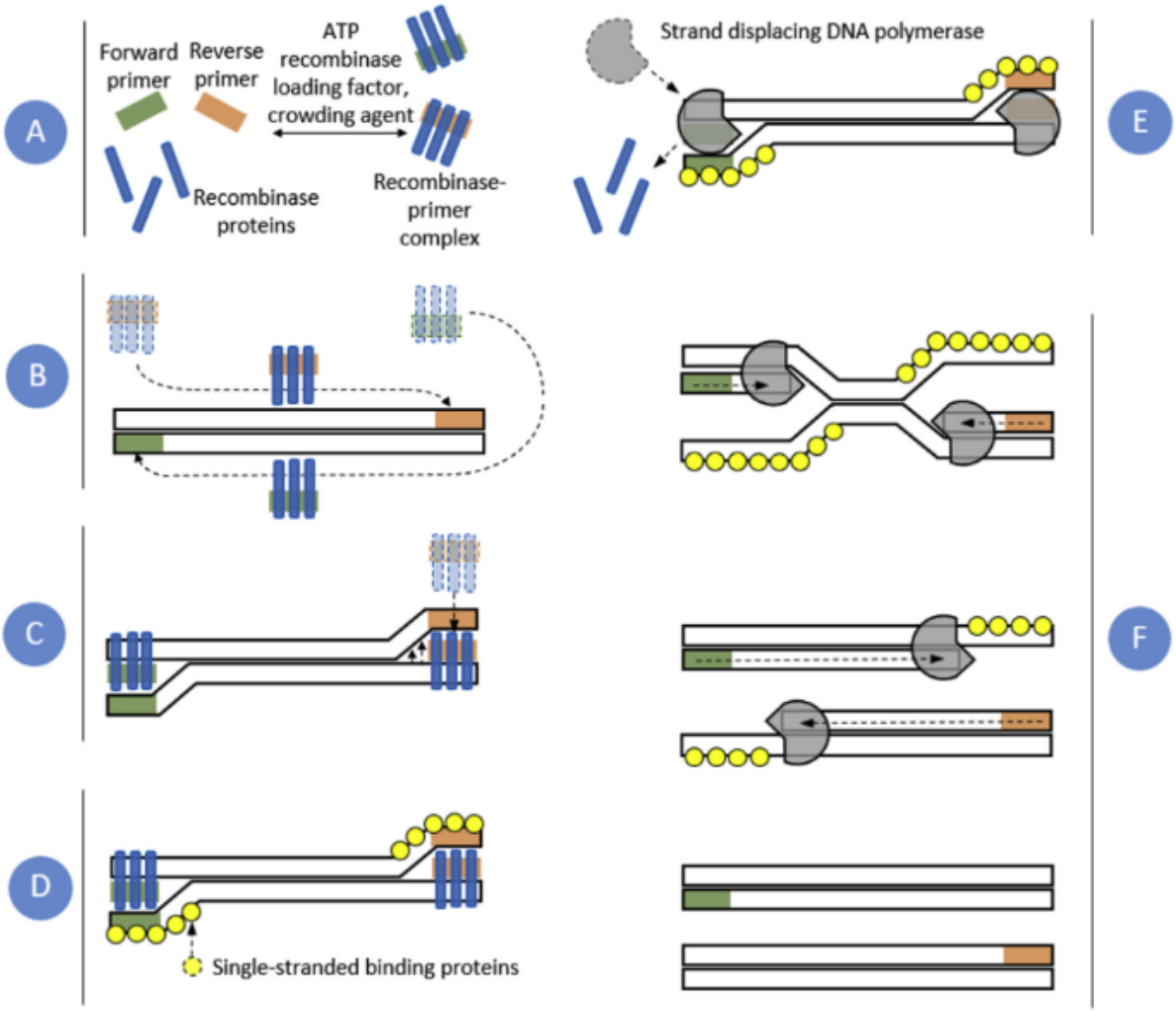

Figure 1.4 Recombinase polymerase amplification (RPA)

The figure is reprinted with permission from ref [51] ©2018, Elsevier.

1.3 Droplet Microfluidics

1.3.1 Introduction of Droplet Microfluidics

Nearly twenty years ago, informed by prior work on the stability of monodisperse emulsions [54,55], an early foray into droplet microfluidics by Thorsen et al. [56] came about when researchers realized the unique and predictable fluid physics within microfluidic channels [57] could be exploited to consistently form droplets between two immiscible fluids such as water and oil. Soon afterward,

a number of studies revealed that a vast array of manipulations and novel analytical applications could be achieved with droplet microfluidics, mainly with aqueous-in-oil droplet formation. Among many other productive research groups, Ismagilov and coworkers suggested rapid dynamics could be explored [58], the Whitesides and Stone laboratories explored device dependent behavior [59], the Weitz group explored high-throughput analytical possibilities and multiple emulsions [55,60], the Mathies laboratory investigated the use of valve-based automation in droplet microfluidics [61,62], and Chiu and coworkers explored precise droplet analysis with fluorescence correlation spectroscopy [63]. Generally, in these and other related studies, microfluidic devices have permitted the generation of precisely defined droplets which served as unique individual micro-reactors (usually pL or nL volume) that could be processed and analyzed downstream in operations such as delivery, merging, mixing, sorting, or analysis [64].

Researchers have leveraged these populations of typically monodisperse droplets to reveal several outstanding benefits [65]. The extraordinarily small volumes not only save reagents, but also enable unique analyses on single cells or even single molecules [66,67]. With nearly identical droplets generated at high throughput (often kHz frequencies), scientists can explore biological systems and generate data sets at larger scales than previously accessible [68]. Numerous biological and chemical applications were empowered by droplet microfluidics in recent years, such as single-cell genome sequencing [69], enzyme kinetics and inhibition [70], combinatorial synthesis and drug discovery [71], protein and nucleic acid quantification [72-74], and cellular secretion detection [75,76]. As such, there are quite a few review articles on droplet microfluidics, and we point the readers to a recent selection having varying perspectives: a thorough review on recent advances [77], a survey of analytical techniques [78], dynamic analysis with droplets [79,80], passive and active formation [81],

droplet tracking and barcoding [82], single-cell analysis [83], tissue engineering and analysis [84], synthetic biology [85], nucleic acid cytometry [86], and drug discovery within droplets [87].

To date, most studies in droplet microfluidics have remained reliant on optical readout of droplet contents (mainly with fluorescence) due to its simplicity, compatibility with micro-channels, and the lack of interference from carrier fluids such as oils. Likewise, the majority of studies have also used passive fluidic features. More recently, several groups have expanded the use of active droplet formation and control using, for example, elastomeric valves, and other analytical steps such as bead-based cleanup and mass spectrometry have been integrated with droplet microfluidics.

1.3.2 Flow Control in Droplet Microfluidics

Passive Droplet Control

In a droplet-based two-phase flow microsystem, two immiscible fluids under flow or pressure regulation meet at a junction, resulting in segments of the one contained in the other that are transported downstream depending on viscous and interfacial forces [88,89]. To drive droplets in a preferred route at a desired speed, passive mechanisms can maintain this balance through regulation of channel geometry, hydrodynamic pressures, surface hydrophilicity/hydrophobicity, viscosity of the continuous phase, and interfacial tension between the two phases [60,68,90]. As surface tension is highly relevant, surfactants play a significant role in modulating droplet properties [50,54,81,91]. Several droplet generation techniques have been developed so far, exploiting different device geometries that can passively regulate droplet size in various ways. In two-phase flow microfluidics, cross-flow, co-flow, and flow-focusing are three of the major generator types, named for how the phases interact the interfaces [81,89,92]. A number of reviews have covered passive droplet formation and maneuvering; for more detailed information, we direct readers to the

thorough survey by Zhu and Wang [81] and to Dressler and coworkers' apt description of formation structures published in the 2017 issue of *Annual Review of Analytical Chemistry*[79].

Active Droplet Control

In realizing the array of applications achieved through droplet microfluidics, precise control over the size, volume, and frequency of formed droplet is of utmost importance. While this can be accomplished passively without external actuation, active regulation provides more authority and precision, albeit at lower throughput and with additional input energy [68,89]. Device-to-device variations, ambient conditions, and surface chemistry fluctuations are example issues that cause droplet formation inconsistencies in passive systems. These issues can be largely negated by active mechanisms, which can be interfaced to a computer to give flexibly programmable droplet formation.

Active mechanisms execute different droplet operations by employing external controllers. Depending on the type of energy applied, these actuations can be classified as mechanical, electrical, thermal, or magnetic [93]. Monolithic membrane valves are the most common mechanical means as they can precisely regulate fluidic flows and mediate droplet generation and other maneuvers [75,76,94-101]. While a thin layer of polydimethylsiloxane (PDMS) is traditionally used to act as the valve gate, 3D printing technology has recently been introduced for rapid, cost-effective production of both normally-open and normally-closed valves that can be actuated at low operational pressures [102-104].

Alternating current (AC) electric fields are often applied externally or within micro-channels with nearby electrodes to aid in destabilizing the fluidic interface and initiating droplet generation, merging, sorting, and more operations [105,106]. The Abate group described a clever approach making this method more accessible, where a concentrated salt solution in a microchannel replaced

traditional metal electrodes and provided further customization of the electrode designs [101,107]. Alternatively, electro-wetting is popular in controlling the dynamics of discrete droplets by tuning its ability to wet a planar surface, a phenomenon subject to an affiliated field of study known as digital microfluidics [108-111].

Magnetic and thermal transducers are other means of active droplet coordination. A permanent magnet or an electromagnet can be used to regulate the size of droplets forming off a ferromagnetic fluid [112,113] depending on its point of application [114], magnetization [81], and strength of the magnetic field [113]. Further, the viscosity and interfacial tension of most fluids decrease fairly linearly with increasing temperature [93], thus integrated heating can tune these properties to enable droplet operations such as thermally mediated breakup and formation [115].

Even though a larger number of off-chip controls may make the initial set-up cumbersome, the automation capability of these active methods can ensure both accuracy and precision, especially in experiments that require precise volume metering or have to be operated for a longer time. For instance, our laboratory has shown that phase-locked detection can permit up to 100-fold improvements in optical limits of detection using a pair of sample and reference droplets, but to do so requires generation in an alternating pattern at very narrow bandwidth [101,116-118]. While passive mechanisms are still far superior for high throughput generation [81]—often one or two orders of magnitude faster compared to active methods [93]—analyses that demand quality over quantity require resorting to active means,

Active Systems Using Membrane Valves

The introduction of integrated membrane valving concepts in microfluidics [96,97,119] was followed by significant further development by the Quake [120,121] and Mathies [96,122] groups. Their work paved the way for a wide variety of unique and impactful microfluidic applications that are

too numerous to adequately review here. Interestingly, for quite a few years, these types of valves were only sparingly used [62,123-126] within the sub-field of droplet microfluidics, perhaps due to the ease with which droplets can be formed passively. Nonetheless, work in this area has continued, and several groups have recently demonstrated unique and powerful capabilities by combining membrane structures to facilitate droplet formation and various movements.

As shown in **Figure 1.5a**, the DeVoe group has recently demonstrated programmable integration of droplet generators, traps, and mergers with membrane valves and strategically placed bypass channels. Various actions were accomplished on-demand, such as trapping in a first-in first-out (FIFO) manner, analysis, selective ejection, merging, and sorting [99]; and the device was applied to single cell trapping and screening. This group then used a microfluidic multiplexer and a novel, multi-depth droplet trap structure (**Figure 1.5b**) to demonstrate random-access trapping and release of arrays of picoliter droplets or cells [100]. Using normally open valves and pumps for droplet formation and downstream analysis, our group has shown that the precise control of droplet frequencies at narrow bandwidths allows lock-in detection for significant reductions in optical detector noise [117,118], in a device termed the μChopper. By further combining this automation and μChopper readout with salt water merging electrodes, a fully programmable device was validated for combinatorial analysis and on-chip immunoassays (**Figure 1.5c**). While a clear disadvantage of these systems is their low droplet frequencies (~0.1–10 Hz), one notable advantage of the programmability is the extraordinary consistency with which users can regulate droplet frequency, size (volume), merging ratios, trapping and retrieval positions, etc.

Unique Droplet Junctions with Active Control

Typical droplet formation and handling structures are based on microchannel network designs with only two channels at each junction or node, such as the T-junction droplet generators shown

in **Figure 1.5a, c**. Doonan and Bailey introduced a clever advancement in 2017, termed the "K-channel", where multiple channels intersect at a single node interfaced to a nearby merging electrode and/or magnet (**Figure 1.5d**). The elegance of this design is that cross-channel flow can be coupled to droplet flow at the intersection point, enabling multiple versatile operations with a single design feature, such as reagent injection, fluid extraction (as shown in **Figure 1.5d**), droplet splitting, and magnetic bead capture. The K-channel is categorized here as "active," since it does require a precisely balanced flow rate in a separate liquid stream. Unlike other active structures, the K-channel operates successfully in the droplet frequency range of 200 – 500 Hz.

Despite the numerous advantages and potential applications of droplet microfluidics, a major limitation has been the lack of robust integration with solid-phase techniques. If these devices are to be successfully applied to solve many biochemical problems, the bottleneck of manual sample cleanup and extraction must be addressed. To attend to this need, the Bailey group recently developed another unique droplet junction, the coalesce-attract-resegment wash (CAR-Wash) design[127] (**Figure 1.5e**). The droplet CAR-Wash structure accepts three inputs with controlled flow (bead-containing droplets segmented in oil, a wash solution, and another oil stream for resegmenting), uses two active on-chip structures (salt water electrode and magnet), and outputs two streams with both aqueous and oil components (waste and resegmented droplets containing washed beads). This approach was useful at over 500 Hz droplet frequencies, it achieved 98% retention of beads, and it allowed over 100-fold dilution in the final droplets. The CAR-Wash design should enable users to integrate more sample preparation steps into on-chip droplet microfluidics workflows. One immediately obvious application could be to adapt multi-step, bead-based immunoassays into segmented flow streams.

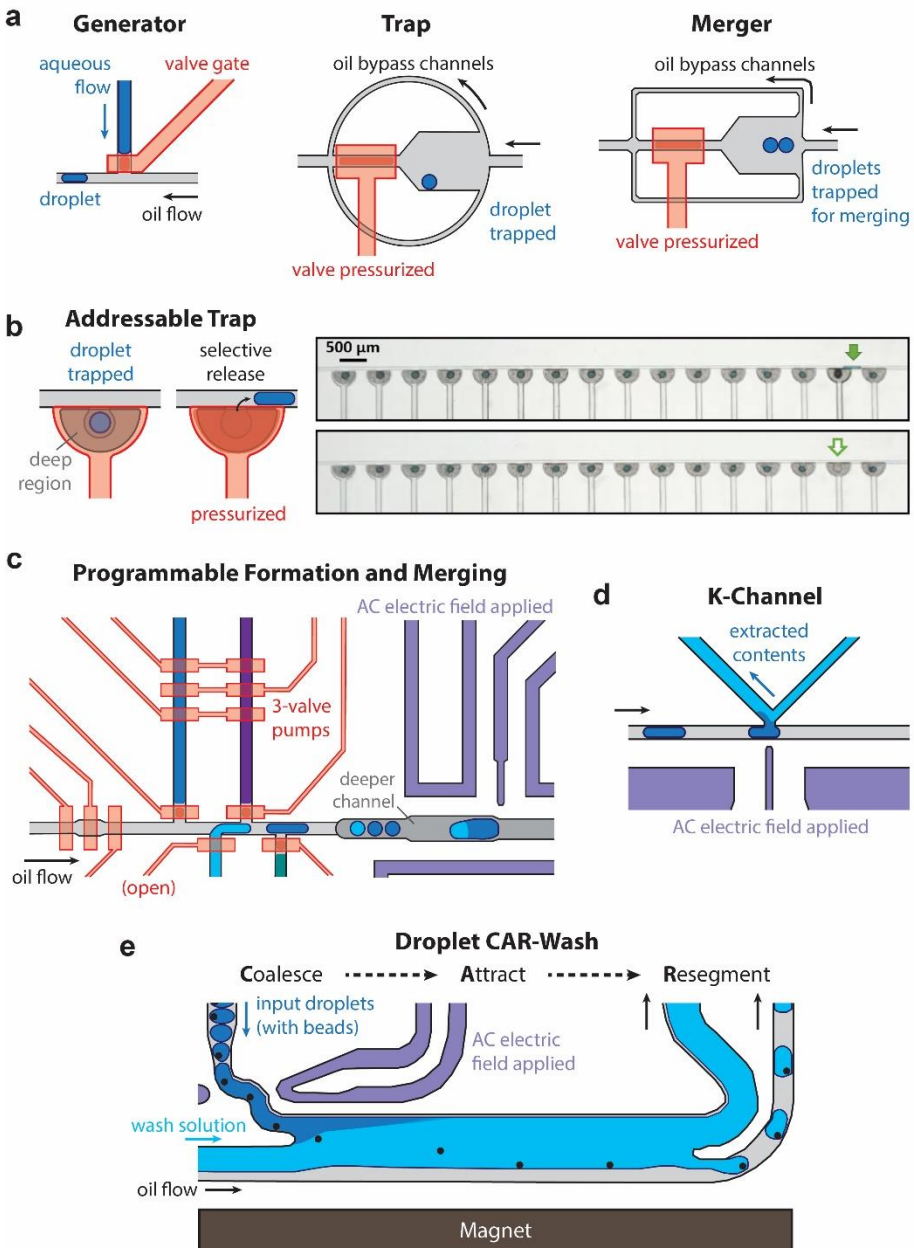

Figure 1.5 Recent advances in active droplet control

(*a*) Membrane valve structures for programmable generation, trapping, and merging of droplets and (*b*) addressable trapping and releasing of droplets or cells. Panel *a* is reprinted with permission from ref [99] ©2019, Royal Society of Chemistry; panel *b* is reprinted with permission from ref [100] ©2020, AIP Publishing.(*c*) Pneumatic valve-based, on-chip pumps combined with salt water electrodes for programmable formation and merging of multiple droplet populations at well-controlled ratios. Figure is reprinted with permission from ref [101]. (*d*) The K-channel architecture enables multiple unique functions, such as selective extraction of contents (dark blue)

into an aqueous stream (light blue) in real time. Figure permission from ref [128] ©2017, American Chemical Society. (*e*)The coalescence, attract, and resegmenting structure for bead washing (CAR-Wash) provides efficient, continuous washing of magnetic beads within droplets. Figure permission from ref [127] ©2019, Royal Society of Chemistry. Gray = oil, Blue colors = aqueous solutions, Red = pneumatic valves, Purple = salt water electrodes.

Applications of Droplet Microfluidics

Picoliter or nanoliter-size droplets have been widely used in biotechnologies because each droplet can be regarded as isolated and well-protected unit for reactions and it is much simpler to add extra manipulations to those individual reactors compared to normal tubes, such as transporting, sorting, merging, mixing, or concentrating[64]. In addition, ultra-low concentration of analytes in small volume can be detected inside droplet that not only saves lots of experiment materials but it also makes possible to analyze single-cell or molecule[67,128]. Highly monodispersed and identical droplets generated with high throughput guarantee researchers to rapidly and easily obtain large-scale data sets[68]. Numerous applications have been applied in droplet microfluidics until now, such as analysis of cells/tissues engineering, biomolecule quantification, single cell sequencing, combinatorial discovery, 3D cell culture and detection, etc. Here, we will specifically emphasize the analysis of engineered tissue and biomolecule measurement within droplets.

1.3.3 Quantification of Analytes in Droplet Microfluidics

Immunoassays are widely recognized as important bioanalytical techniques for quantifying clinical or biological analytes. As discussed above, ELISA is the most important immunoassay in clinical diagnosis and research currently. Considering the benefits of ELISA and droplet microfluidics, an integrated system containing these two techniques should be a powerful platform for sample analysis with low limits of detection. Jung-uk et al. introduced a microdevice which

can format femtoliter-size droplets at 1.3 MHz, incorporating a bead-based immunoassay, and this device enabled detection of 46 fM (1.2 pg/mL) prostate-specific antigen (PSA) in buffer, which is an improvement of nearly 2 orders of magnitude over standard ELISA[129] (**Figure 1.6A**). Matthew et al. also described a wash-free immunoassay for C-reactive proteins (CRP) in droplet-based microchip, and the LOD of CRP was found to be 0.01 μg/mL[72](**Figure 1.6B**).

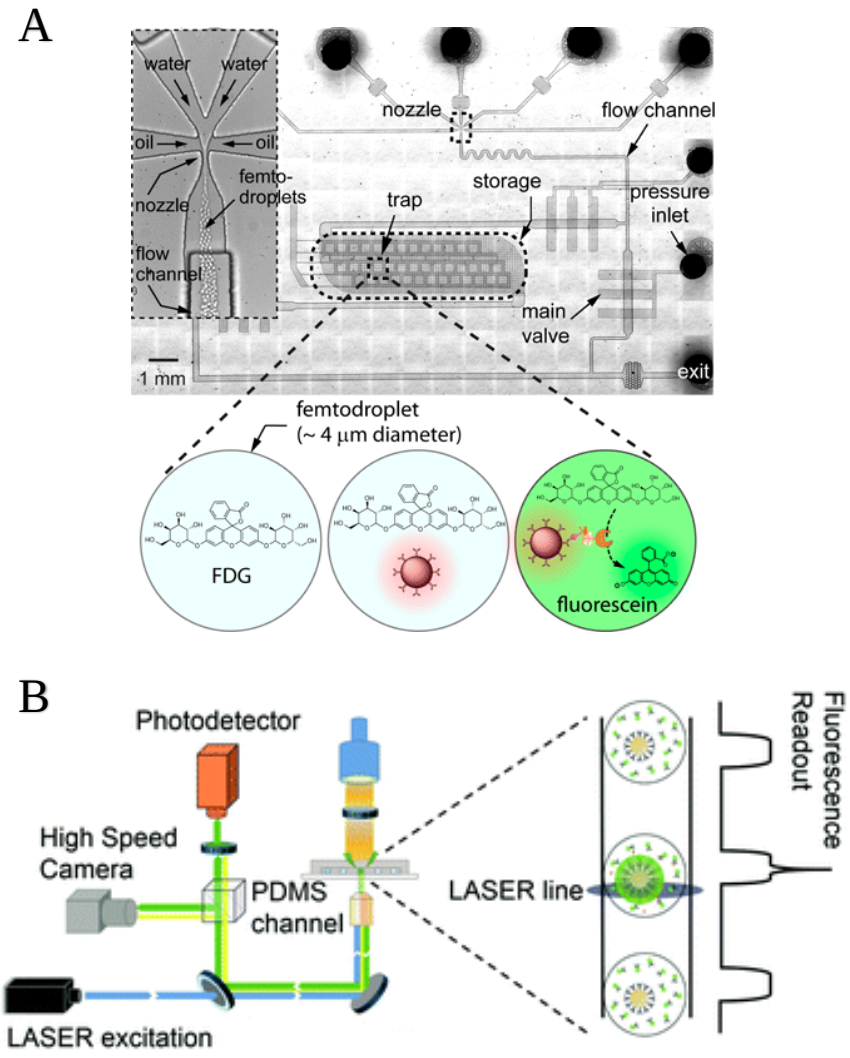

Figure 1.6 Enzyme-linked immunosorbent assay (ELISA) in droplets

(A) Ultrarapid generation of femtoliter microfluidic droplets for single molecule-counting immunoassays. Figure A is reprinted with permission from ref [129] ©2013, American Chemical

Society. (B) One-step immunoassay of C-reactive protein using droplet microfluidics. Figure B is reprinted with permission from ref [72] ©2016, Royal Society of Chemistry.

However, the multiple washing steps, large volume of reagent consumption, and likely insufficiently removal of unbound samples and antibodies can limit the development of standard ELISA immunoassays within droplets. The application of ELISA in small droplet system is also restricted with complicated processing of beads and encapsulating a consistent amount of beads in each droplet. The emergence of homogeneous assays not only overcame the workflow related challenges , consumption of expensive reagents, and long treatment times[72], but they also solved the issues of processing and encapsulating beads. The combination of homogeneous assays and droplet microfluidics should be a simple and rapid method for sample detection. The Niu group designed a droplet-based system with a two-step homogeneous enzymatic assay for real-time continuous measurement of lactate via colorimetry and showed a limit of detection of 0.16 nM[130] (**Figure 1.7A**). Yingzhi et al. developed a droplet microdevice for simultaneously detecting multiple tumor markers with a multiple fluorescence resonance energy transfer (FRET) system. In this type of FRET system, graphene oxide (GO) was viewed as a single quencher, and the multi-color quantum dots (QDs) labeled on different aptamers were used as energy donors. Finally, the detection limits of carcinoembryonic antigen (CEA), prostate-specific antigen (PSA) and vascular endothelial growth factor ($VEGF_{165}$) were calculated to be 0.15ng/mL, 0.035ng/mL, and 0.11ng/mL in this system, respectively[131] (**Figure 1.7B**).

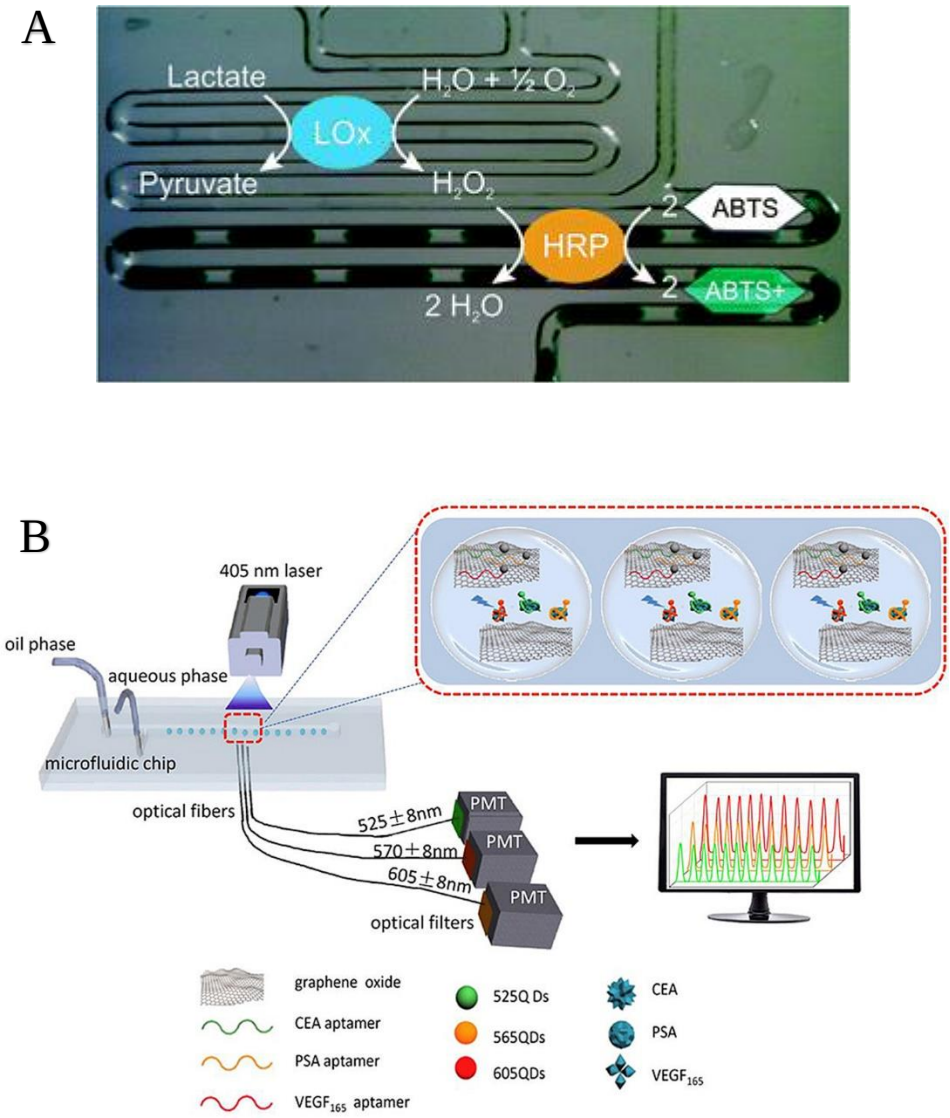

Figure 1.7 Homogeneous assays in droplets

(A) A droplet-based device for real-time continuous lactate measurement with homogeneous enzymatic assays. Figure A is reprinted with permission from ref [130] ©2019, Royal Society of Chemistry. (B) Simultaneous quantitative detection of multiple tumor markers in microfluidic nanoliter-volume droplets. Figure B is reprinted with permission from ref [131] ©2019, Elsevier.

The combination of polymerase chain reaction (PCR) and immunoassays has been approved to have the ability of enhancing the sensitivity of traditional immunoassays in past decades. For analysis of biomolecules and cells with shorter assay time, rapid heating/cooling, and portability, droplet-based PCR platforms were developed by several groups. The Weian Zhao group used the integrated comprehensive droplet digital detection (IC3D) system to simultaneously perform bacterial identification and antibiotic susceptibility from whole blood specimens. This IC3D blood ddPCR permitted high sensitivity (10 CFU per ml) in antibiotic resistance bacteria detection in only one hour[132] (**Figure 1.8A**). Deniz et al. developed a droplet-based method based on digital PCR for quantifying the mutation in *KRAS* oncogene. In this system, the sensitivity was improved by at least a factor of $\sim 10^4$ and DNA could be quantified down to 1 mutant *KRAS*gene in 200 000 wild-type *KRAS*genes with $\sim 10^6$ fluorescent droplets. These results indicate this platform has the potential of sensitively detecting the specific cDNA from early stage tumor[133](**Figure 1.8B**).

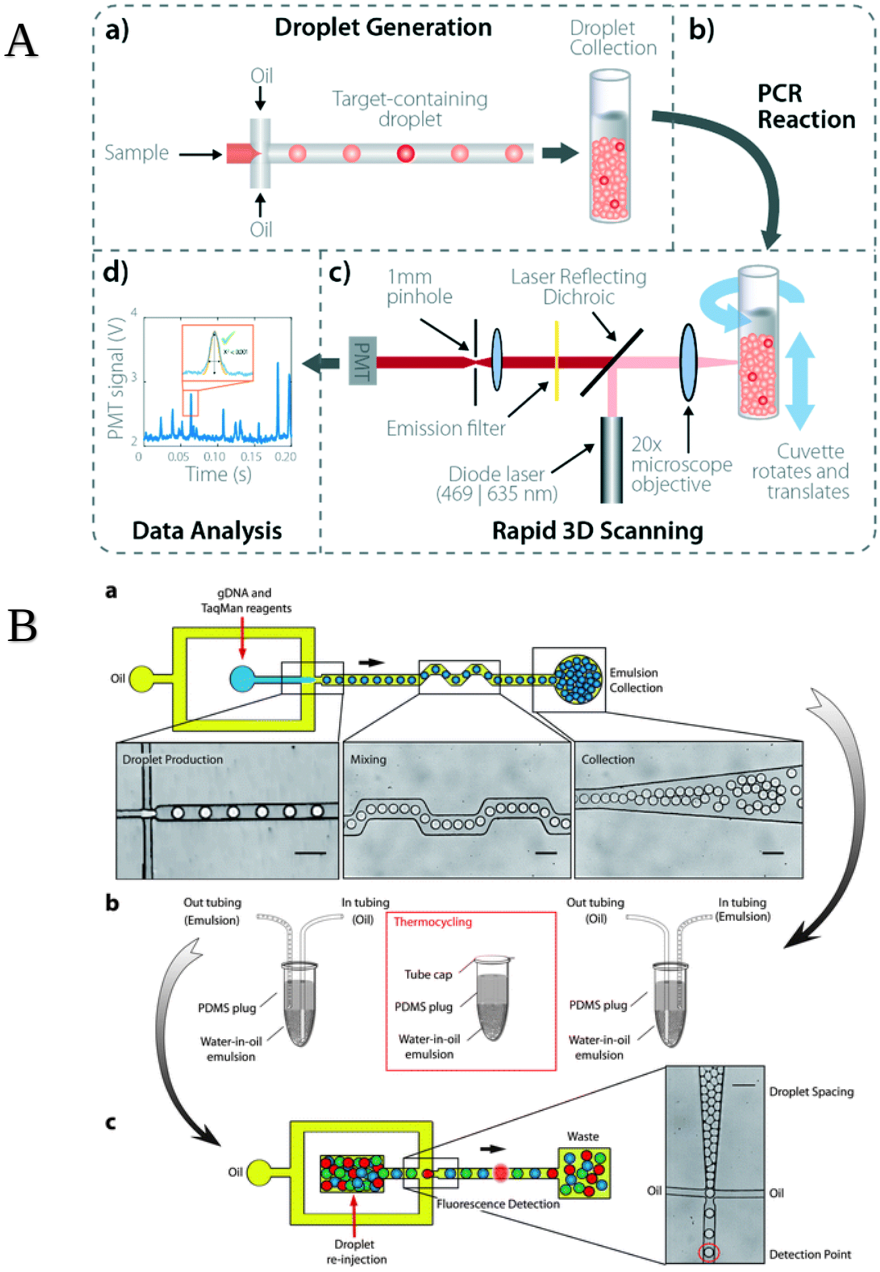

Figure 1.8 Polymerase chain reaction (PCR) in droplets

(A) Rapid bacterial detection and antibiotic susceptibility testing in whole blood using one-step, high throughput blood digital PCR. Figure A is reprinted with permission from ref [132] ©2020, Royal Society of Chemistry. (B) Quantitative and sensitive detection of rare mutations using

droplet-based microfluidics. Figure B is reprinted with permission from ref [133] ©2011, Royal Society of Chemistry.

One obvious drawback in these systems is that samples encapsulated in droplets have to be manually transported from microchip to thermal cycler for accomplishing PCR in **Figure 1.8**. To simplify the detection process while retaining the sensitivity, the concepts of modular and fully integrated analysis on-chip with isothermal amplification were introduced. To break through the bottleneck of temperature management in microchip, droplet-based isothermal amplification techniques were developed. The modular approach means integrating multiple unique microchips to accomplish the full workflow of complex biological analyses[134]. For automated measurements of single-cell miRNA in a high-throughput manner, Chen and co-workers combined two droplet-based microchips as in **Figure 1.9A**[135]. In this automatic system, two micro-devices were fabricated, one to generate and one to detect target droplets, which contained single cells and reagents for miRNA analysis. However, the essential requirements of internal/external pumping, sensitive readout equipment, and the high demand of droplet-control technique (generation, flowing, merging, sorting, etc.) motivated other simpler, non-flowing analysis devices. Instead of using flowing systems for droplet formation for digital methods, a well-based workflow for digital assays is another powerful concept. By portioning bulk samples into ultra-small container clusters, these microfluidic well based methods can detect nucleic acids, proteins, enzyme activity, or even single-cell genotypes and phenotypes with extraordinarily high sensitivity[136-138]. Among these, the SlipChip developed by the Ismagilov group is an automatic, multipurpose type of digital platform without requiring pumps and valves. With a bottom plate containing preloaded ducts, a top plate that contained wells was used as a lid with fluidic paths, and after alignment and sliding (or

"slipping") of the plates enabled solution contact for diffusional reactions to take place.[139,140] Such devices were used to quantify methicillin resistant Staphylococcus aureus (MRSA) via digital polymerase chain reaction (RPA) amplification (39 ℃) with a detection limit of 300 copies/mL and dynamic range of 1400-10^6 copies/mL on this uniform-size-well SlipChips[141](**Figure 1.9B**).

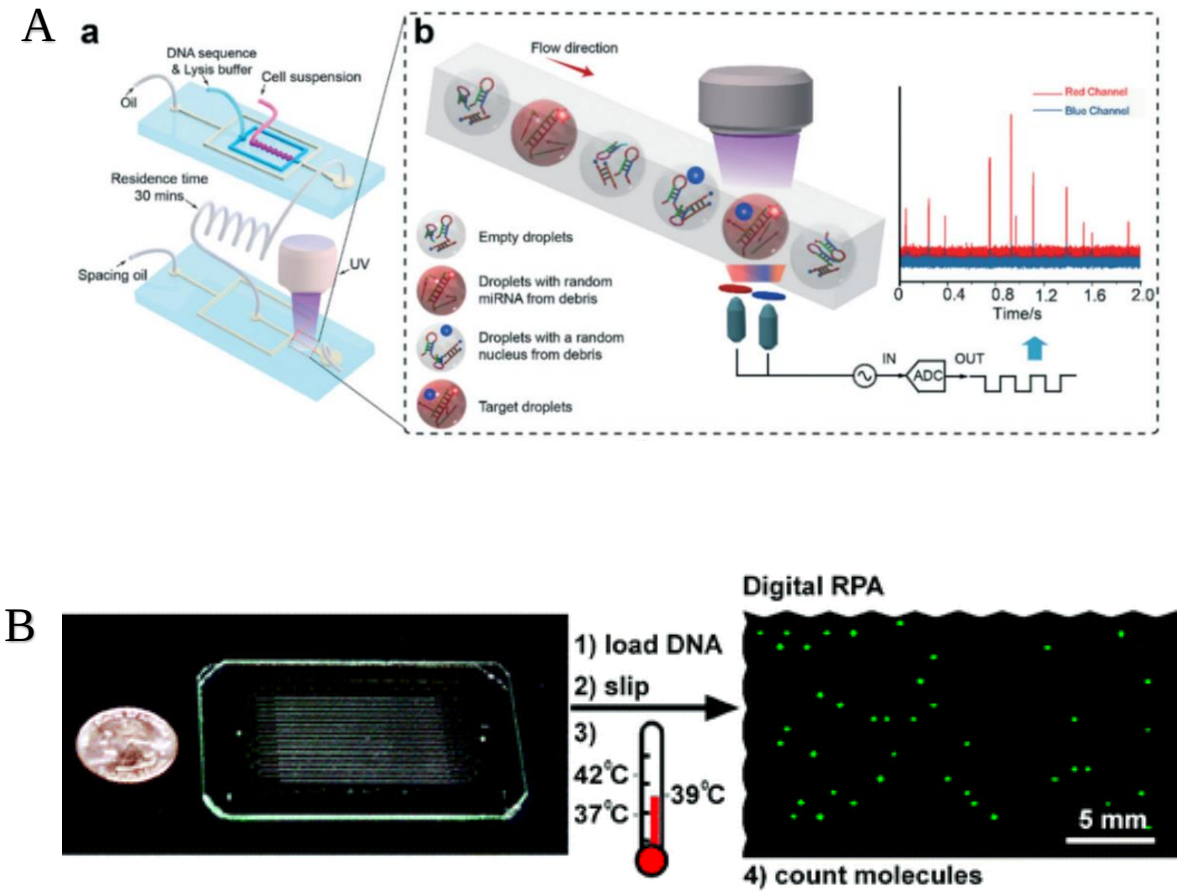

Figure 1.9 Isothermal amplification in droplets

(A) Ultrahigh-throughput droplet microfluidic device for single-cell miRNA detection with isothermal amplification. Figure A is reprinted with permission from ref [135] ©2018, Royal Society of Chemistry. (B) Digital isothermal quantification of nucleic acids via recombinase

polymerase amplification reactions on SlipChip. Figure B is reprinted with permission from ref [141] ©2011, American Chemical Society.

1.3.4 Tissue Engineering and Analysis in Droplet Microfluidics

Introduction

In this part of the document, we will comprehensively review systems that combine tissue engineering and droplet microfluidics by covering cell and tissue culture, related analysis methods, and recent applications. This introduction section will briefly describe conventional and microscale tissue engineering.

Tissue Engineering

Every year, millions of solid organ transplantations are performed worldwide. However, many patients die during the long waiting period to match donor organ sources.[142] Also, chronic rejection and/or destruction over time by the immune system are serious problems for organ transplantation. The field of tissue engineering has emerged, in large part, due to urgent demand of overcoming these issues. Current technology provides the possibility of implanting engineered biological substitutes or of using ex-vivo perfusion systems instead of a real-organ transplantation.[143] By definition, tissue engineering relates to the fabrication of new and functional living tissues by combining living cells, device engineering, new materials, biochemical, and physicochemical methods.[144] Living cells or tissues serve as the core elements of the technology and are viewed as the "heart" of these system around which devices and systems are engineered. Cells are extracted from fluid or solid tissues, and they are normally categorized into seven groups by their sources: autologous cells, allogeneic cells, xenogenic cells, sygenic/isogenic cells, primary cells, secondary cells, or stem cells.

For simulating the extracellular environment of native tissue and supporting the cells' growth *in vitro*, scaffolds are often synthesised to work as essential segments of tissue engineering by providing cells the three-dimensional (3D) architectures for tissue formation and desirable cellular interactions.[145] Some specific requirements are necessary for scaffolds to reconstruct tissue *in vitro*. Firstly, interconnected pores with adequate pore size are demanded to facilitate cell integration and vascularization.[146] Secondly, biocompatibility is an important factor to avoid unwanted tissue response for implants, and biodegradability allows scaffolds to be absorbed by surrounding tissues without extra surgical removal, which promotes the formation of new tissues.[147] For scaffold material selection, the following factors play key roles: material chemistry, polymer molecular weight, surface properties, structure and shape, degradation, and water absorption. What is more, such materials should interact with cells in a way that promotes cellular attachment, growth, and new tissue formation.[148] Over the past decades, an abundance of natural materials (polysaccharides, polypeptides, proteins), synthetic materials (polyglycolic acid (PGA), polylactic acid (PLA), poly-ε-caprolactone (PCL)), and biomaterials (hydroxyapatite (HA), tricalcium phosphate (TCP)) have been investigated for tissue engineering.[149] A variety of methodologies have also been refined for preparing porous scaffolds in tissue engineering, such as nanofiber self-assembly, textile technologies, solvent casting and particulate leaching, gas foaming, emulsification, freeze-drying, thermally-induced phase separation, electrospinning[150,151] or blow spinning[152], CAD/CAM technologies, and laser-assisted bioprinting[153]. To solve the problems of oxygen and nutrient delivery—or mass transport in tissue engineering—several assembly methods including self-assembly, liquid-based template assembly, additive manufacturing, and scaffolding have been explored. Furthermore, tissue culture, creation of interconnected networks of cells/tissues, and on-chip or off-chip analyses are other essential parts of tissue engineering technology.

Microscale Tissue Engineering

Though there are enormous advantages brought by tissue engineering, several difficult challenges still remain, such as construction of vascular networks and creation of adequate approximations of true tissue functions.[154] Constant supplies of oxygen and nutrients as well as removal of wastes and carbon dioxide via blood vessels are basic to the survival of cells in the body.[155] Apart from the several cell types from skin, cartilage, or cornea that enable nutrient and oxygen delivery via diffusion from far-away blood vessels, the vast majority of tissues in the body indeed demand the aid of branched blood vessel systems that are less than 200 μm away from the tissue.[156] Therefore, a sufficient blood vessel system, through true vascularization or sufficient mimics, is very important in tissue engineering. One approach for constructing vascularization is to improve angiogenesis in the tissue scaffolds by seeding endothelial cells (ECs) which can release growth factors for angiogenesis. However, a general drawback of this strategy is that the process is not well controlled, thus growth instabilities can increase the risk of failure. Time of vascularization (or re-vascularization) is also worth considering, since cells may lose viability before proper vessels are formed. Another approach is to synthetically manufacture vascularized scaffolds before implantation of cells, and this method has become feasible with variable biological and synthetic materials and fabrication technologies.

Another major challenge is the difficulty in ensuring proper cell or tissue function after implantation. As scientists have pushed for better standardization and reproducibility of engineered tissues, several unique problems have been uncovered.[157-159] As we know, cell-to-cell contact and tissue architecture play important roles in regulating cell behaviours. On the microscopic level, the whole scaffold provides the boundaries for self-assembly of cells, which is a necessary step in achieving the interactions and communications between cells and to reformat

functional tissue. However, it is difficult to uniformly seed cells throughout the scaffold, because the rapid attachment and proliferation of cells on the scaffold periphery restrict other cells from penetrating to the centre.[160] Altering culture conditions with traditional perfusion systems can address this issue of low seeding efficiency, but this technique is limited *in vitro* systems.[161] Therefore, optimized scaffolds that facilitate both cell and nutrients flow to the centre of its architecture are essential to explore further.

In recent years, microtechnology has provided an effective platform for biomedical and biological application to help tackle these problems. Notably, the application of soft lithography in fabricating microfluidics has enhanced the merging of tissue engineering and microscale technology fields, with microfluidic cell and tissue culture systems showing high potential for addressing the problems mentioned above.[146] Firstly, the scale of microtechnology matches well to that of living tissues, providing large surface-to-volume ratio for nutrient and cell delivery without the need for full vascular systems. For instance, normal diameters of mammalian cells are from 8 to 30 μm, and the common sizes of microfluidic channel are between 10 to 200 μm.[162] Secondly, polydimethylsiloxane (PDMS), the most widely used substrate in the fabrication of microfluidic devices, possesses many benefits when applied as the bulk material of engineered tissues. The material is inexpensive, optically clear, gas permeable, non-toxic, biocompatible, and deformable. Microfluidic devices can thus provide cells adequate nutrients and oxygen through simply or specially designed networks of channels and reservoirs. Thirdly, the application of various physiological stimulations to tissues and monitoring or sampling their responses are readily accomplished with high precision, accuracy, and resolution using microfluidics compared to traditional methods. What is more, the potential for scale-up to complex and powerful micro-bioreactors has aided researchers in achieving lofty goals such as organs-on-chips, which have

already had large influences on biomedical and clinical applications. In recent years, many works involving the combination of tissue engineering and microfluidics have been published[163-173], and we will review such works in this chapter in the context of droplet-based microfluidics. Several recent examples of microscale tissue engineering are shown in **Figure 1.10**.[166,174-176]

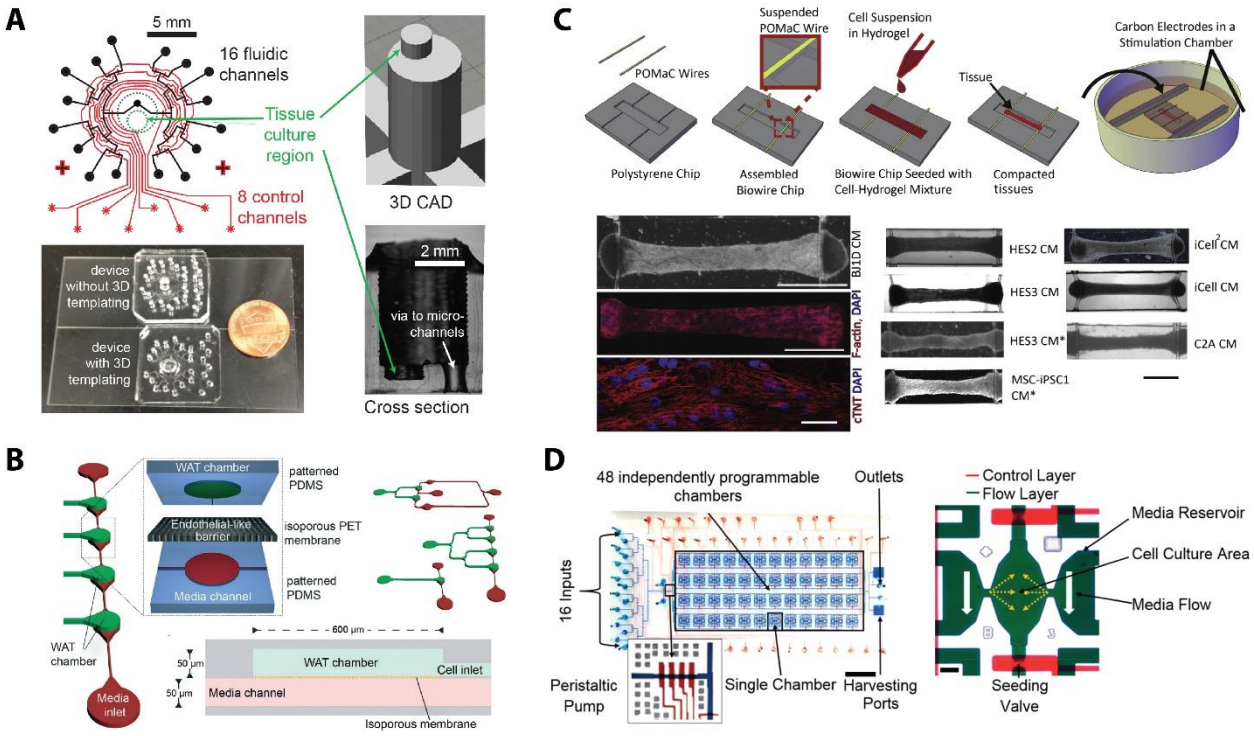

Figure 1.10 Engineered tissue at the microscale

(A) A fully automated, 16-channel microfluidic input/output multiplexer (µMUX) for endocrine tissue culture and secretion sampling. Figure A is reprinted with permission from ref [166] ©2017, Royal Society of Chemistry. (B) Integration of a physiologically relevant microfluidic system for modelling of white adipose tissue (WAT-on-a-chip). Figure B is reprinted with permission from ref [175] ©2017, Royal Society of Chemistry. (C) Biowire II platform for generation of chamber-specific cardiac tissues. Figure C is reprinted with permission from ref [176] ©2019, Elsevier. (D) Microfluidic system for dynamic stimulation and tracking of single cells. Figure D is reprinted with permission from ref [174] ©2018, American Chemical Society.

Analysis of Tissues at the Microscale

With the scaling-down of tissue engineering comes the need for analytical and bioanalytical methods that are suitable to interrogate this smaller size. There are two main strategies used to analyse micro-engineered tissues: off-chip analysis or on-chip (integrated) analysis. To analyse samples gathered from microfluidic devices, conventional off-line analysis methods are still most widely used because many of these methods have yet to be effectively or economically integrated on-chip. Many well-accepted techniques only become quantitative or usable after multiple-step treatments like mixing, incubation, purification, heating, amplification, etc. On the other hand, some analytes demand complicated instrumentation (mass spectrometer, PCR instrument, plate reader) or methods (genomic sequencing, gel electrophoresis, immunoassays)[166,171,173]. While off-chip methods remain the norm, many challenges have yet to be addressed. Compared to common end-point measurements, dynamic monitoring is more accurate and meaningful for tissue detection and medical diagnosis. However, off-chip sampling analysis tends to compromise temporal resolution, thus limiting our ability to understand the dynamic activities of cells and tissues *in vivo*. Particularly, the volumes of samples collected from on-chip tissues can be extremely small and often do not reach the lowest detection volume of some instruments. In addition, the process of sample collection and handling can result in the contamination or even inactivity of targeted analytes. Meanwhile, traditional methodologies usually demand additional time, human resources, and money compared to an equivalent on-chip method.[177]

Direct on-chip measurement is a more convenient and efficient way for sample analysis compared to the off-chip mode. In fact, the inherently small sizes of microfluidic channels, chambers, or reservoirs can offer powerful platforms for quantifying targets with small volumes and for minimizing dilution from cell or tissue samplings. Accomplishing all processes of

sampling, reaction, and detection on-chip can reduce the risks of manual errors and contamination and can minimize waste caused by both manual operations and transportation. In addition, droplet-based microfluidics—a focus in this chapter—can help improve the temporal resolution of tissue sampling and detection[167,178,179], which fits well with the demands of dynamic measurement. However, as expected, there are some additional constraints when using integrated, on-chip analysis. Firstly, applications of widespread heterogeneous assays are restricted on the microchip because extra steps of mixing, washing, and purification are more difficult to achieve on-chip. For more convenient mix-and-read homogeneous assays[167], the needs for mixing multiple reactants and/or long incubation times could still be key issues to overcome for their applications on-chip. Secondly, the hydrophobic property of PDMS can cause adsorption of chemical or biological assay reagents unless effective coating procedures are applied and maintained.

For on-chip analyses, many techniques have been introduced to overcome these challenges in recent years. To enable complex or multi-step biochemical reactions in a microfluidic device, additional on-chip manipulations (mixing, sorting, washing, etc.) are sometimes required. For example, electric fields, magnetic fields, and surface acoustic waves have been applied to improve microfluidic devices' flexibility by the Abate, Bailey, and Huang groups.[127,180-184] Similarly, our group has recently employed on-chip valves for automation of cell and tissue sampling, mixing, droplet formation, reaction, and detection. [167,179] The Ramsey and Kennedy groups have pioneered the integration of microfluidics with mass spectrometry, where assays can work in the platform of the microdevice, and then products could be directly transferred into mass spectrometers for high-performance detection and identification[171,185,186]. Coupling microfluidic chips to capillary electrophoresis is another popular way used by the Roper and Kennedy groups to achieve integrated separation and detection on-chip[187,188]. Considering that on-chip, integrated techniques

should be compatible with ultra-small volumes, low analyte concentrations, or both, optical detection offers an appealing and relatively simple choice. While the small sizes of microfluidic channels makes optical absorbance detection inaccessible for most analytes due to the short optical path lengths, highly sensitive detection via fluorescence excitation and emission is less restricted by the small channels. For this reason, the most commonly used analytical readout for on-chip detection is fluorescence, which can be accomplished with a standard fluorescence microscope or a custom optical system, although it does add the requirement fluorophore-labelled reagents.

Use of Droplet Microfluidics in Engineering and Analysis of Tissue

In traditional biochemical assays, tubes or well-plates are the most common tools for analysing secretion sampling from cells or tissues. In tube- or well-based sampling, not only is a large amount of tissues or cells required, but also the information from such static culture systems can be significantly different from that obtained *in vivo*. Dynamic activities of cells are typically lost by virtue of diffusion and dispersion effects, causing researchers to lose this important information about the target tissues. Even in the earliest days of the technology, microfluidics has been regarded as an important and highly effective tool to analyse and engineer tissues. Over the years, a number of groups have applied continuously flowing fluidics to integrate tissue perfusion and culture with downstream analyses. For example, rapid-injection electrophoretic immunoassays have allowed culture and stimulation of tissue *in vivo* and continuous monitoring of cellular activity[189,190]. While there are a few limitations of these systems, such as the complexity of the flow control and electrophoresis setup or the loss of temporal resolution through dispersion during tissue sampling, these studies have nonetheless proven that microfluidic systems are uniquely qualified for the temporal interrogation of cells[167].

In recent decades, droplet microfluidics has emerged as an appealing platform for studying cellular biology. In a typical droplet-based microfluidic device, monodispersed droplets' diameters range from nanometers to micrometers, imparting several outstanding benefits to researchers. Firstly, each droplet can be regarded as an isolated and well-protected unit for assays and reactions, which can be manipulated individually for operations such as delivery, mixing, sorting, or analysis[64]. Secondly, ultra-small volume reactions (~femtoliters to nanoliters) can be processed inside these droplets, not only saving significantly on experimental reagents, but also enabling unique analyses on single cells or even single molecules[67,128]. Thirdly, compared to traditional reaction scales, droplet reactors can facilitate faster reaction times due to diminished mass transfer times through very short diffusional distances. What is more, monodispersed, nearly identical droplets generated at high throughput (often at kHz frequencies) allow scientists to explore biological systems and generate data sets at larger scales than previously accessible[68]. Numerous biological and clinical applications have been empowered by droplet microfluidics in recent years, such as single-cell genome sequencing analysis[191], protein and nucleic acid quantification[72,73,192], and cellular secretion detection[193].

As reviewed herein, droplet microfluidics displays remarkable potential for both analytical and preperative purposes in the area of tissue engineering. For example, in cellular secretion sampling, the secretory time record can be preserved with high resolution and reconstructed after samples encapsulated in droplets are measured. In contrast to analysis in continuous flow systems where longitudinal broadening restricts the resolution, temporal chemical and biological information can be preserved by digitizing the analogue secretion signal with a droplet-based microfluidic system[167,178,194]. Droplet microfluidics also attracts significant attention for its precision in single-cell analysis, which unmasks the inaccuracies caused by averaging behaviours

of entire cell populations[195]. Encapsulation of single cells into individual droplets makes it possible to sort and culture targeted cells from large cell populations for various purposes downstream[193,196], such as accumulating and quantifying metabolites or even single-cell genetic mapping[197,198]. Additionally, this relatively simple way of generating large numbers of individual droplets enables the examination of phenotypic and genetic variabilities at the single-cell level at ultra-high-throughput[199]. As such, a number of the applications surveyed in our review below have been transformative or have transformative potential to improve our understanding of biological systems.

Cell and Tissue Culture

A principal reason for cell and tissue culture is to isolate different parts from the whole organism for study in experimentally controlled environments. For instance, after removing tissue from an animal, one can maintain its viability in a synthetic, closely controlled medium and keep the tissue alive and functional for extended time periods in which tissue engineering or analysis can take place. The need for standardized nutrients and salts have been established, along with biological media such as serum, and these techniques actually evolved from initial *ex vivo* studies of whole organs or tissue fragments that were kept *in vitro* for varying lengths of time [200]. While the basic methods have been established for many years, innovative concepts continue to emerge, including spheroid systems or microfluidic culture systems, and many of these rely on 3D arrangements of cells and the formation or synthesis of tissue-specific extracellular matrix[201]. Such research has already contributed significantly to our understanding of mammalian biology and physiology.

Cell and tissue Culture Fundamentals

An array of techniques for culturing cell and tissue were available before the turn of the 20th century, most of which were designed with a particular problem in mind [202]. Culture conditions aim to conserve the structure, function, performance, and biology of the cells *in vitro*, and it is important to use sterilized equipment and techniques, prepare appropriate media, conduct cell passaging, properly freeze and store, properly recover frozen stocks, and typically to count workable cells [203]. Different techniques of culturing methodology opened a new era for the advancement in different fields such as virology, morphogenesis, cytology, cytochemistry, toxicology, and molecular biology.

Traditionally, there have been two major types of cultures: primary cultures and cultures of established cell lines. Primary cell and tissue culture are performed from tissues directly taken from a living organism rather than immortalized cells that divide indefinitely. Major advantages of primary cell extraction and culture are that the cells have gone through the various development stages of the organism in the ideal, *in vivo* environment. Researchers have developed thorough protocols to maintain an *in vitro* environment following extraction and ensure viability for varying periods of time. Furthermore, the existence of knock-out animal models permits users the unique opportunity to, for example, compare cells taken from a wild-type mammal and cells derived from a genetically altered mammal [204]. For neurobiological studies, brain tissue can be studied directly in this way. After a brain is removed from an animal, it can be cut into thin sections using a vibratome and kept alive in slice culture. Alternatively, either a brain slice or a brain region can be finely dissected to produce an explant culture. An explant culture can be enzymatically digested into single cells to produce a dissociated cell culture [204]. Primary cells can often show drastically different behaviour and morphology compared to in vitro cultured cell lines [179,205,206], and our group has recently shown this to be true for oscillatory function in adipose tissue [179]. As shown in

Figure 1.11, primary pancreatic islet tissue exists as a highly coupled, multicellular system that exhibits complex spatiotemporal electrical activity such as full-tissue waves of calcium influx [206]. These strong, coordinated calcium waves are not observed in dish-based cell culture. Nonetheless, a major disadvantage of primary cell culture is the limited lifetime of the tissue *in vitro*, and this was the major driving force behind development of immortalized cell lines.

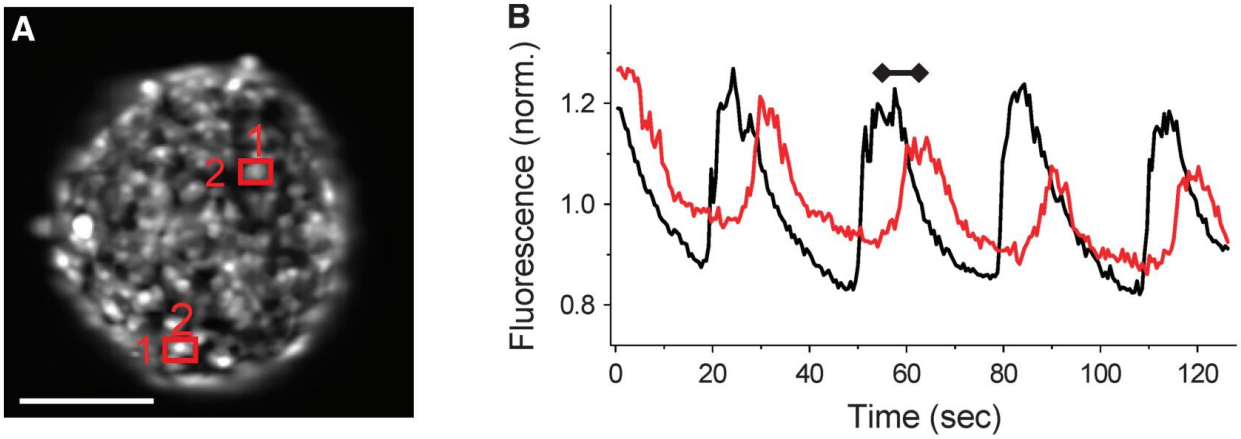

Figure 1.11 Gap junctional coupling in primary pancreatic islet tissue is exemplified by the existence of unique calcium waves

(A) Fluorescence intensity of an islet stained with a calcium binding dye (Fluo-4) in a microfluidic flow device, with two regions of interest (ROIs) marked. (B) Time course of strong calcium waves are shown from each ROI in part A, with a time delay showing evidence of the propagating wave in the tissue. Scale bar represents 100 µm. Figure is reprinted with permission from ref [206] ©2014, Elsevier.

An immortalized cell line is a permanently established cell culture that allows the examination of stepwise alterations in the structural, biological, and genetic makeup of the cells under well-controlled environments [207]. This type of cell culture is more-or-less standardized and does not warrant significant coverage in this chapter. While the function in cell lines often cannot fully recapitulate that of *in vivo* tissues, established cell lines are still highly valuable for complex tissues like the pancreas, which is composed of different cell types and where *in vivo* examination

of single cells is very difficult [207]. Interestingly, organ-on-a-chip based microfluidic systems have recently stimulated major advancements in the usefulness of cell lines, allowing much more realistic modelling of the in vivo organism even while using well-controlled laboratory settings [208].

Off-chip Cell and Tissue Culture

From the microfluidics perspective taken in this book and chapter, cell and tissue culture "off-chip" refers to culture vessels such as flasks, petri dishes, roller bottles, or even multi-well plates—but not a microfluidic chip. Off-chip culture technique usually require a laminar-flow hood or biosafety cabinet as well as a humidified incubator with feedback control of temperature and CO_2 levels. Even today, most biological research depends on individual cell types in petri dishes, using standard culture systems requiring media replenishment manually and regularly on a periodic basis, every 1-7 days [209]. As discussed further in this chapter, microfluidic systems have offered a bridge between such traditional culture models to that of the true *in vivo* environment.

On-chip Cell and Tissue Culture

Again, with a view from the microfluidics perspective, "on-chip" cell and tissue culture allow a reimagining of the cell culture vessel, away from the petri dish and more toward a physical, chemical, and biological environment that closely mimics *in vivo* conditions. Researchers have leveraged their understanding of chemical, biological, biochemical, engineering, and physical systems to develop microfluidic devices and techniques for culturing and studying cells in more appropriate microenvironments [208,210]. By integrating microfluidics and cell biology, scientists have not only proposed to build whole living organs from human stem cell lines, but also to purposefully build minimal functional units that recapitulate tissue and organ-level functions [210]. In one example, cells could be positioned with high precision using micropatterning of

extracellular matrix (ECM) in linear patterns in a microfluidic chamber, and bending of muscle cells during contraction could be carefully measured to determine cell contraction forces under flow [211]. In another example, the Wheeler group took advantage of the computer automation provided by their droplet digital microfluidic (DMF) systems, and they developed a platform that moves the standard mammalian cell culture techniques to the microscale using droplets [212]. The system was capable of growing mammalian cells, frequently seeding new generations in fresh media. An image of their DMF device, which was formed from an array of electrodes used to manipulate the discrete fluidic system, is shown in **Figure 1.12**.

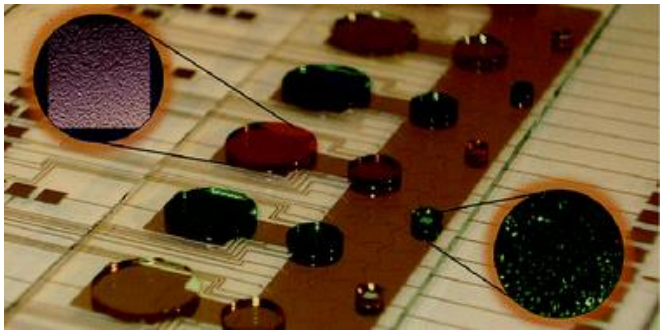

Figure 1.12 Droplet-based digital microfluidics (DMF) was used to automate multi-step cell culture at the microscale

Figure is reprinted with permission from ref [212] ©2010, Royal Society of Chemistry.

Organs-on-Chips or Microchip-based Bioreactors

With the insurgence of organ-on-a-chip systems over the last decade, intense research focus has been placed on the engineering of devices to culture cells and tissues in vitro. From an engineering standpoint, the terms "Organ-on-a-chip" and "Micro-Bioreactor" are considered by some as equivalent terms, both designed for optimal cell-type-specific biological environments at the microfluidic scale [213]**.** Whether for understanding human physiology, drug development, or

bioprocess development, these systems are considered highly valuable, cutting-edge tools in biotechnology [208,214].

One way to delineate the essential functional components necessary for the design of these systems is to use Hubka-Eder mapping [215], allowing one to investigate how the multiple integrated functions can be configured[213]. While the expected usage and outcome of devices will be variable, the connections between biological modules will usually be similar. Examples include a rack of small micro-bioreactors with optical sensors at the bottom of each vessel, compact artificial liver bioreactors with liquid and gas exchange, or small channels with core membranes for transepithelial electrical resistance measurements (TEER) for drug diffusion studies [213]. Other interesting examples include devices developed by the Eddington group, which were shown capable of forming stable oxygen gradients over cells or tissues by leveraging diffusion through polydimethylsiloxane (PDMS) membranes [216,217]. Their systems have been used to study hypoxia-induced activation of transcription factors in human endothelial cells[218] (**Figure 1.13**) or hypoxia-related impairment of encapsulated pancreatic islets (rat and human) [217]. Continuous bioreactor designs can be designed to continuously refresh media and to use feedback regulation of variables (temperature, pH, nutrients, etc.), resulting in mammalian cell chemostats [219]. A number of analogous systems have been developed and reviewed elsewhere, but are outside the scope of this chapter.

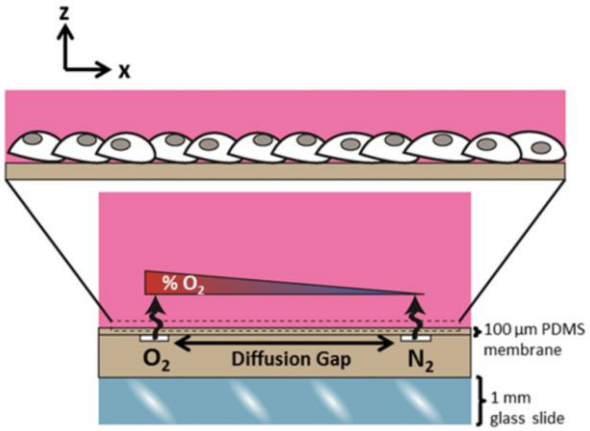

Figure 1.13 Constant perfusion of compressed oxygen and nitrogen gases into micro-channels It allows precise control of spatial gradients of oxygen. Hypoxia-induced effects on cell or tissue function can be studied in this way. Figure is reprinted with permission from ref [218] ©2017, Oxford University Press.

Human Cell Derived Tissues On-chip

Recently microfluidic systems are being used for stem cell culture, processing, and manipulation, and functionalities include trapping, sorting, and categorizing of stem cells and their analysis [220]. For example, geometry based trapping methods have used polyethylene glycol microstructures to capture mouse embryonic stem cells[221], or predictable laminar flow combined with microfabricated geometric obstacles[222]. With this approach, defined pairing of two cell types in close proximity was accomplished and used for the fusion of embryonic stem cells[222]. Another microfluidic cell trapping device aimed at single cell analysis features 2048 single-cell traps, analysed using automated image cytometry[223]. Zhang et al. [224] developed a cell separation device, where stiff cells are trapped in micro-barriers while deformable stem-cell like cells, such as metastatic cancer cells, pass through the sorting device. Water-in-oil droplets have also been leveraged to encapsulate cells for long-term culture[225], and this methodology is discussed further below.

Ex-vivo Tissue Culture on-chip

Measurements or experiments that are done with tissue from outside of an organism in an external environment, if possible by minimally changing the natural conditions, are referred to as *ex-vivo* tissue culture. Comparing to *in vivo* experiments, *ex vivo* studies have some unique benefits, including the ability to study multi-cellular tissues, organs, or micro-organs that have fully developed in their natural environment within the organism prior to experimentation. To obtain adequate amount of cells in culture and experiments, *ex vivo* methods involve living cells or tissues extracted from a living organism by surgery, then cultured in a microdevice under sterile conditions that mimic the tissue's natural atmosphere as closely as possible. Microfluidic systems with continuous perfusion have already been shown to be highly useful for *ex vivo* tissue experiments compared to traditional static culture systems that do not incorporate continuous media exchange, especially for long term culture [226-228]. *In vivo* experiments are much more technically challenging and are not usually able to maintain nutrients, oxygen, or other solution delivery rate because of dependency on environmental and physiological factors such as stress, exercise, and diet. On the contrary, continuous media perfusion can be applied to *ex vivo* tissue, which leads to consistent media composition and consistent supply of nutrients and removal of wastes[226,229].

Recently Xiao et al.[227] presented a device consisting of multiple interconnected, modular culture chambers. Tissue explants were connected by microfluidic channels and electromagnetically actuated micropumps to drive media flow and physiological hormones. This system (example shown in **Figure 1.14**) was able to co-culture ovary, fallopian tube, uterus, cervix, and liver explant tissues in series, and it also allowed for hormonal and cellular communication to occur between the tissue chambers. Importantly, the murine ovarian follicles were shown to

produce the human 28-day menstrual cycle hormone profile, and this output was able to control human female reproductive tract and peripheral tissue dynamics. This kind of *ex vivo* culture system provides evidence of the strong capability of microfluidics to be used to boost culture times, viability, and functionality of complex tissue and organ modules and to aid in our understanding of physiological systems.

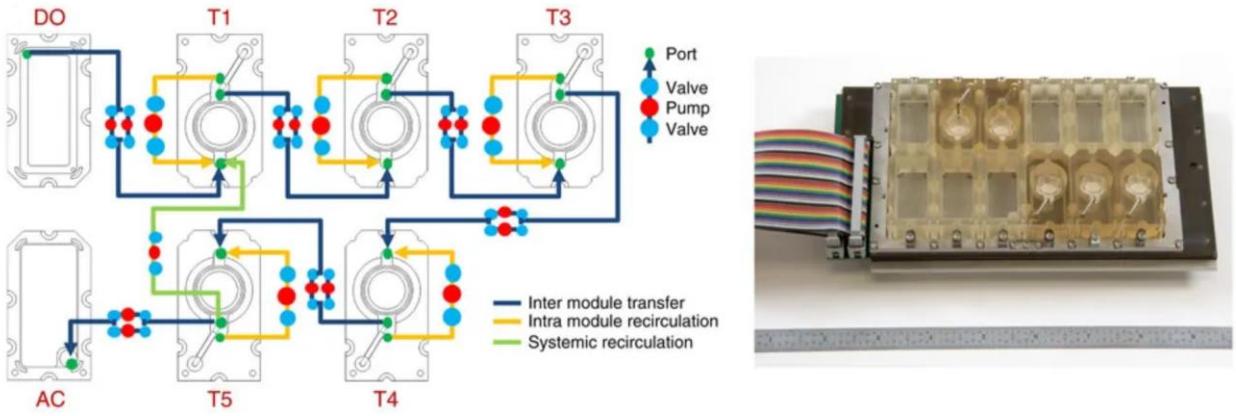

Figure 1.14 Explants of ovary, fallopian tube, uterus, cervix, and liver tissues were cultured and connected in series using microfluidic modules

This interconnected system of tissues was shown to recapitulate function of the human reproductive tract and exhibited a 28-day menstrual cycle. Figure is reprinted with permission from ref [227] ©2017, Royal Society of Chemistry.

Droplet Enabled Cell and Tissue Culture

While we focus more of this chapter on droplet-enabled analysis of cells and tissues, a number of important studies have shown that microfluidic droplet formation can be used as a unique preparative tool in cell biology. Xu et al. [230] used microfabrication to form droplet arrays that gelled into columns on a microdevice, providing a sandwich structure with liquid on top, cells in the middle columns, and gas exchange channels on bottom. This easy-to-use system was shown to provide high cell viability and should be useful for high throughput studies. Agarwal and

coworkers [231] showed that a droplet-based microfluidic system could be used for one-step generation of mouse embryonic stem cell-laden microcapsules that consisted of an alginate hydrogel shell and an aqueous liquid core of cells (**Figure 1.15**). The cells showed high viability, and they compared the cardiac differentiation to conventional hanging drop models [231].

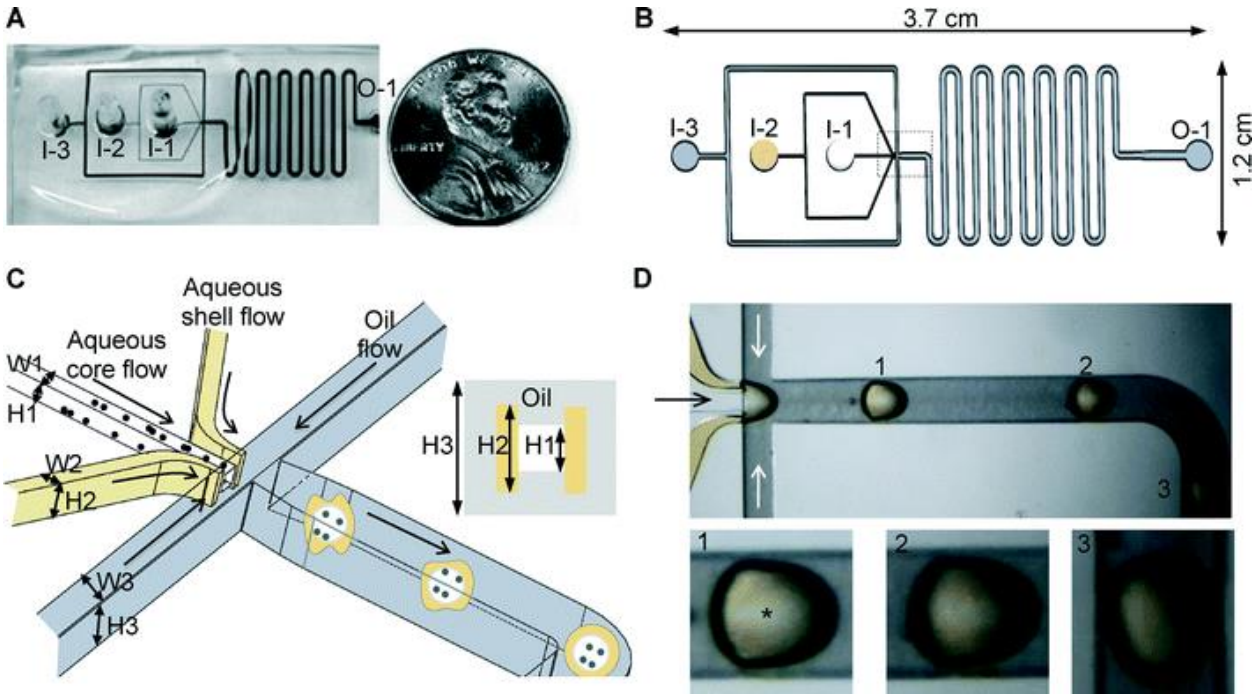

Figure 1.15 Droplet-based microdevice enabled fabrication of alginate hydrogel shells with an aqueous liquid core of cells with a simple, one-step workflow.
The internal cells showed high viability and their cardiac differentiation was similar to conventional hanging drop models. **(A)** Device overview, **(B)** schematic, **(C)** 3D depiction of flow-focusing junction, and **(D)** typical images of droplets showing gradual formation of the shell. Figure is reprinted with permission from ref [231] ©2013, Royal Society of Chemistry.

Water-in-oil droplets combined with unique, photopolymerizabel material properties have also been leveraged to encapsulate cells for long-term culture. Oakey and coworkers[225] showed that human lung adenocarcinoma epithelial cells (A549s) could be maintained viable for weeks within their microfluidically generated polyethylene glycol norborene (PEGNB) droplets, which

were polymerized with UV light after making the emulsion on-chip. This droplet microencapsulation approach was shown to generate cell-laden hydrogel microspheres at high rates, with monodisperse size distributions, and with high long-term cell viability that outperformed current materials. Similarly, in our recent work, we were able to encapsulate 3T3-L1 adipocytes (fat cells) into agarose droplets using a valve-controlled droplet generator, then we used the resultant adipocyte spheroids as biological controls to compare the function of cell lines to *ex vivo* murine adipose tissue explants [179]. These types of studies show that microfluidic droplet formation provides an innovative tool for culture of cells by enabling generation of micrometer-scale containers laden with cells or tissue.

Integrated Droplet-based Analysis of Cells and Tissues

Our group and others have validated continuous-flow, microfluidic sampling as a powerful method of studying dynamic changes in metabolites such as insulin, glucose, glycerol, and fatty acids in pancreas, liver, and adipose tissues.[165,166,170,171,191,232] Nonetheless, the problem of longitudinal broadening—through dispersion and laminar diffusion within microchannels—has persisted as a major limitation on temporal resolution of sampling and analysis from cells and tissues. This loss of resolution can result in the loss of important and detailed information about biological activities. Additionally, single-cell analyses in the continuous-flow setting is limited due to the very small amount of starting material. Although droplet microfluidics has already been recognized as a powerful tool for single-cell analysis, there has been little research on the dynamics of single cell behaviour, such as single-cell like breakdown, absorption of nutrients, and uptake/release of metabolites.[167,195] In this realm, we contend that droplet microfluidics can provide unique analytical solutions. Droplet sampling is known to preserve temporal chemical information[167,178,179], even at the millisecond time scale if carefully designed.[194] Moreover, clever

manipulation of time- and frequency-domain chemical information contained in droplets can be shown to drastically improve analytical sensitivity.[195,233,234]

Using these enhancements in analytical sensitivity, our lab recently quantified the amount of the labelled free fatty acid (FFA*) that was taken up by single 3T3-L1 adipocytes using a droplet-based microfluidic system via lock-in analysis.[195] Precise nanoliter flow control was enabled by active, pneumatic push-up valves (Quake style[235]), allowing droplet formation to be strictly phase-locked to the fluorescence emission detector at narrow bandwidth (±0.04 Hz) for droplets generated at 3.50 Hz. Using this "μChopper" concept[233], alternative generation of sample and reference droplets (**Figure 1.16A**) allows real-time detector drift correction, permitting very low signals to be recovered from noise. Compared to conventional single droplet fluorescence detection, the noise magnitude was reduced by more than 50-fold (**Figure 1.16B**). Rather than averaging the cell population, this μChopper system could precisely quantify single-cell FFA* uptake rates in 3T3-L1 adipocytes to be $3.5 \pm 0.2 \times 10^{-15}$ mol cell^{-1} for the first time (**Figure 1.16C**). Overall, the μChopper was able to reduce limits of detection (LODs) in absorbance[233] and fluorescence[195] by as much as 200-fold and 50-fold, respectively. We propose that significant performance enhancements should be achievable in various other detection modes, whether using optical readout, electrochemical detection, mass spectrometry, etc.

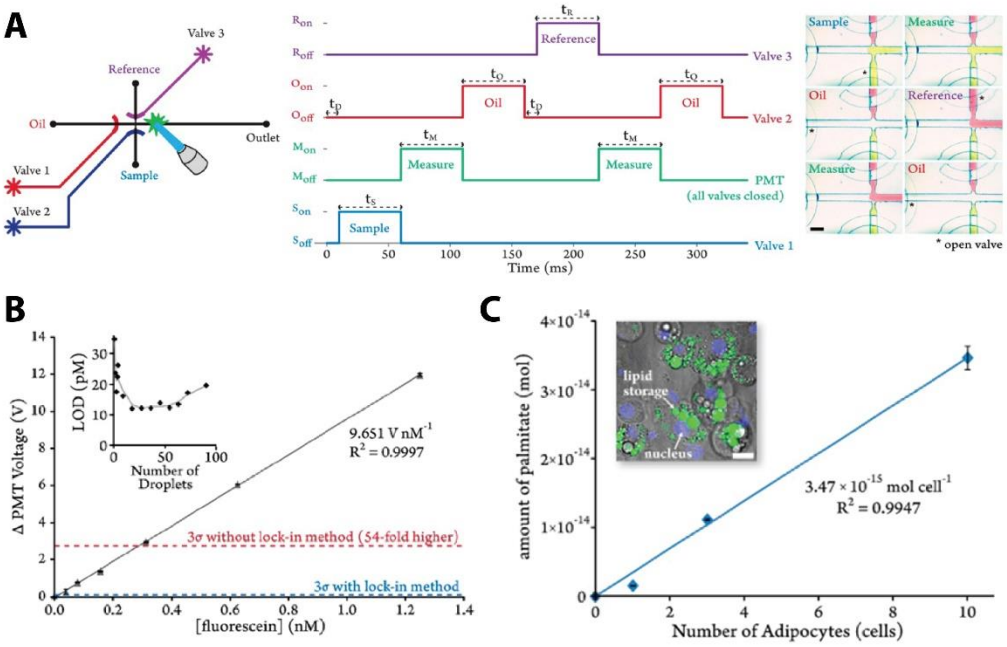

Figure 1.16 Lock-in detection with the μChopper device concept

(A) Automated device with valve-controlled segmentation of sample, oil, and reference liquids. (B) With noise reduced by more than 50-fold, an LOD of 12 pM fluorescein was achieved with standard microscope optics. (C) Single-cell fatty acid uptake by 3T3-L1 adipocytes was quantified for the first time with the μChopper system. Figure is reprinted with permission from ref [195] ©2017, American Chemical Society.

Realizing the importance of improving temporal resolution to interrogate tissue secretions, Easley et al.[178] developed a novel passive droplet-based microfluidic sampling method to monitor glucose-stimulated secretion of zinc ions from pancreatic islets with high temporal resolution (**Figure 1.17**). Zn^{2+} secretion sampled and stored into a continuous stream of small droplets (~0.5 nL) preserved the temporal information and allowed reconstruction of the secretory time record through downstream analysis (**Figure 1.17A-C**). Bursts in Zn^{2+} secretion as high as ~800 fg islet^{-1} min^{-1} were captured and quantified, and two major classes of rapid and slow oscillations (~20-40 s and ~5-10 min) were observed. In later work from our group, we showed that automation of

the secretion sampling μChopper with pneumatic valves could be combined with a customized, mix-and-read immunoassay to monitor insulin secretion directly at high temporal resolution[167] (**Figure 1.17D-H**). During secretion sampling of single pancreatic islets, bursts in glucose-stimulated insulin secretion were captured into droplets at 15-second temporal resolution, revealing fast insulin secretion oscillations (~20-30 s) which matched with the timing of well-known calcium signals within islets.[236]

These systems provide clear validation of the effectiveness of droplet-based sampling for high-resolution analysis of cells and tissues. By integrating passive[178] or automated[167] droplet sampling with on-chip tissue culture, reagent mixing, on-chip homogeneous assay incubation, and optical readout through lock-in detection, these unique analytical systems revealed bursts in secreted ions or hormones that had previously not been quantified from tissue.

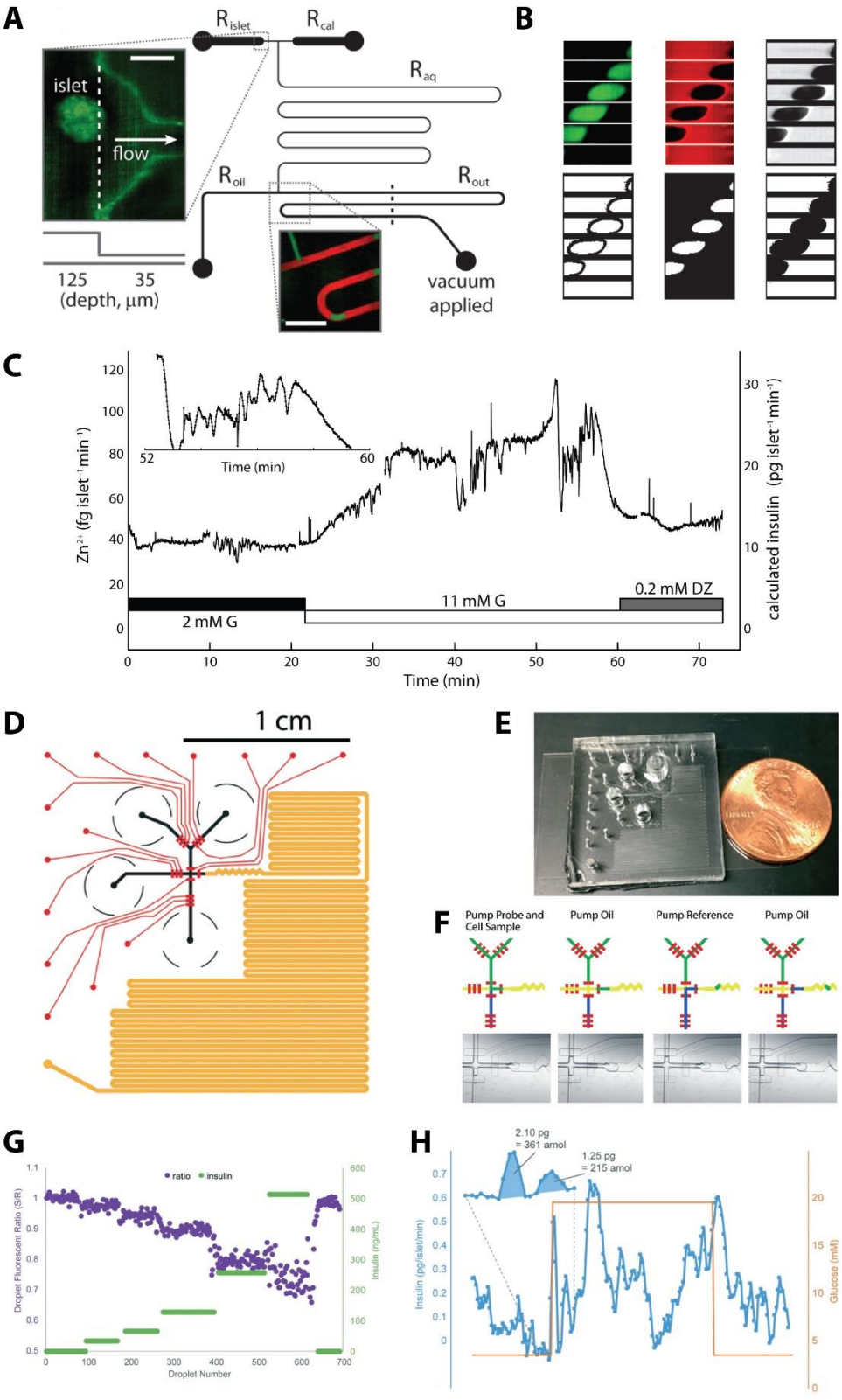

Figure 1.17 Droplet-based secretion sampling at high temporal resolution with µChopper

(A) Device layout for passive sampling. (B) Novel image analysis for phase-locking droplet signals to oil signals. (C) Zn^{2+} secretion from pancreatic islet tissue was sampled into droplets and quantified by lock-in analysis, allowing the capture of bursts of secretion under showing both rapid and slow oscillations (~20-40 s and ~5-10 min). Figure A-C are reprinted with permission from ref [178] ©2009, American Chemical Society. (D) Device layout for automated secretion sampling and lock-in analysis. (E) Image of complete device. (F) Automation of μChopper workflow. (G) Homogeneous immunoassays showed predictable sample-to-reference ratios (S/R) as a function of insulin concentration, with an LOD of 10 amol in a single droplet. (H) Single-islet insulin secretion rates shown in pg $islet^{-1}$ min^{-1} (blue) along with imposed glucose waveforms (orange). This device gave 15 second resolution and observed both fast and slow insulin oscillations, with burst on the order of hundreds of attomoles. Figure D–H are reprinted with permission from ref [167] ©2018, Royal Society of Chemistry.

Recent Applications in Tissue Engineering and Analysis with Droplet Microfluidics

In this section, we review recent applications of droplet-based microfluidic devices to analyze and interrogate cells and tissues. These applications are organized based on the cells or tissues studied, and coverage includes the bioanalysis of hepatocytes, pancreatic islets, adipose tissue, and neuronal cells.

Hepatocytes

Hepatocytes take up 70 to 85% of the liver and carry out most of the metabolism and biosynthetic processes in the liver. However, the effects of insulin and glucagon on hepatic metabolism have not been extensively investigated.[143,168] The Roper group developed a modular microfluidic system to monitor the growth and function of HepG2 cells (human hepatocarcinoma cell line).[168] This bioreactor included a cell culture incubator for HepG2 growth, automated perfusion for delivering glucose and insulin stimulants, droplet-based sampling and mixing with enzymatic assay reagents, and on-line optical detection for measuring glucose consumption by the HepG2 cells (**Figure 1.18A**). Another modular bioanalysis platform integrating a cell culture device and a droplet-generating device was introduced by the Revzin group for multiplexed analysis of injury response of hepatocyte spheroids.[134] Three types of secretion—glucose, total bile acids, and lactate dehydrogenase (LDH)—were monitored simultaneously with colorimetric and fluorescence detection methods in this automated droplet-based microfluidic system (**Figure 1.18B**). To investigate cell-to-cell communication in the liver, the Revzin lab also introduced a device to fabricate microcapsules with liquid core and polyethylene glycol (PEG) shells to assemble and culture rat hepatocyte spheroids inside[237] (**Figure 1.18C**). The functions of encapsulated hepatocytes, the hepatic gene expression, and the interaction of 3T3-J2 fibroblasts and hepatocytes were demonstrated in this work. Similarly, the Weitz group recently reported a

method that applied biocompatible 3D core-shell hydrogel scaffolds to construct tissue-in-droplets.[238] Highly permeable water-water-oil (w/w/o) double emulsions were used to create hepatocyte cores with fibroblast shells, giving "artificial liver" spheroids that were used to study cell-cell interactions (**Figure 1.18D**). With the alternative approach using their digital microfluidics (DMF) devices, the Wheeler group developed a microfluidic organoid culture device for drug screening (MODS).[239]. Individual, free-floating, and 3D hydrogel-based liver organoids were generated and cultured on-chip for studying cytochrome P450 enzyme activity and hepatotoxicity with the MODS platform (**Figure 1.18E**). By co-culturing HepG2 and NIH-3T3 cells in droplets, the resultant hepatic organoids demonstrated fibroblast-dependent contractile behaviour and favourable albumin and cytochrome P450 secretion activities.

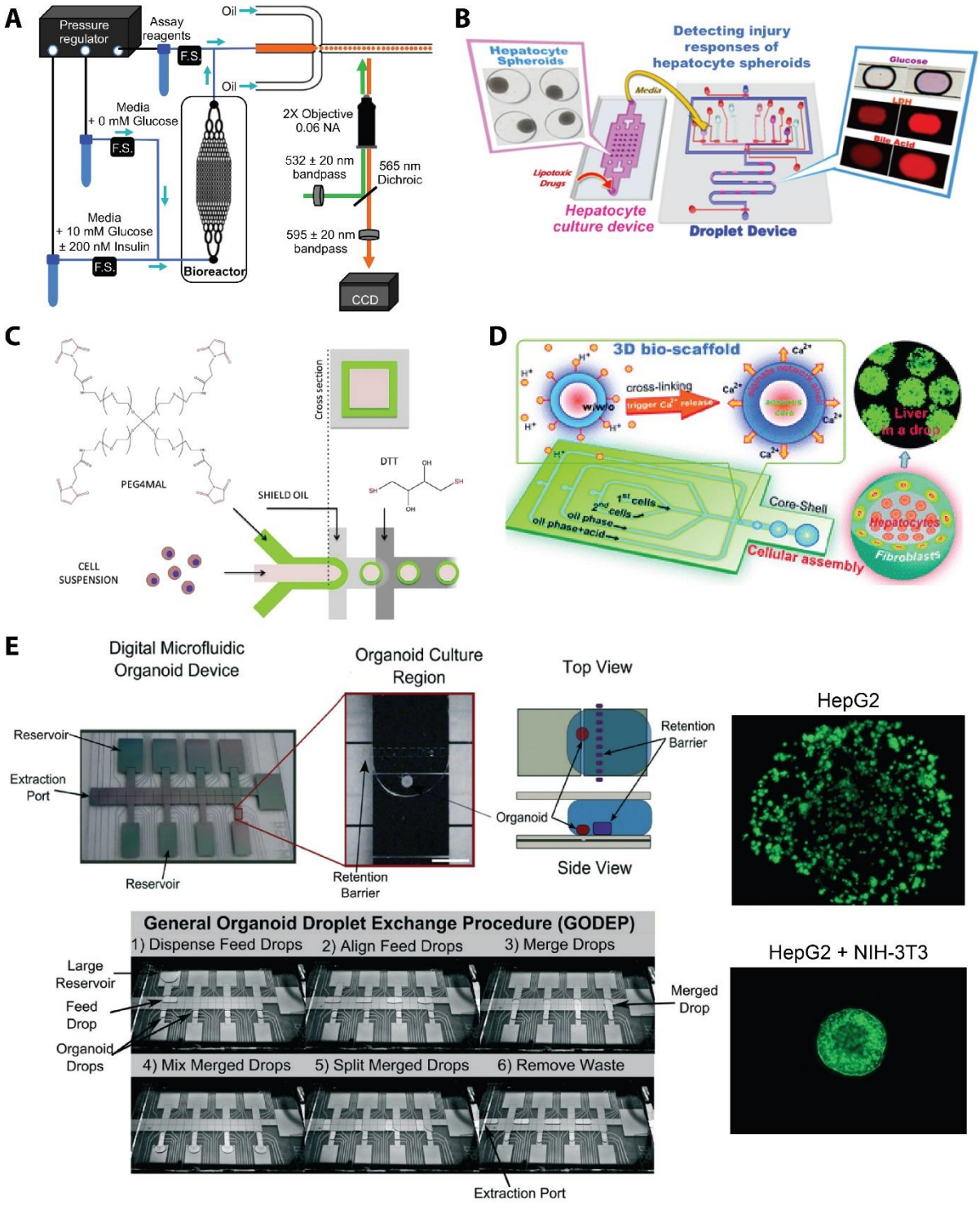

Figure 1.18 Hepatocyte culture and analysis with droplet-based microfluidics

(A) Schematic of integrated system for perfusion, droplet sampling, and online glucose consumption analysis of HepG2 cells. Figure A is reprinted with permission from ref [168] ©2019,

American Chemical Society. (B) Multi-analyte secretory analysis (glucose, total bile acids, lactate dehydrogenase) with a modular system of cell culture device coupled to a droplet sampling and analysis device. Figure B is reprinted with permission from ref [134] ©2019, American Chemical Society. (C) Device used to fabricate PEG/hepatocyte spheroids. Figure C is reprinted with permission from ref [237] ©2017, Elsevier. (D) Multicellular core-shell capsules were generated using droplet-based microfluidics to make artificial liver spheroids. Figure D is reprinted with permission from ref [238] ©2016, Royal Society of Chemistry. (E) Microfluidic organoids for drug screening (MODS) were made with digital microfluidics (DMF) automation. Figure E is reprinted with permission from ref [239] ©2014, Royal Society of Chemistry.

Pancreatic Islets

The exocrine pancreas produces and releases digestive enzymes for nutrient digestion and absorption, while the endocrine pancreas—consisting of the islets of Langerhans—are central to the endocrine system for maintaining glucose homeostasis. The pancreas is thus a key organ in both the digestive and endocrine system. Here we will focus on pancreatic islets; the importance of understanding this small organ (i.e. microorgan) for research and clinical purpose has been well-established.[240] In recent decades, droplet-based microfluidics have been approved as an important tool to investigate the function and properties of the pancreatic islet in microscale. In fact, we have already presented and discussed a variety of microdevices that were used to study islets (**Figure 1.17**[167,178]), and we have discussed several groups that are active in this area, including our own group. In other work, Chen et al.[241] developed a droplet device to encapsulate rat islets with an oxygen-sensitive dye. They quantified secreted ATP and insulin under varying protocols, and they demonstrated the effects of oxygen consumption rate on the metabolism and function of islets within the hydrogel microcapsules. Hai-Tao Liu et al.[242] introduced a unique biocompatible water-in-water droplet system, controlled by valves, to encapsulate and culture rat pancreatic cell lines (β-TC6), where PEG and dextran were used as continuous and dispersed phases, respectively.

Insulin secretion was measured, and the system was shown to have strong potential for tissue engineering applications. In earlier work, to probe the dynamics of stimulated islets with good temporal resolution, Ismagilov and co-workers developed the "chemistrode"[243], a droplet-based microfluidic system coupled with off-line detection instruments (fluorescence correlation spectroscopy, MALDI-MS, fluorescence microscopy, ELISA).

Adipose Tissue

Adipose tissue is a complex, essential, and active metabolic and endocrine organ that sends out and responds to signals that involve modulating appetite, energy expenditure, insulin sensitivity, bone metabolism, inflammation, and immunity. Adipose tissue accounts 5 to 50% of the human body weight and can be divided into two major types: white adipose tissue (WAT) and brown adipose tissue (BAT).[244-246] Though our understanding of adipose tissue has improved greatly in the past several decades, some functions and mechanisms of this organ are still mysterious to researchers because of constraints on traditional bioanalytical methodology. Droplet microfluidics offers unique platforms for investigating adipose tissue at the microscale, which are cost-effective, low volume, high spatial and resolution. Sakai and co-workers reported a microfluidic flow-focusing system where gelatin (high cell adhesiveness, nontoxicity, and biodegradability) was used as material for engineering tissue.[247] This device enabled continuous generation of small droplets, and adipose-derived cells were encapsulated (**Figure 1.19A**). Rather than encapsulating the cells, Deveza and co-workers introduced a droplet-based microfluidic device to produce biodegradable PEG-based microspheres for controlling release of growth factors and DNA nanoparticles (**Figure 1.19B**)[248]. In this work, the mesh size and degradation rate of droplets were studied at varying concentrations of PEG polymer from 7.5 to 15% (w/v), which

would determine the release rate of encapsulated proteins and DNA. Released growth factor was studied for its effects on adipose-derived stem cells (ADSCs).

In work using droplets for high resolution analysis of adipose tissue, our laboratory has recently improved our automated μChopper concept to achieve an unprecedented resolution of 3.5 seconds, and this device was applied for secretion sampling from primary murine adipose explants[179] (**Figure 1.19C**). In this study, both of peaks and valleys of glycerol secreted from cells and tissues of wild-type, aged, and obese mice were captured. Sampling *ex vivo* epididymal white adipose tissue (eWAT) explants from mice, previously unreported rapid oscillations in glycerol secretion at frequencies of 0.2 to 2.0 min^{-1} (periods of ~30 to 300 s) were demonstrated, enabled by the high temporal resolution; these oscillations were not present in clustered cell lines. This study is the first to report cell-to-cell communication in adipose tissue that is similar to that of pancreatic endocrine tissue, and one example of this unique technology-enabled analysis is depicted by glycerol secretion spectrographs shown in **Figure 1.19D**. Since have continued to conduct research in this area, much of this dissertation document is devoted to analysis of adipose tissue using droplet-based microfluidics, where I have improved upon the methods shown in **Figure 1.19C-D**.

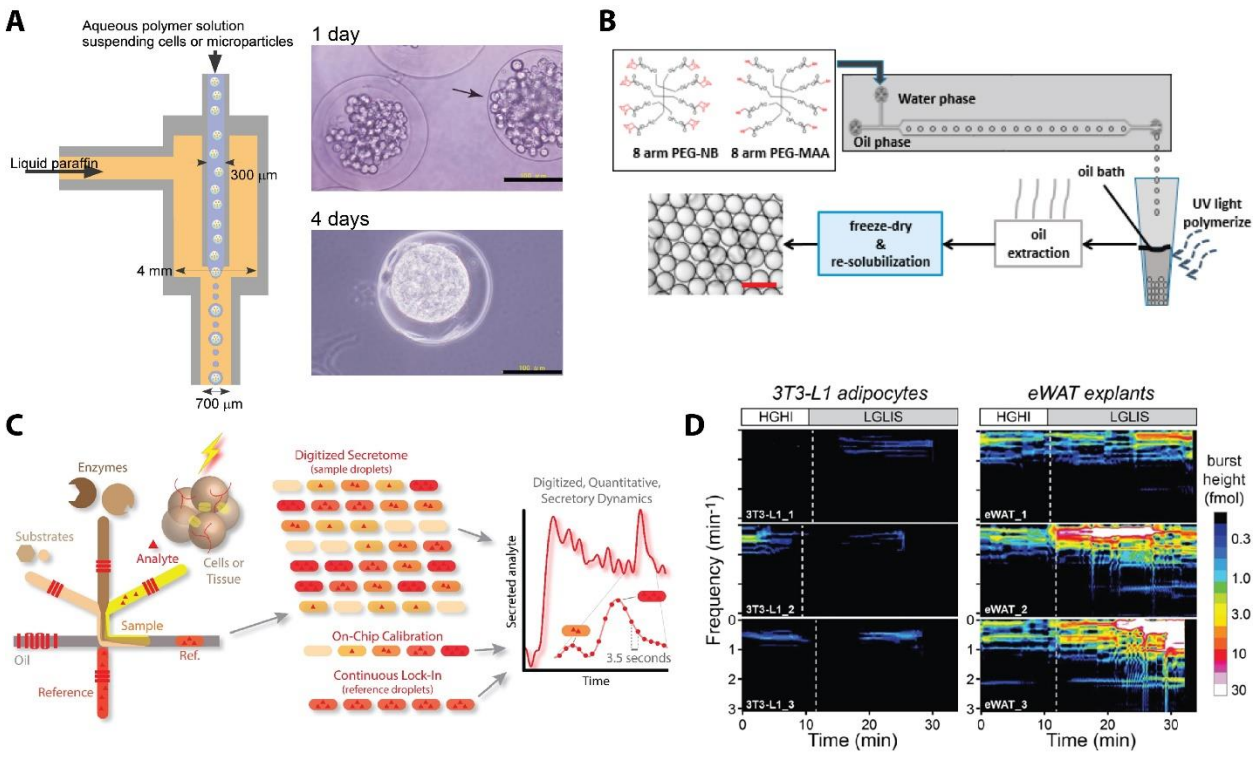

Figure 1.19 Adipose tissue culture and analysis with droplet-based microfluidics

(A) Schematic of a microfluidic flow-focusing device for adipose-derived cell encapsulation. Figure A is reprinted with permission from ref [247] ©2011, AIP Publishing. (B) Droplet formation was also used to form biodegradable microspheres for controlled release of growth factors to adipose cells. Figure B is reprinted with permission from ref [248] ©2015, American Chemical Society. (C) High-resolution, automated sampling with an improved µChopper device enabled 3.5-second resolution measurement of glycerol secretion from adipose tissue. This valve-automated device integrated tissue culture, enzyme and reagent mixing, droplet-based sampling, and downstream optical analysis with lock-in detection. (D) Unique oscillation analysis of glycerol release (FFT spectrograms) was enabled by the microfluidic tools developed in this work, where previously unreported lipolytic oscillations were observed from the eWAT tissue. Figure C-D is reprinted with permission from ref [179] ©2020, Royal Society of Chemistry.

Neuronal Tissue

Due to their central importance in physiological function, neuronal tissue engineering has attracted much attention in recent decades. However, traditional cell culture and tissue engineering methods cannot overcome the challenges brought by the complexity of the nervous system.[249] Microfluidic techniques have shown much promise in the field of microscale tissue engineering including high resolution *in situ* imaging, simultaneous multiple assay performance, and constructing integrated system mimicking the interactions of cells and extracellular matrix (ECM).[250-252] Alessandri et al. introduced a 3D-printed microfluidic device to produce functionalized microcapsules for incubating and differentiating human neuronal stem cells (hNSC)[253]. The encapsulated neuronal stem cells, a layer of reconstituted micro-thick ECM, and protective alginate shell formed hollow micro-hydrogels (**Figure 1.20A**). This project reveals the enormous potential of combining droplet-based microfluidics and 3D-printing technology for microscale tissue engineering. In other work, Jianhua Qin's group coupled a floatage-based trap array and a tapered immobilization channel array to a droplet-based microfluidic device for investigating multiple responses of individual *C. elegans* organisms to a neurotoxin, 6-hydroxydopamine (6-OHDA).[254] All the processes of generating, trapping, and immobilizing droplets, encapsulating worms, evaluating the behaviors, and image analysis were accomplished in one integrated system (**Figure 1.20B**). This study in particular showed that whole-animal assays and high-throughput drug screening for neurodegenerative diseases at single animal resolution can be accomplished through clever tissue engineering and droplet-based device engineering.

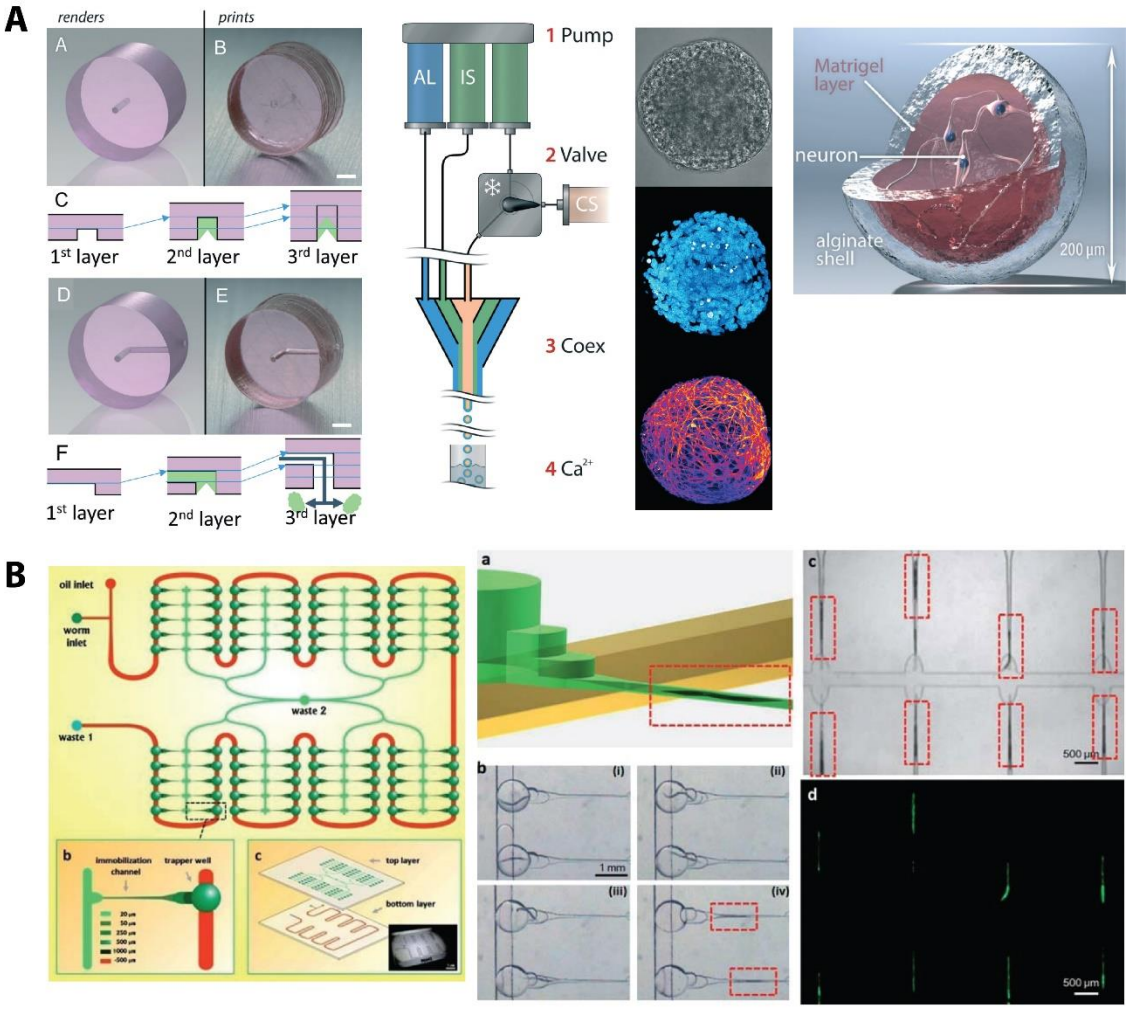

Figure 1.20 Neuronal tissue culture and analysis with droplet-based microfluidics

(A) Combining 3D printing with droplet-based devices allowed production of functionalized microcapsules for incubating and differentiating human neuronal stem cells. Figure A is reprinted with permission from ref [253] ©2016, Royal Society of Chemistry. (B) Schematic and photograph of an integrated microfluidic system for individual *C. elegans* assays, using a tapered immobilisation channel array for immobilizing and imaging the worms to study neurotoxicity. Figure B is reprinted with permission from ref [254] ©2010, Royal Society of Chemistry.

Chapter 2

Integration of Salt-water Electrodes and Merging Channels into Automated Droplet-based Microfluidic Devices: Design and Validation

2.1 Introduction

Droplet microfluidics is an important subcategory of microfluidics where nanoliter or microliter monodisperse droplets are generated and manipulated[65]. These small-volume droplet reactors possess lots of outstanding benefits compared to conventional tube or well plate. Firstly, each droplet can be regarded as isolated and well-protected unit for assays and reactions, and it is extremely convenient and useful for adding extra manipulations to these individual reactors like transporting, sorting, merging, mixing and analyzing[64]. Secondly, ultra-low concentrations of analytes in small volumes can be detected inside droplets, not only saving experimental materials but also making it possible to analyze single cells or even single molecules[67,128]. Thirdly, the small droplet reactors facilitate faster reaction times due to elimination of mass transfer time and diffusion distance at the microscale/nanoscale. What is more, highly monodispersed and essentially identical droplets generated with high throughput allow users to obtain large-scale data sets[68]. Numerous applications have been conducted based on these remarkable advantages of microreactors, such as resolving secretion dynamics of islets[75], nucleic acid amplification via

polymer chain reaction[140], improving fluorescence detection sensitivity with lock-in system[117], and so on.

In order to promote droplet microfluidics suitable for complicate biochemical reactions, some subsequent manipulations are indeed demanded after droplet generation. Merging diverse droplets contained different chemicals, dilutions or concentrations is requirement to initiate the follow-up reactions. Particularly, it is necessary to precisely control the velocity of droplets for bringing them close until coalescence via special channel geometry design[255]. In addition, some external equipment are useful to merge stabilized droplets, such as optical heating, surface acoustic waves and electro-coalescence. Laser point changes the temperature and surface tension of droplets interface to induce adjacent droplets merging[256]. Surface acoustic waves merge neighboring droplets by generating acoustic radiation force to destabilize the droplets surface[257]. Especially, electro-control is the most representatively active coalescence method among the mentioned technology above. The disrupted arrangement of surfactant molecules on interface make droplets polarized which boosts droplets approach in electric field and the stable interfaces of droplets are deformed to promote droplets merging[258]. Additionally, frequency and magnitude of voltage are beneficial to destabilize the interface of droplets and induce droplets coalescence[107,259].

To address the problem that applying droplets in multiple-step reactions, many techniques have been developed to accurately manipulated droplets. Niu et al. (2011) designed a micro-dilutor to generate various concentrations of target droplets with high-throughput screening in passive manner[260]. However, this microchannel design mainly focused on the dilution function and the accuracy of dilution decreased with accumulation of droplet number in sequential dilution. Easley's group (2018) utilized active peristaltic pumps to maintain the constant mixing ratio of

insulin and probe[75]. However, it was difficult to ensure the exact proportion of insulin and probe, because the two laminar might mix and diffuse partially before formatting final target droplets. Eujin et al. (2013) introduced a droplet system for chemical synthesis, dilution and adjusting pH via fixed geometry[261]. In this system, it was very important yet difficult to accurately determine the time that gas bubbles flow into the droplet array. Therefore, integration of active-controlled droplet and electro-coalescence probably is a good way to accomplish multi-step reactions with high precision in small volume.

As we know, on-chip, three-valve pumps provide programmable generation and on-demand numbers and sizes of droplets. Further, compared to solder electrodes and liquid metal electrodes, salt water electrodes not only simplify chip fabrication but also provide powerful and constant electric fields for droplet merging[107]. Considering these benefits, a droplet-based system coupled with pneumatically controlled micro-pumps and salt water electrode is presented in this chapter. This powerful system ensures achieving constant merging and varying combinations of droplets via regulating the distances between droplets and their sizes. In this work, the effects of voltage frequency and magnitude on droplets coalescence, precise serial dilution and pH adjustment of sample are explored, respectively. Furthermore, detection limit of homogeneous immunoassay is demonstrated via automatically merging various ratios of sample and probe droplets with our lock-in technique[116].

2.2 Experimental Design

2.2.1 Materials and Reagents

All buffers in the experiments were prepared with the deionized water that was produced by Barnstead™ MicroPure™ Water Purification system (ThermoFisher Scientific, serial No. 42034239). Critic acid, sodium phosphate and sodium chloride were from Millipore Sigma

(Burlinton, Massachusetts). PDMS (Polydimethylsiloxane) precursors, SYLGARD® 184 silicone elastomer base and curing agent were purchased from Dow Corning (Midland, MD).The silicon wafers were acquired from Polishing Corporation of America (Santa Clara, CA). SU-8 2015, SU-8 2050 and SU-8 developer were purchased from the Microchem (Westborough, MA). AZ 40XT-11D and AZ 300 MIF developer were bought from the AZ Electronic Materials USA (Somerville, NJ). Fluorescein was purchased from Alfa Aesar (Ward Hill, MA, USA). Bovine serum albumin (BSA) were from VWR (West Chester, PA). Human insulin FRET-PINCER assay kits were obtained from Mediomics, LLC (Saint Louis, MO). Pico-Surf 2% in Novec 7500 was purchased from Dolomite Microfluidics (Norwell, MA). Novec^{TM} 7500 Engineered Fluid (HFE 7500) was from 3M. High-voltage amplifier model 2220 was from Trek, Inc. (Lockport, NY, USA).

2.2.2 Microfluidic Master Wafer Fabrication

Two master wafers for liquid channels and control channels were fabricated by photolithography. The channel layouts were designed in Adobe illustrator (San Jose, CA) and photomasks were printed by Fineline Imaging (Colorado Spring, CO) at 50,800 dpi resolution. For pneumatic control channel layer, 20-μm SU-2015 was spin-coated on the silicon wafer which was washed by H_2SO_4 (1 M) and water in advance. And the wafer was soft baked at 95 ℃ for 5 min, then UV exposure for 2 min was done at an in-house ultraviolet lithography light unit. Finally, the wafer was developed for 5 min with SU-developer solution after 5-min hard baking on hot plate.

The flow layer wafer contained two-step photolithography and negative photoresist was made firstly. 60-μm thick SU-2050 was spun onto the pretreated silicon wafer, soft bake at 95 ℃ for 7 min, UV exposure for 90 s, hard bake at 95 ℃ for 6 min, and developed to form SU-8 micro pattern. Secondly, 40-μm thick AZ 40 XT was spin-coated on the wafer after warmed to room temperature. The silicon wafer was baked at 115 ℃ for 5 min, and a photomask was aligned on

the positive photoresist coated wafer after cooling passively down to room temperature. Then the wafer was exposed to UV light at 330 mJ/cm^2, hard baked at 115 ℃ for 1.5 min, developed, and finally heated to 120 ℃ for 10 min to round out the cross-section of AZ defined channel for purposes of valving.

2.2.3 Microchip Fabrication

36 g of well-mixed PDMS precursor mixture (5:1 ratio, monomer: curing agent) were poured on the flow channel silicon wafer, wrapped within aluminum foil, after degassing under vacuum. 5.12 g of PDMS precursor mixture (15:1 ratio, monomer: curing agent) was spin coated on the control layer at 2100 rpm for 45 s. Both of fluid layer and control layer were baked at 65℃ for 30 min in the oven. After cutting to size, punching pneumatic connectors, and washing, the flow channels were aligned with the control channels and then the two layers were baked in the oven at 65 ℃ overnight. This PDMS device was then peeled from the wafer, diced, and punched for fluidic reservoirs, and then the device was bonded to a glass slide irreversibly by plasma oxidization. Finally, the assembled microfluidic device was ready to use after it was thermally aged at 65℃ overnight, which helps to limit surface chemistry changes due to uncured PDMS monomer leakage.

2.2.4 Flow Control

A total of twelve pneumatic push-up valves in the microfluidic chip were programmatically controlled by an in-house written LabVIEW application, which was interfaced to solenoid switches system (LHDA0533115H, the Lee Company, Westbrook, CT) for generating on-demand droplets. These pneumatic solenoid valves were actuated by nitrogen with 23-psi pressure and outlet was

linked to hand-held 100 mL syringe via Tygon tubing (0.02″ I.D. X 0.06″ O.D., Cole-Parmer, Vernon Hills, IL) which supplied vacuum for promoting flow.

2.3 Results and Discussion

2.3.1 Microchip Design and Operation

We have previously reported a droplet-based microfluidic system for real-time quantifying insulin secretion from a single islet. This device specially consists of a Y-shaped channel for mixing reagents and sample, a long incubation channel for providing enough incubation time for homogeneous immunoassay, and a pneumatic control layer for automate generation of droplet and reference for the phase lock technique[75]. This system supplies an efficient platform for precisely controlling the sizes of droplets contained reagent or sample, quantifying glucose-stimulated insulin secretion and revealing fast secretion oscillations. However, the Y-shaped mixing channel sometimes introduced inconsistencies in mixing probe and sample (intended as a ratio of 1:1), and this system also required manual switching to vary concentrations of sample and probe.

PDMS devices have the characterization of gas permeability and solution non-permeability. This allows a dead-end salt-water electrode channel to be connected with a pressurized syringe and filled with salt water, providing a powerful electric field near the fluidic channels for merging droplets (**Figure 2.1**). The grounded moat channel is arranged strategically around the stimulating electrode to prevent the electric field from affecting droplets at other location. Both the electrode and moat were filled with 5 M NaCl solution. Compared to metal and liquid metal electrodes, salt-water electrodes are simple to create and suitable in most cases at room temperature, though its conductivity is certainly lower than the metal one[69,107]. For improving the efficiency of droplet merging, an expansion chamber was designed to slow droplets down to promote coalescence.

In this device, droplets are generated by alternatively pumping sample/reference and oil fluids with active three-valve pumps which are accurately controlled by custom LabVIEW program (**Figure 2.1.2**)[126,235]. Compared to off-chip controlled droplet-based microfluidic devices that utilize vacuum and external pumps to format droplets[178,262], this system can accurately and simply determine droplets sizes by adjusting fluid pump cycles. Droplet numbers, droplet generation frequencies, and distances between droplets or droplet groups are digitally controlled on-demand by LabVIEW programming. Both the electrode and active valve pumps are included in this system, which provides the possibility of digitally merging droplets in different combinations. The magnitude and frequency of voltage and droplet size determine the maximum number of merging droplet in each group.

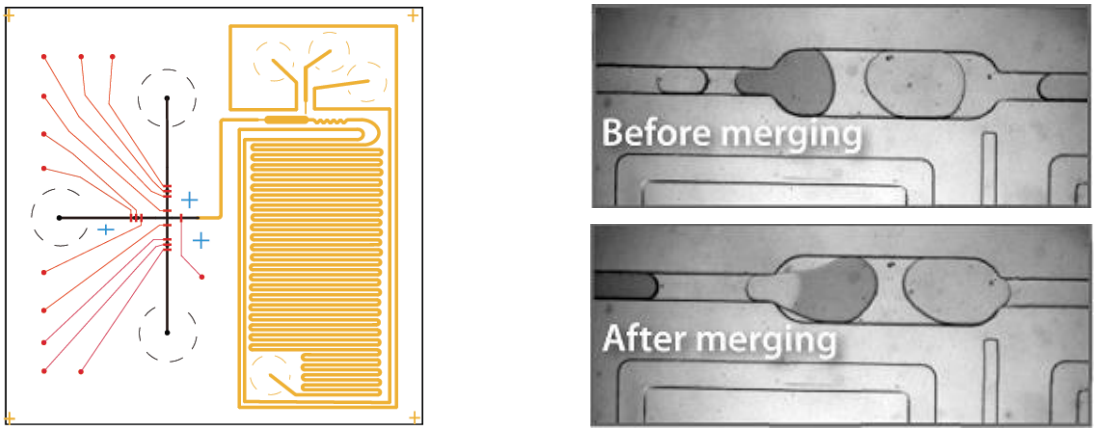

Figure 2.1 Two-layer microchip design with salt-water electrode

(A) T-junctions for droplet formation (black); valves for control flow (red); and assay incubation channel (orange); (B) Images of droplets before and after merging with an AC electric field.

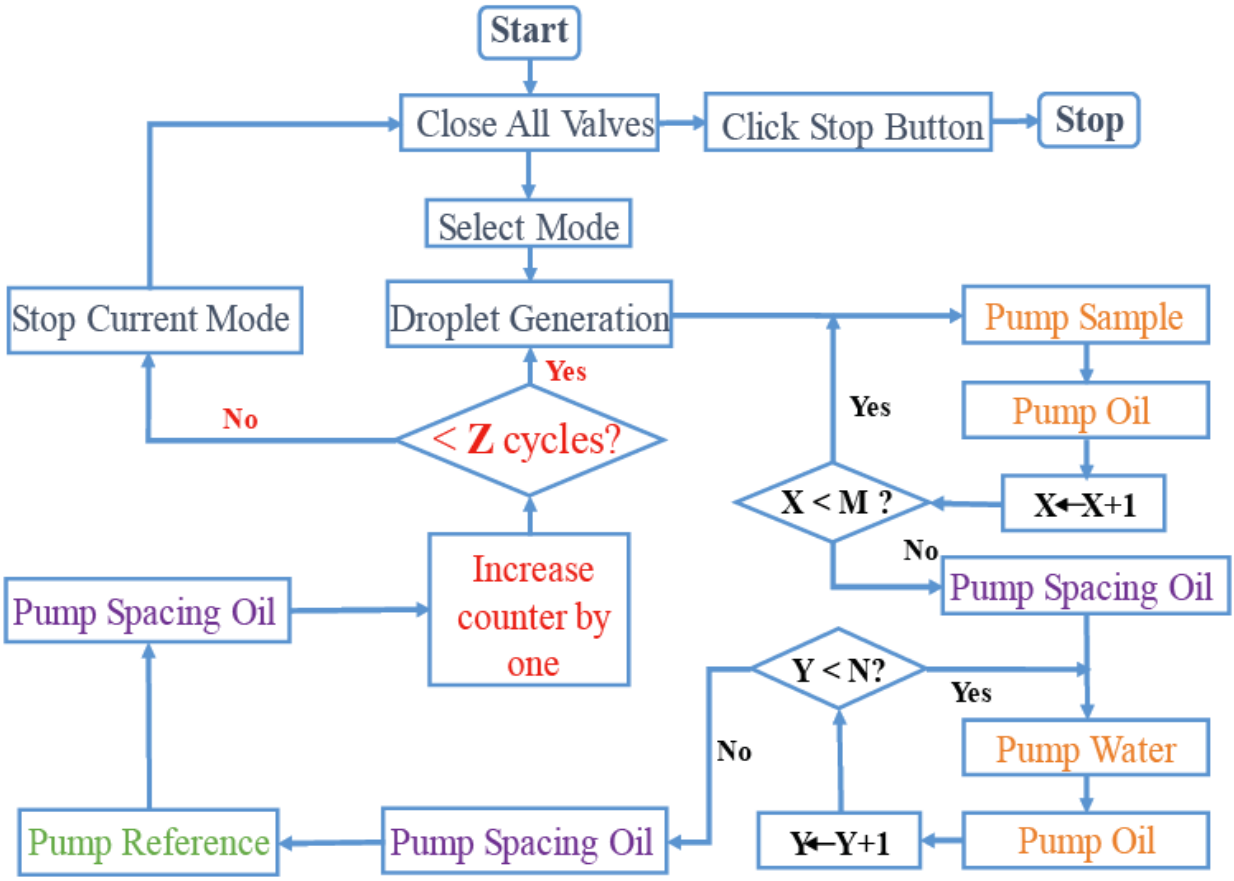

Figure 2.1.1 Programmatic flow chart of LabVIEW application for microfluidic automation

2.3.2 Effects of Magnitude and Frequency of Voltage on Droplet Merging

In this experiment, three main means were applied to generate high electric field that caused coalescence of droplets: (1) highly concentrated NaCl solution (5 M) was injected into electrode, (2) a high-voltage amplifier (Trek, Model 2220) that enhanced voltage by 200 fold was connected to the electrode, and (3) the electrode was arranged close to the coalescence chamber. Pairs of 1.8 nL and 8.6 nL aqueous droplets carried by perfluorocarbon oil (Novec 7500; 3M, St. Paul, MN) with 0.5% surfactant (Pico-Surf 1; Dolomite, Royston, UK) were formatted from two aqueous channels, respectively. An expansion zone was added to slow and assemble the pair of

droplets, and those daughter droplets would merge at the entrance or exit of the chamber where they were feasible to deform. **Figure 2.2** clearly shows the effects of electric field on two droplets' coalescence. Two regions are observed in this diagram based on voltage magnitude and frequency: droplet merging (blue area) and non-merging (white area). It obviously indicates that high voltage and frequency are helpful for droplet coalescence at the entrance of restriction, and all droplets coalesced when voltage is above 800 V.

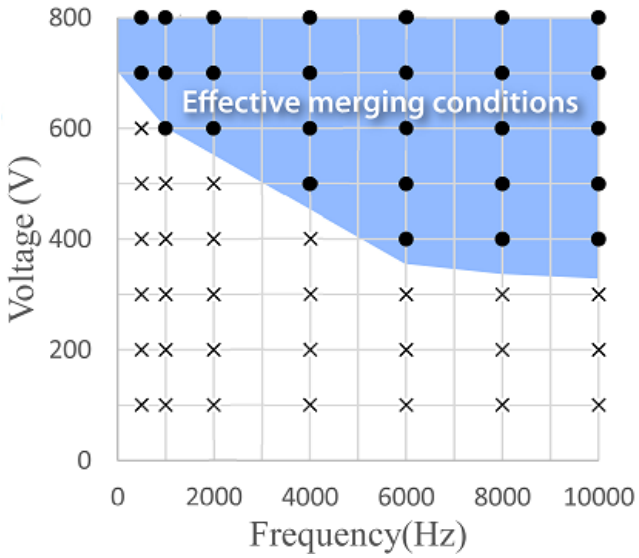

Figure 2.2 Effects of magnitude and frequency of AC voltage on droplet merging. Droplet merging (blue area) and stable droplet pair (white area).

2.3.3 Digital Concentration Gradients Generated by Nanoliter-sized Droplets

Molecular and cellular assays, enzymatic kinetics measurements, and secretion dynamics have been successfully applied in microfluidic systems in the past decade[177,263-265] [169,266,267]. Serial dilutions and concentration gradients are quite important in biological reactions, chemical analyses, and determination of enzymatic activity and dynamic ranges of assays. In droplet-based

microfluidic systems, concentration gradient are normally achieved by merging or splitting sample droplets and diluent droplets[268]. One methodology of serial dilution is to trap a big sample droplet or sample droplet array with multiple buffer droplets[269]. However, this approach risks cross-contamination among the droplets containing different reagents, and it is not precise enough to obtain the on-demand concentrations. To address these issues, Heon-Ho et al. (2015) and Sachin at al. (2011) added microvalves to microfluidic devices, which they showed to improve the accuracy distinctly of generating concentration gradients[269,270].

With all of this in mind, our system containing valve pumps integrated with the merging electrode was validated to generate a digital concentration gradient. Sizes and numbers of droplets were determined by the number of cycles of valve pumping and the switching frequency of oil and aqueous flows. Various combinations of sample and diluent droplets were merged in the specific coalescence region. The processes of different groups of droplet generation were programmed as followed: Firstly, one sample droplet containing fluorescein solution was generated from one dispensing channel; Secondly, varying numbers of water droplets were formatted from the other aqueous channel; Thirdly, one much larger sample droplet was generated and used as a continuous reference. Finally, all of sample and water droplets merged when they arrived at the restriction region. At the analysis part, the signal ratio of merged target droplet and reference droplet was used to correct drift caused by low frequency noise over time. Shortening the distance of neighboring droplets was effective to improve droplet fusion. However, it was also extremely important to maintain reasonably enough space between sample/water droplet array and reference droplet for avoiding reference droplet injecting into droplet-merging array. The proportions of sample droplet and water droplet were set at 1/5, 1/4, 1/3, 1/2 and 1/1, respectively. Following our lock-in analysis method [75,101,116-118,179], the theoretical ratios of intensity of merged droplet and

reference droplet were 0.167, 0.2, 0.25, 0.33 and 0.5, respectively. A highly linear and well-correlated response (R^2=0.9997) of experimental and theoretical values was observed in the nanoliter scale (**Figure 2.3**). This result indicates that combination of this automated, flexible, multi-droplet system and lock-in analysis is a powerful tool to precisely and simply accomplish serial dilution.

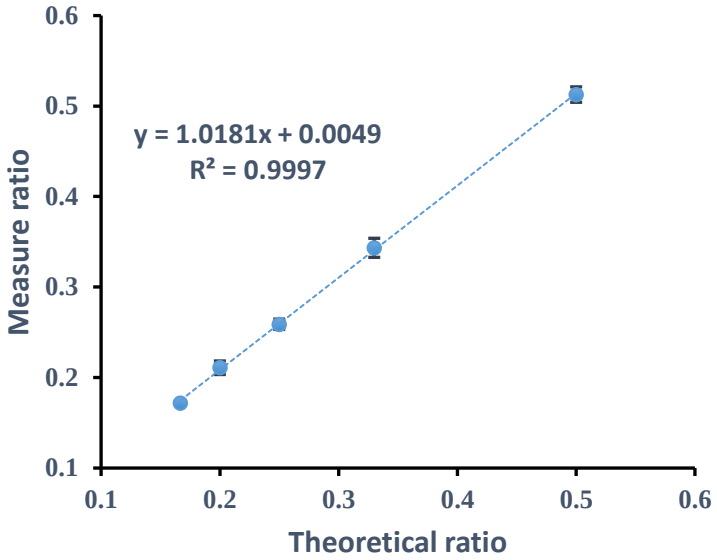

Figure 2.3 Standard curve represented the accuracy of automated dilution on-chip by comparing theoretical value to measurement result

2.3.4 Droplet-based pH Regulator

It is crucial to establish specific and suitable pH environments in microfluidics, since pH plays an important role in chemical and biological reactions and cell cultures[271,272]. Miniaturization of conventional acid and base titration integrated within this device provides the possibility to format a digital pH gradient based on varying combinations of acid and base droplets at the

nanoliter level. Fluorescein can be protonated or deprotonated in aqueous solution, with a pK_a of 6.4, which results in fluorescence properties that are easily affected by pH[273]. As such, fluorescein was utilized as an indicator in this droplet-controlled pH gradient experiment. 0.2 M sodium phosphate (basic) with fluorescein and 0.1 M citric acid were added into the inlets of two droplet generators, and the reservoir contained dye-labelled basic solution to serve as a reference. The proportions of acidic and basic droplets, as well as the corresponding pH of merged droplet are showed in **Figure 2.4B**. Comparison of pH data from chip and plate reader demonstrates ansimilar tendency (**Figure 2.4A**). However, the intensity ratios (I_s/I_r) from plate reader were always slightly higher than that measured on-chip. This phenomenon might be caused by the small differences of the excitation and emission wavelengths between those two instruments.

Considering the simple operation and low reagent consumption in this droplet-based chip, a deeper relationship of fluorescence intensity and pH was explored via mixing multiple combinations of 80 nM fluorescein droplets and buffer droplets containing five gradients of pH solution (pH 4, pH 5, pH 6, pH 7, pH 7.6) (**Figure 2.5**). Finally, five serial concentrations (13.3, 26.6, 40, 53.3, 66.7 nM) of sample droplets were generated automatically with five proportions (1/5, 2/4, 3/3, 4/2, 5/1) (**Figure 2.5A**) of dye and buffer droplets coalescing. This means that twenty-five combinations could be obtained via manually changing five variables, and this technique significantly improves the working efficiency, saves reagent volumes, and reduces the possible error induced by manual, human operations. The intensity ratios (I_s/I_r) showed the expected correlation of concentrations and pH after combinatorial injections (**Figure 2.5B** and **Figure 2.5C**). The results are summarized to follow the trend that higher fluorescence intensity ratios were obtained at higher concentrations of fluorescein and at higher pH values.

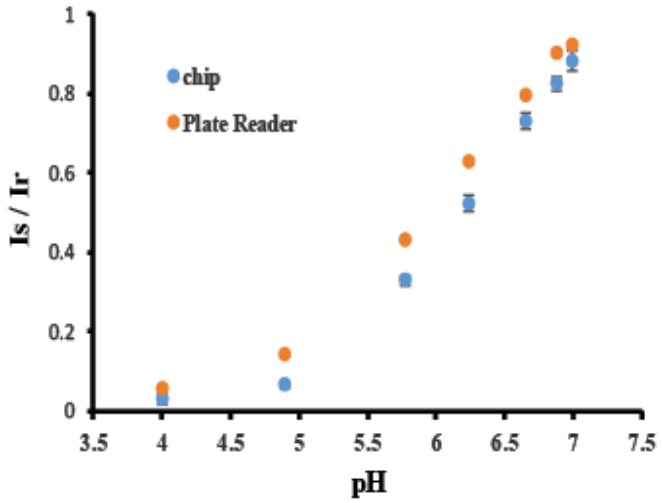

#A-droplet	#B-droplet	pH
3	2	4
3	3	4.9
2	3	5.78
2	4	6.24
1	3	6.65
1	4	6.88
1	5	7

Figure 2.4 Regulating pH with nanoliter-size droplets

Varying proportions (**right table**) of acidic droplets (0.1 M citric acid) and fluorescein labelled basic droplets (0.2 M sodium phosphate) were merged together to produce different pH solution and measured with lock-in detection.

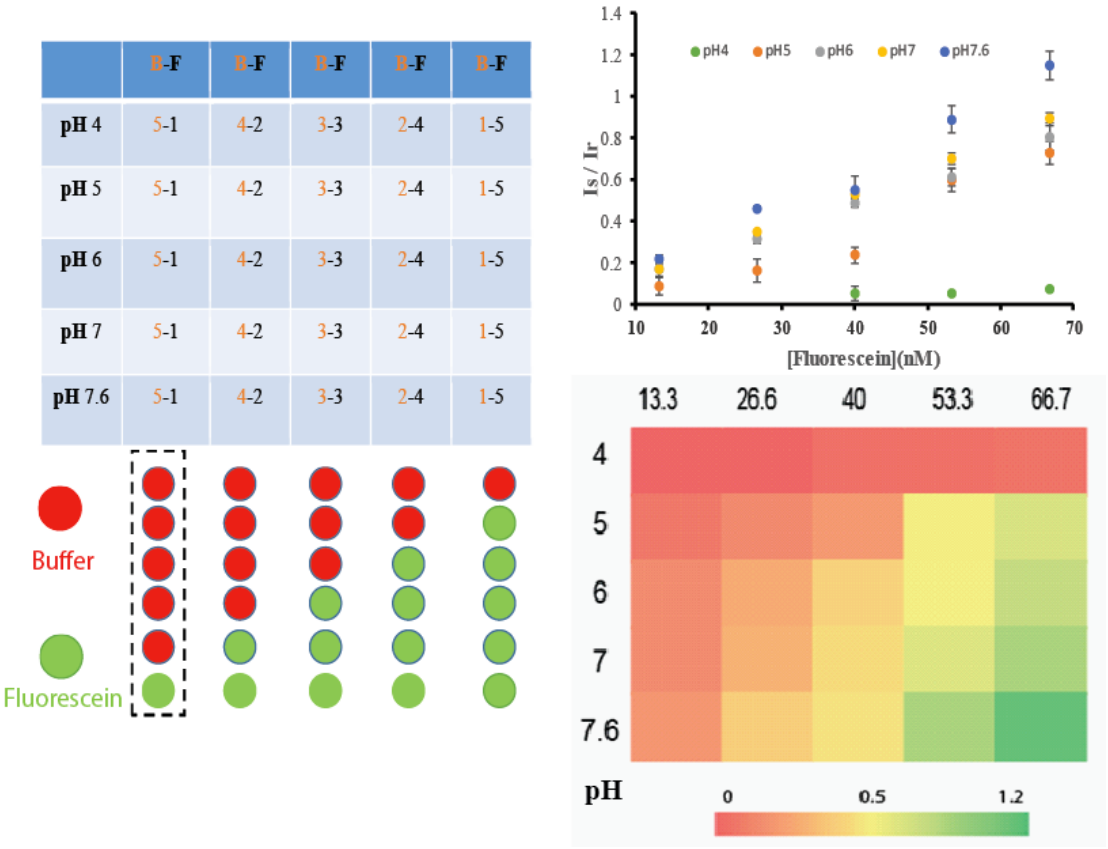

Figure 2.5 Droplet-based pH-sensing Fluorescein Platform

(A) This table and figure show different combinations of buffer and fluorescein droplets (5-1, 4-2, 3-3, 2-4, 1-5). (B) Characterization of five serial concentrations of fluorescein (13.3, 26.6, 40, 53.3, 66.7 nM) in five pH buffer (pH 4, pH 5, pH 6, pH 7, pH 7.6) was studied with about total 3 μL solution on chip. (C) The heat map which is corresponding to (B)

2.3.5 Exploring Human Insulin Pincer Assay Detection Range within Droplets

Previously, several studies on the insulin quantification and islet insulin secretion dynamic with the human insulin pincer assay were reported[75,117,274]. This fluorescence quenching based homogeneous immunoassay supplies a simple and fast way to measure the insulin concentration in buffers and culture medium[275]. The intensity of FRET (fluorescent resonance energy transfer) signal is proportional to the insulin concentration within the detection range. In this assay, two specific antibodies are used to recognize different epitopes on human insulin, which means the

result would be not correct if the ratio of insulin molecules to antibodies is more than ~1.0 in the final reaction solution. Therefore, it is necessary to accurately obtain the lowest and highest detection range in each unit of probe in advance of biological measurements. The normal, laboratory scale method conducted with tubes or well plate requires significatn amounts of the expensive reagents (antibody-oligo conjugates) and user effort. Additionally, in an experiment such as secretion sampling from cells, the amount of glucose-stimulated insulin secretion from islets in the tissue-sampling experiment may not be measurable in advance, making it a challenge to decide the optimal concentration of probe to be used. In previous reports, users just added highly concentrated probes to avoid extensive optimization, yet this was non-optimal and squandered expensive reagents. Our multifunctional, programmable, small volume microfluidic system (**Figure 2.1**) should provide a cost-effective and simple platform to study the detection range of this human insulin pincer assay or other homogeneous immunoassay with nanoliter droplets.

Automated and constant droplets with insulin and probe could be formatted at on-demanded ratio in each group. Long incubation channel provided enough time (~30 min in this case) to make sure the assay reaction was complete in the merged droplets. Insulin concentrations were manually changed (0, 32, 64, 128, 256, 512 ng/mL) in one aqueous reservoir, and the other aqueous reservoir was filled with 4× probe compared to the recommended concentration in the commercial kit. Proportions (1/5, 2/4, 3/3, 4/2, 5/1) of insulin and probe droplets were programmed, coalesced, and incubated before the target droplet arrived in the fluorescence detection region. As shown in **Figure 2.6**, at the final concentration of insulin was 213.3 ng/mL, the intensity signal nearly reached the lowest level (donor signal detection). To explore the wide detection range of pincer assay, those total 240 treatments only required about 3 μL of expensive insulin and probe reagents that worth about 3 dollars in the droplet microchip system. In comparison, more than 5,000 dollars will

be costed to accomplish the same amount of tests with conventional methods at a much larger volume scale.

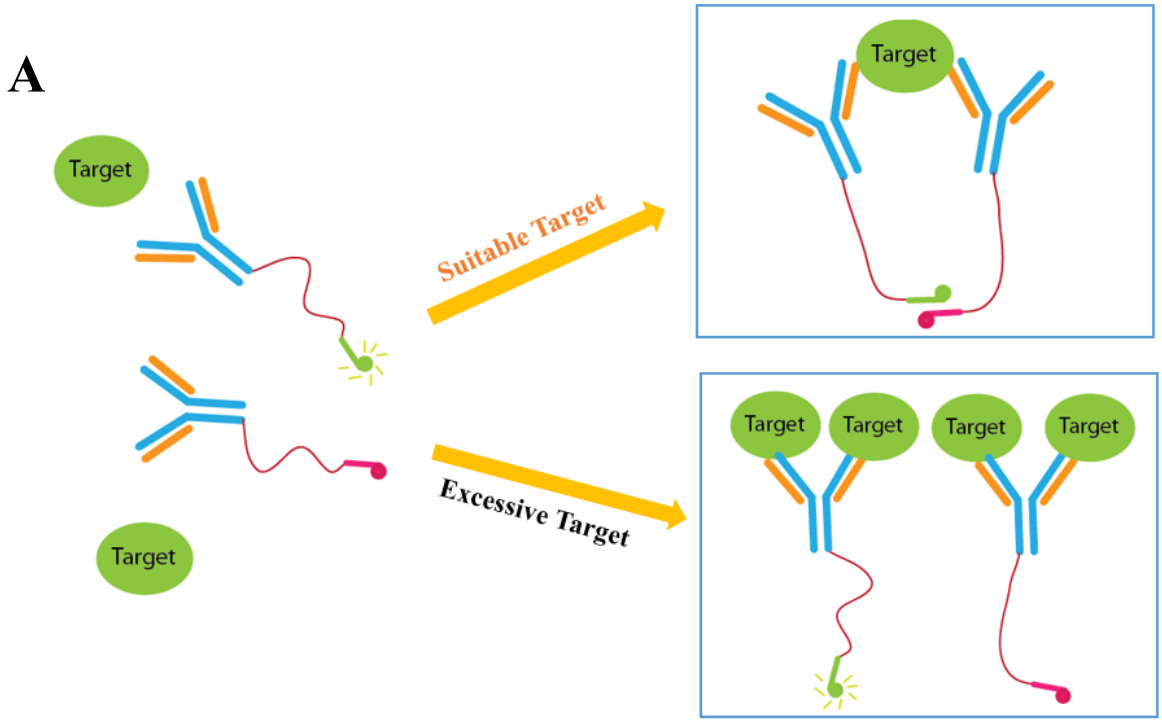

B

	S-P	S-P	S-P	S-P	S-P
512	5-1	4-2	3-3	2-4	1-5
256	5-1	4-2	3-3	2-4	1-5
128	5-1	4-2	3-3	2-4	1-5
64	5-1	4-2	3-3	2-4	1-5
32	5-1	4-2	3-3	2-4	1-5
0	5-1	4-2	3-3	2-4	1-5

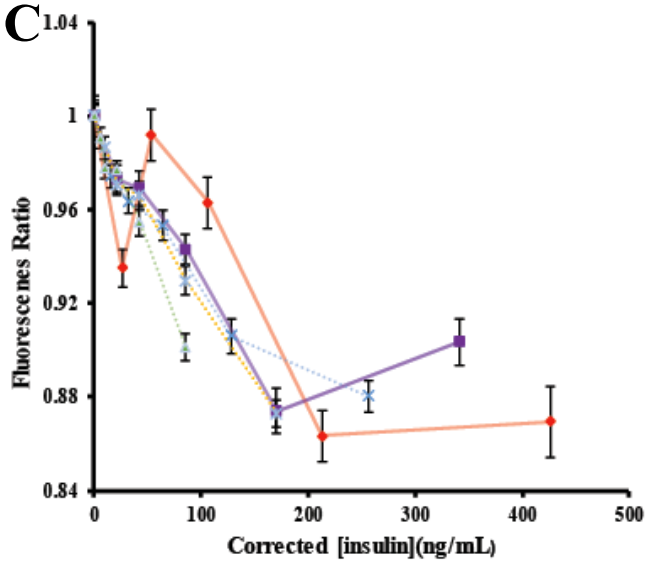

Figure 2.6 Pincer Assay Detection Range Exploration

(A) At the suitable number of insulin target compared to the probe amount, FRET will happened between target and probe; However, if at the condition of the excessive insulin, FRET will not happened and it cannot quantify the target correctly. (B) Different ratios of sample and probe droplets at six levels of 0, 32, 64, 128, 256, 512 ng/mL insulin. (C) LOD of pincer assay was accurately quantified by programmably merging Insulin droplets based on the varying conditions.

2.4 Conclusion

In summary, this research introduces a useful method of generating and merging droplets of multiple combinations with a wide variety of conditions, while only consuming a small amount of reagents. Integration of droplet formation junctions, pressure driven push-up valves, and a salt water merging electrode makes it possible to digitally control the reactants ratios on demand. The device was first validated using serial dilution of fluorescent standards, then by nanoliter-scale pH regulation. Finally, the programmable device was used to examine a wide range of conditions with a homogeneous immunoassay without consuming much of the expensive probes.

Chapter 3

Programmable μChopper Device with On-Chip Droplet Mergers for Continuous Assay Calibration

3.1 Introduction

Droplet-based microfluidics is an important subcategory of microfluidic technology. In these type of micro-devices, small droplets are generated and viewed as individual reactors, and they provide powerful platforms for confining samples to small volumes for subsequent manipulation, reaction, and analysis [276]. In the recent decade, droplet microfluidics has been widely used in a broad range of biochemical fields, such as nucleic acid/molecule analysis [277,278], drug delivery [279], cell-to-cell communication [280], cell screening [281], tissue analysis [75,76,117], and so on. To ensure constant and predictable outcomes in these applications, it is essential to generate highly uniform droplet volumes [50,116,178], and researchers have developed various methods to do so.

Microfluidic droplet formation techniques can be divided into two categories: passive and active. High throughput droplet generation is much simpler and faster to achieve with passive methods, an obvious advantage in applications that require enormous experimental throughput [180]. By contrast, a major benefit of active droplet generation is its higher flexibility in droplet volume and production rate [81]. Because the vast majority of biochemical reactions and analyses require multiplexed reagents, multiple timed steps, and often multiple conditions (temperature, pH, ionic strength, etc.), tools that allow precise control of droplets on-demand are becoming increasingly

important. Significant efforts have been focused on active droplet formation using various approaches such as electric, magnetic, thermal, and mechanical control [93,126,127,282]. Considering the exquisite level of control that they provide, on-chip pneumatic valves [283] have been demonstrated as important players that provide active, programmable droplet generation with high precision [75,76,118,126,284,285].

To improve programmability and precision, our laboratory has moved from passive droplet formation [50,116], to active fluidic resistors [285], to gating of fluids with single pneumatic valves [117,118], and finally to on-chip valve-based pumps [75,76]. During this time, we revealed one less obvious benefit of active control, the ability to precisely control the frequency and phase of droplets, lock-in the photodetector to that signal, and greatly reduce detection limits—an approach we refer to as the μChopper [116-118]. With a control bandwidth of ±0.04 Hz using gating valves, fluorescence detection limits were reduced more than 50-fold using simple microscope detection optics, and even single-cell fatty acid uptake was quantifiable in droplets [117]. An improved iteration of the μChopper with six aqueous input channels enabled several analytical modes to be programmed automatically, such as real-time continuous calibration, standard addition, and a mixed mode [118]. Despite these benefits, there remains a drawback with respect to the workflow in this type of microsystem. Reagents for multi-step or timed reactions must be manually pre-mixed and transported to the input micro-reservoirs, increasing bench time and potential operator errors. The logical step is to add on-chip reagent mixing or to incorporate programmable droplet mergers.

The Ismagilov group and others have successfully initiated mixing of reagents at the droplet forming structure [58,75,286,287], which can start reactions at a predictable position and provide control over timing. However, several issues limit the accuracy and preclude universal application of this approach. Firstly, inconsistent flow rates of solutions from individual aqueous channels can lead

to fluctuating reagent volume ratios and significantly affect assay outcomes. Secondly, it is difficult to precisely and arbitrarily change the volume ratio of reagents, meaning that new channel designs will be needed for even minor adjustments. Several techniques to coalesce neighboring droplets were introduced to avoid these issues, such as hydrodynamic, magnetic, electric, or acoustic coalescence [107,257,288-290]. Among these, electrocoalescence has been the most widely used in droplet microfluidics by merging adjacent droplets with an AC electric field, and the development of salt water electrodes has made this approach even more accessible [107].

Considering the benefits of pneumatically controlled droplet generation and electrocoalescence, here we have integrated our µChopper approach with active valve-based pumps and salt-water electrodes for the first time. This approach permits fully automated, on-demand production and merging of several types of droplets in a programmable way. In this proof-of-concept work, we apply the device to real-time, continuous calibration of fluorescent labels, then we validate the system for continuous calibration of a homogeneous insulin immunoassay that exhibits a nonlinear response. With the significant savings in reagent use, assay cost, and user time that are incurred, this device provides a novel means to carry out economical measurements with precious reagents in a static or real-time manner.

3.2 Materials and Methods

3.2.1 Materials and Equipment

All materials and equipment were obtained from sources within the USA. Buffers were prepared using deionized water filtered with a Barnstead MicroPure Water Purification system (ThermoFisher Scientific). Citric acid, sodium phosphate, and sodium chloride were obtained from Millipore Sigma (Burlington, MA). Polydimethylsiloxane (PDMS) precursors, SYLGARD 184 silicone elastomer base and curing agent, were purchased from Dow Corning (Midland, MI). The

silicon wafers were acquired from Polishing Corporation of America (Santa Clara, CA). Negative photoresists (SU-8 2015 and SU-8 2050) and SU-8 developer were purchased from MicroChem (Westborough, MA). Positive photoresist (AZ 40XT-11D) and AZ 300 MIF developer were obtained from AZ Electronic Materials USA (Somerville, NJ). Fluorescein was purchased from Alfa Aesar (Ward Hill, MA), and bovine serum albumin (BSA) was purchased from VWR (West Chester, PA). Human Insulin FRET-PINCER Assay Kits were obtained from Mediomics, LLC (Saint Louis, MO). Pico-Surf (2% in Novec 7500 oil) was purchased from Dolomite Microfluidics (Norwell, MA). Novec 7500 Engineered Fluid (HFE 7500) was acquired from 3M. A high voltage amplifier (Model 2220) was purchased from Trek, Inc. (Lockport, NY).

3.2.2 Microfluidic Master Wafer Fabrication

Two master wafers for templating liquid channels and pneumatic control channels were fabricated using standard photolithography as described previously [76]. Channel layouts were designed in Adobe Illustrator software, and photomasks were printed at Fineline Imaging (Colorado Springs, CO) at 50,800 dpi resolution. For the pneumatic control channel layer, a ~20 μm layer of SU-2015 was spin-coated on the silicon wafer, which had been washed by 1 M H_2SO_4 and water in advance. The wafer was soft baked at 95 °C or 5 min, then UV exposure for 2 min was accomplished on an in-house built UV lithography light exposure unit [291]. Finally, the wafer was developed for 5 min in SU-8 developer solution after a 5 min hard bake on a hot plate at 115 °C. The fluidic layer wafer was fabricated in a two-step protocol with both negative and positive photoresists, respectively. First, a 60 μm layer of SU-8 2050 was spun onto the pretreated silicon wafer, and the wafer was soft baked at 95 °C for 7 min. UV exposure with the first photomask was carried out for 90 s, hard baking was applied at 95 °C for 6 min, then the SU-8 developer was applied. Next, a 40 μm layer of AZ 40 XT was spun onto the wafer at room temperature. The wafer

was baked at 115 °C for 5 min, cooled to room temperature passively, and the second photomask was aligned over the wafer then exposed to UV light. A final hard bake at 115 °C as applied for 1.5 min, AZ developer was applied, and the AZ portion of the wafer was annealed to allowed templating of rounded channel cross-sections by baking at 120 °C for 10 min.

3.2.3 Microchip Fabrication

After degassing under vacuum, 36 g of well-mixed PDMS precursor mixture (5:1 ratio, monomer: curing agent) was poured onto the flow channel patterned silicon wafer in an aluminum foil boat. Again after degassing, 5.12 g of PDMS precursor mixture (15:1 ratio, monomer:curing agent) was spin coated onto the control layer at 2100 rpm for 45 s, creating a layer of ~40 μm thickness. Both the fluid layer and control layer were baked at 65 °C for 30 min in an oven. The flow channel layer was then cut to shape, then aligned and mated to the valve channel layer. The two mated layers were baked in oven at 65 °C overnight to facilitate permanent bonding. The PDMS was peeled from the wafer, diced into individual devices, access reservoirs were punched, and surfaces were washed with methanol and dried with N_2 gas. Each device was then bonded to a glass slide irreversibly by plasma oxidization (Harrick Plasma; Ithaca, NY). The assembled microfluidic devices were finally thermally aged at 65 °C overnight to limit uncured PDMS monomer leakage, and these devices were then ready to use.

3.2.4 Flow Control

For generating droplets on-demand, a total of 19 pneumatic push-up valves on the microfluidic chip were programmatically controlled by an in-house written LabVIEW application which was interfaced to a custom manifold of solenoid switches (LHDA0533115H; the Lee Company, Westbrook, CT). These solenoid valves were actuated by 5 V signals to controllably switch a

pressurized nitrogen supply (25 psi), and only 13 solenoids were needed due to redundancy in operating some valves in the peristaltic pumps. For periodic rinsing of the microdevice, the outlet could also be connected to a hand-held 100 mL syringe via Tygon tubing (0.02'' I.D. X 0.06'' O.D.; Cole-Parmer, Vernon Hills, IL) to allow a small vacuum to be applied.

3.3 Results and Discussion

3.3.1 Microfluidic Device Design and Operation

As shown in **Figure 3.1A**, the microdevice was defined by several regions: (1) four different aqueous inlet reservoirs (colored) and an oil inlet reservoir (black); (2) T-junction channels for aqueous-in-oil droplet generation (colored and black); (3) pneumatic control channels (light gray) for automated chip operation through LabVIEW, with some three-valve pumps integrated to improve efficiency; (4) salt water electrodes for droplet coalescence with high AC voltage (two tones of dark blue); (5) a widened merging region near the salt water electrodes, at the sharpest electric field gradients; (6) a zig-zag channel (orange) for quickly and completely mixing reagents contained in droplets; and (7) a long incubation channel for storing and analyzing target droplets (orange). Regions (1) and (2) were valve-controlled AZ-defined rounded channels of ~40 μm depth, region (3) was SU-8 defined rectangular channels of ~20 μm depth, and regions (4) – (7) were SU-8 defined rectangular channels of ~55 μm depth.

In a typical assay workflow, calibration curves are regularly generated to allow measurement and calculation of an unknown sample concentration. The conventional method is to quantify sequential standard solutions followed by each sample, then calculate the response curve and quantify samples post-measurement. Particularly when using expensive reagents—such as antibodies, protein standards, enzymes, bioconjugates, etc.—this traditional process not only wastes significant amounts of materials, but it also increases the workload of operators. To

improve the accuracy and efficiency of building standard curves, we recently developed a six-channel μChopper to automatically carry out a continuous calibration mode [118], allowing real-time determination of slope, y-intercept, and correlation coefficients along with unknown quantification. In this report, we improve upon this concept by introducing downstream droplet mergers via electrocoalescence, and we provide even more precise control using on-chip pneumatic pumps.

To achieve full automation, we developed the device design in **Figure 3.1A**, which allows programmable generation of droplets of various combinations from any of four input aqueous reservoirs. An example of programmable calibration is shown in **Figure 3.1B**, where droplets containing dye solution (mimicking assay standards) and buffer are generated in various ratios. The images show droplets prior to merging into a single, larger droplet. Videos of programmable droplet formation (Video S-1) and downstream merging (Video S-2) are provided as supporting information. In this work, the total droplet number was limited due to the size of the coalescence region, however this number could be increased by simply enlarging the dimensions of this region. With 4 input reservoirs and the total droplet count fixed at 6, this system allowed 84 possible solution combinations to be programmed into the finally merged droplet (16.6 nL). Notably, if the total droplet count were expanded to be 1 through 6—easily accomplished with this device—there would be 209 possible solution combinations. The upper limit can be extended if the coalescing region is made larger; for example, if 24 total droplets were allowed (6 from each reservoir), then combinations would be accessible.

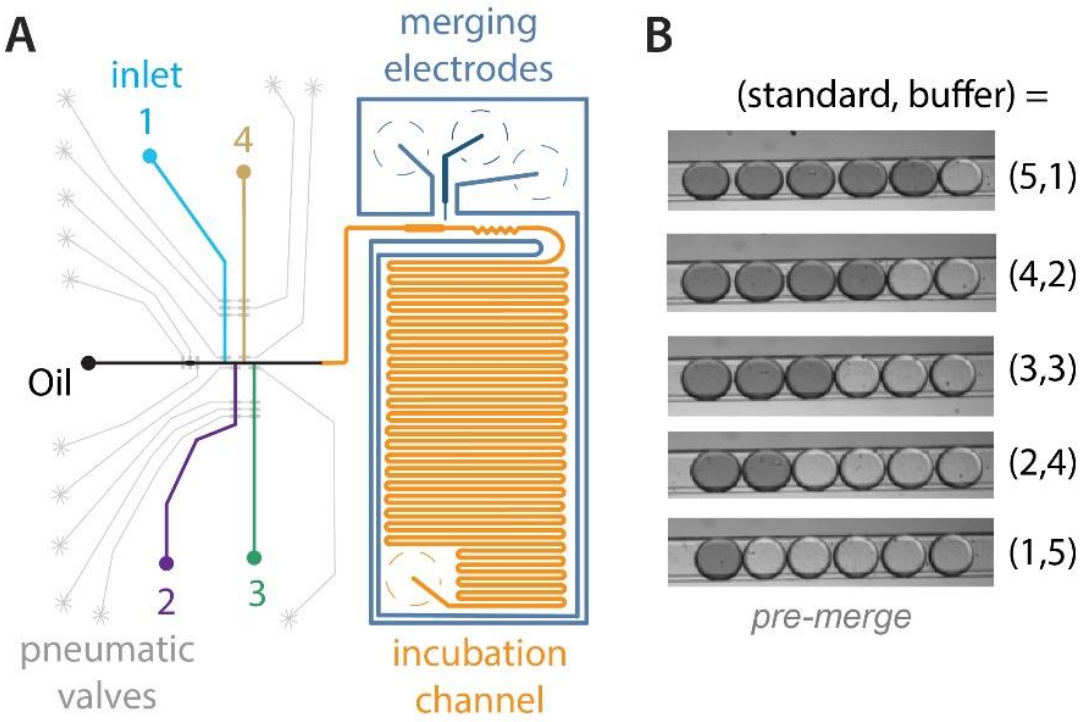

Figure 3.1 Microdevice design and operation

(A) Inlet aqueous reservoirs (1-4, colored) and one oil reservoir (black) were sampled by computer-controlled pumps based on pneumatic valves (light gray). Merging electrodes (dark blue) facilitated droplet coalescence in the widened merging region (orange), merged droplets were mixed in a zig-zag channel, and then assays were incubated in a long delay channel (orange) if needed prior to optical detection. (B) In this example, five ratios of standard mimics (dark) and buffer (transparent) were programmed on-demand, then merged downstream. Images show the droplet groups prior to merging.

3.3.2 Programmable Droplet Generation and Merging

User-defined time and channel programs for automatically building real-time five-point calibrations within sequentially merged droplets were preloaded into an in-house written LabVIEW application (Figure S-2). Briefly, sequential groups of six droplets (2.77 nL each) were formed and separated in space to prevent group-to-group merging, and these six droplets were merged (16.6 nL in each larger droplet) using electrocoalescence downstream. As such, two types of oil segments were programmed: very short oil segments to keep droplets in the same group as

close as possible and longer oil segments to partition the sequential droplet groups. As discussed above, 84 possible solution combinations could be programmed into the finally merged droplet under the conditions investigated here. When applicable, the concentrations of an unknown sample could be determined in real time using continuous calibration curves, and signal drifts were corrected using the µChopper concept.

3.3.3 Microdevice Characterization with Continuous Linear Calibration

To verify the automation capabilities of our device, fluorescein standard (165 nM), buffer, and an unknown fluorescein sample were loaded into reservoirs #1, #2, and #3, respectively (see **Figure 3.1A**). Five calibration standards were formulated by sequentially generating and coalescing groups of six droplets at varying ratios of fluorescein standard and buffer (1-5, 2-4, 3-3, 4-2, 5-1; akin to **Figure 3.1B**). For unknown measurements, a single larger-volume droplet was sampled from reservoir #3 and kept separate from standard droplets. The blue and green traces in **Figure 3.2A** show a 20-min record of raw fluorescence data measured at the incubation channel during continuous calibration. To challenge the system during continuous calibration, the excitation light was changed from a higher (initial settings) to a lower intensity (final settings). Although the unknown droplet's signal decreased, all of the calibration standards decreased proportionally, allowing accurate calibration to be maintained despite the challenge. **Figure 3.2B** shows a magnified view of signal from one group of calibration standards and an unknown, and **Figure 3.2C** highlights the detector-dependent, low-frequency drift (noise) that can be corrected using the lock-in based µChopper method.

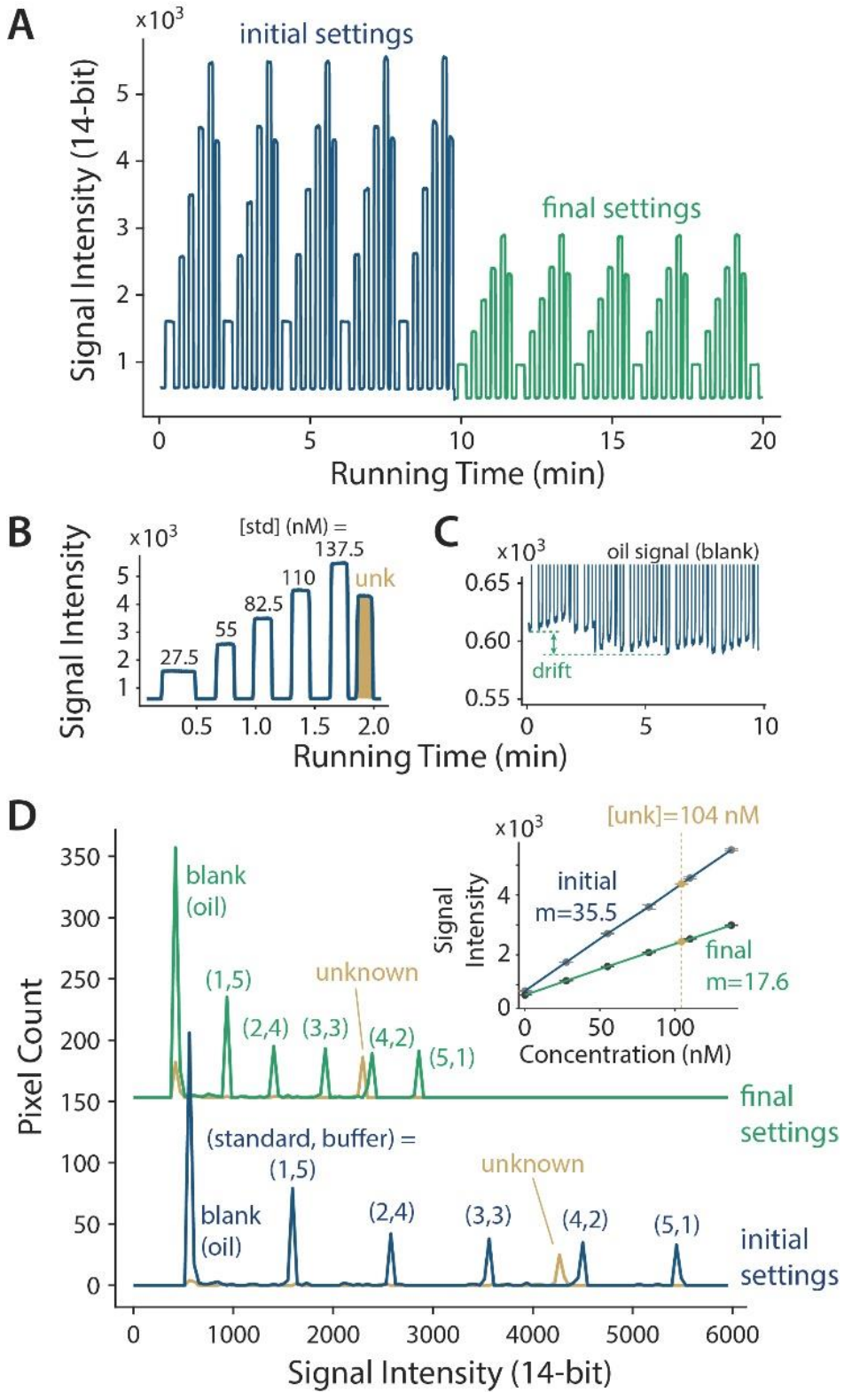

Figure 3.2 Continuous calibration with automated droplet formation and merging.

(A) Raw fluorescence emission data shows that droplet contents were programmable. Data is shown under initial settings at higher excitation light intensity (blue) and with final settings after decreasing the light (green) in real time. (B) A magnified segment of this data, with pulses labeled using final, post-merge concentrations of fluorescein standard. Data from the unknown droplet is shaded in gold. (C) Magnified view of the oil signal shows typical optical system drift that can be corrected using our μChopper method[116-118]. (D) Histogram analysis reveals the method's capability for highly precise control of droplet contents. Peaks are labeled with the pre-merge, programmed numbers of standard and buffer droplets. Inset shows linear calibrations under initial and final settings.

As shown in **Figure 3.2D**, programmable droplet formation and merging enables high-precision control over the final droplet composition. Essentially, this device operates as a microfluidic digital-to-analog converter, albeit at relatively low resolution. The intensity histograms show that fluorescence intensities were accurately controlled by the programmed ratios of standard and buffer droplets, from (1,5) to (5,1). Initial settings (blue) showed that the unknown fluorescence was nearly as high as the (4,2) droplet, and after the light intensity challenge, the final settings (green) showed the same order and position, just at lower intensity. The inset calibration curves in **Figure 3.2D** show that the light intensity decrease mainly affected the calibration slope, while the unknown was determined to be at a concentration of 104 nM, independent of excitation light intensity. These data point to a major advantage of continuous calibration, where the system can automatically adjust to drastic changes in the environmental conditions.

3.3.4 Unique Data Reshaping Using MATLAB Code

Since on-chip valves provide highly precise and programmable droplet intensities with repeatable timing, we surmised that the raw data could be readily reshaped into a more easily readable image format. Using custom MATLAB code (see Supporting Information), the raw data from **Figure 3.2A** was sliced into segments representing the repeating groups of larger droplets

(116-second slices), and these slices were restacked over the running time of ~20 min and presented as the image in **Figure 3.3A**. The image intensity represents the 14-bit camera signal intensity using a custom colormap depicted in the legend. The five stripes of intense signal in this image represent a tracked intensity of each type of merged droplet, and the darker regions are the larger oil segments that separate them. For example, the blue stripe near the bottom of the image is a reshaping of data from multiple 27.5 nM standard droplets, where (standard,buffer) = (1,5), and this image allowed facile tracking of their intensities over time. Indeed, re-slicing of the image horizontally (shown above the image) gave time traces of each standard (gold) and the unknown (blue). Again, with the change in light intensity, it is obvious that all calibration standards shifted along with the unknown to maintain calibration integrity. Conversely, by re-slicing the image vertically the original data can be recovered, as shown at the right during both initial (blue) and final (green) settings. This novel data reshaping approach is well-suited to automated, droplet-based continuous calibration, and it was enabled by the precision of valve-based control. It should be noted that lock-in analysis was not yet applied to the data in this reshaped image, but further development of image analysis algorithms in the future will allow lock-in analysis directly from these types of images.

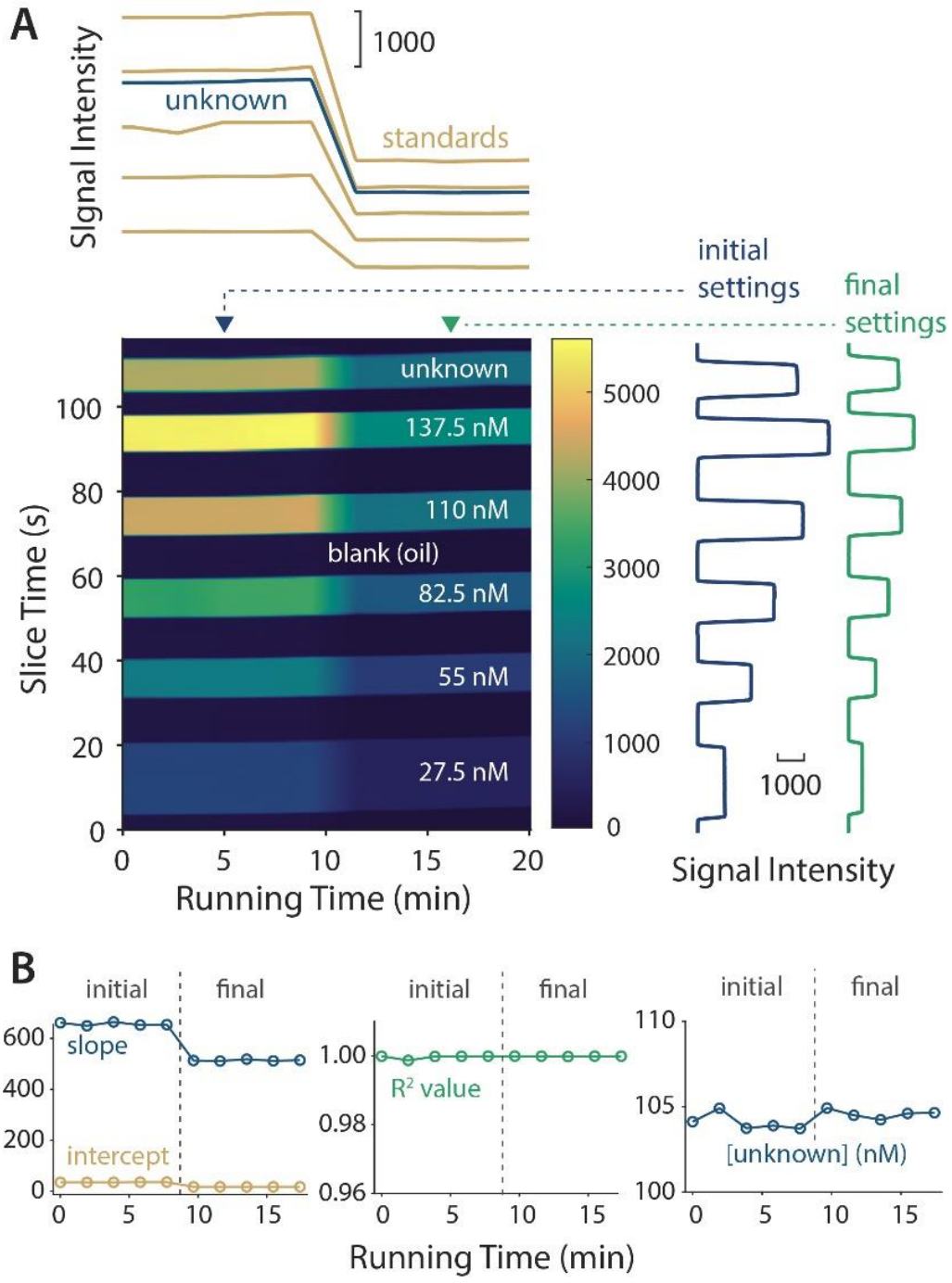

Figure 3.3 Data reshaping allowed a unique visual inspection of the system, enabled by precise droplet control with valves

(A) The raw data vector over time was reshaped into an image array using custom MATLAB code, and image re-slicing permitted temporal tracking of each type of droplet (above) or original data recovery (right). (B) The system responded to the light intensity decrease by adjusting calibration parameters, while fit linearity and unknown determination were essentially unaffected.

This analysis gives a unique, visual means to showcase the system's ability to respond to environmental changes. Following lock-in analysis, **Figure 3.3B** depicts the system's response to the challenge, where the major adjustment was a decrease in slope (blue) of the linear calibration curve and a small change in the y-intercept (gold). The R^2 value (green) remained at a high level near 1.00 over the course of the sampling, and the unknown determination was steady at 104 nM despite the change in excitation light intensity (blue data at right, magnified to 100 – 110 nM range).

3.3.5 Continuous Calibration using a Nonlinear Homogeneous Immunoassay

Finally, we tested the performance of this droplet-based system using a more complex assay response. Using antibody-oligonucleotide conjugates (Ab-oligos) as probes (**Figure 3.4B**), where DNA arms are labeled with a fluorophore and quencher, it is possible to quantify a protein analyte with high specificity through a mix-and-read workflow [75,274,292] that is ideal for detection within droplets. However, recovery of the sometimes small, unamplified signal changes can be challenging, particularly in biologically relevant ranges for a hormone such as insulin (low ng mL^{-1}; pM to nM). We previously showed that our µChopper method provides a key enhancement to enable homogeneous immunoassays within droplets [117], and the combined techniques even allowed high-resolution sampling of insulin secretion from single pancreatic islets [75]. The disadvantages in these devices were that mixing ratios of Ab-oligos and sample were device-dependent, the assay timing was restricted by the flow rates of on-chip pumps, and calibrations had to be carried out before or after experiments in a serial fashion. Here (**Figure 3.4A**), we show that by forming aqueous-in-oil droplets of Ab-oligo probes (blue), insulin analyte (green), and

buffer (gold) in a programmable way, then merging them downstream with integrated electrocoalescence, all of these aforementioned problems can be solved.

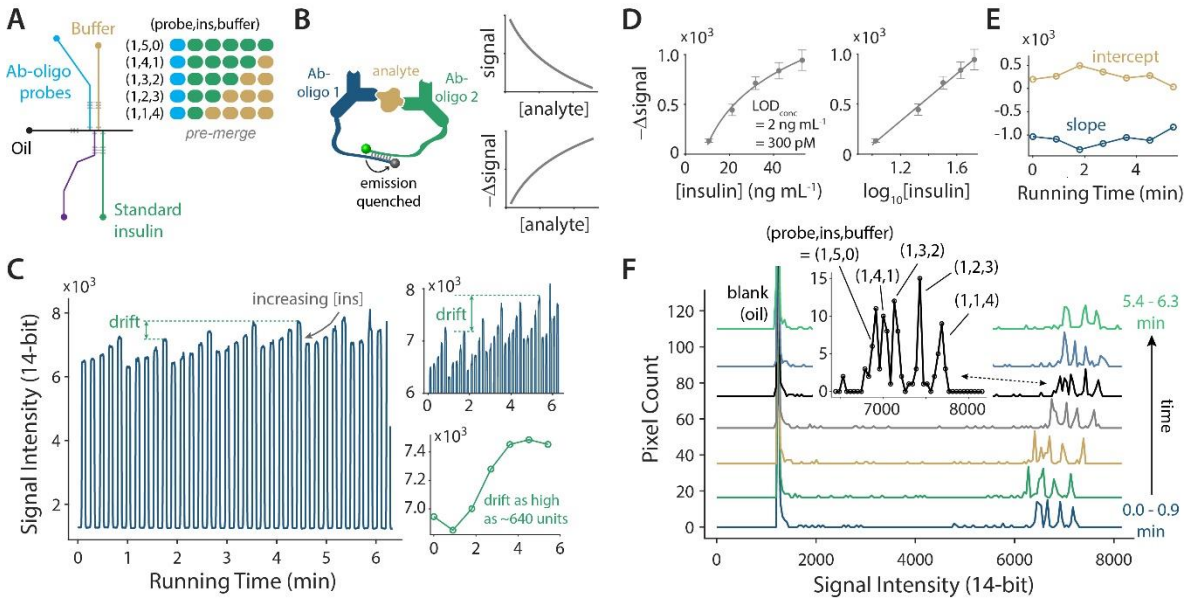

Figure 3.4 Automated homogeneous immunoassays in nanoliter droplets

(A) Device was operated with three inlets to program the pre-merge ratio of Ab-oligo probe, insulin, and buffer droplets. (B) Fluorescence quenching based homogeneous immunoassay with Ab-oligo probes. Signal quenching is proportional to analyte concentration with a nonlinear response curve. (C) Raw emission data from automated continuous calibration. Upper inset is a zoomed view of detector drift, and the lower inset shows the magnitude of the drift is similar to the overall assay response. (D) Lock-in detection with the µChopper method allows reliable correction and calibration. Signal change is shown versus [insulin] (left) and $\log_{10}$[insulin] (right). LOD_{conc} = 2 ng mL^{-1} = 300 pM, while LOD_{amt} = 5 amol. (E) Continuous linear calibration parameters versus $\log_{10}$[insulin] show slope and y-intercept to be responsive to significant detector drifts. (H) Intensity histograms show that assay responses over the 10 – 50 ng mL^{-1} insulin range were closely clustered, and drift could also be observed. Calibration standards followed the drift, giving reliable calibrations over time as in part (D) and (E).

By virtue of valve-based automation and downstream droplet merging, precious Ab-oligo reagents did not need to be diluted, premixed, or incubated with samples. For each measurement, a single drop of the stock Ab-oligo was sampled from inlet #1 (blue) and grouped with varying numbers of insulin (#3, green) and buffer (#4, gold) droplets (**Figure 3.4A**), and these six droplets were merged, mixed, and incubated downstream to allow continuous calibration. The raw emission data in **Figure 3.4C** shows that quenching within droplets was proportional to [insulin]. Also shown is the magnitude of the detector drift (two inset plots), which becomes highly significant compared to the signal changes in these homogeneous immunoassays at low analyte concentrations. In fact, the drift as high as ~640 intensity units was similar to the overall assay change for the full calibration range. Using the μChopper approach [116-118], these drifts were negated to give consistent calibration results over the entire experiment. The average curves are shown in **Figure 3.4D**, while the real-time curve parameters (linear fits versus $\log_{10}$[insulin]) are shown in **Figure 3.4E**. Continuous calibration allowed drifts and/or environmental changes to be negated, where the system continuously adjusted by modifying the slope and y-intercept. The concentration limit of detection (LOD_{conc}) was 2 ng mL^{-1} (300 pM), while the number of moles that were detectable (LOD_{amt}) was 5 amol (5×10^{-18} mol). This LOD is the best achieved to date for homogeneous insulin immunoassays using droplet-based microfluidics [75,117]. These data prove that the programmable device can give highly precise amounts of probe, calibration standards, and buffer—a significant improvement compared to the laminar flow sampling method in prior devices, where chip-to-chip variations were significant.

The histograms shown in **Figure 3.4F** highlight some challenges that may arise using nonlinear, homogeneous immunoassays at low concentration ranges compared to simple direct fluorescence (as shown in **Figure 3.2D**). Calibration intensities were clustered together between

6000 and 8000 intensity units, and the drift could be readily observed. The inset magnified plot shows that the three highest [insulin] values—made with droplet ratios (1,5,0), (1,4,1), and (1,3,2)—were just barely resolved under these conditions. Fortunately, the μChopper method can compensate for these effects [116-118]. Overall, the data in **Figure 3.4** show that automated sampling and downstream merging, when combined with lock-in detection, provide a highly reliable way to perform mix-and-read immunoassays in nanoliter droplets. The system can even be applied to real-time quantification of proteins. These benefits were achieved with minimal user intervention, where the workflow consisted of adding merely three solutions to the inlet reservoirs then starting the system.

Lastly, an additional and noteworthy improvement is related to cost. Using this device, the total volume used in one five-point calibration for the insulin immunoassay was 83.1 nL (5 merged droplets of 16.6 nL). For the most expensive components, Ab-oligo probes, only 13.85 nL was required. Because a five-point calibration in the standard 384-well plate version of the assay requires 2.25 μL of probes, our device reduced the needed volume by 160-fold, translating to an equivalent 160-fold reduction in cost for these precious bioconjugate components.

3.4 Conclusions

A fully automated microchip was introduced to precisely and rapidly form droplets of sequential calibration standards, allowing quantitative analyte measurements in the nanoliter range and in real time. The key novelty of this device was the integration of valve-based automation, on-chip droplet electrocoalescence, and μChopper data analysis. User workflow was minimized to a few solution transfer steps at the beginning of the experiment, and cost reductions of more than two orders of magnitude (160-fold) were realized with homogeneous insulin immunoassays. Further, full calibrations required <1 min, and this system also posted the lowest LOD achieved to

date using droplet-based homogeneous immunoassays (insulin LOD_{conc} = 2 ng mL^{-1} = 300 pM; LOD_{amt} = 5 amol). The highly precise, programmable control also permitted unique data reshaping into images, with which lock-in detection or continuous referencing should be feasible through image analysis improvements.

Of course, some challenges remain with this system that could be addressed in future work. To accommodate serial sampling of multiple droplets and formation of groups of calibration standards, the overall sample flow rate using on-chip pumps was lowered, causing about an order of magnitude loss in temporal resolution of sampling. Thus, the method timing is not yet competitive with our own state-of-the-art sampling resolution of 3.5 seconds [76]. While this issue is a cost of automation that is partially offset by the benefits, it could likely be improved by using gating valves [117] instead of full three-valve pumps. Finally, increases in the size or volume of the merging region would allow more droplets to be merged (>6). Changing this feature along with increasing the input reservoir number would exponentially increase the number of possible solution combinations, perhaps making it more palpable to refer to the chip as a microfluidic digital-to-analog converter.

Chapter 4

Development of Droplet-compatible, Nicking Enzyme Signal Amplification (NESA) Methods for Nanoliter-Scale Isothermal DNA Amplification and Biomolecule Quantification

4.1 Introduction

Biomolecules play important roles in biological research and clinic diagnosis. However, protein and nucleic acid biomarkers often exist at low concentration[42] . Highly sensitive and accurate assays are crucial for biotechnological applications[31]. Numerous detection strategies with electrochemical[32] , optical[293] and other sensors[36] have been developed over the past decades. Among them, the enzyme-linked immunosorbent assay (ELISA) is the gold standard in these immunoassays along with aptamer-based assays which are applied for protein quantification. ELISA requires several hours of incubation and washing steps though it has high sensitivity and selectivity for antigen detection[274]. In the simpler homogeneous assays, they do not have washing steps, but some antibodies and aptamers have low association constants that limit the sensitivity in the homogeneous assays.

A variety of amplification methods are introduced to obtain the high detection sensitivity, such as the polymerase chain reaction (PCR)[224,294,295], rolling circle amplification (RCA)[296-298], recombinase polymerase amplification (RPA)[50], nicking enzyme signal amplification

(NESA)[299,300], and proximity ligation assay (PLA)[301]. Among these amplification approaches, PCR is the first tool developed to amplify and detect nucleic acid, and it is regarded as the best way up-to-date. However, multiple-step temperature cycling and expensive thermal cycler hamper its widespread use. Compared to PCR, isothermal amplifications offer more advantages of nucleic acid analysis under simple and convenient conditions. However, RCA technology requires 4-8 hours to complete the whole reaction at constant 60 ℃, though it has been verified to be an efficient method of amplifying RNA or DNA target[302]. The RPA technique has the ability of measuring biological samples in 5-20 min at 37-42 ℃[49,141], but various-size microparticles introduced through mixing reagents are often still present even after sonication and vortexing, limiting the applications of RPA in micro devices. Poor stability and higher price of the proximity ligation assay (PLA) and the need for a real-time PCR instrument limit its application though this is a simple, rapid, and sensitive method[303].

Recently, isothermal nicking endonuclease signal amplification (NESA) has attracted attention for biosensing purposes due to the high cleavage efficiency and specificity of nicking enzymes. This type of restriction endonuclease only cleaves the single strand DNA when it interacts with the double stranded recognition region, providing NESA the potential of quick and sensitive target quantification[304]. For the basic NESA detection, target ssDNA hybridizes with complementary probe to form dsDNA containing restriction site which will be recognized by the enzyme, which will then cleave the probe repeatedly, and the target ssDNA can work as template[224]. According to previous report, one target molecule led to the cleavage of about100 probes, and the detection limit was estimated to be about 6.2 pM. The LOD of this assay then was improved to 85 fM after combining with RCA[299]. Liyun et al. (2012) measured thrombin with LOD as low as 100 pM based on homogenous nicking enzyme amplification technology at constant 37 ℃[305]. For

extended NESA, Jinghong's group (2019) sensitively quantified microRNA with the detection limit of 512 aM via improving NESA to cascade transcription amplification[306].

In this work, we show a fast and highly sensitive measurement method of DNA and anti-digoxigenin antibodies via isothermal and homogeneous nicking enzyme signal amplification (NESA) on a droplet-based microfluidic chip. The particularly isothermal and homogeneous nature of NESA allows it to be applied easily in microchip. On the other side, the droplet microfluidic system also provides an extremely high-throughput platform for the quantification of nucleic acid and proteins, and the monodisperse micro-droplets generated with active pump-valves can be treated as independent reactors which greatly reduce consumption of reagents. In addition, salt water electrode connected to voltage amplifier ensures the droplets containing varying reagents can be merged, and the reaction will be started up consistently. Additionally, we also improve this basic NESA to an extended NESA where a proximity structure is adopted for accurate detection of anti-digoxigenin antibodies, verifying the potential of NESA on quantifying proteins.

4.2 Experimental Design

4.2.1 Materials and Reagents

All buffers in the experiments were prepared with the deionized water that was produced by Barnstead™ MicroPure™ Water Purification system (ThermoFisher Scientific, serial No. 42034239). Sodium chloride was from Millipore Sigma (Burlinton, Massachusetts). Isoproterenol hydrochloride (>98%, purity) and Bovine serum albumin (BSA) were from VWR (West Chester, PA). Oligonucleotides and nicking enzyme were obtained from Integrated DNA Technologies (IDT; Coralville, Iowa) and New England Biolab Inc., respectively. Anti-digoxigenin was bought from Roche. PDMS (Polydimethylsiloxane) precursors, SYLGARD® 184 silicone elastomer base

and curing agent were purchased from Dow Corning (Midland, MD).The silicon wafers were acquired from Polishing Corporation of America (Santa Clara, CA). SU-8 2015, SU-8 2050 and SU-8 developer were purchased from the Michrochem (Westborough, MA). AZ 40XT-11D and AZ 300 MIF developer were purchased from the AZ Electronic Materials USA (Somerville, NJ). Pico-Surf 2% in Novec 7500 was purchased from Dolomite Microfluidics (Norwell, MA). Novec^{TM} 7500 Engineered Fluid (HFE 7500) was from 3M. High-Voltage amplifier Model 2220 was from Trek, Inc. (Lockport, NY, USA).

4.2.2 Microfluidic Master Wafer Fabrication

Wafers for two-layer microfluidic devices with integrated valves and salt water electrodes were fabricated as described previously, in sections 2.2.2 and 2.2.3.

4.2.3 Microchip Fabrication

Two-layer microfluidic devices with integrated valves and salt water electrodes were fabricated as described previously, in sections 2.2.2 and 2.2.3.

4.2.4 Flow Control

Total thirteen pneumatic push-up valves were programmatically controlled by in-house written LabVIEW application which was interfaced to solenoid switch system (LHDA0533115H, the Lee Company, Westbrook, CT) for formatting on-demanding droplets. These pneumatic solenoid valves were actuated by N_2 gas, and the fluidic outlet was connected to 100 mL syringe via Tygon tubing (0.02″ I.D. X 0.06″ O.D., Cole-Parmer, Vernon Hills, IL) which supplied vacuum for facilitating solution flow.

4.2.5 Microfluidic Device Design

The device shown in **Figure 4.1** is similar to that shown in **Figure 3.1**. Several components were included in this microchip: (1) T-junction channels for droplet generation; (2) salt water electrode for droplet merging; (3) pneumatic control layer for automated chip operation with LabVIEW program; (4) zig-zag channel to ensure reagents mixing completely in droplets; (5) long incubation channel for meeting biological reaction time requirements; (6) salt water electrode for droplets linked with high-voltage amplifier for merging effectively; and (7) a higher volume inlet pump for the oil channel, compared to the device in **Figure 3.1**. One specific feature of this chip was that partial integrated pump-valves lowered the number of control channels and improve the working efficiency of microfluidic chip.

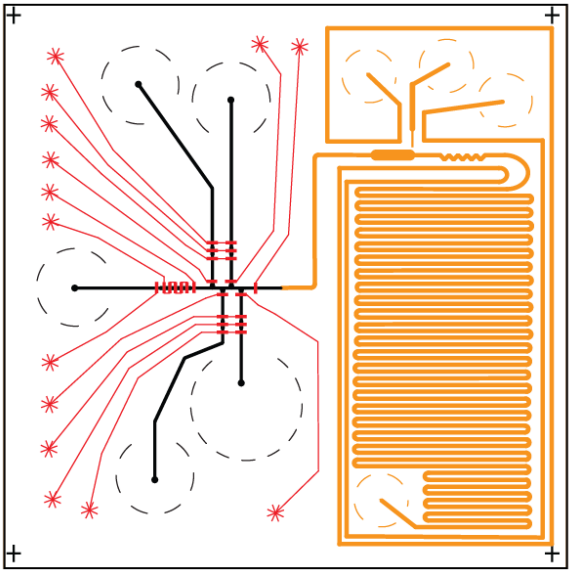

Figure 4.1 Four-channel microchip design with salt-water electrode
T-junctions for droplet formation (black), valves for control flow (red) and assay incubation channel (orange)

4.2.6 Programmable Droplet Merging

In the droplet-based microchip, pneumatically controlled three-valve pumps not only pushed fluid flow but also accurately controlled the aqueous-in-oil droplet volume and number with specified cycles of pumping and switching times, and the salt water electrode also could generate stable electric field which ensures nearby droplets merging. The device applied in this work contained both of the components which made it possible that merging droplets programmatically. As shown in Chapter 3, this integrated technique provided a novel platform for on-demand altering reagents volumes in chemical/biological reaction automatically and it reduces errors lead by manual operations and enhance the working efficiency of micro devices (**Figure 4.2**).

Firstly, Target DNA was dissolved in Tris buffer (tris(hydroxymethyl)aminomethane) and diluted to varying concentrations. Then the probe was obtained via mixing two complementary single strand oligonucleotides (FAM, BFQ) and incubating at room temperature for 30 min. After the preparation procedure, Nb.BbvCI enzyme, probe in 6X NESA buffer, Tris buffer, and Target DNA were transferred to the four reservoirs in microchip, respectively. The droplets contained different reagents were merged in the electric field and mixed well in zig-zag channel. The product fluorescence intensity was measured after incubation at 37 ℃.

Figure 4.2 Precise, programmable reagent mixing for automated NESA with minimal reagents Five serial concentrations of sample via progressively automatic adjusting the droplet numbers of tris-buffer and Target DNA (0-4, 1-3, 2-2, 3-1, 4-0) in this device.

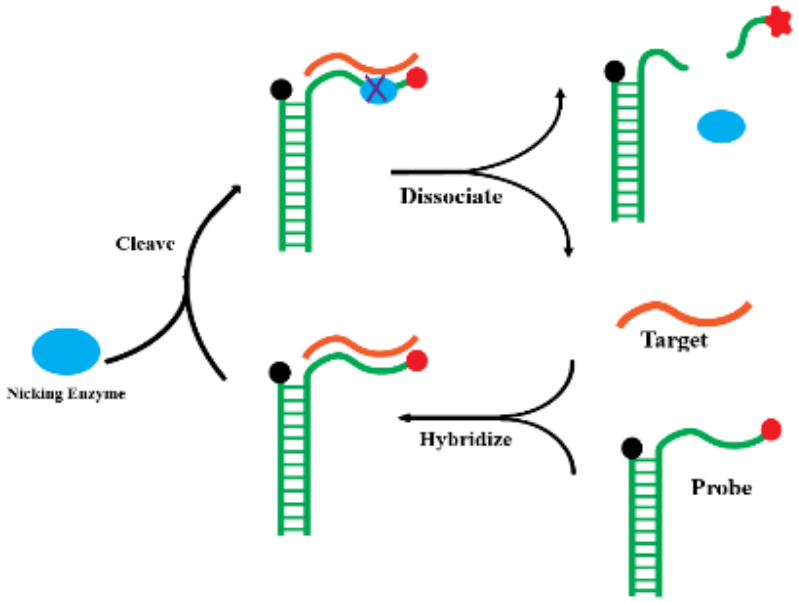

Figure 4.3 Basics of our version of the nicking enzyme signal amplification (NESA) method. This system contains nicking enzyme (blue), complementary Target DNA (orange), and an excess amount of probe strands (green). Cleaved probe segments release the fluorophore (red) from the quencher (black), providing increased fluorescence emission in proportion to the amount of Target DNA.

4.2.7 Nicking Enzyme Signal Amplification (NESA)

The NESA approach used in our work is similar to that discussed in Chapter 1 and shown in **Figure 1.3**. However, our approach was modified to accommodate future applications to protein detection. As shown in **Figure 4.3**, the fluorophore (red) and quencher (black) modifications were made on separate strands, which were then assembled by hybridization to form the "Probe" strands (green). When the Target DNA (orange) is present, the nicking enzyme cleaves the probe segments to release the fluorophore (red) from the quencher (black), providing increased fluorescence emission in proportion to the amount of Target DNA.

4.2.8 Extended NESA assay

The schematic for Extended NESA is shown in **Figure 4.6** below. Firstly, (DG-1, Arm-1) and (DG-2, Arm-2) were hybridized in a tube. Then antibody and probe were added, mixed well with a pipette, and incubated at 37 ℃ for 20 min. At the third step, this mixture, Nb.BbvCI enzyme, CutSmart buffer (New England Biolabs), and reference solution were added to the four chip inputs. Finally, the merged droplets were stored in incubation channel before detected at 37 ℃.

4.3 Results and Discussion

4.3.1 Exploring Optimal Reaction Conditions in the Device

Nicking enzyme, Nb.BbvCI, was determined to be the best choice for this isothermal NESA on chip because the recommended optimal incubation time and temperature of this reaction is 60 min and 37 ℃ at conventional instruments. However, the chemical or biological reactions may be accelerated in nanoliter scale droplets, since the high surface area to volume ratio of droplet shortens the time of heat, mass transfer, and the diffusion distance[68]. Therefore, it was necessary to optimize the detection time of NESA in this droplet-based microfluidic chip. Additionally, optimizing the concentration ratio of Target DNA and probe will improve the measurement accuracy of the NESA on chip, since the Xie group[299] has proven the molar ratio of Target DNA and molecular beacon influenced the efficiency of amplification, which determined the limit and sensitivity of detection.

It was obvious that all the 20 nM probe was nicked completely by low concentrations of Target DNA (2.9, 4.35, 5.8 nM) within 30 min in **Figure 4.4A**, and this meant that high molar ratio of template and probe affected the accuracy of quantifying analytes with NESA. As shown in **Figure 4.4B,** high concentration ratio of target and probe apparently improved the accuracy of

NESA, and it also clearly indicated that 6-min is the optimal detection time for this amplification in this chip in contrast to 2 min and 30 min. In addition, comparing to 3.33 U/mL enzyme in the system, relatively high concentration (16.7 U/mL) of nicking endonuclease increased the reaction rate and detection sensitivity (**Figure 4.4B** and **Figure 4.4C**). These results demonstrated that 166 nM probe, 16.7 U/mL and 6-min incubation time were the optimal reaction condition for initial 8.7 nM target DNA at 37 ℃ on the device.

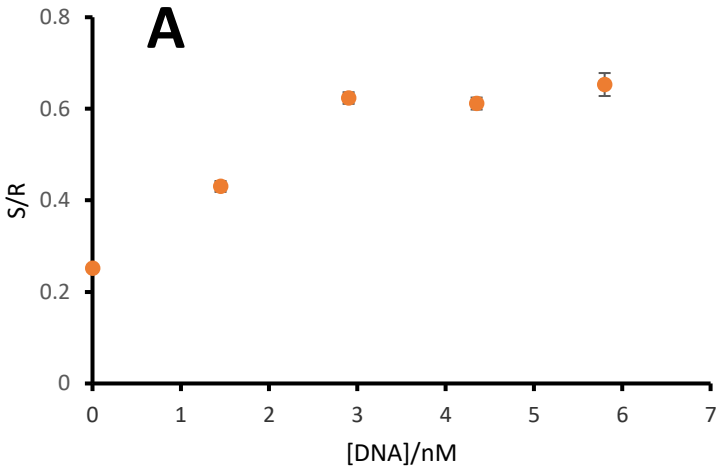

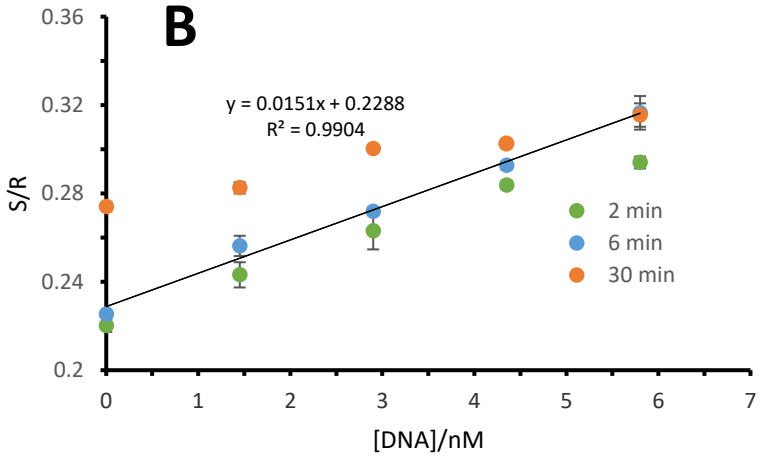

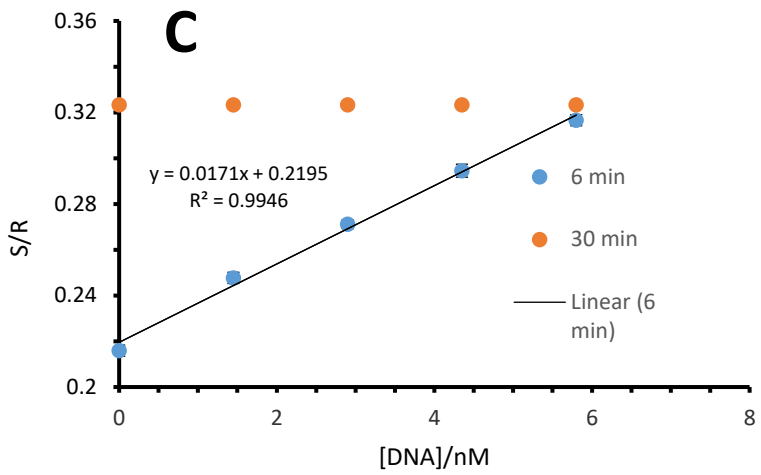

Figure 4.4 Optimal Reaction Conditions in the Device

Initial [Target DNA] = 8.7 nM; incubation T = 37 °C. (A) [Probe] = 20 nM; [Enzyme] = 66.7 U/mL, incubation t = 30 min. (B) [Probe] = 166 nM; [Enzyme] = 3.33 U/mL; t = (2, 6, 30) min. (C) [Probe] = 166 nM; [Enzyme] = 16.7 U/mL; t = (6, 30) min.

4.3.2 Effects of varying [Target DNA] and [Probe] on NESA and Limit of Detection (LOD)

In a chemical and biological reactions, unexpected products may form from side reactions that can be triggered by adding different amounts of reactants. Therefore, it is also important to figure out the optimal reaction concentrations of assay and target, and to explore the assay detection range for effectively quantitatively measuring the samples. Conventional laboratory experiments of this type can consume significant time, human resources, and finances to test varying reagent concentrations and optimize reaction conditions. Droplet microfluidics offer a unique platform to explore the influences of varying concentrations on the homogeneous reactions with isolated and uniform nanoliter-size droplets in simple, fast, precise, and low-cost way[116,307]. In contrast to previous droplet chip, this automatically, integrated device has great advantage of achieving this

goal with less time, materials and manual operations, and the higher flow rate oil pump in **Figure 4.1** provides enhanced operation speed.

Keeping the nicking enzyme at constant concentration of 16.7 U/mL and manually changing the Target-DNA solution (0.87, 8.7, 87 nM) and probe (166, 500, 1000 nM) within the reservoirs, where a constant assay probe droplet was treated as reference for lock-in analysis method which would eliminate the effects of drift from instrument and increase the limit of detection[117]. As shown in **Figure 4.5A,** 166 nM probe always gave the best signal performance at different concentrations of Target-DNA. In addition, higher concentration of template would speed up the reaction rate at the level of 0.87 nM to 87 nM. It could be explained that one target molecule was viewed as 'mobile catalytic site' and cleaved of lots of probes, the more target, the higher speed of nicking, and it was consistent with previous reports[17]. Longer incubation time (30 min) and lower concentration of probe (16.7nM) would improve the limit of detection of this assay on chip based on the conclusion above. Finally, the LOD and single-droplet mass LOD were calculated to be 14 fM (1.4×10^{-14} M) and 170 ymol (1.7×10^{-22} mol) using our lock-in technique with a 40× objective lens(**Figure 4.5B**). These data indicated that NESA was functional and efficient within aqueous-in-oil droplets on our droplet microfluidic device, and the data also revealed the strong potential of monitoring small amounts of secreted analytes from tissue or cells within picoliter or nanoliter droplets in the future.

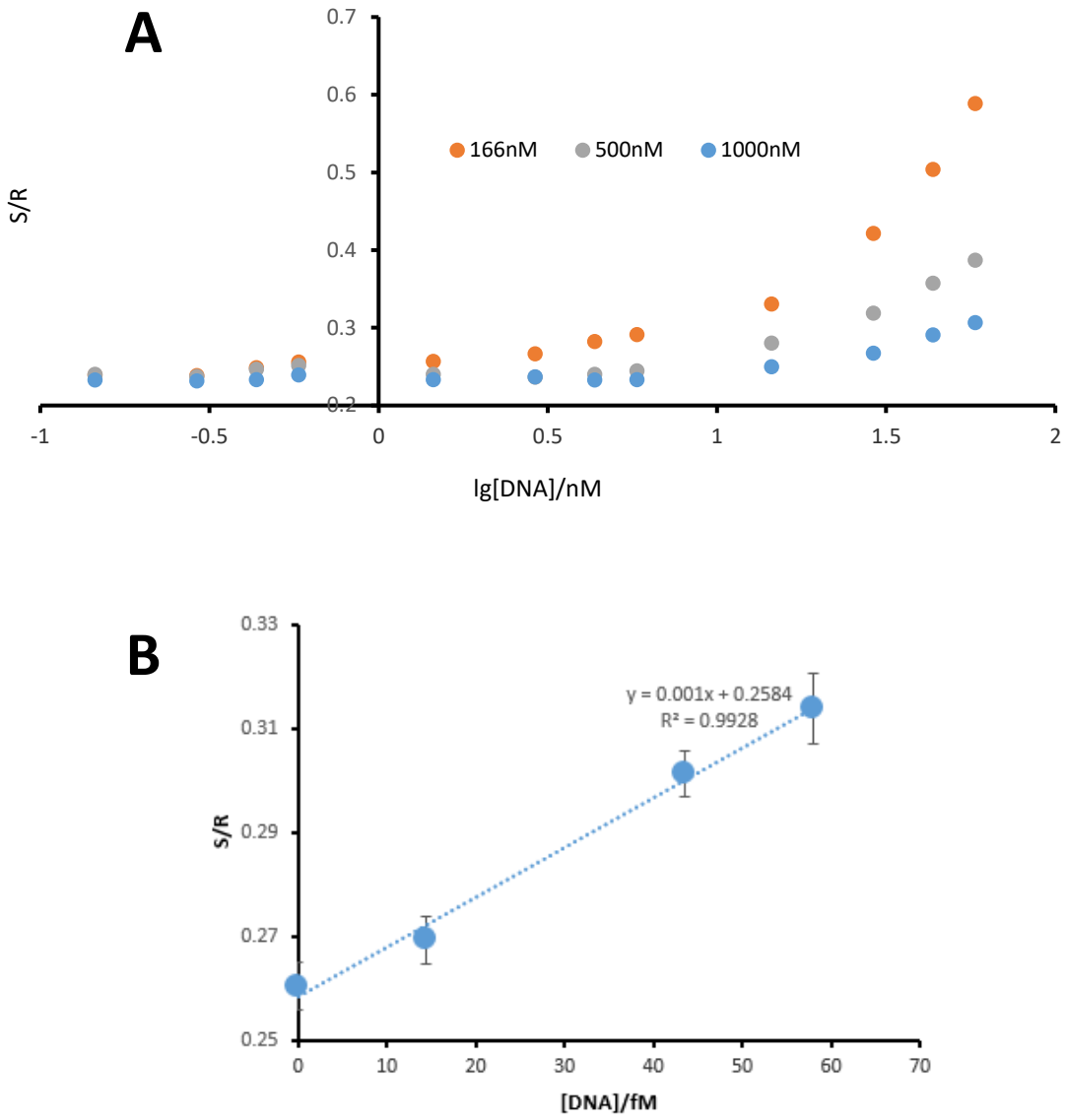

Figure 4.5 Effects of varying [Target DNA] and [Probe] on NESA Limit of Detection (A) Incubated for 6 min at 37 ℃ with 20x objective lens; [Target] = (0.87, 8.7, 87) nM; [Enzyme] = 16.7 U/mL; [Probe] = (166, 500, 1000) nM; a total of thirteen [Target] were studied at each level of probe. (B) LOD was obtained at [Probe] = 16.7 nM; [Enzyme] = 16.7 U/mL; t = 30 min incubation; 40x objective lens.

4.3.3 Analytical Performance of Extended NESA for Anti-digoxigenin Detection

Specific antibody detection plays an important role in diagnosis of human disorders including infectious and autoimmune diseases. Methodologies of antibody measurement of programmable nucleic acid nanoswitches and antibody-templated assembly of the spinach aptamer just achieved sensitivities in the nanorange[309,310]. Although standard NESA is only suitable to quantify targets which contain the recognition sequence of nicking enzymes, we hypothesized that NESA could be adapted to detect antibodies instead of just nucleic acid targets. Other groups have improved NESA in similar ways in recent years. Li-juan et al. utilized excision repair-initiated enzyme-assisted bicyclic cascade signal amplification to quantify Uracil-DNA glycosylase with a LOD of 0.0001U/mL and Yingfeng et al. also lowered the sensitivity of nucleic acid to 5.6 fM with the label-free enzymatic-assisted cascade signal amplification[311,312].

In this work, we report a novel detection method of anti-digoxigenin antibody (anti-Dig), namely a proximity-induced nicking enzyme signal amplification (**Figure 4.6**). Keeping the nicking enzyme, NESA buffer, and Reference at constant concentrations and only manual changing the mixture in the **reservoir #1** which contained varying concentrations of Anti-Dig, constant Arm, DG and probe (**Figure 4.7A**). Under the optimized experimental conditions, the limit of detection was calculated to 51 fM and mass LOD was 612 yoctomole (6.12×10^{-22} mole) in a single merged droplet (**Figure 4.7B**)

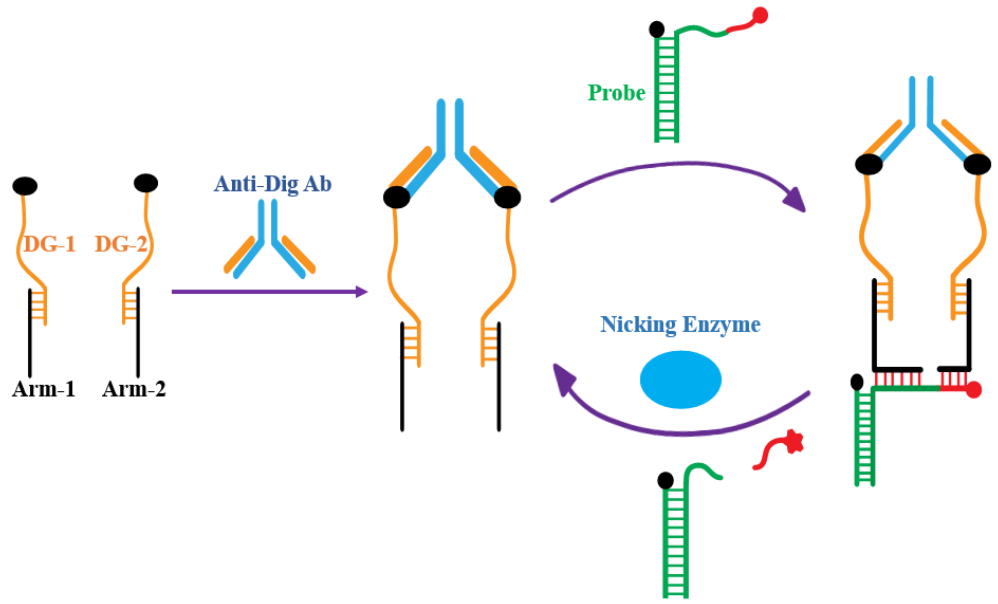

Figure 4.6 Proximity-induced nicking enzyme signal amplification

The system contains: (1) Two Dig- oligonucletodes (DG-1, DG-2); (2) Two arms (Arm-1, Arm-2) which are complementary to DG-1 and DG-2, respectively; (3) Target (Anti-Dig Ab) which is binding with Dig; (4) Probe which formats proximity structure with Arm-1 and Arm-2; (5) Nicking Enzyme (Nb.BbvCI) which cleaves probe at recognition sites.

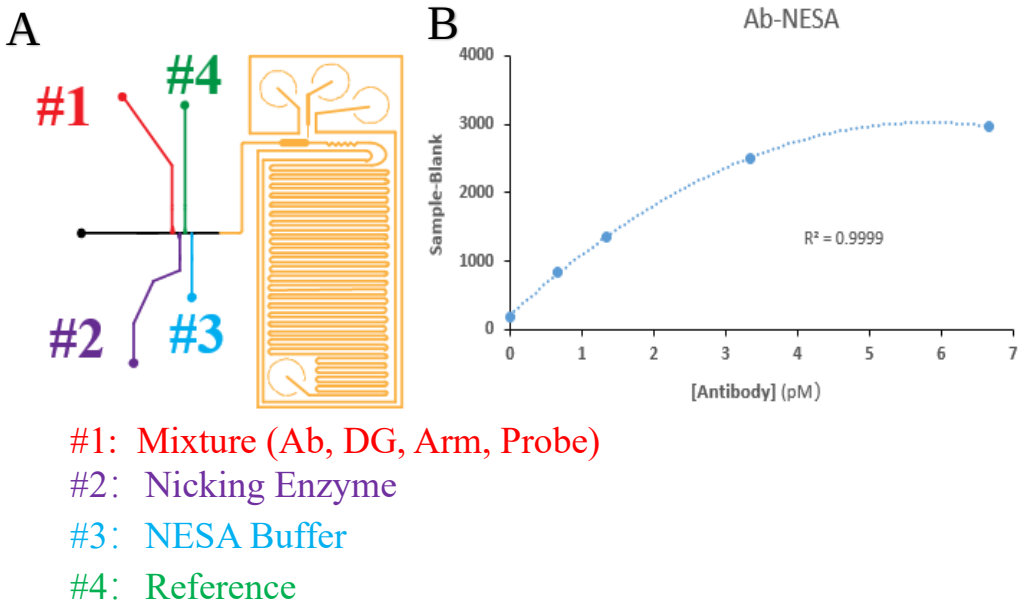

Figure 4.7 Extended NESA for Anti-digoxigenin Detection

(A) Programmable reagent mixing for extended NESA with minimal reagents in droplet microfluidic; (B) Calibration curve of antibody with extended NESA in droplet. The data was fitted to a second order polynomial model with $R^2 = 0.9999$.

4.4. Conclusions

An integrated microfluidic device containing pneumatic valve-based pumps and salt water electrodes was designed to generate, merge, and incubate droplets for biological assays. A highly sensitive and homogeneous detection system for analytes with isothermal NESA was constructed on this automatic device. This system shortened the reaction time, decreased the cost of biological measurements, and improved the accuracy of quantifying nucleic acids (**Table 3**). What is more, antibody was accurately monitored by extended NESA (proximity-induced nicking enzyme signal amplification), and this work indeed indicated the potential of combining isothermal amplification and droplet-based microfluidic for precisely analyzing protein and monitoring small amount secretion from single-cell in medical/biological research and early clinic diagnostics.

Sequence Name	Sequence (5'→ 3')
T-DNA	GTGGTGT CCTCAGC CGGTTT
FAM-1	/56-FAM/AAA CCG GCT GAG GAC ACC ACC GGA GAC TGT CCG CGC GGC G
BFQ	CGC CGC GCG GAC AGT CTC CG/3IABkFQ/
FAM-2	/56-FAM/TG GCTGAGG ACA CCA CAG AGC TCG GAG ACT GTC CGC GCG GCG
DG-1	AC TGC ATC GAC TAG CAT CGA CTA CG /3Dig-N/
Arm-1	ATG CTA GTC GAT GCA GTT TTT TTT TTT TTT TTT TTT TTC TGT GGT GT
DG-2	/5DigN/ AC TGC ATC GAC TAG CAT CGA CTA CG
Arm-2	CCTCAGC TGGT TTA ATT TTT TTT TTT CGT AGT CGA TGC TAG TC

Table 2 Single-stranded DNA (ssDNA) sequences used in this study

	Normal Tube	Microchip
Volume	**20 µL**	**12 nL**
Reaction time	**60 min**	**5 min**
LOD	**Picomolar**	**Femtomolar**
Single Assay Cost	**~ $2.0 × 10^{-2}**	**~ $1.2 × 10^{-5}**

Table 3 Comparison of basic NESA in conventional tube and droplet microchip

Chapter 5

Development of a Real-time, Quantitative Free Fatty Acid (FFA) Uptake Assay for Adipose Tissue in Droplet-based Microfluidics

5.1 Introduction

Adipose tissue is a complex, essential and active metabolic and endocrine organ with profound systemic effects, altering function in nearly all other organ systems[313]. It has been demonstrated that adipose tissue is closely related to diabetes, Alzheimer's disease, compromised immunity, and other diseases[314-316]. Though our understanding of adipose tissue has improved greatly in last several decades, specific functions and mechanisms about dynamic metabolism and nutrient uptake are still mysteries for researchers because of the constraints from traditional bioanalytical methodology. For tissue analysis with conventional techniques, temporal resolution normally ranges from minutes to hours that probably leads to lose some fast-changing biological information[75]. In traditional tube- or well-based sampling, not only a large amount of tissues and cells are required but also the results from static culture system are significantly different from that obtained *in vivo*[20]. In addition, the severe challenge caused by adipocytes buoyance indeed influences the development of adipose tissue analysis with the conventional tools[317].

In recent decades, microfluidics have been proved as an effective tool for cell/tissue culture and bioanalysis[165,169,177,318-320]. First of all, the microfluidic chips supply extremely suitable

platforms for cellular growth, proliferation and response to stimuli in collaboration with material and 3D printing technology[165,321]. Additionally, the microscale channels and reservoirs provide a large surface-to-volume ratio and also well mimic the *in vivo* situation[162]. One very important advantage is this small tool enables users to collect and access the metabolites from cells or single-cell whose volumes and concentrations normally are in ultra-low level. And the benefit of this technology is significantly improving human understanding on the metabolic activities of organs and cells under various conditions[267,322]. To explore the specific dynamic changes of metabolites such as glucose, insulin, glycerol, fatty acids from liver, pancreas, and adipose tissue, integrated microfluidics contained multiplexed functions like cellular culture, sampling, and monitoring were developed by our groups and others[75,165,173,267,323-325]. With the efforts of Kennedy, Roper, and our group in developing high sampling resolution in continuous-flow system and automated droplet-based microfluidics, several secretion dynamics about adipose tissue and pancreatic islet have been accurately revealed[75,267,287,317,326]. Compared to continuous-flow system, our automated droplet microchips with mix-and-read immunoassay have improved the temporal resolution of sampling to 3.5-seconds in secreted glycerol measurements[317].

It is obvious that metabolism of adipose tissue attracts much attention in past years and microfluidics already have shown its superiorities in this field. Therefore, researchers are curious whether the process of nutrient uptake can be accurately monitored with this micro-technology. Recently, lots of work indicate fatty acid uptake enables visualized and quantified with fluorescence imaging and encapsulated droplet via using bodipy-modified free fatty acids (FFA), respectively[117,267]. However, the real-time dynamic quantification of nutrient uptake rate never achieve in adipose tissue because of the constraints from inappropriate devices and the buoyance of adipocytes. Since the automated droplet-based microfluidics enable resolving adipose tissue

secretion dynamics with specific 3D template, we expected these systems to be well-suited for also measuring the nutrient uptake process at high temporal resolution. To discover the tiny response from endocrine tissue, the specific phase-locking technology developed in our lab has been successfully applied to eliminate the noise from instrument and improve the accuracy of detection[117,267,317]. Subsequently, a more precise continuous calibration mode was put forward in a multichannel, microfluidic droplet-based sample chopper by the Easley lab. In the continuous calibration mode, each sample is flanked by several calibration standards to allow full and real-time calibration, and this approach has the potential to be used in studying temporal responses of system, like dynamics of cellular function and reaction kinetics[118].

In this work, an automated, multiplexed droplet microfluidic system is introduced integrating four aqueous channels and one oil channel with peristaltic pumping for precisely generating droplets, specific reservoirs and 3D templates for trapping eWAT, and sensitive droplet-based lock-in or continuous calibration detection. This unique chip had improved flexibility for several modes in real-time accessing eWAT FFA uptake dynamics, including continuous calibration mode (CCM), multiple tissue mode (MTM), and complexed mode which was the special integration of CCM and MTM. Especially, the effects of various treatments and protein palmitoylation inhibitor (2-bromopalmitic acid) on eWAT FFA uptake were demonstrated in this system.

5.2 Experimental Design

5.2.1 Materials and Reagents

All buffers in the experiments were prepared with the deionized water that was produced by BarnsteadTM MicroPureTM Water Purification system (ThermoFisher Scientific, serial No.

42034239). Isoproterenol hydrochloride (>98%, purity) was bought from VWR (West Chester, PA). Fatty acid free bovine serum albumin (FAF-BSA) was obtained from Akron Biotech (Boca Raton, FL). 2-(bromopalmitic acid), D-glucose, HEPES (4-2-hydroxyethyl-1-piperazineethanesulfonicacid), penicillin-streptomycin, human insulin solution, NaCl, $CaCl_2 \cdot 2H_2O$, KCl, $MgCl_2 \cdot 6H_2O$ were purchased from Sigma-Aldrich (St. Louis, Missouri). BODIPY™ FL C16 (4,4-Difluoro-5,7-Dimethyl-4-Bora-3a,4a-Diaza-s-Indacene-3-Hexadecanoic Acid, cat.# D3821), DMEM (Dulbecco's Modified Eagle Medium, low glucose, L-glutamine, sodium pyruvate and phenol red, cat.# 11885084), DMEM (no glucose, no glutamine, no phenol red, cat.# A11430-01), MEM Non-Essential Amino Acids Solution (100X) (cat.# 111400502), Sodium Pyruvate (100 mM) (cat.# 11360070), Fetal Bovine Serum (qualified, USDA-approved regions, cat.# 10437010), Penicillin-Streptomycin (10,000 U/mL) (cat.# 15140122) and Dulbecco's Phosphate Buffered Saline (DPBS) from ThermoFisher Scientific (Grand Island, New York). PDMS (Polydimethylsiloxane) precursors, SYLGARD® 184 silicone elastomer base and curing agent were purchased from Dow Corning (Midland, MD).The silicon wafers were acquired from Polishing Corporation of America (Santa Clara, CA). SU-8 2015, SU-8 2050 and SU-8 developer were purchased from the Michrochem (Westborough, MA). AZ 40XT-11D and AZ 300 MIF developer were bought from the AZ Electronic Materials USA (Somerville, NJ). Pico-Surf 2% in Novec 7500 was purchased from Dolomite Microfluidics (Norwell, MA). NovecTM 7500 Engineered Fluid (HFE 7500) was from 3M. The human insulin concentration was confirmed by protein absorbance at 280 nm (A280) using a NanoDrop 1000 spectrophotometer (ThermoFisher).

5.2.2 Microfluidic Master Wafer Fabrication

Wafers for two-layer microfluidic devices with integrated valves and salt water electrodes were fabricated as described previously, in sections 2.2.2 and 2.2.3.

5.2.3 Microchip Fabrication

Two-layer microfluidic devices with integrated valves and salt water electrodes were fabricated as described previously, in sections 2.2.2 and 2.2.3. .

5.2.4 Flow Control

Flow control was accomplished as previously described in section 4.2.4.

5.2.5 Extraction of Murine Epididymal White Adipose Tissue (eWAT)

C57BL/6J male mice were used in this work. All of animal experiments were done in compliance with relevant laws and institutional guidelines and protocols 2017-3101 and 2020-3787 were approved by the institutional animal care and use committee (IACUC) of Auburn University. Epididymal white adipose tissue (eWAT) pads were extracted from mice described in previous papers[165,267]. After eWAT pads were extracted from the mice, they were transferred into 10 mL phosphate-HEPES buffer (10 mM HEPES, 135.3 mM NaCl, 2.2 mM $CaCl_2 \cdot 2H_2O$, 1.2 mM $MgSO_4 \cdot 7H_2O$, 0.4 mM KH_2PO_4, 2.2 mM Na_2HPO_4, 0.4 mM D-glucose, 2% BSA, pH 7.4). Fat pads were placed in the 60 mm Petri dish with phosphate-HEPES buffer and extra vasculature was removed by Iris micro dissecting scissor. 2-mm dimeter explants were punched from the fat pads with 2 mm sterile disposable biopsy punch and stored in glass tube contained 4 mL phosphate-HEPES buffer. The explants were washed with the phosphate-HEPES buffer for three times with centrifuging at 1000 rpm for 3 min. The 3 mL buffer was removed by the syringe after centrifuge and 3 mL fresh buffer was added for next washing cycle. Then the phosphate-HEPES buffer was switched to fat serum media (DMEM + low glucose and phenol red with 12% fetal bovine serum, 120 units/mL Nystatin, 120 units/mL Penicillin-Streptomycin and 1.2X MEM NEAA), and the explants were washed in the serum media for another two times. After washed, they were stored

in the sterile 96-well plate with 200 μL fat serum media and specific 3D-printed anchors were used to avoid the buoyance of fat tissue, and each piece of explant was placed in one well. The explants were cultured in the 37 ^{o}C incubator with 5% CO_2, and they can survive up to 7-10 days if the serum media was refreshed twice per day. The explant for each experiment was washed and pretreated on-demand in media without serum for 30 min before loading on the microchip.

5.2.6 Quantification of Free Fatty Acid Uptake by eWAT

BODIPY-FL-C16 was used as the labeled long free fatty acid (FFA*) in this work. The whole microchip was mounted with a microscope stage-top incubator (Tokai Hit, Japan) which was set at 37 ^{o}C. In the four aqueous inlets, the necessary number of reservoirs were loaded with samples (eWAT explants) and references (different concentration of FFA*). For the explant reservoir, the small trap region was filled with treatment solution contained 2 μM FFA* before loading the small eWAT tissues. A 3D-printed insert was set on the top of trap region for counteracting the buoyancy of the eWAT explant, and then the whole culture reservoir was injected with the same culture solution by pipette. The FFA* solution was continuously flowed over the explant, and eluted FFA* was encapsulated into droplets and quantified with a CCD camera (40× objective lens) downstream. This allowed measurement of eWAT explant absorption of FFA* in a quantitative manner by comparing sampled droplets to neighboring droplets containing various concentrations of FFA* generated from reference inlets. Our device could be used for real-time locked-in or continuous calibration modes to accomplish this quantitatively.

5.2.7 FFA Uptake Dynamic Study at Varying Treatments

The explants for experiment were washed 3x with fresh serum free media, and incubated with pretreatment solution for 30 min in a 96-well plate. 3D-printed tissue traps were used to

ensure explants were immersed completely in solution (similar to that shown in **Figure 5.1B**). After 30-min off-chip culture, eWAT was took out and 0.75 mm size explant was punched out and then trapped into the bottom reservoir in the tissue culture inlet containing treatment solution on-chip (**Figure 5.1B**). The pretreatment and treatment solutions of HGHI (25 mM glucose and 2 nM insulin in DMEM (no glucose, no glutamine, no phenol red) with 0.2% FF-BSA) and LGLIS (3 mM glucose, 50 pM insulin with 20 μM isoproterenol in DMEM (no glucose, no glutamine, no phenol red) with 0.2% FF-BSA) were specifically combined (**Table 2**) to study the treatment dependence of adipose tissue FFA uptake kinetics.

5.2.8 CD36 transport blocker and its effect on FFA uptake

All the process in this part were similar to that of the above treatment study except that only pretreatment solutions were added with 100 μM 2-bromopalmitic acid (2-BP) and the culture time of explants in 96-well plate was extended to 1.5 h. In addition, a small piece of eWAT was punched from 2-mm explanted and the effects of 2-BP on FFA uptake explored at 0.5 h and 1.5 h, respectively.

5.3 Results and Discussion

5.3.1 Microfluidic Chip Design and Modes of Operation

As shown in **Figure 5.1**, this microfluidic chip included the following components: (1) one oil channel and four aqueous channels for multiplexed sample and reference droplets generation; (2) connected pneumatic controlled pumps for eliminating numbers of solenoid and improving the frequency of droplet formatting; (3) 3D-templated reservoirs and 3D-printed tissue traps for culturing and trapping explants,; and (4) four individual valves for managing the patterns of droplet generation.

In comparison to our previous designs for tissue analysis with droplet[75,117,317], this four-channel droplet microchip not only addressed several limitations of them, but it also expand the benefits of combining control-valve and pump-valves to manage an aqueous channel. The backstage LabVIEW program was utilized to command the activity of microchip consisted of control-valves on/off, and the frequency and cycle of pump-valve. In this work, the main difference from previous programs was that all of the valve-based pumps run continuously, and we only regulated the control-valves as needed. The non-stop pumping stored some pressure in the aqueous channel, and this energy would push the solution flowing into oil-channel faster, further reducing time to generate the appropriate volume of droplet, and improving the temporal resolution of tissue sampling. Meanwhile, this multiplexed device enables access to multiple tissue-analysis modes depended on the arrangement of the four reservoirs, including continuous calibration mode (CCM), multiple tissue mode (MTM), and the special combination of CCM and MTM. Further discussion about this three modes will be included below.

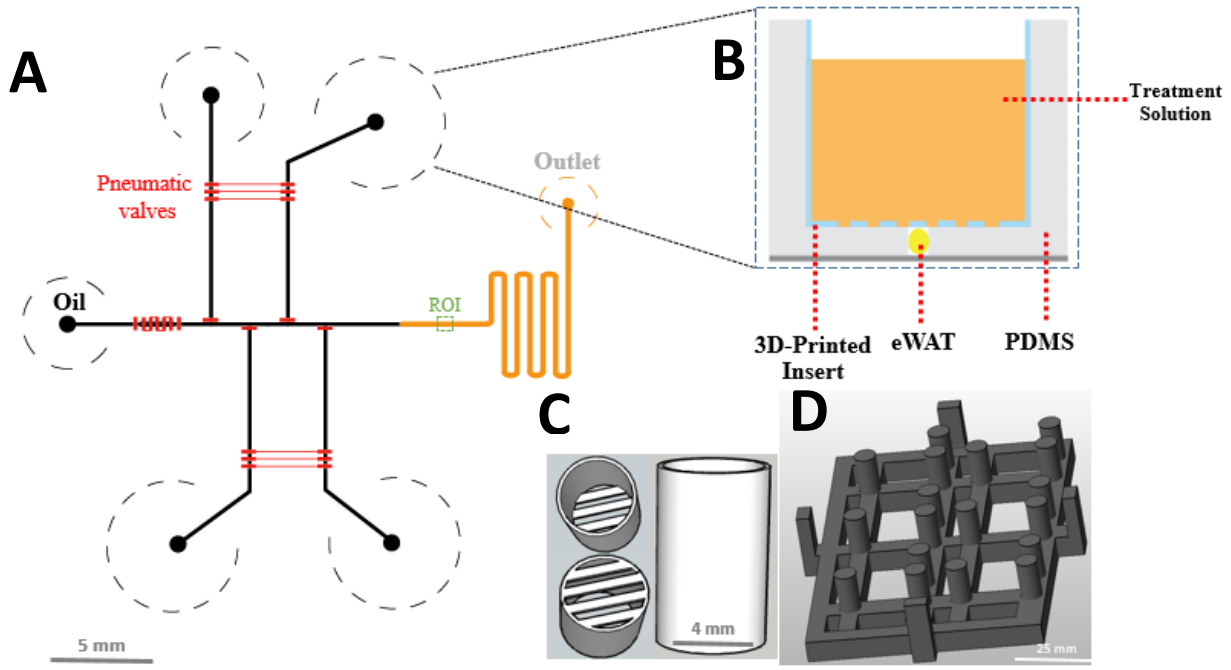

Figure 5.1 Microfluidic Chip Design

(A) Layout of Microchip with round fluidic channels (black), squared fluidic channel (orange), and pneumatic valves (red). (B) Schematic figure of crossing-section of tissue-culture reservoir. (C) Top, bottom and side views of 3D-printed insert (white) which is applied to trap eWAT explant on the bottom of reservoir (D) 3D-printed template (gray) for tissue culture reservoir fabrication, respectively.

5.3.2 Calibration of Labelled Free Fatty Acid (FFA*) in Microfluidic Droplets

Though surfactant (0.5% Pico-Surf) was added into the oil, which contributed to generate and stabilize the water-in-oil droplets, the encapsulated FFA* was observed to leak into the channel and absorb into the PDMS (**Figure 5.2A**). This problem is a result of the lower solubility of fatty acid molecules in aqueous solution and their preferential solubility into more hydrophobic liquids (oil) or surfaces (PDMS). To address this problem (**Figure 5.2B**), two main steps were conducted before each experiment. All the aqueous reservoirs and channels should be treated with 2% FF-BSA (fatt- acid-free bovine serum albumin) for 1 hour to inhibit both the partitioning of FFA* into the oil and the PDMS surface from absorbing FFA*[262]. Note also that all of the aqueous solutions used in this work were mixed with 0.2% FF-BSA to improve the solubility of hydrophobic bodipy-FL-C16 and for avoiding the leakage and adsorption of FFA*. After the BSA-coating treatment of microchip, various concentrations of FFA* (1.25, 2.5, 5, 10 μM) were loaded into the four aqueous reservoirs. The images of droplets containing different concentrations of FFA* were collected in the region of interest (ROI shown in **Figure 5.1A**) downstream. After the process of Octave (or Matlab), ImageJ, and Excel, **Figure 5.3** obviously showed that the fluorescence intensity was determined by the FFA* concentration.

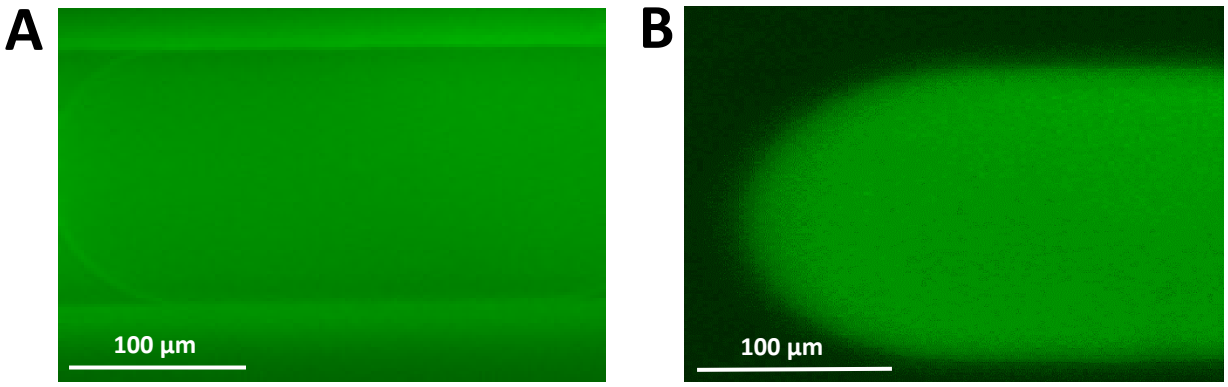

Figure 5.2 BSA coated PDMS channel

(A) Image of non-FF-BSA droplet and non-coated channel surface. (B) Image of droplet contained 0.2% FF-BSA with channel-coating treatment in advance. The images were captured with 20X objective lens and FITC channel in fluorescent inverted microscope (Nikon Eclipse Ti-E)

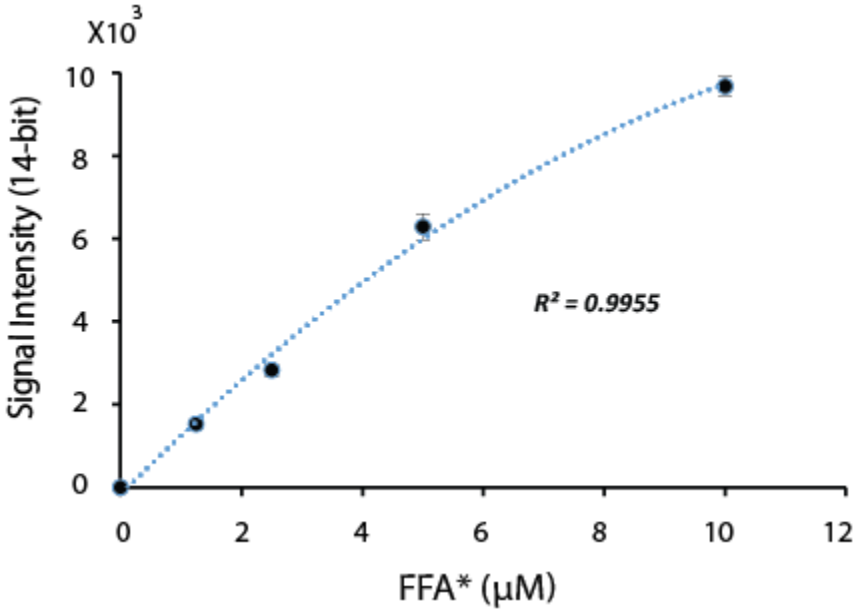

Figure 5.3 Calibration of FFA* in droplet-based microfluidics

Data was fitted to a second-order polynomial model, where $R^2 = 0.9955$

5.3.3 Continuous Calibration Mode (CCM): real-time, 3-point calibration

The **Figure 5.4A** shows the continuous calibration mode in the four-channel droplet microchip. This automated chip supports to cyclically generate uniform size droplets with four types of contents. The discrepancy of peak widths was caused by the different flow rates of solution from aqueous channels and main oil channel. Use CCM for monitoring the FFA uptake rate by adipose tissue, three aqueous reservoirs were loaded with three concentrations of FFA* (0.5, 1, 2 μM) as references and one aqueous inlet contained 2 μM FFA* and the eWAT explant as tested sample. In this mode, each sample droplet was corrected by a real-time, 3-point calibration curve approximately every 10 seconds (**Figure 5.4B**). A benefit of this method is that calibrations and sample are obtained simultaneously, which omits the extra process to construct a standard curve for device users. Compared to previous methods used by our laboratory and others, this real-time correction is more precise and appropriate to be widely applied in studying the dynamics of cellular function and chemical/biological reaction kinetics[118].

5.3.4 Multiple Tissue Mode (MTM): multiplexed sampling with lock-in detection

In studying real-time dynamics of tissue in a microfluidic chip, complicated chip design and lots of auxiliary tools are committed to culture and monitor the activity of only single tissue or cell. Because comparing to the static imaging and access of cell and tissue, the cellular dynamic exploration demands several main components, such as specific culture chamber/reservoir, continuous power system, complexed fluidic channels, and sensitive detection instrument. The biggest challenge is integrating all of the components together to format a whole system where every part accurately collaborates with each other for satisfying the need of dynamic analysis of tissue[134,178,325,327]. However, it is somewhat wasteful to measure a single tissue explant once with

such a significant investment of time and resources. Simultaneous multiple-tissue-on-a-chip detections could save researchers time and reduce errors caused by different microchips and constantly changing experimental conditions. Fortunately, our device (**Figure 5.1**) is also compatible with running in a multiple tissue mode (MTM). In MTM, 0.75 µM FFA* solution was injected into one inlet as reference, and the other three reservoirs respectively contained 2 µM FFA* solution as well as a trapped eWAT explant; an example data set is shown in **Figure 5.4C**. Therefore, three sample droplets and one reference droplet were detected successively at the region of interest during one cycle, and eventually three quantitative, dynamic curves of FFA uptake rates by explants were obtained using our lock-in approach (**Figure 5.4C**). From this proof of concept, it is obvious that the amount of tested samples can be expanded even further with the increasing number of input channels in certain range to maximize the benefits of time and instrument usage.

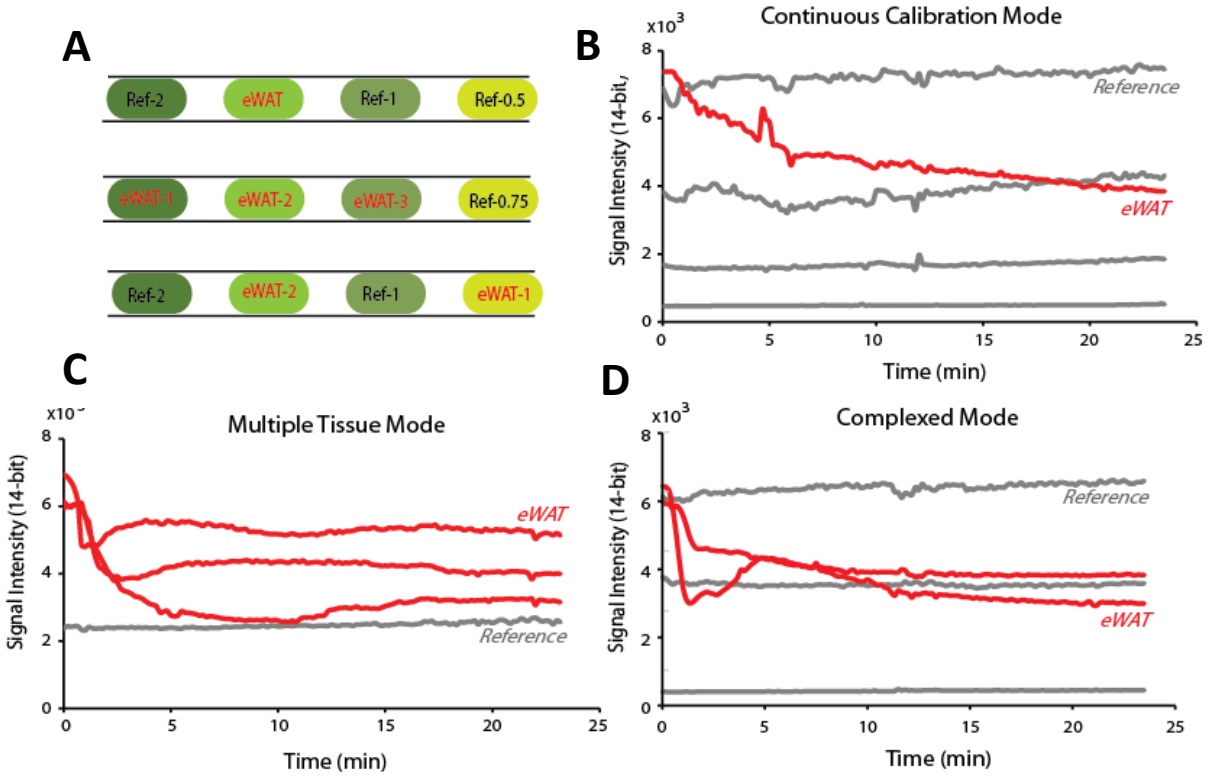

Figure 5.4 Data for three modes of operations with four-channel droplet microchip

B, C and D were the schematics of continuous calibration mode (top), multiple tissue mode (middle) and complexed mode (bottom) in the droplet microfluidic device, respectively. (B) Stitched data of continuous calibration mode obviously indicated that one tissue (red) and three references reservoirs (gray) were contained on the microchip. (C) Processed data of multiple tissue mode reveals that three different eWAT explants (red) were simultaneously monitored with lock-in approach. (D) Two sample (red) and three reference traces (gray) were included in the temporal data of complexed mode.

5.3.5 Complexed Mode: multiplexed sampling with continuous calibration

Considering both of the advantages of precise continuous calibration and high-throughput multiple tissue modes, a complexed mode was developed which consisted of two tissue reservoirs and two reference inlets containing 2 µM and 1 µM labeled free fatty acid solution. In this mode, the continuous oil phase was viewed as 0 µM FFA* reference, and it was utilized to construct 3-point calibration curves with the two references mentioned above for real-time correcting of the neighboring sample droplets. Therefore, a real-time, three-point calibration with droplets from two different samples formatted a cycle of this multiplexed mode (**Figure 5.4D**). As **Figure 5.4D** shows, two 25-min dynamic traces described the FFA uptake rate by small eWAT explants, and these were demonstrated alongside real-time, three-point calibration curves. Next, this highly efficient mixed mode was subsequently applied to explore how various treatments including concentrations of insulin, glucose, and isoproterenol, as well as a FFA transport blocker (2-bromopalmitic acid) influenced the adipose tissue absorbing free fatty acid (see below).

5.3.6 Analysis of Data from Multiple Sources

In this work, several processes and software were required to analyze the raw data with multiplexed signals. As **Figure 5.5A** and **Figure 5.5B** showed, five different peaks were included

in a ~10-second cycle, and there were a total of 150 cycles in an analytical mode. It would take an individual researcher almost 2 hours to manually select and sort these various signal responses (in software such as Excel) for only one trial, and several errors also were introduced during data selection. Consequently, it was important to address this issue with smarter methods. With our modified approach, raw data was processed with mathematical software (Octave or Matlab; codepresented in **Table 5.1**), and it was then divided into five types consisting of three references and two samples (Ref-2, Ref-, Ref-0, eWAT-1 and eWAT-2). These five bands are graphically depicted in **Figure 5.5C**, and the corresponding results (see **Figure 6)** would be presented after additional two simple steps in ImageJ and Excel. In comparison to manual analysis, this developed analytical methodology not only shortened the time of accessing data from 2 hours to 5 minutes, but it also promoted accuracy of data sorting. In short, this novel data processing approach largely improves the working efficiency and is well-matched with the operation of our droplet sampling device..

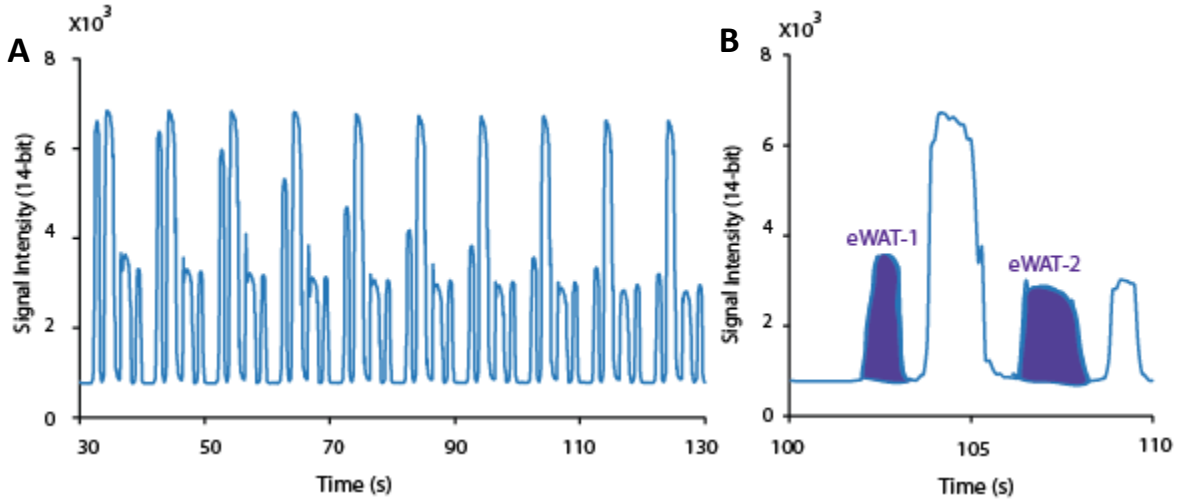

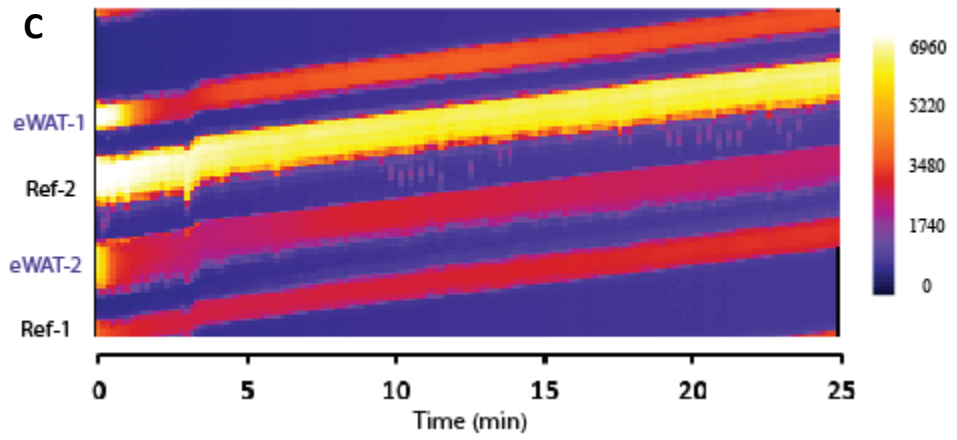

Figure 5.5 Data processed with Octave

(A) 100 s record of raw fluorescence data in complexed mode from four-channel droplet microchip. (B) Zoomed view of 10 second windows of data from (A). (C) Heat map consisted of five colorful bands (two samples and three references) were obtained after processed with Octave and ImageJ.

Table 4 Octave Code

```
S = zeros(5,2);
data2 = data(:,2);
for n = 1:window:(size(data2,1)-2*window);
 if n==1;
  n2=n;
 else
  n2=n2+window+Mins(ceil(n/window)-1);
 endif
 sync = 16;  % width of sync window
 for m = -sync:sync;
  diff = data2(n2:n2+window-1) - data2(n2+window+m:n2+2*window-1+m);
  diffSq = diff.^2;
  S(m+sync+1,:) = [m sum(diffSq)];   % note than in S(m+?,:) the ? must be max(m)+1
 endfor

 [minval row] = min(S(:,2),[],1);
 M = S(row,1);   % M is the m value that minimizes diffSq
 Mins(ceil(n/window)) = M;

 if n==1;
  EnTwo(ceil(n/window))=n;
 else
  EnTwo(ceil(n/window))=n2;
 endif
```

```
for n = 1:(size(data(:,2),1));
A(mod(n,105)+1,ceil(n/105))=data(n,2);
end
>> imshow(A)
>> save img1.txt A -ascii;
>> contour(A)
```

5.3.7 CD36 Transport Blocker and Its Influence on Fatty Acid Uptake

Long-chain fatty acids are mainly taken up across the membrane of adipocytes via protein-mediated pathways. Except the contributions of transport proteins and fatty acid-binding proteins in the process of fatty acid, fatty acid translocase CD36 (cluster of differentiation 36) is the main high-affinity receptor significantly facilitating FFA uptake into adipocytes[328]. 2-bromopalmitic acid (2-BP) has been proven to effectively block fatty acylation of proteins in general and palmitoylation in particular[329]. In addition, Jan et al. introduced DHHC4 and DHHC5 to facilitate fatty acid uptake by palmitoylating and targeting CD36 to the plasma membrane[330]. Therefore, 2-bromopalmitic acid (2-BP) is an appropriate choice to verify the function of CD36 on free fatty acid uptake by adipose tissue. In this work, 2-BP was added into pretreatment solutions (HEPES-phosphate buffer with 0.2% FF-BSA contained LGLIS or HGHI) and incubated at different times to explore the effects of various insulin and glucose concentrations and drug doses on FFA uptake. **Figure 5.6** indicated that FFA uptake amounts of adipose explants pre-cultured with LGLIS buffer contained 100 μM 2-BP decreased significantly, yet the FFA absorption amount of those explants pre-treated without 2-BP did not have obvious change. These results significantly demonstrated that 2-BP has effects in fatty acid uptake by eWAT. When we replaced LGLIS solution with HGHI solution to pre-culture eWAT, the FFA uptake amount did not affected by 2-BP in this condition. Herein, we assumed though 2-BP reduced the amount of CD36 on the cellular membrane in the HGHI solution, high concentrations of insulin and glucose probably stimulated other transport proteins or enzymes to make up fatty acid absorption for adipocytes. In contrast to HGHI solution, 2-BP culture time had greater impact on FFA uptake in LGLIS condition and the longer culture time lead to less amount of FFA absorption (**Figure 5.7A** and 5.**7B)**.

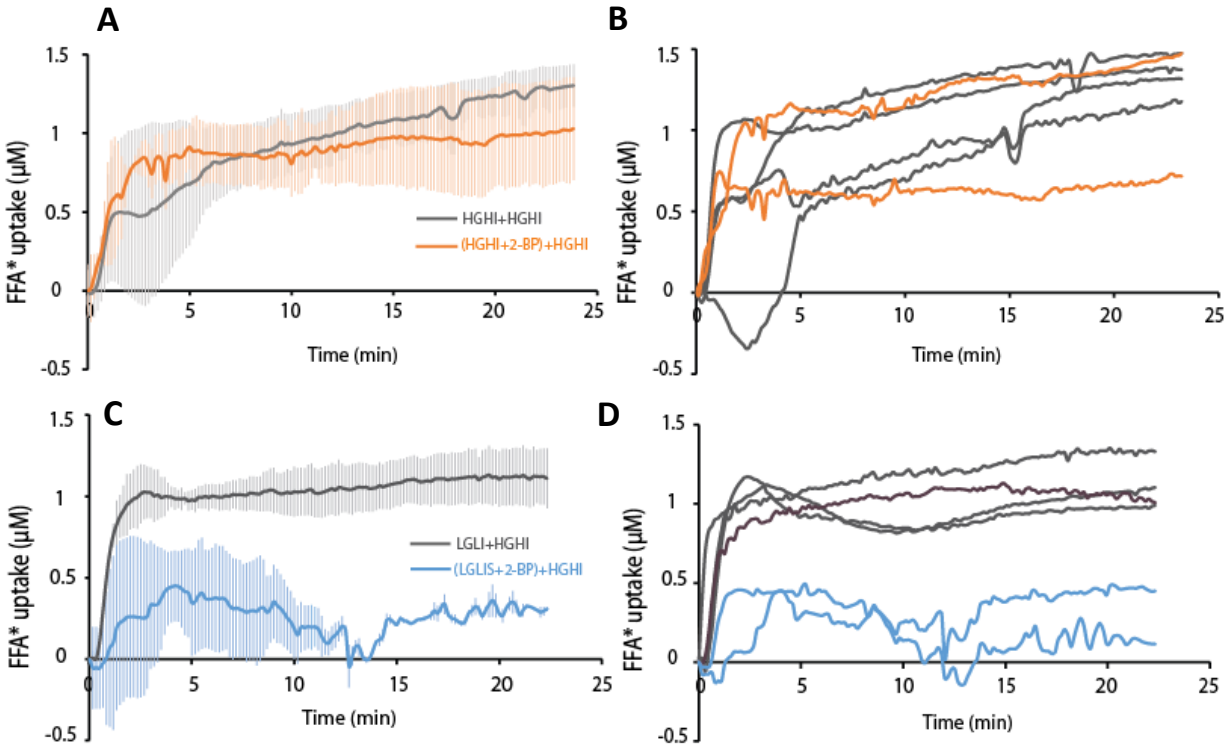

Figure 5.6 Effect of inhibitor (2-BP) on fatty acid uptake

(A) and (B) The orange and gray traces represent the fatty acid uptake dynamics of explants pre-treated with 100 μM 2-BP and control group without 2-BP in HGHI, respectively. (C) and (D) FFA uptake dynamics from explants treated with 2-BP in advance (blue) and no drug (gray) in LGLIS media.

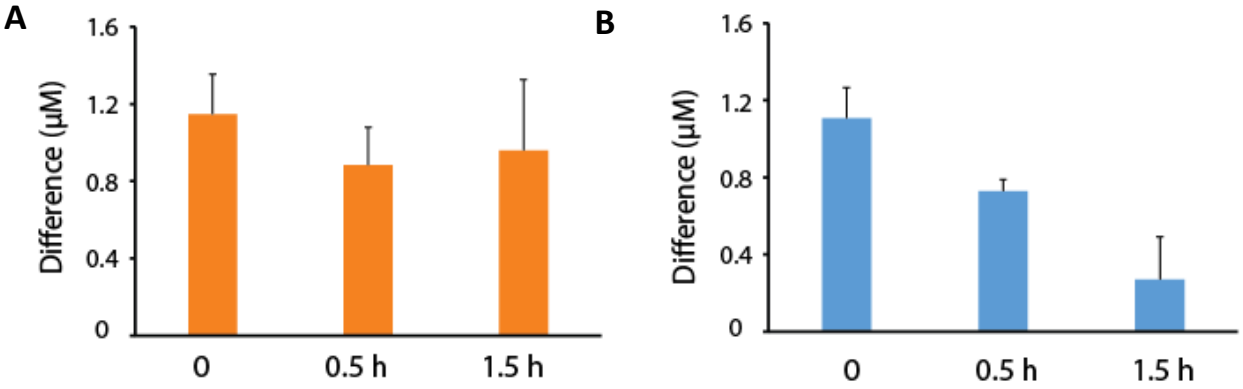

Figure 5.7 Effects of 2-BP treatment time on free fatty acid uptake amount of adipose tissue in HGHI (orange) and LGLIS (blue). Error bars represent the standard deviation from 3 explants undergoing each treatment.

5.4 Conclusion

An automated droplet-based microfluidic system was developed for real-time monitoring of free fatty uptake dynamics by adipose tissue. To our knowledge, this device enabled dynamics of eWAT FFA uptake rates and amounts to be analyzed quantitatively at high temporal resolution for the first time. To improve the efficiency and accuracy of this system, two eWAT explants were detected simultaneously along with real-time 3-point calibrations. Meanwhile, effects of varying treatments and CD36 transport blocker (2-BP) on fatty acid uptake were demonstrated with this device.

However, to more deeply understand the dynamics and mechanisms of fatty acid uptake, more work should be conducted. The devices developed in this chapter should prove to be very useful in these future studies. Droplet-based multichannel microchips could be introduced to detect more than two tissues at the same time, which will save researchers lots of time and improve the credibility of results. In the future, a large amount of quantitative, dynamic data about the effects of insulin and glucose on FFA uptake could enable us to build better mathematic models for predicting the conditions of adipose tissue in certain untested conditions. These results could have lasting medical and economic significance. More immediately, because transport blockers of CD36 do not effectively inhibit fatty acid uptake after pretreatment in high concentrations of insulin and glucose, we need to explore and verify whether HGHI actually stimulate the amount of CD36 or other transport proteins increasing, or there are other reasons. What is more, longer detection time is required to confirm whether the amount and rate of FFA uptake will go back to zero or just stay at a raised level indefinitely following these treatments.

Chapter 6

Automated Microfluidic Droplet Generation and Merging to Simultaneously Resolve White Adipose Tissue (WAT) Nutrient Uptake and Secretion Dynamics

6.1 Introduction

As discussed in detail above, adipose tissue as an endocrine tissue has an important role in the global epidemic obesity and diabetes. Currently, adipose tissue has been proven as an organ for absorbing and storing excess energy, as well as synthesizing and secreting various hormones, cytokines, and adipokines to regulate other endocrine organs.[4,331] In feeding conditions, adipose tissue absorbs and stores nutrients in the form of lipid droplets within each cell. Under fasting or nutrient deficient conditions, the reserved triglycerides (TGs) will be enzymatically cleaved into glycerol and non-esterified fatty acids through lipolytic pathways.[332] However, neither nutrient uptake nor metabolism has been explored quantitatively at high temporal resolution due to limitations of traditional instruments and methods. Development of tissue engineering and microfluidic techniques requires culture and access adipose tissue explants or adipocytes, and even bio-analyzing their ultra-small volume sampling.[20,266,333-335] The Kennedy group pioneered integrating culture and stimulation of adipose cells on microchips.[170,326,336] To simplify experimental manipulations and control the expenditure, our lab completely combined tissue/cell culture, stimulation and measurement on-chip, and we were the first group to do so with intact,

murine tissue explants (ex vivo).[117,165,267,320] Compared to more traditional, low-resolution methods, dynamic studies of cellular nutrient absorption and metabolism could provide us lots of information to more deeply understand the physiological mechanism of tissues and cells. In the field of microfluidic technology, both of perfusion and droplet system have been introduced to rapidly stimulate and real-time monitoring the secretion dynamic from cells and tissues.[75,168,187,317]

As we know, most of intracellular activities and mechanisms of transferring absorbed nutrients to metabolites have been described qualitatively without accurate measurement. However, quantifying the amounts of nutrient absorption, intermediates and secretions is much more helpful for researchers to precisely understand the biochemical mechanisms of cells and tissues compared to traditionally qualitative way. Microfluidics has improved this capability, although the vast majority of previous work mainly focused on the detection of an individual analyte secreted from cells using microfluidic devices[75,168,172,178], although some have shown multiplexed analysis. In the application of perfusion systems, the Roper lab developed a microfluidic device to monitor insulin and islet amyloid polypeptide (IAPP) secreted form islets at the same time.[322] The Kennedy group used two types of fluorescent assays to simultaneously measure non-esterified fatty acid (NEFA) and glycerol release from 3T3-L1 adipocyte cells, and they indicated that part of the NEFAs were re-esterified back to triglycerides.[326] In contrast to a continuous perfusion system, droplet-based microfluidics have higher temporal resolution and effectively avoid undersampling caused by intermittent sampling. The Ismagilov group applied their "chemistrode" to record and analyze intercellular Ca^{2+} and extracellular insulin secretion of islets with high resolution, measured in parallel.[243]

All of this previously mentioned work mainly quantified released metabolites and ignored the uptake process. To better understand tissues or cells, it is important to demonstrate the

relationship between their absorption and secretion processes, and doing so simultaneously could better shed light on their mechanistic connections. The response of metabolism to nutrient uptake might be extremely rapid when external stimulations suddenly change. Therefore, techniques with stimulation and recording at high temporal resolution are indeed required for this type of research, such as our droplet-based microfluidic technique.

In this work, we developed a unique droplet-based microfluidic device to simultaneously quantify both labeled free fatty acid (FFA*) uptake and glycerol secretion from eWAT with our highly sensitive, optical lock-in detection. Integration of pneumatic valves and a salt-water electrode ensured constant mixing of aqueous-in-oil segments with glycerol assay reagents and samplings from epididymal white adipose tissue (eWAT). Because unabsorbed FFA* and secreted glycerol was encapsulated within the same droplets, two-color detection filters (green and red; FITC and TRITC) were adapted to simultaneously monitor FFA* and glycerol signal on-line with 9-second temporal resolution. Furthermore, the significant change of FFA absorption and glycerol secretion traces was demonstrated during exposure to 20 μM isoproterenol and various concentrations of insulin and glucose. These results and the underlying methodology should help to improve our understanding of the dynamic functionality of adipose tissue.

6.2 Experimental Design

6.2.1 Materials and Reagents

All buffers in the experiments were prepared with the deionized water that was produced by BarnsteadTM MicroPureTM Water Purification system (ThermoFisher Scientific, serial No. 42034239). Isoproterenol hydrochloride (>98%, purity) was bought from VWR (West Chester, PA). Fatty acid free bovine serum albumin (FAF-BSA) was obtained from Akron Biotech (Boca

Raton, FL). Glycerol Assay Kit (cat.#MAK117-1KT), D-glucose, HEPES (4-2-hydroxyethyl-1-piperazineethanesulfonicacid), penicillin-streptomycin, human insulin solution, NaCl, $CaCl_2 \cdot 2H_2O$, KCl, $MgCl_2 \cdot 6H_2O$ were purchased from Sigma-Aldrich (St. Louis, Missouri). BODIPY™ FL C16 (4,4-Difluoro-5,7-Dimethyl-4-Bora-3a,4a-Diaza-s-Indacene-3-Hexadecanoic Acid, cat.# D3821), DMEM (Dulbecco's Modified Eagle Medium, low glucose, L-glutamine, sodium pyruvate and phenol red, cat.# 11885084), DMEM (no glucose, no glutamine, no phenol red, cat.# A11430-01), MEM Non-Essential Amino Acids Solution (100X) (cat.#111400502), Sodium Pyruvate (100 mM) (cat.#11360070), Fetal Bovine Serum (qualified, USDA-approved regions, cat.#10437010), Penicillin-Streptomycin (10,000 U/mL) (cat.#15140122) and Dulbecco's Phosphate Buffered Saline (DPBS) from ThermoFisher Scientific (Grand Island, New York). PDMS (Polydimethylsiloxane) precursors, SYLGARD® 184 silicone elastomer base and curing agent were purchased from Dow Corning (Midland, MD).The silicon wafers were acquired from Polishing Corporation of America (Santa Clara, CA). SU-8 2015, SU-8 2050 and SU-8 developer were purchased from the Michrochem (Westborough, MA). AZ 40XT-11D and AZ 300 MIF developer were bought from the AZ Electronic Materials USA (Somerville, NJ). Pico-Surf 2% in Novec 7500 was purchased from Dolomite Microfluidics (Norwell, MA). NovecTM 7500 Engineered Fluid (HFE 7500) was from 3M. The human insulin concentration was confirmed by protein absorbance at 280 nm (A280) using a NanoDrop 1000 spectrophotometer (ThermoFisher). High-Voltage amplifier Model 2220 was from TREC, INC (Lockport, NY, USA).

6.2.2 Microfluidic Master Wafer Fabrication

Wafers for two-layer microfluidic devices with integrated valves and salt water electrodes were fabricated as described previously, in sections 2.2.2 and 2.2.3.

6.2.3 Microchip Fabrication

Two-layer microfluidic devices with integrated valves and salt water electrodes were fabricated as described previously, in sections 2.2.2 and 2.2.3. .

6.2.4 Flow Control

Flow control was accomplished as previously described in section 4.2.4.

6.2.5 Extraction of Murine Epididymal White Adipose Tissue (eWAT)

Mouse surgeries, tissue extractions, and treatment procedures were conducted as described above, in section 5.2.5.

6.2.6 Measurement Method of FFA Uptake and Glycerol Release

BODIPY-FL-C16 was used as the labeled long free fatty acid (FFA*) in this work. The whole microchip was mounted with a microscope stage-top incubator (Tokai Hit, Japan) which was set at 37 ^{o}C. eWAT explants were trapped and cultured in special reservoir molded with 3D template. Firstly, the bottom trapped region was fulfilled with treatment solution contained 2 μM FFA* before loading small eWAT explant. Then the same culture solution was injected into the upper open culture reservoir by pipette after the 3D-printed trap was inserted on the top to counteract the buoyancy of the eWAT explant. The leftover FFA* was encapsulated into droplets and quantified in downstream, after eWAT explant absorbed certain amount of FFA* from stock solution. Moreover, the secreted glycerol from trapped explant was included in each sample droplet, and glycerol secretion was quantified via merging a sample droplet and its neighboring reactant segment contained a mixture of dye, ATP, and enzymes (MAK117-1KT, Sigma-Aldrich). The signals of fatty acid and glycerol were imaged at 525 ± 25 nm (green) and 620 ± 30 nm (red) after excitation, respectively. Paired sample and reference droplets containing both FFA* and

glycerol assay reagents were analyzed with our lock-in technique to greatly reduce low-frequency noise during detection.

6.3 Results and Discussion

6.3.1 Microfluidic Chip Design and Operation

As shown in **Figure 6.1**, the microfluidic device consisted of several components: (1) T-junction channels for aqueous-in-oil droplet generation; (2) salt water electrode for droplets coalescence; (3) pneumatic control layer for automated chip operation with LabVIEW program; (4) zig-zag channel for quickly and completely mixing reagents; (5) long incubation channel for storing and analyzing target droplets; (6) linked pneumatic valves decreased the required numbers of control channel and improved working efficiency of chip; (7) 3D-printed traps and 3D-templated reservoir for tissue culturing (**Figure 6.1B**, **6.1C**). In this system, sample droplets were generated from 3D-templated reservoir with cultured eWAT explant, and reference droplets containing glycerol assay were sampled from channel clusters linked with three different inlets. The computer-controlled pump valves improved consistency of reactant volume ratios inside a reference droplet compared to individually controlled valve-based pumps, which was used in our previous microchip.[75,317]

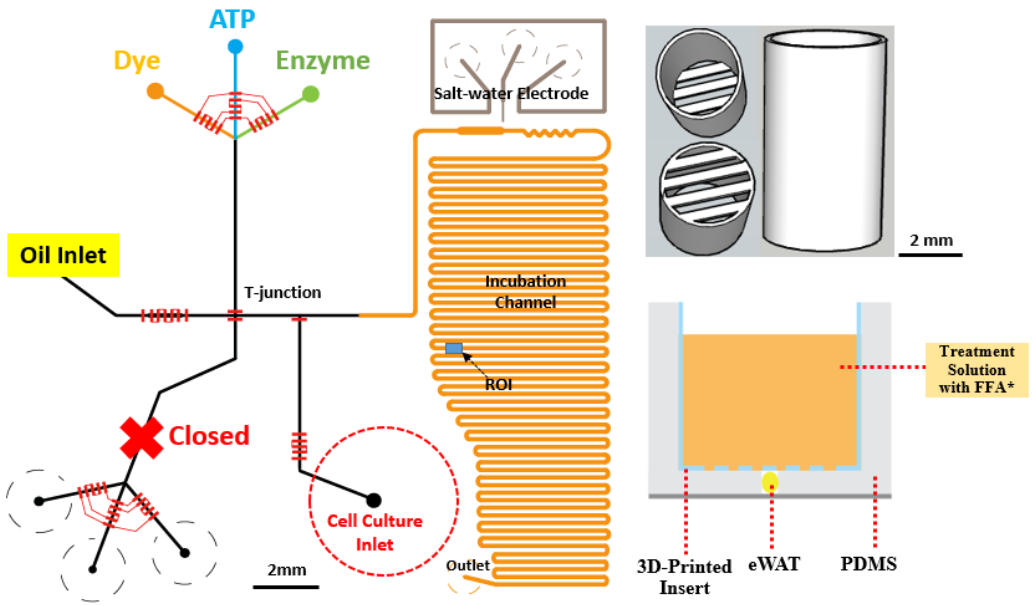

Figure 6.1 Droplet-based microdevice design

(A) Schematic of two-layer microfluidic channel layout, with rounded channels shown in black, squared fluidic channels in orange, control channels in red and salt-water channel in gray. (B) 3D-printed insert for trapping eWAT in the reservoir. (C) Cross-section of tissue-cultured reservoir with 3D-printed anchor.

6.3.2 Simultaneous Detection of Two Analytes, FFA* and Glycerol

Labelled free fatty acid (FFA*) and glycerol included in sample droplets were separately revealed via rapidly switching FITC and TRITC channel every 200 ms as shown in **Figure 6.2A**. Representative raw data of FFA*, glycerol signal, and reference signal were clearly indicated in **Figure 6.2B**. All of encapsulated FFA* and glycerol were quantified rapidly because those two analytes could be completely imaged with red and green detection channels within ~200 ms. However, sometimes a relatively small reference droplet would only be detected at the droplet edge, giving signals with much lower than actual fluorescence intensity of droplet center. Therefore, it was essential to consider the relative effects of flow rate, droplet volume, and detection time in measuring multiple signals in one segment. To test whether the glycerol assay would precisely measure sample in nanoliter aqueous-in-oil droplets and the effects of FFA* on

this enzymatic reaction, two calibration curves with high R^2 were obtained and shown in **Figure 6.3**. It was obviously indicate this enzymatic glycerol assay worked well in droplets containing FFA*, although FFA* did interfere with the intensity of reaction signals somewhat.

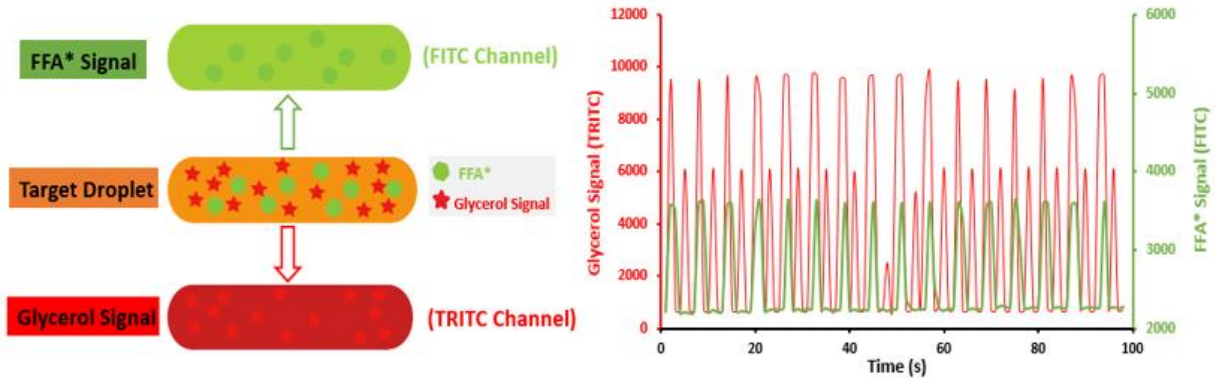

Figure 6.2 Multiplexed detection of sample droplet

(A) FFA* and glycerol included in target droplet (middle) are imaged in FITC (top) and TRITC (bottom) channels, respectively. (B) Representative raw temporal data for 1 µM labelled fatty acid (green peak), 50 µM glycerol signal (tall red peak) and reference (low red peak).

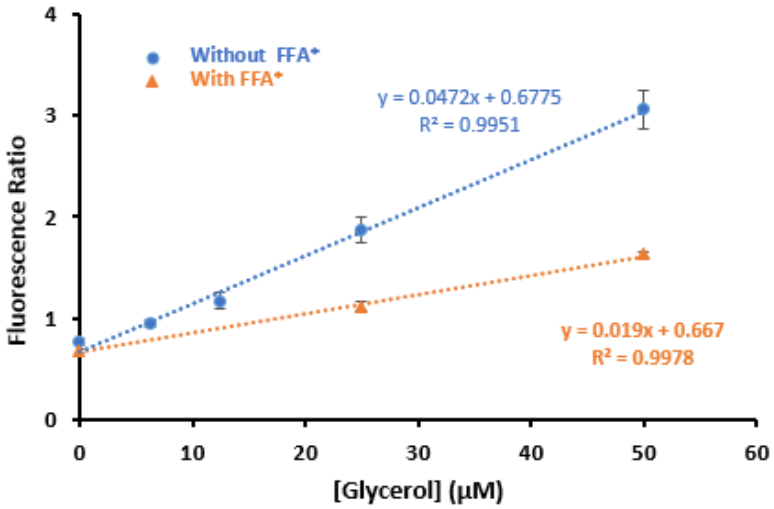

Figure 6.3 Calibration curves for glycerol at two conditions with (orange) and without FFA* present (blue) in the droplets.

6.3.3 Simultaneous Dynamics of Glycerol Release and FFA Uptake from eWAT

The dynamic traces of both FFA absorption and glycerol secretion from eWAT at varying glucose, insulin, and isoproterenol concentrations were demonstrated in **Figure 6.4**. In this work, we stimulated primary murine eWAT with two treatment combinations: pretreated with LGLI and dynamically treated with HGHI (LGLI+HGHI) and pretreated with LGLI plus isoproterenol and dynamically treated with HGHI (LGLIS+HGHI). At both of two patterns, it was clear to see nutrient uptake rates enhanced rapidly at the beginning and arrived equilibrium after several minutes. But the dynamics of glycerol release were much more stable during the same detection time, and LGLIS solution slightly heightened amount of secreted glycerol in comparison to LGLI treatment (**Figure 6.5A**). Furthermore, fast and dramatic changes of glycerol secretion were observed immediately after changing the treatment, and this indicates fasting process of eWAT explants were extremely sensitive to stimulations. However, the response of uptake process to treatments was significantly influenced by isoproterenol via comparing **Figure 6.4A** and **Figure 6.4B**. At the condition of pattern I (LGLI+HGHI), FFA* absorption rate decreased immediately after changing treatment from LGLI to HGHI (**Figure 6.4A**). At the pattern II (LGLIS+HGHI) where 20 μM isoproterenol was added, FFA* uptake traces raised after a several-minute delay when stimulation solution was changed (**Figure 6.4B**), and the delay times are 1.24, 0.82 and 3.61 min (**Figure 6.5B**). Finally, oscillations of glycerol secretion were also demonstrated though droplets were sampled from tissue or cells at 9-second temporal resolution, which matched well with our previous report. However, there was no obvious and consistent oscillation at the absorption dynamics.

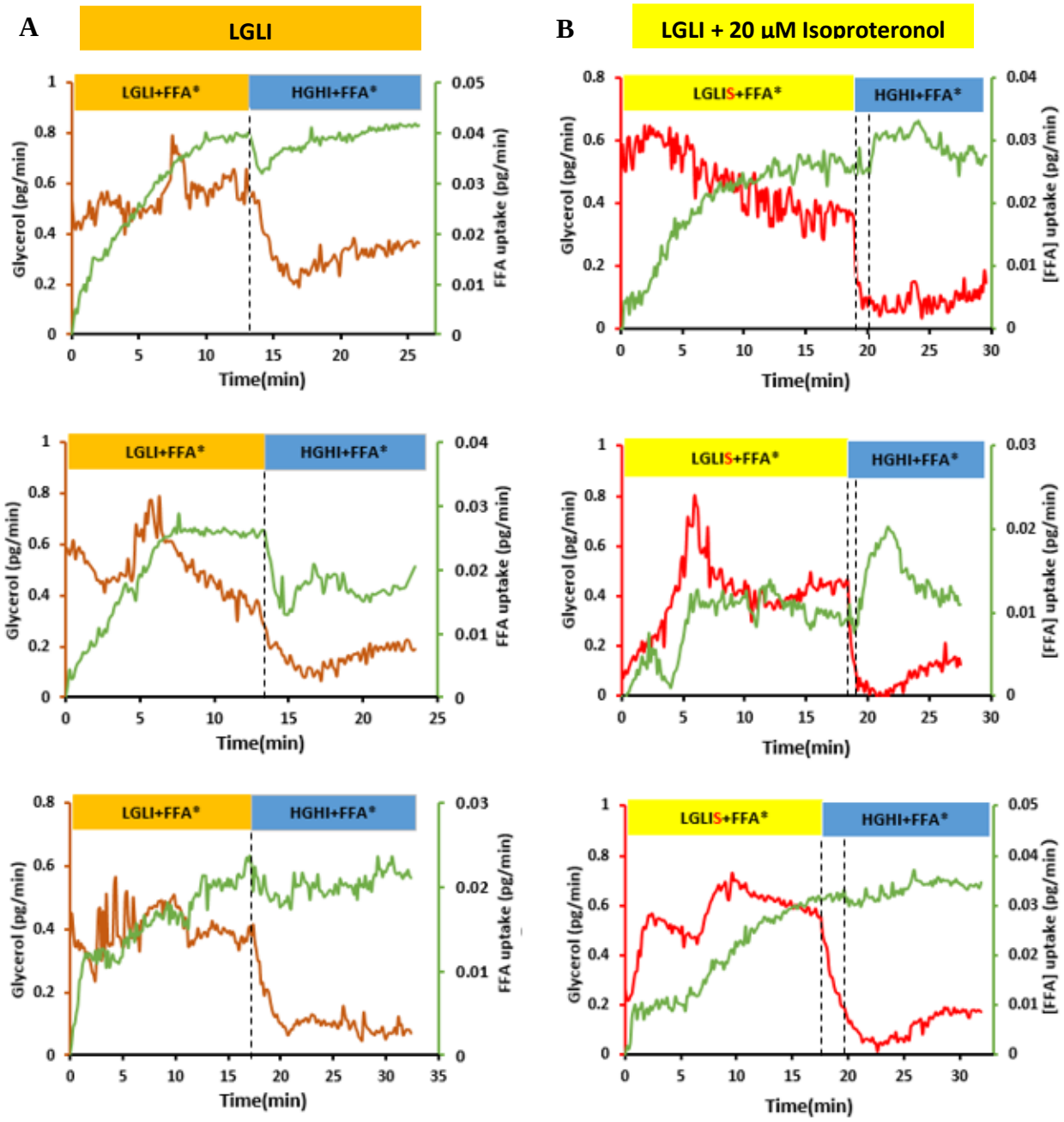

Figure 6.4 Simultaneous FFA* absorption and glycerol secretion profiles

(A) FFA* uptake (green) and glycerol secretion (dark red) dynamic traces exposed to LGLI and HGHI solutions (B) FFA* absorption (green) and glycerol release (red) profiles at LGLI**S** and HGHI solutions.

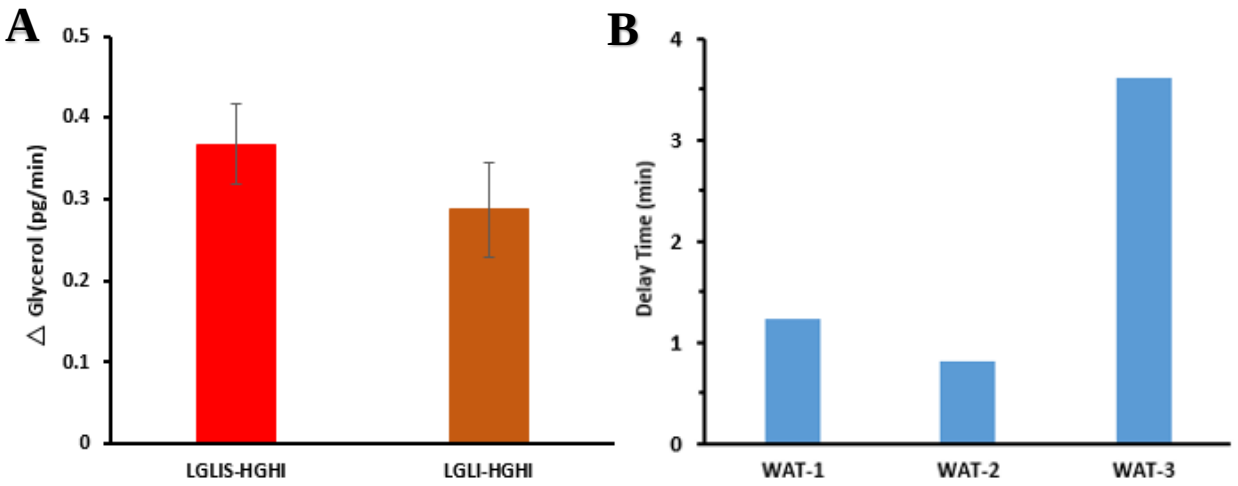

Figure 6.5 20 μM Isoproterenol affects the amount of glycerol secretion (A) and the sensitivity of WAT to stimulation solutions (B).

6.4 Conclusion

A microfluidic system with automated droplet generator and merger was developed to simultaneously monitor the nutrient absorption and metabolism of primary eWAT with 9-second temporal resolution. Connected valve-based pumps ensured the consistency of mixing ratios in enzymatic assay reagents, and inserted salt-water electrodes also provided a platform to continuously coalesce droplets to initiate reactions. With the addition even more assay input channels, this device should be capable of simultaneously studying several absorption and secretion dynamics of adipose tissue or other tissues or cell types in the future. Compared to individually studying tissue dynamics, synchronous exploration of multiple dynamics should reveal hidden trends and information, such as the amount ratios of intermediates and products,

relationships of absorption and secretion rates, as well as their responses to sudden changes of treatments. This automated microfluidic system has the potential to be adapted to other tissues or cells and improve our quantitative understanding of their dynamic functionality.

Chapter 7

Conclusion and Future Work

7.1 Conclusion

The aims of projects in this dissertation were to improve the automation and functionalities of our droplet-based microfluidic devices for quantifying biomolecules, culturing white adipose tissues, and monitoring their uptake and secretion dynamics at high temporal resolution using homogeneous assay platforms. In this chapter, we will conclude my major work over the past 4.5 years, perceived challenges, and my future outlook.

7.1.1 Automated Droplet-Based Microchip Integrated with Salt-water Electrodes

In my work, several microfluidic devices were developed with two-phase flow containing computer-controlled pneumatic valves, and moat and salt-water electrodes were designed to ensure consistent, programmable merging of droplets, on-demand. This permitted droplets to encapsulate different chemicals to trigger various reactions. There were classes of valves which were managed with in-house written LabVIEW programs in those devices. Some valves worked as the switches of channels, and the other valve-based pumps controlled the sizes of droplets and the flow rates of the two phases. Both of these classes of valves determined the amounts and types of different droplets. One guide channel filled with 5M NaCl solution served as an electrode to generate a

strong AC electric field with the assistance of a high-voltage amplifier, used to merge droplets that are nearby. The channel-based moat, which was attached to electrical ground, had the ability of shielding the high electric field from the rest of the device.

In the first testing phase (Chapter 2), this system supplied a powerful platform for achieving precise serial dilution, pH regulation, and exploring assay responses of a homogeneous immunoassay. In the second device testing phase (Chapter 3), these chips with four aqueous channels were applied to real-time, continuous calibration of fluorescent labels, then we validated the system for continuous calibration of a homogeneous insulin immunoassay that exhibits a nonlinear response. Those applications did demonstrate the benefits of these microchips in measuring precious reagents with a static or real-time manner and deepen our understanding about these automatic devices.

7.1.2 Biological Applications of Programmable Droplet Microdevice

In Chapter 4, we validated the devices for highly sensitive, nanoliter-volume detection of both DNA and antibodies, where droplets were programmed to merge reagents for homogeneous, isothermal nicking enzyme signal amplification (NESA); limits of detection were 10 fM for DNA and 50 fM for anti-digoxigenin antibodies. Then, in Chapter 5, this system was applied to resolve dynamics of uptake and metabolism of white adipose tissue (eWAT), a tissue of high functional importance in obesity and diabetes. Firstly, nutrient uptake analysis was explored with the microchips. High-precision programmability improved flexibility for three modes of quantitative analysis in real time, resolving eWAT free fatty acid uptake dynamics via continuous calibration mode (CCM), multiple tissue mode (MTM), and a complexed mode . Using this device, we evaluated the effects of switching from fasting (low glucose and insulin, LGLI) to feeding conditions (high levels, HGHI), with and without a protein palmitoylation inhibitor (2-

bromopalmitic acid, or 2-BP). 2-BP appeared to only partially inhibit short term uptake (<5 min) but largely inhibit sustained uptake (>10 min). These data suggested a ready pool of fatty acid transporters (e.g. CD-36) were available independent of protein palmitoylation, while this process might play a larger role in transporter synthesis.

Next, in Chapter 6, we evaluated whether nutrient absorption and lipolytic secretions could be simultaneously monitored by modifying the device, where both labeled free fatty acid (FFA*) uptake and glycerol secretion were quantified with highly sensitive, optical lock-in detection. Integration of valves and merging electrodes ensured precise mixing of glycerol assay reagent droplets with sampled droplets from WAT at high temporal resolution (~9 s). Because unabsorbed FFA* and secreted glycerol were both encapsulated, two-color fluorescence detection (FITC and TRITC) was used. We observed that FFA uptake reversed direction upon isoproterenol treatment (epinephrine analog) after switching nutrient levels, yet lipolysis dynamics were essentially unaffected.

7.2 Challenges and Future Work

While certainly advantageous, most active droplet regulation methods mentioned in this review remain much slower (0.1 – 10 Hz) than their passive counterparts (1 – 10 kHz). Thus, there is a clear need for faster approaches to droplet formation and maneuvering while maintaining narrow bandwidth. One possible solution would be to fabricate on-chip valves with more rigid materials, and recent 3D-printed valves may help address the challenge. Alternatively, off-chip controls that operate through continuous feedback from measurements of droplet frequency may suffice.

Efforts to interface with more analytical techniques should also continue. Optical readout by fluorescence has been most popular, but there are still opportunities to interface rapid-readout

spectrometers to interrogate droplet streams. As exemplified by the new MADS technique, the droplet fluidics/MS combination can be particularly powerful, and we hope to see more MS experts embrace droplet microfluidics as a compatible, enabling technology. Likewise, the droplet CAR-Wash design (see **Figure 1.5e**) opens up new possibilities in high-throughput, continuous bead-based sample preparation in droplets, which is an area that needs more attention.

It is important for users to carefully evaluate the volumes of cells and tissues that are examined in their devices, since the scaling of tissues should differ depending on their true physiological scale. Tissue scaling can have profound impacts on the function under study, and this issue may pose limitations to the temporal resolutions or analyte sensitivities that are accessible to the researcher. The individual, *ex vivo* white adipocyte has great value and possibility to be studied with our microdevices, because the sizes of white adipocytes are around 0.1 mm in intact tissue, which matches well with the microwells and microchannels. However, currently the rigorous challenge about analysis of white adipocyte is that its density is lower than buffer, which brings problems with trapping and fixing them in place during sampling.

References

(1) Blüher, M. *Nature Reviews Endocrinology* **2019**, *15*, 288-298.
(2) Chooi, Y. C.; Ding, C.; Magkos, F. *Metabolism* **2019**, *92*, 6-10.
(3) Tsatsoulis, A.; Paschou, S. A. *Current obesity reports* **2020**, *9*, 109-120.
(4) Luo, L.; Liu, M. *Journal of endocrinology* **2016**, *231*, R77-R99.
(5) Frayn, K.; Karpe, F.; Fielding, B.; Macdonald, I.; Coppack, S. *International journal of obesity* **2003**, *27*, 875-888.
(6) Chait, A.; den Hartigh, L. J. *Frontiers in cardiovascular medicine* **2020**, *7*.
(7) Cinti, S. *Nutrition, metabolism and cardiovascular diseases* **2006**, *16*, 569-574.
(8) Pant, R.; Firmal, P.; Shah, V. K.; Alam, A.; Chattopadhyay, S. *Frontiers in Cell and Developmental Biology* **2020**, *8*.
(9) Min, S. Y.; Kady, J.; Nam, M.; Rojas-Rodriguez, R.; Berkenwald, A.; Kim, J. H.; Noh, H.-L.; Kim, J. K.; Cooper, M. P.; Fitzgibbons, T. *Nature medicine* **2016**, *22*, 312-318.
(10) Ibrahim, M. M. *Obesity reviews* **2010**, *11*, 11-18.
(11) Maurovich-Horvat, P.; Massaro, J.; Fox, C. S.; Moselewski, F.; O'Donnell, C. J.; Hoffmann, U. *International journal of obesity* **2007**, *31*, 500-506.
(12) Bódis, K.; Roden, M. *European journal of clinical investigation* **2018**, *48*, e13017.
(13) Ferre, P.; Foufelle, F. *Hormone Research in Paediatrics* **2007**, *68*, 72-82.
(14) Vázquez-Vela, M. E. F.; Torres, N.; Tovar, A. R. *Archives of medical research* **2008**, *39*, 715-728.
(15) Herman, M. A.; Peroni, O. D.; Villoria, J.; Schön, M. R.; Abumrad, N. A.; Blüher, M.; Klein, S.; Kahn, B. B. *Nature* **2012**, *484*, 333-338.
(16) Eissing, L.; Scherer, T.; Tödter, K.; Knippschild, U.; Greve, J. W.; Buurman, W. A.; Pinnschmidt, H. O.; Rensen, S. S.; Wolf, A. M.; Bartelt, A. *Nature communications* **2013**, *4*, 1-11.
(17) Zimmermann, R.; Strauss, J. G.; Haemmerle, G.; Schoiswohl, G.; Birner-Gruenberger, R.; Riederer, M.; Lass, A.; Neuberger, G.; Eisenhaber, F.; Hermetter, A. *Science* **2004**, *306*, 1383-1386.
(18) Lafontan, M.; Langin, D. *Progress in lipid research* **2009**, *48*, 275-297.
(19) Fasshauer, M.; Blüher, M. *Trends in pharmacological sciences* **2015**, *36*, 461-470.
(20) Li, X.; Easley, C. J. *Analytical and bioanalytical chemistry* **2018**, *410*, 791-800.
(21) Blüher, M.; Mantzoros, C. S. *Metabolism* **2015**, *64*, 131-145.
(22) Henry, B. A.; Clarke, I. J. *Journal of neuroendocrinology* **2008**, *20*, 842-849.
(23) Morton, G. J.; Schwartz, M. W. *Physiological reviews* **2011**, *91*, 389-411.
(24) Hansen, G. H.; Niels-Christiansen, L.-L.; Danielsen, E. M. *Journal of Histochemistry & Cytochemistry* **2008**, *56*, 677-685.
(25) Hui, X.; Lam, K. S.; Vanhoutte, P. M.; Xu, A. *British journal of pharmacology* **2012**, *165*, 574-590.
(26) Nagaev, I.; Smith, U. *Biochemical and biophysical research communications* **2001**, *285*, 561-564.

(27) Steppan, C. M.; Bailey, S. T.; Bhat, S.; Brown, E. J.; Banerjee, R. R.; Wright, C. M.; Patel, H. R.; Ahima, R. S.; Lazar, M. A. *Nature* **2001**, *409*, 307-312.
(28) Banerjee, R. R.; Rangwala, S. M.; Shapiro, J. S.; Rich, A. S.; Rhoades, B.; Qi, Y.; Wang, J.; Rajala, M. W.; Pocai, A.; Scherer, P. E. *Science* **2004**, *303*, 1195-1198.
(29) Sheng, C. H.; Di, J.; Jin, Y.; Zhang, Y. C.; Wu, M.; Sun, Y.; Zhang, G. Z. *Endocrine* **2008**, *33*, 135-143.
(30) Verma, S.; Li, S.-H.; Wang, C.-H.; Fedak, P. W.; Li, R.-K.; Weisel, R. D.; Mickle, D. A. *Circulation* **2003**, *108*, 736-740.
(31) Huang, Y.; Chen, J.; Zhao, S.; Shi, M.; Chen, Z.-F.; Liang, H. *Analytical chemistry* **2013**, *85*, 4423-4430.
(32) Hu, J.; Yu, Y.; Brooks, J. C.; Godwin, L. A.; Somasundaram, S.; Torabinejad, F.; Kim, J.; Shannon, C.; Easley, C. J. *Journal of the American Chemical Society* **2014**, *136*, 8467-8474.
(33) Hu, J.; Wang, T.; Kim, J.; Shannon, C.; Easley, C. J. *Journal of the American Chemical Society* **2012**, *134*, 7066-7072.
(34) Kim, J.; Hu, J.; Bezerra, A. B.; Holtan, M. D.; Brooks, J. C.; Easley, C. J. *Analytical chemistry* **2015**, *87*, 9576-9579.
(35) Heyduk, E.; Moxley, M. M.; Salvatori, A.; Corbett, J. A.; Heyduk, T. *Diabetes* **2010**, *59*, 2360-2365.
(36) Filla, R. T.; Schrell, A. M.; Coulton, J. B.; Edwards, J. L.; Roper, M. G. *Analytical chemistry* **2018**, *90*, 2414-2419.
(37) Bezerra, A. B.; Kurian, A. S.; Easley, C. J. *Analytical Chemistry* **2020**.
(38) Zhang, H.; Xu, T.; Li, C.-W.; Yang, M. *Biosensors and Bioelectronics* **2010**, *25*, 2402-2407.
(39) Hu, J. **2018**.
(40) Adamcova, M.; Šimko, F. *Acta Pharmacologica Sinica* **2018**, *39*, 1068-1072.
(41) Mayer, G. *Angewandte Chemie International Edition* **2009**, *48*, 2672-2689.
(42) Tan, Y.; Guo, Q.; Zhao, X.; Yang, X.; Wang, K.; Huang, J.; Zhou, Y. *Biosensors and Bioelectronics* **2014**, *51*, 255-260.
(43) Gill, P.; Ghaemi, A. *Nucleosides, Nucleotides and Nucleic Acids* **2008**, *27*, 224-243.
(44) Hofmann, W. P.; Dries, V.; Herrmann, E.; Gärtner, B.; Zeuzem, S.; Sarrazin, C. *Journal of clinical virology* **2005**, *32*, 289-293.
(45) Shi, C.; Liu, Q.; Ma, C.; Zhong, W. *Analytical chemistry* **2014**, *86*, 336-339.
(46) Cho, E. J.; Yang, L.; Levy, M.; Ellington, A. D. *Journal of the American Chemical Society* **2005**, *127*, 2022-2023.
(47) Becherer, L.; Borst, N.; Bakheit, M.; Frischmann, S.; Zengerle, R.; von Stetten, F. *Analytical Methods* **2020**, *12*, 717-746.
(48) Vincent, M.; Xu, Y.; Kong, H. *EMBO reports* **2004**, *5*, 795-800.
(49) Daher, R. K.; Stewart, G.; Boissinot, M.; Bergeron, M. G. *Clinical chemistry* **2016**, *62*, 947-958.
(50) DeJournette, C. J.; Kim, J.; Medlen, H.; Li, X.; Vincent, L. J.; Easley, C. J. *Analytical chemistry* **2013**, *85*, 10556-10564.
(51) Lobato, I. M.; O'Sullivan, C. K. *Trac Trends in analytical chemistry* **2018**, *98*, 19-35.
(52) Kiesling, T.; Cox, K.; Davidson, E. A.; Dretchen, K.; Grater, G.; Hibbard, S.; Lasken, R. S.; Leshin, J.; Skowronski, E.; Danielsen, M. *Nucleic acids research* **2007**, *35*, e117.
(53) Qian, C.; Wang, R.; Wu, H.; Ji, F.; Wu, J. *Analytica chimica acta* **2019**, *1050*, 1-15.
(54) Bibette, J.; Morse, D. C.; Witten, T. A.; Weitz, D. A. *Physical Review Letters* **1992**, *69*, 2439-2442.
(55) Umbanhowar, P. B.; Prasad, V.; Weitz, D. A. *Langmuir* **2000**, *16*, 347-351.
(56) Thorsen, T.; Roberts, R. W.; Arnold, F. H.; Quake, S. R. *Phys Rev Lett* **2001**, *86*, 4163-4166.
(57) Squires, T. M.; Quake, S. R. *Reviews of modern physics* **2005**, *77*, 977.
(58) Song, H.; Tice, J. D.; Ismagilov, R. F. *Angewandte Chemie International Edition* **2003**, *42*, 768-772.
(59) Garstecki, P.; Fuerstman, M. J.; Stone, H. A.; Whitesides, G. M. *Lab on a Chip* **2006**, *6*, 437-446.
(60) Link, D. R.; Anna, S. L.; Weitz, D. A.; Stone, H. A. *Physical Review Letters* **2004**, *92*, 054503.

(61) Kumaresan, P.; Yang, C. J.; Cronier, S. A.; Blazej, R. G.; Mathies, R. A. *Analytical Chemistry* **2008**, *80*, 3522-3529.
(62) Zeng, Y.; Novak, R.; Shuga, J.; Smith, M. T.; Mathies, R. A. *Analytical Chemistry* **2010**, *82*, 3183-3190.
(63) Chiu, D. T. *Anal Bioanal Chem* **2010**, *397*, 3179-3183.
(64) Zhu, Y.; Fang, Q. *Analytica chimica acta* **2013**, *787*, 24-35.
(65) Belder, D. *Angewandte Chemie International Edition* **2005**, *44*, 3521-3522.
(66) Chiu, D. T.; Lorenz, R. M. *Accounts of chemical research* **2009**, *42*, 649-658.
(67) Zheng, F.; Fu, F.; Cheng, Y.; Wang, C.; Zhao, Y.; Gu, Z. *Small* **2016**, *12*, 2253-2282.
(68) Teh, S.-Y.; Lin, R.; Hung, L.-H.; Lee, A. P. *Lab on a Chip* **2008**, *8*, 198-220.
(69) Kim, S. C.; Clark, I. C.; Shahi, P.; Abate, A. R. *Analytical chemistry* **2018**, *90*, 1273-1279.
(70) Sjostrom, S. L.; Joensson, H. N.; Svahn, H. A. *Lab on a Chip* **2013**, *13*, 1754-1761.
(71) Price, A. K.; MacConnell, A. B.; Paegel, B. M. *Analytical chemistry* **2016**, *88*, 2904-2911.
(72) Tang, M. Y.; Shum, H. C. *Lab on a Chip* **2016**, *16*, 4359-4365.
(73) Gao, R.; Cheng, Z.; deMello, A. J.; Choo, J. *Lab on a Chip* **2016**, *16*, 1022-1029.
(74) Wippold, J. A.; Wang, H.; Tingling, J.; Leibowitz, J. L.; de Figueiredo, P.; Han, A. *Lab on a Chip* **2020**.
(75) Li, X.; Hu, J.; Easley, C. J. *Lab on a Chip* **2018**, *18*, 2926-2935.
(76) Hu, J.; Li, X.; Judd, R. L.; Easley, C. J. *Lab on a Chip* **2020**, *20*, 1503-1512.
(77) Ding, Y.; Howes, P. D.; deMello, A. J. *Analytical Chemistry* **2020**, *92*, 132-149.
(78) Liu, W.-w.; Zhu, Y. *Analytica Chimica Acta* **2020**, *1113*, 66-84.
(79) Dressler, O. J.; Casadevall i Solvas, X.; DeMello, A. J. *Annual Review of Analytical Chemistry* **2017**, *10*, 1-24.
(80) Feng, S.; Shirani, E.; Inglis, D. W. *Biosensors* **2019**, *9*, 80.
(81) Zhu, P.; Wang, L. *Lab on a Chip* **2017**, *17*, 34-75.
(82) Duncombe, T. A.; Dittrich, P. S. *Current Opinion in Biotechnology* **2019**, *60*, 205-212.
(83) Matula, K.; Rivello, F.; Huck, W. T. S. *Advanced Biosystems* **2020**, *4*, 28.
(84) Shi, N. M., M.; Easley, C. J. In *Droplet Microfluidics*, Ren, C. L., A., Ed.; Royal Society of Chemistry: Cambridge, UK, 2020, pp 221-258.
(85) Gach, P. C.; Iwai, K.; Kim, P. W.; Hillson, N. J.; Singh, A. K. *Lab on a Chip* **2017**, *17*, 3388-3400.
(86) Clark, I. C.; Abate, A. R. *Lab on a Chip* **2017**, *17*, 2032-2045.
(87) Price, A. K.; Paegel, B. M. *Analytical Chemistry* **2016**, *88*, 339-353.
(88) Pit, A. M.; Duits, M. H. G.; Mugele, F. *Micromachines* **2015**, *6*, 1768-1793.
(89) Shang, L.; Cheng, Y.; Zhao, Y. *Chemical Reviews* **2017**, *117*, 7964-8040.
(90) Chabert, M.; Viovy, J.-L. *Proceedings of the National Academy of Sciences* **2008**, *105*, 3191.
(91) Seemann, R.; Brinkmann, M.; Pfohl, T.; Herminghaus, S. *Reports on Progress in Physics* **2011**, *75*, 016601.
(92) Christopher, G. F.; Anna, S. L. *Journal of Physics D: Applied Physics* **2007**, *40*, R319-R336.
(93) Chong, Z. Z.; Tan, S. H.; Gañán-Calvo, A. M.; Tor, S. B.; Loh, N. H.; Nguyen, N.-T. *Lab on a Chip* **2016**, *16*, 35-58.
(94) Au, A. K.; Lai, H.; Utela, B. R.; Folch, A. *Micromachines* **2011**, *2*, 179-220.
(95) Choi, J.-H.; Lee, S.-K.; Lim, J.-M.; Yang, S.-M.; Yi, G.-R. *Lab on a Chip* **2010**, *10*, 456-461.
(96) Grover, W. H.; Skelley, A. M.; Liu, C. N.; Lagally, E. T.; Mathies, R. A. *Sensors and Actuators B: Chemical* **2003**, *89*, 315-323.
(97) Unger, M. A.; Chou, H.-P.; Thorsen, T.; Scherer, A.; Quake, S. R. *Science* **2000**, *288*, 113.
(98) Zhang, W.; Lin, S.; Wang, C.; Hu, J.; Li, C.; Zhuang, Z.; Zhou, Y.; Mathies, R. A.; Yang, C. J. *Lab on a Chip* **2009**, *9*, 3088-3094.
(99) Babahosseini, H.; Misteli, T.; DeVoe, D. L. *Lab on a Chip* **2019**, *19*, 493-502.
(100) Babahosseini, H.; Padmanabhan, S.; Misteli, T.; DeVoe, D. L. *Biomicrofluidics* **2020**, *14*, 014112.
(101) Shi, N.; Easley, C. J. *Micromachines* **2020**, *11*, 620.

(102) Gong, H.; Woolley, A. T.; Nordin, G. P. *Lab on a Chip* **2016**, *16*, 2450-2458.
(103) Dang, B. V.; Hassanzadeh-Barforoushi, A.; Syed, M. S.; Yang, D.; Kim, S.-J.; Taylor, R. A.; Liu, G.-J.; Liu, G.; Barber, T. *ACS Sensors* **2019**, *4*, 2181-2189.
(104) Lee, Y.-S.; Bhattacharjee, N.; Folch, A. *Lab on a Chip* **2018**, *18*, 1207-1214.
(105) Link, D. R.; Grasland-Mongrain, E.; Duri, A.; Sarrazin, F.; Cheng, Z.; Cristobal, G.; Marquez, M.; Weitz, D. A. *Angewandte Chemie International Edition* **2006**, *45*, 2556-2560.
(106) Tan, S. H.; Semin, B.; Baret, J.-C. *Lab on a Chip* **2014**, *14*, 1099-1106.
(107) Sciambi, A.; Abate, A. R. *Lab on a Chip* **2014**, *14*, 2605-2609.
(108) Grimmer, A.; Wille, R. In *Designing Droplet Microfluidic Networks: A Toolbox for Designers*; Springer International Publishing: Cham, 2020, pp 3-11.
(109) Pollack, M. G.; Fair, R. B.; Shenderov, A. D. *Applied Physics Letters* **2000**, *77*, 1725-1726.
(110) Sung Kwon, C.; Hyejin, M.; Chang-Jin, K. *Journal of Microelectromechanical Systems* **2003**, *12*, 70-80.
(111) Choi, K.; Ng, A. H.; Fobel, R.; Wheeler, A. R. *Annual review of analytical chemistry* **2012**, *5*, 413-440.
(112) Kahkeshani, S.; Di Carlo, D. *Lab on a Chip* **2016**, *16*, 2474-2480.
(113) Liu, J.; Tan, S.-H.; Yap, Y. F.; Ng, M. Y.; Nguyen, N.-T. *Microfluidics and Nanofluidics* **2011**, *11*, 177-187.
(114) Tan, S.-H.; Nguyen, N.-T.; Yobas, L.; Kang, T. G. *Journal of Micromechanics and Microengineering* **2010**, *20*, 045004.
(115) Ting, T. H.; Yap, Y. F.; Nguyen, N.-T.; Wong, T. N.; Chai, J. C. K.; Yobas, L. *Applied Physics Letters* **2006**, *89*, 234101.
(116) Deal, K. S.; Easley, C. J. *Analytical chemistry* **2012**, *84*, 1510-1516.
(117) Negou, J. T.; Avila, L. A.; Li, X.; Hagos, T. M.; Easley, C. J. *Analytical chemistry* **2017**, *89*, 6153-6159.
(118) Negou, J. T.; Hu, J.; Li, X.; Easley, C. J. *Analytical methods* **2018**, *10*, 3436-3443.
(119) Ismagilov, R. F.; Rosmarin, D.; Kenis, P. J. A.; Chiu, D. T.; Zhang, W.; Stone, H. A.; Whitesides, G. M. *Analytical Chemistry* **2001**, *73*, 4682-4687.
(120) Thorsen, T.; Maerkl, S. J.; Quake, S. R. *Science* **2002**, *298*, 580-584.
(121) Melin, J.; Quake, S. R. *Annual Review of Biophysics and Biomolecular Structure* **2007**, *36*, 213-231.
(122) Jensen, E. C.; Grover, W. H.; Mathies, R. A. *Journal of Microelectromechanical Systems* **2007**, *16*, 1378-1385.
(123) Zeng, S.; Li, B.; Su, X. o.; Qin, J.; Lin, B. *Lab on a Chip* **2009**, *9*, 1340-1343.
(124) Leung, K.; Zahn, H.; Leaver, T.; Konwar, K. M.; Hanson, N. W.; Pagé, A. P.; Lo, C.-C.; Chain, P. S.; Hallam, S. J.; Hansen, C. L. *Proceedings of the National Academy of Sciences* **2012**, *109*, 7665-7670.
(125) Lin, R.; Fisher, J. S.; Simon, M. G.; Lee, A. P. *Biomicrofluidics* **2012**, *6*, 024103.
(126) Zeng, Y.; Shin, M.; Wang, T. *Lab on a Chip* **2013**, *13*, 267-273.
(127) Doonan, S. R.; Lin, M.; Bailey, R. C. *Lab on a Chip* **2019**, *19*, 1589-1598.
(128) Chiu, D. T.; Lorenz, R. M.; Jeffries, G. D.; ACS Publications, 2009.
(129) Shim, J.-u.; Ranasinghe, R. T.; Smith, C. A.; Ibrahim, S. M.; Hollfelder, F.; Huck, W. T.; Klenerman, D.; Abell, C. *Acs Nano* **2013**, *7*, 5955-5964.
(130) Leong, C. L.; Coleman, S.; Nightingale, A. M.; Hassan, S.-u.; Voegeli, D.; Boutelle, M. G.; Niu, X. *Analytical Methods* **2019**, *11*, 6119-6123.
(131) Zhang, Y.; Ye, W.; Yang, C.; Xu, Z. *Talanta* **2019**, *205*, 120096.
(132) Abram, T. J.; Cherukury, H.; Ou, C.-Y.; Vu, T.; Toledano, M.; Li, Y.; Grunwald, J. T.; Toosky, M. N.; Tifrea, D. F.; Slepenkin, A. *Lab on a Chip* **2020**, *20*, 477-489.
(133) Pekin, D.; Skhiri, Y.; Baret, J.-C.; Le Corre, D.; Mazutis, L.; Salem, C. B.; Millot, F.; El Harrak, A.; Hutchison, J. B.; Larson, J. W. *Lab on a Chip* **2011**, *11*, 2156-2166.
(134) Cedillo-Alcantar, D. F.; Han, Y. D.; Choi, J.; Garcia-Cordero, J. L.; Revzin, A. *Analytical chemistry* **2019**, *91*, 5133-5141.

(135) Guo, S.; Lin, W. N.; Hu, Y.; Sun, G.; Phan, D.-T.; Chen, C.-H. *Lab on a Chip* **2018**, *18*, 1914-1920.
(136) Wang, J.; Ramakrishnan, R.; Tang, Z.; Fan, W.; Kluge, A.; Dowlati, A.; Jones, R. C.; Ma, P. C. *Clinical chemistry* **2010**, *56*, 623-632.
(137) Rissin, D. M.; Kan, C. W.; Campbell, T. G.; Howes, S. C.; Fournier, D. R.; Song, L.; Piech, T.; Patel, P. P.; Chang, L.; Rivnak, A. J. *Nature biotechnology* **2010**, *28*, 595.
(138) Basu, A. S. *SLAS TECHNOLOGY: Translating Life Sciences Innovation* **2017**, *22*, 369-386.
(139) Du, W.; Li, L.; Nichols, K. P.; Ismagilov, R. F. *Lab on a Chip* **2009**, *9*, 2286-2292.
(140) Shen, F.; Sun, B.; Kreutz, J. E.; Davydova, E. K.; Du, W.; Reddy, P. L.; Joseph, L. J.; Ismagilov, R. F. *Journal of the American Chemical Society* **2011**, *133*, 17705-17712.
(141) Shen, F.; Davydova, E. K.; Du, W.; Kreutz, J. E.; Piepenburg, O.; Ismagilov, R. F. *Analytical chemistry* **2011**, *83*, 3533-3540.
(142) Khademhosseini, A.; Langer, R.; Borenstein, J.; Vacanti, J. P. *Proceedings of the National Academy of Sciences* **2006**, *103*, 2480-2487.
(143) Andersson, H.; Van Den Berg, A. *Lab on a Chip* **2004**, *4*, 98-103.
(144) Lanza, R.; Langer, R.; Vacanti, J. P. *Principles of tissue engineering*; Academic press, 2011.
(145) Khademhosseini, A.; Langer, R. *Nature protocols* **2016**, *11*, 1775.
(146) Karageorgiou, V.; Kaplan, D. *Biomaterials* **2005**, *26*, 5474-5491.
(147) Oladapo, B. I.; Zahedi, S.; Adeoye, A. *Composites Part B: Engineering* **2019**, *158*, 428-436.
(148) Wu, J.; Brazile, B.; McMahan, S. R.; Liao, J.; Hong, Y. *Journal of Biomedical Materials Research Part B: Applied Biomaterials* **2019**, *107*, 1732-1740.
(149) Poddar, S.; Agarwal, P. S.; Mahto, S. K. *Engineering of Biomaterials* **2018**, *21*.
(150) Chen, C.; Mehl, B. T.; Sell, S. A.; Martin, R. S. *Analyst* **2016**, *141*, 5311-5320.
(151) Mehl, B. T.; Martin, R. S. *Analytical Methods* **2019**, *11*, 1064-1072.
(152) Chen, C.; Townsend, A. D.; Sell, S. A.; Martin, R. S. *Analytical Methods* **2017**, *9*, 3274-3283.
(153) Raeisdasteh Hokmabad, V.; Davaran, S.; Ramazani, A.; Salehi, R. *Journal of Biomaterials science, Polymer edition* **2017**, *28*, 1797-1825.
(154) Mellati, A.; Fan, C. M.; Tamayol, A.; Annabi, N.; Dai, S.; Bi, J.; Jin, B.; Xian, C.; Khademhosseini, A.; Zhang, H. *Biotechnology and bioengineering* **2017**, *114*, 217-231.
(155) Khademhosseini, A.; Langer, R. *Biomaterials* **2007**, *28*, 5087-5092.
(156) Bertassoni, L. E.; Cecconi, M.; Manoharan, V.; Nikkhah, M.; Hjortnaes, J.; Cristino, A. L.; Barabaschi, G.; Demarchi, D.; Dokmeci, M. R.; Yang, Y. *Lab on a Chip* **2014**, *14*, 2202-2211.
(157) Novosel, E. C.; Kleinhans, C.; Kluger, P. J. *Advanced drug delivery reviews* **2011**, *63*, 300-311.
(158) Sekine, H.; Shimizu, T.; Sakaguchi, K.; Dobashi, I.; Wada, M.; Yamato, M.; Kobayashi, E.; Umezu, M.; Okano, T. *Nature communications* **2013**, *4*, 1399.
(159) Auger, F. A.; Gibot, L.; Lacroix, D. *Annual review of biomedical engineering* **2013**, *15*, 177-200.
(160) Chang, H.-I.; Wang, Y. In *Regenerative medicine and tissue engineering-cells and biomaterials*; InTechOpen, 2011.
(161) Gaspar, D. A.; Gomide, V.; Monteiro, F. J. *Biomatter* **2012**, *2*, 167-175.
(162) Sung, J. H.; Esch, M. B.; Prot, J.-M.; Long, C. J.; Smith, A.; Hickman, J. J.; Shuler, M. L. *Lab on a Chip* **2013**, *13*, 1201-1212.
(163) Godwin, L. A.; Pilkerton, M. E.; Deal, K. S.; Wanders, D.; Judd, R. L.; Easley, C. J. *Anal Chem* **2011**, *83*, 7166-7172.
(164) Godwin, L. A.; Brooks, J. C.; Hoepfner, L. D.; Wanders, D.; Judd, R. L.; Easley, C. J. *Analyst* **2015**, *140*, 1019-1025.
(165) Brooks, J. C.; Ford, K. I.; Holder, D. H.; Holtan, M. D.; Easley, C. J. *Analyst* **2016**, *141*, 5714-5721.
(166) Li, X.; Brooks, J. C.; Hu, J.; Ford, K. I.; Easley, C. J. *Lab Chip* **2017**, *17*, 341-349.
(167) Li, X.; Hu, J.; Easley, C. J. *Lab Chip* **2018**, *18*, 2926-2935.

(168) Adams, A. G.; Bulusu, R. K. M.; Mukhitov, N.; Mendoza-Cortes, J. L.; Roper, M. G. *Analytical chemistry* **2019**, *91*, 5184-5190.
(169) Bandak, B.; Yi, L.; Roper, M. G. *Lab on a Chip* **2018**, *18*, 2873-2882.
(170) Lu, S.; Dugan, C. E.; Kennedy, R. T. *Analytical chemistry* **2018**, *90*, 5171-5178.
(171) Dugan, C. E.; Grinias, J. P.; Parlee, S. D.; El-Azzouny, M.; Evans, C. R.; Kennedy, R. T. *Anal Bioanal Chem* **2017**, *409*, 169-178.
(172) Kaestli, A. J.; Junkin, M.; Tay, S. *Lab on a Chip* **2017**, *17*, 4124-4133.
(173) Lin, J.; Jordi, C.; Son, M.; Van Phan, H.; Drayman, N.; Abasiyanik, M. F.; Vistain, L.; Tu, H.-L.; Tay, S. *Nature communications* **2019**, *10*, 1-10.
(174) Dettinger, P.; Frank, T.; Etzrodt, M.; Ahmed, N.; Reimann, A.; Trenzinger, C.; Loeffler, D.; Kokkaliaris, K. D.; Schroeder, T.; Tay, S. *Anal Chem* **2018**, *90*, 10695-10700.
(175) Loskill, P.; Sezhian, T.; Tharp, K. M.; Lee-Montiel, F. T.; Jeeawoody, S.; Reese, W. M.; Zushin, P. H.; Stahl, A.; Healy, K. E. *Lab Chip* **2017**, *17*, 1645-1654.
(176) Zhao, Y.; Rafatian, N.; Feric, N. T.; Cox, B. J.; Aschar-Sobbi, R.; Wang, E. Y.; Aggarwal, P.; Zhang, B.; Conant, G.; Ronaldson-Bouchard, K.; Pahnke, A.; Protze, S.; Lee, J. H.; Davenport Huyer, L.; Jekic, D.; Wickeler, A.; Naguib, H. E.; Keller, G. M.; Vunjak-Novakovic, G.; Broeckel, U.; Backx, P. H.; Radisic, M. *Cell* **2019**, *176*, 913-927.e918.
(177) Easley, C. J.; Karlinsey, J. M.; Bienvenue, J. M.; Legendre, L. A.; Roper, M. G.; Feldman, S. H.; Hughes, M. A.; Hewlett, E. L.; Merkel, T. J.; Ferrance, J. P. *Proceedings of the National Academy of Sciences* **2006**, *103*, 19272-19277.
(178) Easley, C. J.; Rocheleau, J. V.; Head, W. S.; Piston, D. W. *Analytical chemistry* **2009**, *81*, 9086-9095.
(179) Hu, J.; Li, X.; Judd, R. L.; Easley, C. J. *Lab on a Chip* **2020**.
(180) Sciambi, A.; Abate, A. R. *Lab on a Chip* **2015**, *15*, 47-51.
(181) Sahore, V.; Doonan, S. R.; Bailey, R. C. *Analytical methods* **2018**, *10*, 4264-4274.
(182) Clark, I. C.; Thakur, R.; Abate, A. R. *Lab on a Chip* **2018**, *18*, 710-713.
(183) Zhang, P.; Chen, C.; Guo, F.; Philippe, J.; Gu, Y.; Tian, Z.; Bachman, H.; Ren, L.; Yang, S.; Zhong, Z. *Lab on a Chip* **2019**.
(184) Tian, Z.; Yang, S.; Huang, P.-H.; Wang, Z.; Zhang, P.; Gu, Y.; Bachman, H.; Chen, C.; Wu, M.; Xie, Y. *Science advances* **2019**, *5*, eaau6062.
(185) Gilliland Jr, W. M.; Mellors, J. S.; Ramsey, J. M. *Analytical chemistry* **2017**, *89*, 13320-13325.
(186) Steyer, D. J.; Kennedy, R. T. *Analytical chemistry* **2019**.
(187) Wang, X.; Yi, L.; Roper, M. G. *Analytical chemistry* **2016**, *88*, 3369-3375.
(188) Jin, S.; Furtaw, M. D.; Chen, H.; Lamb, D. T.; Ferguson, S. A.; Arvin, N. E.; Dawod, M.; Kennedy, R. T. *Analytical chemistry* **2016**, *88*, 6703-6710.
(189) Reid, K. R.; Kennedy, R. T. *Analytical chemistry* **2009**, *81*, 6837-6842.
(190) Yi, L.; Wang, X.; Dhumpa, R.; Schrell, A. M.; Mukhitov, N.; Roper, M. G. *Lab Chip* **2015**, *15*, 823-832.
(191) Schrell, A. M.; Mukhitov, N.; Yi, L.; Adablah, J. E.; Menezes, J.; Roper, M. G. *Analytical Methods* **2017**, *9*, 38-45.
(192) Chaipan, C.; Pryszlak, A.; Dean, H.; Poignard, P.; Benes, V.; Griffiths, A. D.; Merten, C. A. *Cell chemical biology* **2017**, *24*, 751-757. e753.
(193) Huang, M.; Bai, Y.; Sjostrom, S. L.; Hallström, B. M.; Liu, Z.; Petranovic, D.; Uhlén, M.; Joensson, H. N.; Andersson-Svahn, H.; Nielsen, J. *Proceedings of the National Academy of Sciences* **2015**, *112*, E4689-E4696.
(194) Song, H.; Ismagilov, R. F. *J Am Chem Soc* **2003**, *125*, 14613-14619.
(195) Negou, J. T.; Avila, L. A.; Li, X.; Hagos, T. M.; Easley, C. J. *Anal Chem* **2017**, *89*, 6153-6159.
(196) Cole, R. H.; Tang, S.-Y.; Siltanen, C. A.; Shahi, P.; Zhang, J. Q.; Poust, S.; Gartner, Z. J.; Abate, A. R. *Proceedings of the National Academy of Sciences* **2017**, *114*, 8728-8733.

(197) Klein, A. M.; Mazutis, L.; Akartuna, I.; Tallapragada, N.; Veres, A.; Li, V.; Peshkin, L.; Weitz, D. A.; Kirschner, M. W. *Cell* **2015**, *161*, 1187-1201.
(198) Del Ben, F.; Turetta, M.; Celetti, G.; Piruska, A.; Bulfoni, M.; Cesselli, D.; Huck, W. T.; Scoles, G. *Angewandte Chemie International Edition* **2016**, *55*, 8581-8584.
(199) Segaliny, A. I.; Li, G.; Kong, L.; Ren, C.; Chen, X.; Wang, J. K.; Baltimore, D.; Wu, G.; Zhao, W. *Lab on a Chip* **2018**, *18*, 3733-3749.
(200) Honegger, P. *Curr Protoc Pharmacol* **2001**, *Chapter 12*, Unit12 11.
(201) Sittinger, M.; Bujia, J.; Rotter, N.; Reitzel, D.; Minuth, W. W.; Burmester, G. R. *Biomaterials* **1996**, *17*, 237-242.
(202) Al-Lamki, R. S.; Bradley, J. R.; Pober, J. S. *Front Med (Lausanne)* **2017**, *4*, 148.
(203) Phelan, K.; May, K. M. *Curr Protoc Mol Biol* **2017**, *117*, A 3F 1-A 3F 23.
(204) Carter, M.; Shieh, J. C. *Guide to Research Techniques in Neuroscience*; Elsevier Academic Press Inc: San Diego, 2010, p 1-375.
(205) Klaunig, J. E.; Goldblatt, P. J.; Hinton, D. E.; Lipsky, M. M.; Trump, B. F. *In Vitro* **1981**, *17*, 926-934.
(206) Benninger, R. K.; Zhang, M.; Head, W. S.; Satin, L. S.; Piston, D. W. *Biophys J* **2008**, *95*, 5048-5061.
(207) Ulrich, A. B.; Schmied, B. M.; Standop, J.; Schneider, M. B.; Pour, P. M. *Pancreas* **2002**, *24*, 111-120.
(208) Bhatia, S. N.; Ingber, D. E. *Nat Biotechnol* **2014**, *32*, 760-772.
(209) Whitesides, G. M. *Nature* **2006**, *442*, 368-373.
(210) Young, E. W.; Beebe, D. J. *Chem Soc Rev* **2010**, *39*, 1036-1048.
(211) Agarwal, A.; Goss, J. A.; Cho, A.; McCain, M. L.; Parker, K. K. *Lab Chip* **2013**, *13*, 3599-3608.
(212) Barbulovic-Nad, I.; Au, S. H.; Wheeler, A. R. *Lab Chip* **2010**, *10*, 1536-1542.
(213) Mandenius, C. F. *Bioengineering (Basel)* **2018**, *5*.
(214) Hemmerich, J.; Noack, S.; Wiechert, W.; Oldiges, M. *Biotechnol J* **2018**, *13*, e1700141.
(215) Hubka, V.; Eder, W. E. *Design Science: Introduction to the Needs, Scope and Organization of Engineering Design Knowledge*; Springer-Verlag London: London, UK, 1996, p XVI, 251.
(216) Rexius-Hall, M. L.; Rehman, J.; Eddington, D. T. *Integr Biol (Camb)* **2017**, *9*, 742-750.
(217) Nourmohammadzadeh, M.; Lo, J. F.; Bochenek, M.; Mendoza-Elias, J. E.; Wang, Q.; Li, Z.; Zeng, L.; Qi, M.; Eddington, D. T.; Oberholzer, J.; Wang, Y. *Analytical Chemistry* **2013**, *85*, 11240-11249.
(218) Rexius-Hall, M. L.; Rehman, J.; Eddington, D. T. *Integrative Biology* **2017**, *9*, 742-750.
(219) Lee, K. S.; Boccazzi, P.; Sinskey, A. J.; Ram, R. J. *Lab Chip* **2011**, *11*, 1730-1739.
(220) Ertl, P.; Sticker, D.; Charwat, V.; Kasper, C.; Lepperdinger, G. *Trends Biotechnol* **2014**, *32*, 245-253.
(221) Khademhosseini, A.; Yeh, J.; Jon, S.; Eng, G.; Suh, K. Y.; Burdick, J. A.; Langer, R. *Lab Chip* **2004**, *4*, 425-430.
(222) Skelley, A. M.; Kirak, O.; Suh, H.; Jaenisch, R.; Voldman, J. *Nat Methods* **2009**, *6*, 147-152.
(223) Kobel, S. A.; Burri, O.; Griffa, A.; Girotra, M.; Seitz, A.; Lutolf, M. P. *Lab Chip* **2012**, *12*, 2843-2849.
(224) Zhang, W.; Kai, K.; Choi, D. S.; Iwamoto, T.; Nguyen, Y. H.; Wong, H.; Landis, M. D.; Ueno, N. T.; Chang, J.; Qin, L. *Proc Natl Acad Sci U S A* **2012**, *109*, 18707-18712.
(225) Jiang, Z.; Xia, B.; McBride, R.; Oakey, J. *J Mater Chem B* **2017**, *5*, 173-180.
(226) Atac, B.; Wagner, I.; Horland, R.; Lauster, R.; Marx, U.; Tonevitsky, A. G.; Azar, R. P.; Lindner, G. *Lab Chip* **2013**, *13*, 3555-3561.
(227) Xiao, S.; Coppeta, J. R.; Rogers, H. B.; Isenberg, B. C.; Zhu, J.; Olalekan, S. A.; McKinnon, K. E.; Dokic, D.; Rashedi, A. S.; Haisenleder, D. J.; Malpani, S. S.; Arnold-Murray, C. A.; Chen, K.; Jiang, M.; Bai, L.; Nguyen, C. T.; Zhang, J.; Laronda, M. M.; Hope, T. J.; Maniar, K. P.; Pavone, M. E.; Avram, M. J.; Sefton, E. C.; Getsios, S.; Burdette, J. E.; Kim, J. J.; Borenstein, J. T.; Woodruff, T. K. *Nat Commun* **2017**, *8*, 14584.
(228) McLean, I. C.; Schwerdtfeger, L. A.; Tobet, S. A.; Henry, C. S. *Lab Chip* **2018**, *18*, 1399-1410.
(229) Halldorsson, S.; Lucumi, E.; Gomez-Sjoberg, R.; Fleming, R. M. T. *Biosens Bioelectron* **2015**, *63*, 218-231.
(230) Xu, B. Y.; Hu, S. W.; Qian, G. S.; Xu, J. J.; Chen, H. Y. *Lab Chip* **2013**, *13*, 3714-3720.

(231) Agarwal, P.; Zhao, S.; Bielecki, P.; Rao, W.; Choi, J. K.; Zhao, Y.; Yu, J.; Zhang, W.; He, X. *Lab Chip* **2013**, *13*, 4525-4533.
(232) Skardal, A.; Murphy, S. V.; Devarasetty, M.; Mead, I.; Kang, H.-W.; Seol, Y.-J.; Zhang, Y. S.; Shin, S.-R.; Zhao, L.; Aleman, J. *Scientific reports* **2017**, *7*, 8837.
(233) Deal, K. S.; Easley, C. J. *Anal Chem* **2012**, *84*, 1510-1516.
(234) Negou, J. T.; Hu, J.; Li, X.; Easley, C. J. *Anal Methods* **2018**, *10*, 3436-3443.
(235) Unger, M. A.; Chou, H.-P.; Thorsen, T.; Scherer, A.; Quake, S. R. *Science* **2000**, *288*, 113-116.
(236) Gilon, P.; Ravier, M. A.; Jonas, J.-C.; Henquin, J.-C. *Diabetes* **2002**, *51*, S144-S151.
(237) Siltanen, C.; Diakatou, M.; Lowen, J.; Haque, A.; Rahimian, A.; Stybayeva, G.; Revzin, A. *Acta biomaterialia* **2017**, *50*, 428-436.
(238) Chen, Q.; Utech, S.; Chen, D.; Prodanovic, R.; Lin, J.-M.; Weitz, D. A. *Lab on a Chip* **2016**, *16*, 1346-1349.
(239) Au, S. H.; Chamberlain, M. D.; Mahesh, S.; Sefton, M. V.; Wheeler, A. R. *Lab on a Chip* **2014**, *14*, 3290-3299.
(240) Cabrera, O.; Berman, D. M.; Kenyon, N. S.; Ricordi, C.; Berggren, P.-O.; Caicedo, A. *Proceedings of the National Academy of Sciences* **2006**, *103*, 2334-2339.
(241) Chen, W.; Shu, Z.; Gao, D.; Shen, A. Q. *Advanced healthcare materials* **2016**, *5*, 223-231.
(242) Liu, H. T.; Wang, H.; Wei, W. B.; Liu, H.; Jiang, L.; Qin, J. H. *Small* **2018**, *14*, 1801095.
(243) Chen, D.; Du, W.; Liu, Y.; Liu, W.; Kuznetsov, A.; Mendez, F. E.; Philipson, L. H.; Ismagilov, R. F. *Proceedings of the National Academy of Sciences* **2008**, *105*, 16843-16848.
(244) Fantuzzi, G. *Journal of Allergy and clinical immunology* **2005**, *115*, 911-919.
(245) Kershaw, E. E.; Flier, J. S. *Journal of Clinical Endocrinology & Metabolism* **2004**, *89*, 2548-2556.
(246) Li, X.; Easley, C. J. *Anal Bioanal Chem* **2018**, *410*, 791-800.
(247) Sakai, S.; Ito, S.; Inagaki, H.; Hirose, K.; Matsuyama, T.; Taya, M.; Kawakami, K. *Biomicrofluidics* **2011**, *5*, 013402.
(248) Deveza, L.; Ashoken, J.; Castaneda, G.; Tong, X.; Keeney, M.; Han, L.-H.; Yang, F. *ACS Biomaterials Science & Engineering* **2015**, *1*, 157-165.
(249) Karimi, M.; Bahrami, S.; Mirshekari, H.; Basri, S. M. M.; Nik, A. B.; Aref, A. R.; Akbari, M.; Hamblin, M. R. *Lab on a Chip* **2016**, *16*, 2551-2571.
(250) Shin, Y.; Han, S.; Jeon, J. S.; Yamamoto, K.; Zervantonakis, I. K.; Sudo, R.; Kamm, R. D.; Chung, S. *Nature protocols* **2012**, *7*, 1247.
(251) Harink, B.; Le Gac, S.; Truckenmüller, R.; van Blitterswijk, C.; Habibovic, P. *Lab on a Chip* **2013**, *13*, 3512-3528.
(252) Ghorbanian, S.; Qasaimeh, M. A.; Akbari, M.; Tamayol, A.; Juncker, D. *Biomedical microdevices* **2014**, *16*, 387-395.
(253) Alessandri, K.; Feyeux, M.; Gurchenkov, B.; Delgado, C.; Trushko, A.; Krause, K.-H.; Vignjević, D.; Nassoy, P.; Roux, A. *Lab on a Chip* **2016**, *16*, 1593-1604.
(254) Shi, W.; Wen, H.; Lu, Y.; Shi, Y.; Lin, B.; Qin, J. *Lab on a Chip* **2010**, *10*, 2855-2863.
(255) Bremond, N.; Thiam, A. R.; Bibette, J. *Physical review letters* **2008**, *100*, 024501.
(256) Baroud, C. N.; de Saint Vincent, M. R.; Delville, J.-P. *Lab on a Chip* **2007**, *7*, 1029-1033.
(257) Sesen, M.; Alan, T.; Neild, A. *Lab on a Chip* **2014**, *14*, 3325-3333.
(258) Zagnoni, M.; Le Lain, G.; Cooper, J. M. *Langmuir* **2010**, *26*, 14443-14449.
(259) Leman, M.; Abouakil, F.; Griffiths, A. D.; Tabeling, P. *Lab on a Chip* **2015**, *15*, 753-765.
(260) Niu, X.; Gielen, F.; Edel, J. B.; Demello, A. J. *Nature chemistry* **2011**, *3*, 437.
(261) Um, E.; Rogers, M. E.; Stone, H. A. *Lab on a Chip* **2013**, *13*, 4674-4680.
(262) Godwin, L. A.; Pilkerton, M. E.; Deal, K. S.; Wanders, D.; Judd, R. L.; Easley, C. J. *Analytical chemistry* **2011**, *83*, 7166-7172.
(263) Easley, C. J.; Karlinsey, J. M.; Landers, J. P. *Lab on a Chip* **2006**, *6*, 601-610.

(264) Miller, E. M.; Wheeler, A. R. *Analytical Chemistry* **2008**, *80*, 1614-1619.
(265) Mazutis, L.; Baret, J.-C.; Treacy, P.; Skhiri, Y.; Araghi, A. F.; Ryckelynck, M.; Taly, V.; Griffiths, A. D. *Lab on a Chip* **2009**, *9*, 2902-2908.
(266) Dugan, C. E.; Grinias, J. P.; Parlee, S. D.; El-Azzouny, M.; Evans, C. R.; Kennedy, R. T. *Analytical and bioanalytical chemistry* **2017**, *409*, 169-178.
(267) Li, X.; Brooks, J. C.; Hu, J.; Ford, K. I.; Easley, C. J. *Lab on a Chip* **2017**, *17*, 341-349.
(268) Wang, X.; Liu, Z.; Pang, Y. *RSC Advances* **2017**, *7*, 29966-29984.
(269) Jeong, H.-H.; Jin, S. H.; Lee, B. J.; Kim, T.; Lee, C.-S. *Lab on a Chip* **2015**, *15*, 889-899.
(270) Jambovane, S.; Kim, D. J.; Duin, E. C.; Kim, S.-K.; Hong, J. W. *Analytical chemistry* **2011**, *83*, 3358-3364.
(271) Zhou, H.; Li, G.; Yao, S. *Lab on a Chip* **2014**, *14*, 1917-1922.
(272) Kirchhof, K.; Andar, A.; Yin, H.; Gadegaard, N.; Riehle, M.; Groth, T. *Lab on a Chip* **2011**, *11*, 3326-3335.
(273) Sjöback, R.; Nygren, J.; Kubista, M. *Spectrochimica Acta Part A: Molecular and Biomolecular Spectroscopy* **1995**, *51*, L7-L21.
(274) Hu, J.; Easley, C. J. *Analytical chemistry* **2017**, *89*, 8517-8523.
(275) Wang, R. E.; Tian, L.; Chang, Y.-H. *Journal of pharmaceutical and biomedical analysis* **2012**, *63*, 165-169.
(276) Lorenz, R. M.; Fiorini, G. S.; Jeffries, G. D.; Lim, D. S.; He, M.; Chiu, D. T. *Analytica chimica acta* **2008**, *630*, 124-130.
(277) Lan, F.; Haliburton, J. R.; Yuan, A.; Abate, A. R. *Nature communications* **2016**, *7*, 11784.
(278) Coelho, B.; Veigas, B.; Fortunato, E.; Martins, R.; Águas, H.; Igreja, R.; Baptista, P. *Sensors* **2017**, *17*, 1495.
(279) Lee, J. Y.; Carugo, D.; Crake, C.; Owen, J.; de Saint Victor, M.; Seth, A.; Coussios, C.; Stride, E. *Advanced Materials* **2015**, *27*, 5484-5492.
(280) Jin, S. H.; Lee, S. S.; Lee, B.; Jeong, S.-G.; Peter, M.; Lee, C.-S. *Analytical chemistry* **2017**, *89*, 9722-9729.
(281) Terekhov, S. S.; Smirnov, I. V.; Stepanova, A. V.; Bobik, T. V.; Mokrushina, Y. A.; Ponomarenko, N. A.; Belogurov, A. A.; Rubtsova, M. P.; Kartseva, O. V.; Gomzikova, M. O. *Proceedings of the National Academy of Sciences* **2017**, *114*, 2550-2555.
(282) O'Donovan, B.; Eastburn, D. J.; Abate, A. R. *Lab on a Chip* **2012**, *12*, 4029-4032.
(283) Li, X. P.; Brooks, J. C.; Hu, J.; Ford, K. I.; Easley, C. J. *Lab on a Chip* **2017**, *17*, 341-349.
(284) Chen, C.-T.; Lee, G.-B. *Journal of microelectromechanical systems* **2006**, *15*, 1492-1498.
(285) Godwin, L. A.; Deal, K. S.; Hoepfner, L. D.; Jackson, L. A.; Easley, C. J. *Analytica Chimica Acta* **2013**, *758*, 101-107.
(286) Kang, D.-K.; Ali, M. M.; Zhang, K.; Huang, S. S.; Peterson, E.; Digman, M. A.; Gratton, E.; Zhao, W. *Nature communications* **2014**, *5*, 5427.
(287) Clark, A. M.; Sousa, K. M.; Jennings, C.; MacDougald, O. A.; Kennedy, R. T. *Analytical chemistry* **2009**, *81*, 2350-2356.
(288) Niu, X.; Gulati, S.; Edel, J. B.; demello, A. J. *Lab on a Chip* **2008**, *8*, 1837-1841.
(289) Sander, J. S.; Erb, R. M.; Denier, C.; Studart, A. R. *Advanced materials* **2012**, *24*, 2582-2587.
(290) Doonan, S. R.; Bailey, R. C. *Analytical Chemistry* **2017**, *89*, 4091-4099.
(291) Erickstad, M.; Gutierrez, E.; Groisman, A. *Lab on a Chip* **2015**, *15*, 57-61.
(292) Heyduk, E.; Dummit, B.; Chang, Y.-H.; Heyduk, T. *Analytical chemistry* **2008**, *80*, 5152-5159.
(293) Kim, J.; Hu, J.; Sollie, R. S.; Easley, C. J. *Analytical chemistry* **2010**, *82*, 6976-6982.
(294) Millon, L.; Larosa, F.; Lepiller, Q.; Legrand, F.; Rocchi, S.; Daguindau, E.; Scherer, E.; Bellanger, A.-P.; Leroy, J.; Grenouillet, F. *Clinical Infectious Diseases* **2013**, *56*, e95-e101.
(295) Eastburn, D. J.; Sciambi, A.; Abate, A. R. *Analytical chemistry* **2013**, *85*, 8016-8021.

(296) Deng, R.; Tang, L.; Tian, Q.; Wang, Y.; Lin, L.; Li, J. *Angewandte Chemie International Edition* **2014**, *53*, 2389-2393.
(297) Zhuang, J.; Lai, W.; Chen, G.; Tang, D. *Chemical communications* **2014**, *50*, 2935-2938.
(298) Xu, W.; Xie, X.; Li, D.; Yang, Z.; Li, T.; Liu, X. *small* **2012**, *8*, 1846-1850.
(299) Li, J. J.; Chu, Y.; Lee, B. Y.-H.; Xie, X. S. *Nucleic acids research* **2008**, *36*, e36.
(300) Zhang, X.; Xiao, K.; Cheng, L.; Chen, H.; Liu, B.; Zhang, S.; Kong, J. *Analytical chemistry* **2014**, *86*, 5567-5572.
(301) Gullberg, M.; Gústafsdóttir, S. M.; Schallmeiner, E.; Jarvius, J.; Bjarnegård, M.; Betsholtz, C.; Landegren, U.; Fredriksson, S. *Proceedings of the National Academy of Sciences* **2004**, *101*, 8420-8424.
(302) Li, Y.; Liang, L.; Zhang, C.-y. *Analytical chemistry* **2013**, *85*, 11174-11179.
(303) Wei, L.; Wang, X.; Wu, D.; Li, C.; Yin, Y.; Li, G. *Chemical communications* **2016**, *52*, 5633-5636.
(304) Huang, R.; Zhou, X.; Zhang, C.; Xing, D. *Sensors and Actuators B: Chemical* **2018**, *264*, 169-176.
(305) Xue, L.; Zhou, X.; Xing, D. *Analytical chemistry* **2012**, *84*, 3507-3513.
(306) Zhou, M.; Teng, X.; Li, Y.; Deng, R.; Li, J. *Analytical chemistry* **2019**, *91*, 5295-5302.
(307) Stephenson, W.; Donlin, L. T.; Butler, A.; Rozo, C.; Bracken, B.; Rashidfarrokhi, A.; Goodman, S. M.; Ivashkiv, L. B.; Bykerk, V. P.; Orange, D. E. *Nature communications* **2018**, *9*, 1-10.
(308) Huang, C.-B.; Xu, L.; Zhu, J.-L.; Wang, Y.-X.; Sun, B.; Li, X.; Yang, H.-B. *Journal of the American Chemical Society* **2017**, *139*, 9459-9462.
(309) Li, N.; Liu, L.; Xiang, M.-H.; Liu, J.-W.; Yu, R.-Q.; Jiang, J.-H. *Chemical communications* **2019**, *55*, 4387-4390.
(310) Porchetta, A.; Ippodrino, R.; Marini, B.; Caruso, A.; Caccuri, F.; Ricci, F. *Journal of the American Chemical Society* **2018**, *140*, 947-953.
(311) Wang, L.-j.; Ren, M.; Zhang, Q.; Tang, B.; Zhang, C.-y. *Analytical chemistry* **2017**, *89*, 4488-4494.
(312) Qin, Y.; Liao, S.; Huang, Y.; Zhao, J.; Zhao, S. *Analytica chimica acta* **2018**, *1039*, 91-97.
(313) Rutkowski, J. M.; Stern, J. H.; Scherer, P. E. *J Cell Biol* **2015**, *208*, 501-512.
(314) Kahn, S. E.; Hull, R. L.; Utzschneider, K. M. *Nature* **2006**, *444*, 840.
(315) A Dar, T.; A Sheikh, I.; A Ganie, S.; Ali, R.; R Singh, L.; Hua Gan, S.; A Kamal, M.; A Zargar, M. *CNS & Neurological Disorders-Drug Targets (Formerly Current Drug Targets-CNS & Neurological Disorders)* **2014**, *13*, 290-298.
(316) MacLaren, R.; Cui, W.; Cianflone, K. In *Current topics in complement II*; Springer, 2008, pp 1-21.
(317) Hu, J.; Judd, R. L.; Easley, C. **2019**.
(318) Shackman, J. G.; Dahlgren, G. M.; Peters, J. L.; Kennedy, R. T. *Lab on a Chip* **2005**, *5*, 56-63.
(319) Dishinger, J. F.; Kennedy, R. T. *Analytical chemistry* **2007**, *79*, 947-954.
(320) Godwin, L. A.; Brooks, J. C.; Hoepfner, L. D.; Wanders, D.; Judd, R. L.; Easley, C. J. *Analyst* **2015**, *140*, 1019-1025.
(321) Bruzewicz, D. A.; McGuigan, A. P.; Whitesides, G. M. *Lab on a Chip* **2008**, *8*, 663-671.
(322) Lomasney, A. R.; Yi, L.; Roper, M. G. *Analytical chemistry* **2013**, *85*, 7919-7925.
(323) Dishinger, J. F.; Reid, K. R.; Kennedy, R. T. *Analytical chemistry* **2009**, *81*, 3119-3127.
(324) Zhang, C.; Tu, H.-L.; Jia, G.; Mukhtar, T.; Taylor, V.; Rzhetsky, A.; Tay, S. *Science Advances* **2019**, *5*, eaav7959.
(325) Glieberman, A. L.; Pope, B. D.; Zimmerman, J. F.; Liu, Q.; Ferrier, J. P.; Kenty, J. H.; Schrell, A. M.; Mukhitov, N.; Shores, K. L.; Tepole, A. B. *Lab on a Chip* **2019**, *19*, 2993-3010.
(326) Dugan, C. E.; Cawthorn, W. P.; MacDougald, O. A.; Kennedy, R. T. *Analytical and bioanalytical chemistry* **2014**, *406*, 4851-4859.
(327) Yi, L.; Wang, X.; Dhumpa, R.; Schrell, A. M.; Mukhitov, N.; Roper, M. G. *Lab on a Chip* **2015**, *15*, 823-832.
(328) Pepino, M. Y.; Kuda, O.; Samovski, D.; Abumrad, N. A. J. A. r. o. n. **2014**, *34*, 281-303.
(329) Webb, Y.; Hermida-Matsumoto, L.; Resh, M. D. *Journal of Biological Chemistry* **2000**, *275*, 261-270.

(330) Wang, J.; Hao, J.-W.; Wang, X.; Guo, H.; Sun, H.-H.; Lai, X.-Y.; Liu, L.-Y.; Zhu, M.; Wang, H.-Y.; Li, Y.-F. *Cell reports* **2019**, *26*, 209-221. e205.
(331) Coelho, M.; Oliveira, T.; Fernandes, R. *Archives of medical science: AMS* **2013**, *9*, 191.
(332) Choe, S. S.; Huh, J. Y.; Hwang, I. J.; Kim, J. I.; Kim, J. B. *Frontiers in endocrinology* **2016**, *7*, 30.
(333) Cheung, H. K.; Han, T. T. Y.; Marecak, D. M.; Watkins, J. F.; Amsden, B. G.; Flynn, L. E. *Biomaterials* **2014**, *35*, 1914-1923.
(334) Rossi, E.; Gerges, I.; Tocchio, A.; Tamplenizza, M.; Aprile, P.; Recordati, C.; Martello, F.; Martin, I.; Milani, P.; Lenardi, C. *Biomaterials* **2016**, *104*, 65-77.
(335) Loskill, P.; Sezhian, T.; Tharp, K. M.; Lee-Montiel, F. T.; Jeeawoody, S.; Reese, W. M.; Zushin, P.-J. H.; Stahl, A.; Healy, K. E. *Lab on a Chip* **2017**, *17*, 1645-1654.
(336) Dugan, C. E.; Kennedy, R. T. In *Methods in enzymology*; Elsevier, 2014, pp 195-209.

Appendix

LabVIEW Codes

A. LabVIEW application for voltage of salt-water electrode control

B. LabVIEW application for two-channel droplet microfluidics

C. LabVIEW application for four-channel droplet microfluidics

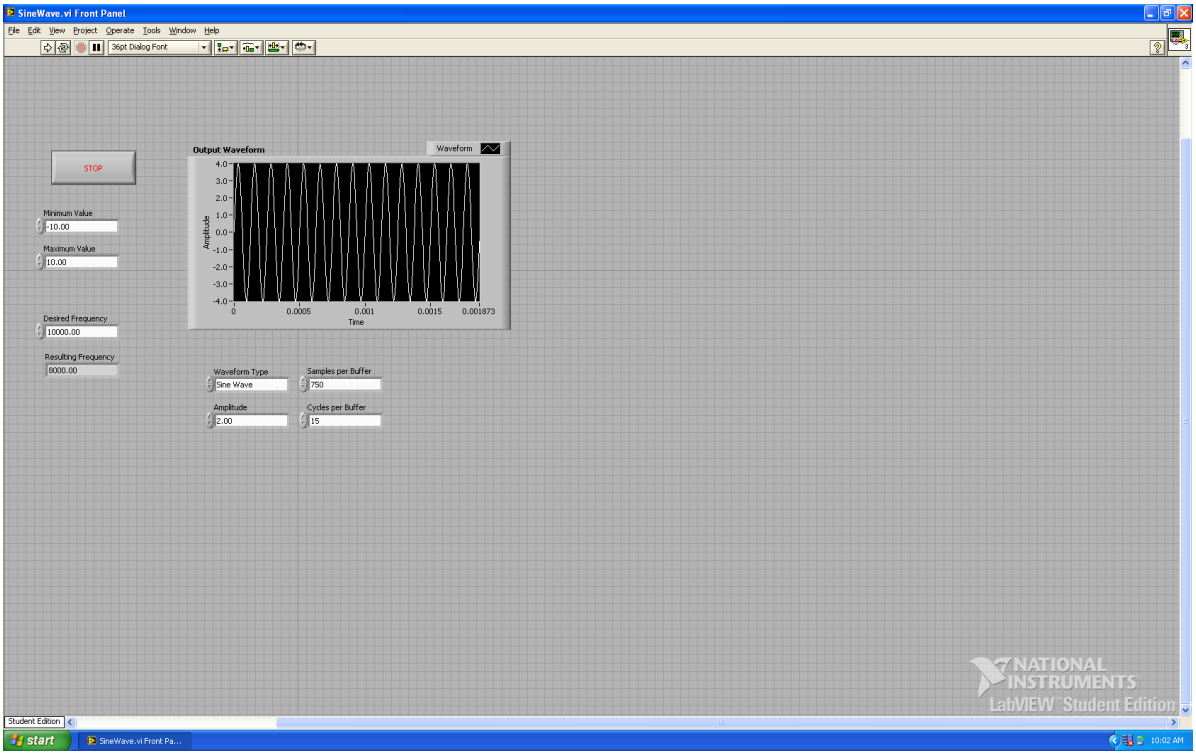

Figure A.1 Front panel of salt-water electrode control (frequency & magnitude)

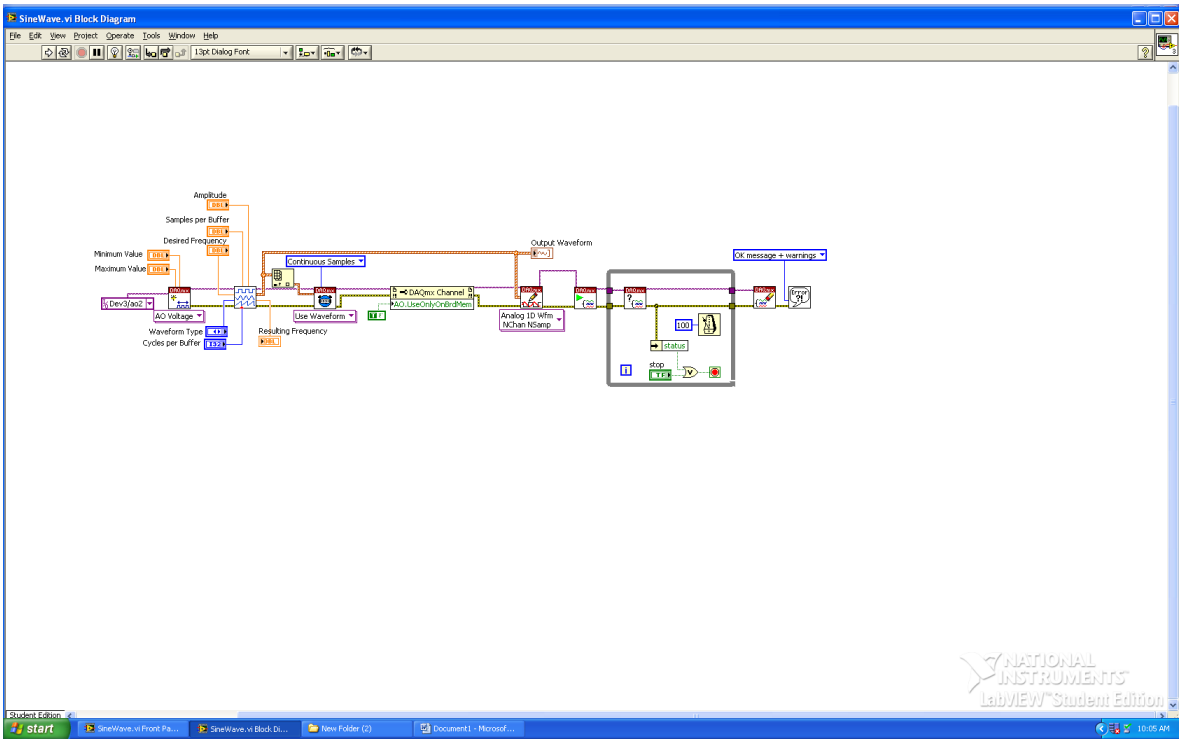

Figure A.2 Block diagram of salt-water electrode control (frequency & magnitude)

Two channel program

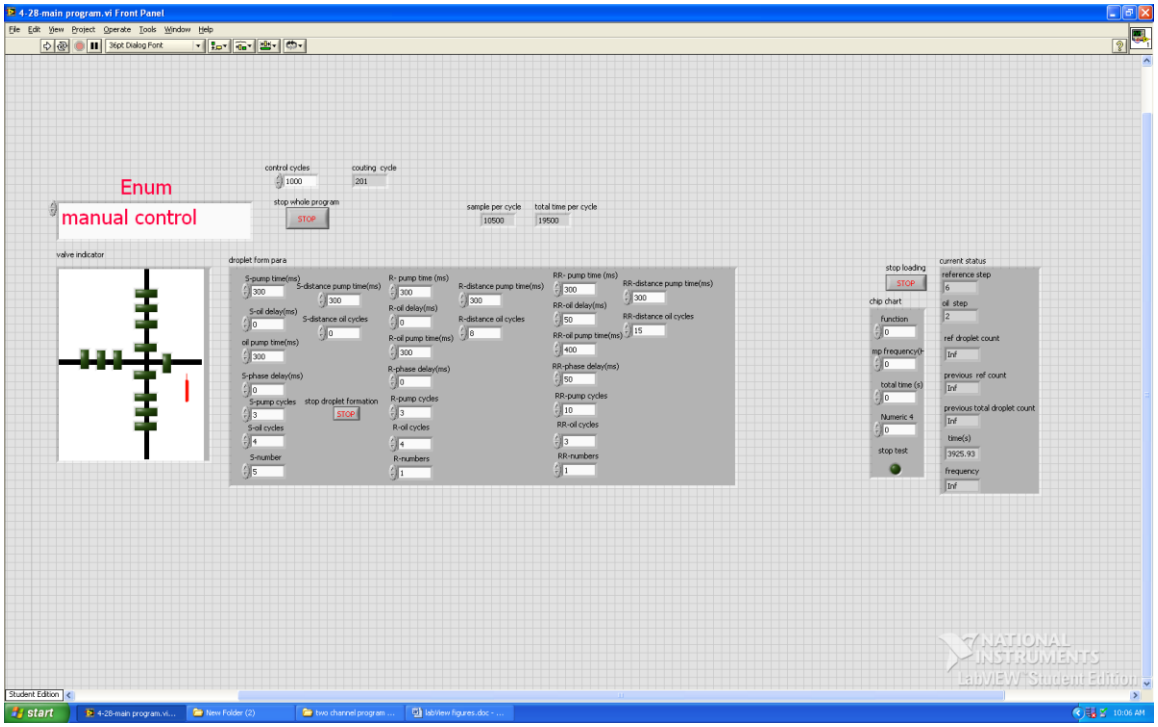

Figure B.1 Front panel of two-channel control

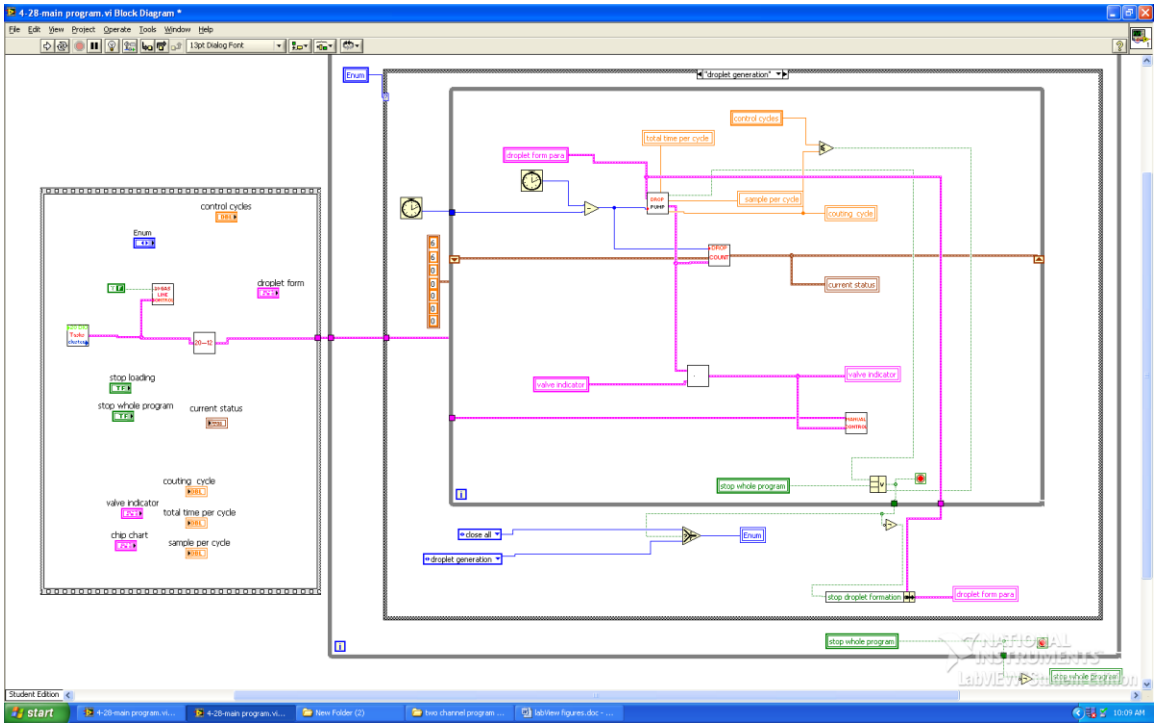

Figure B.2 Block diagram of two-channel control

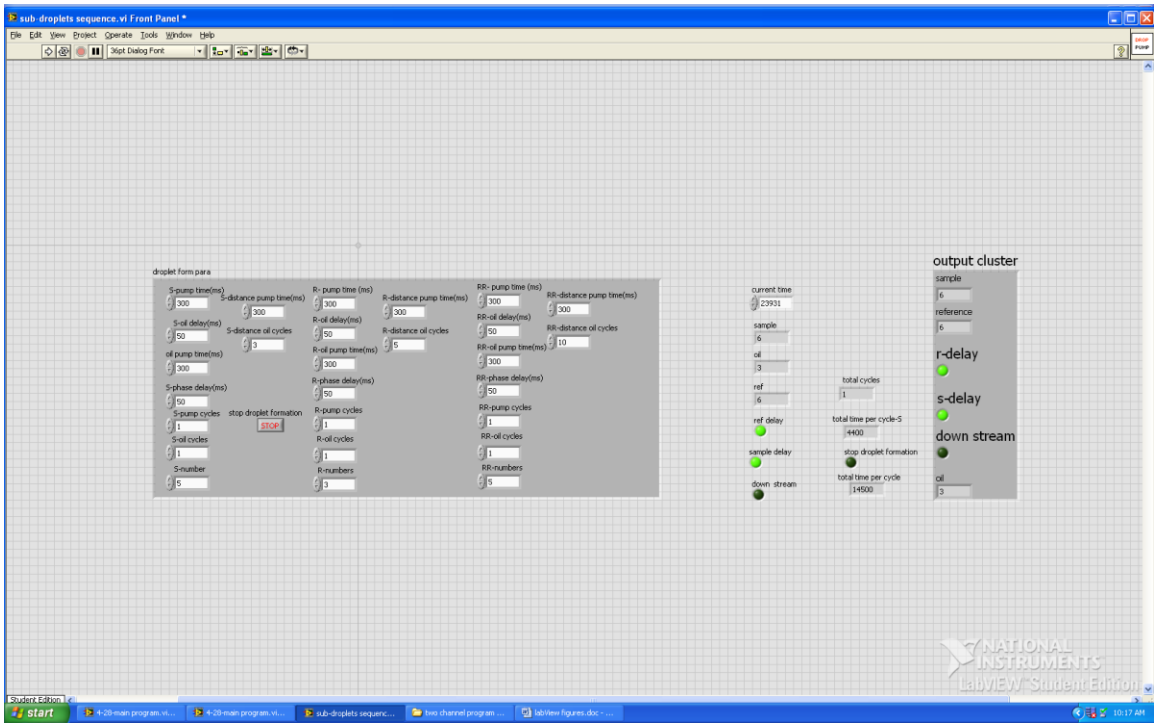

Figure B.3 Sub VI-front panel of droplet generation

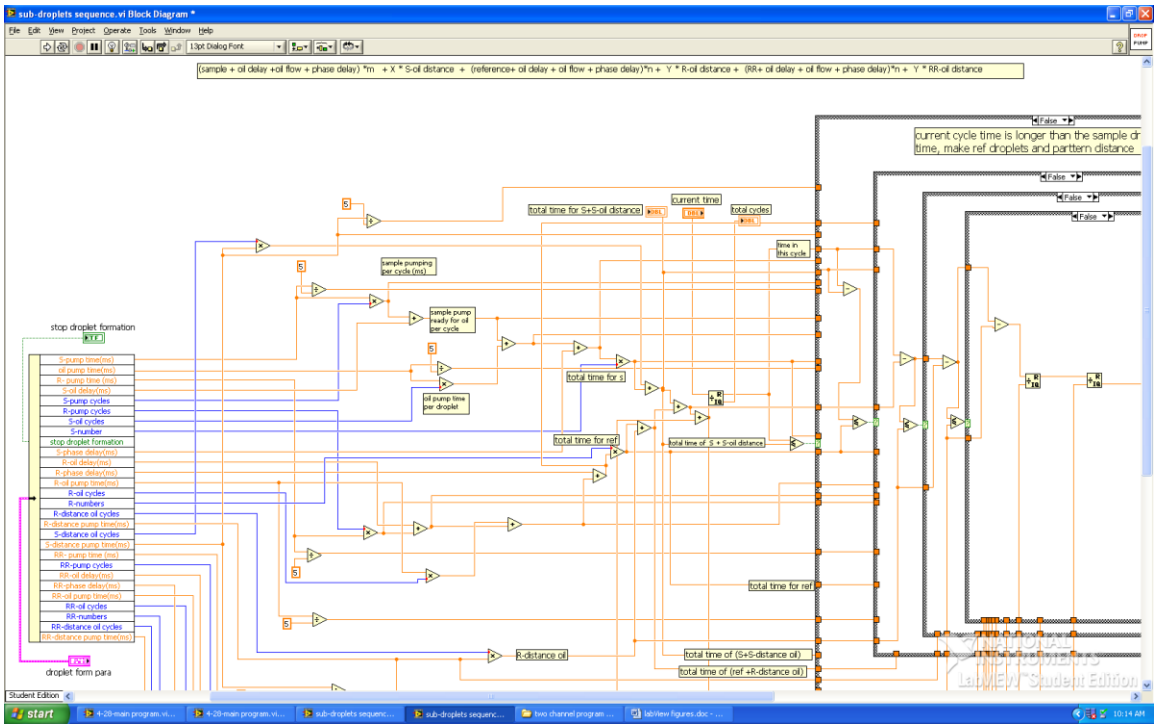

Figure B.4 Sub VI-block diagram of droplet generation-1

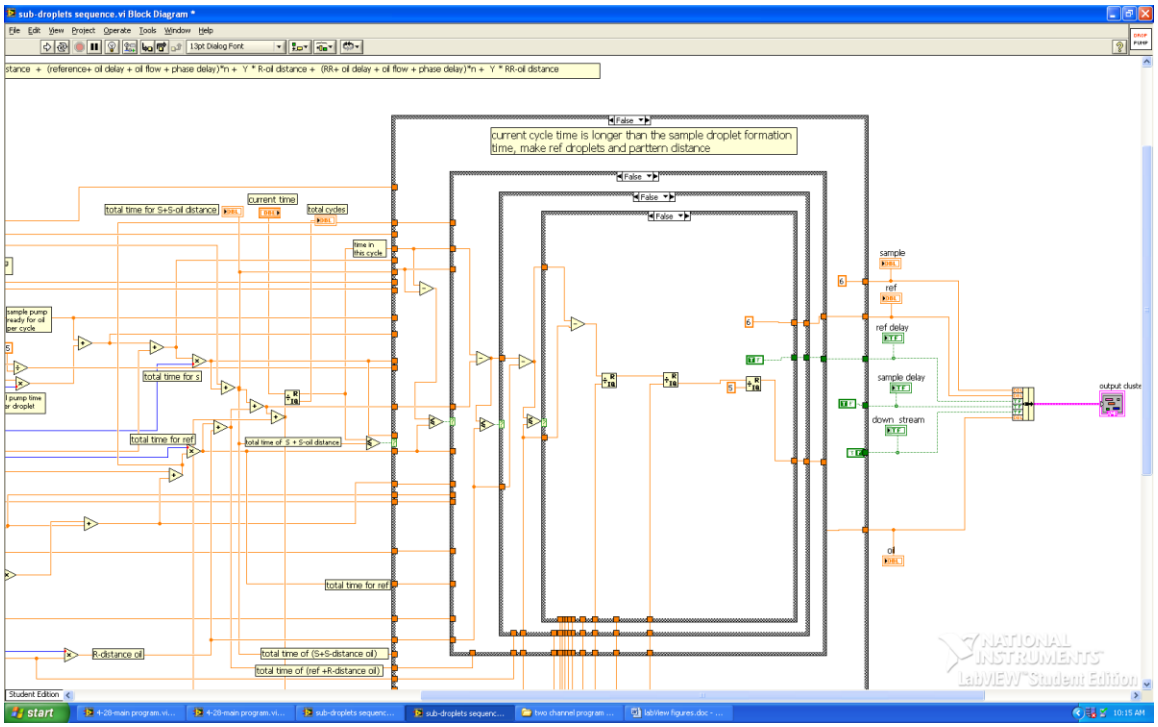

Figure B.5 Sub VI-block diagram of droplet generation-2

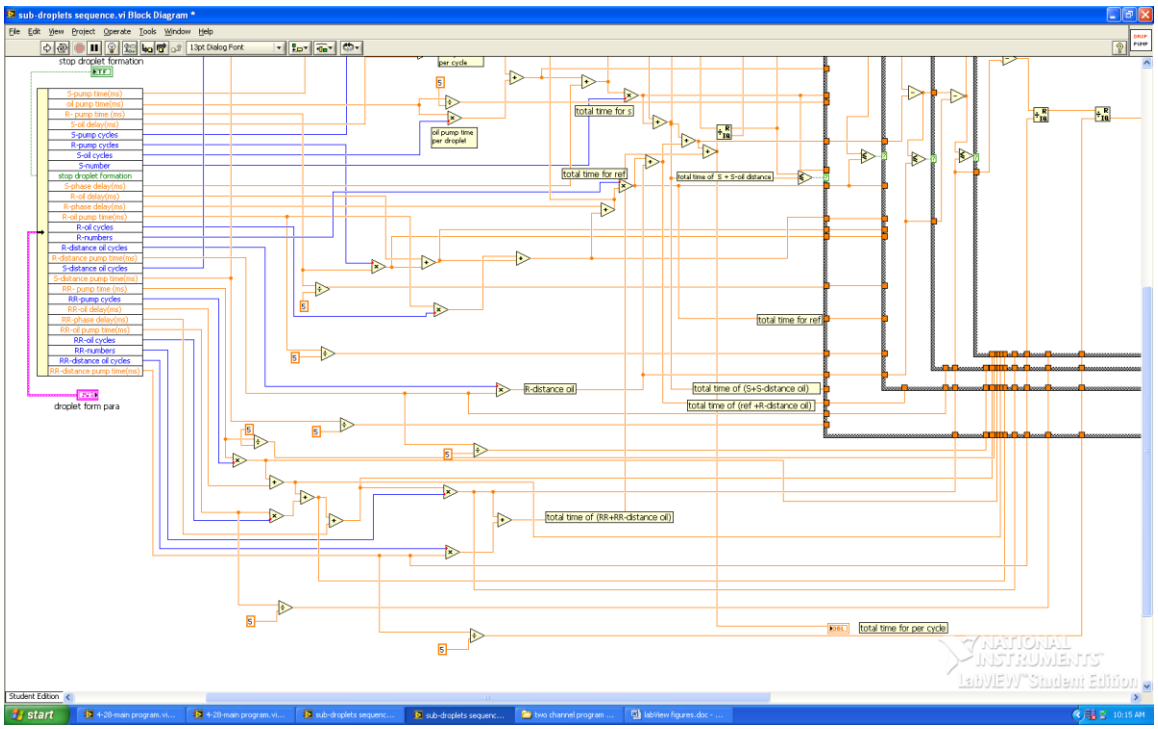

Figure B.6 Sub VI-block diagram of droplet generation-3

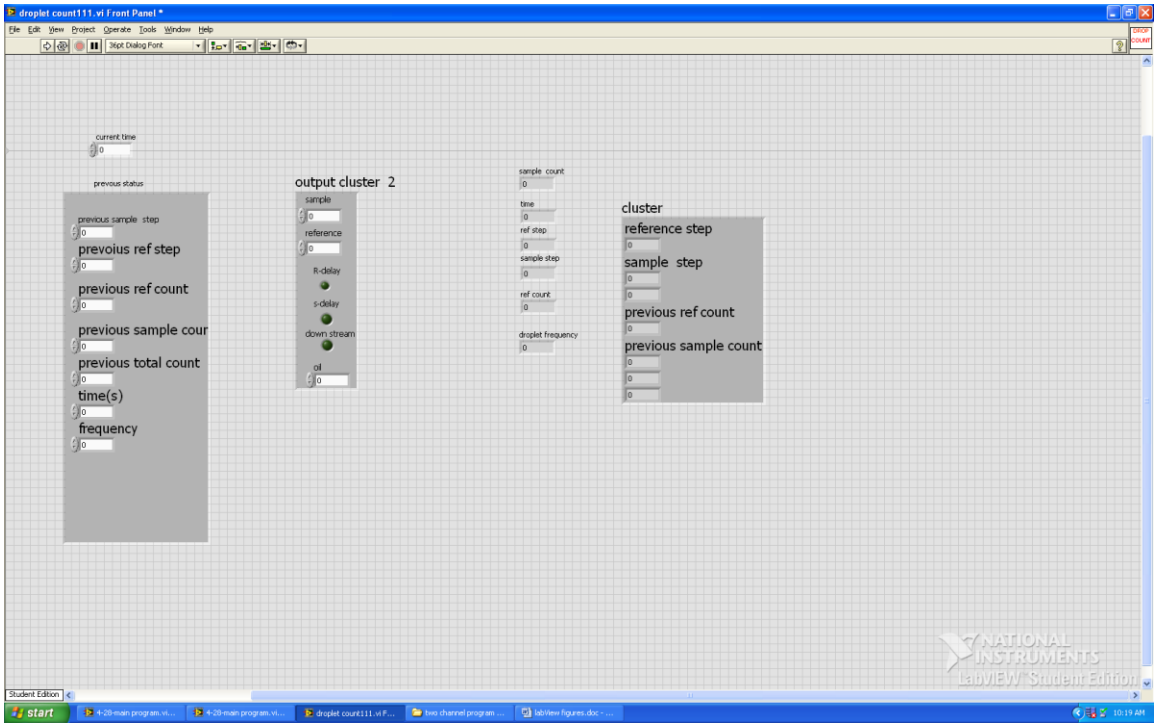

Figure B.7 Sub VI-front panel of droplet number counts

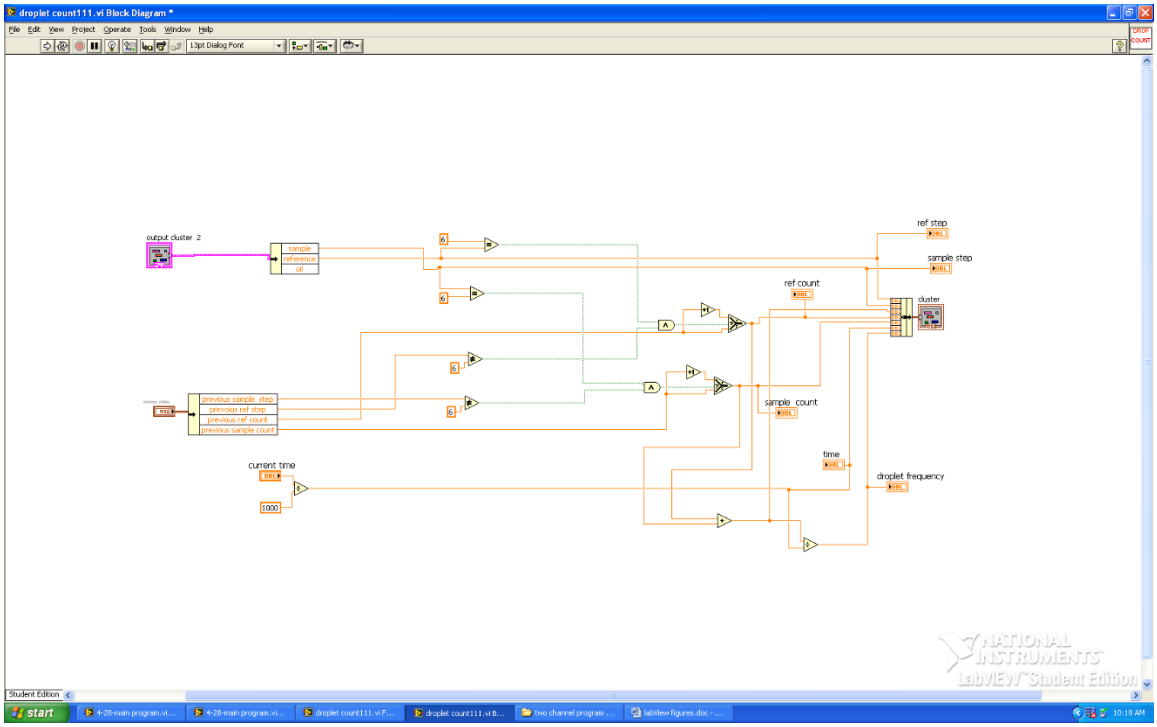

Figure B.8 Sub VI-block diagram of droplet number counts

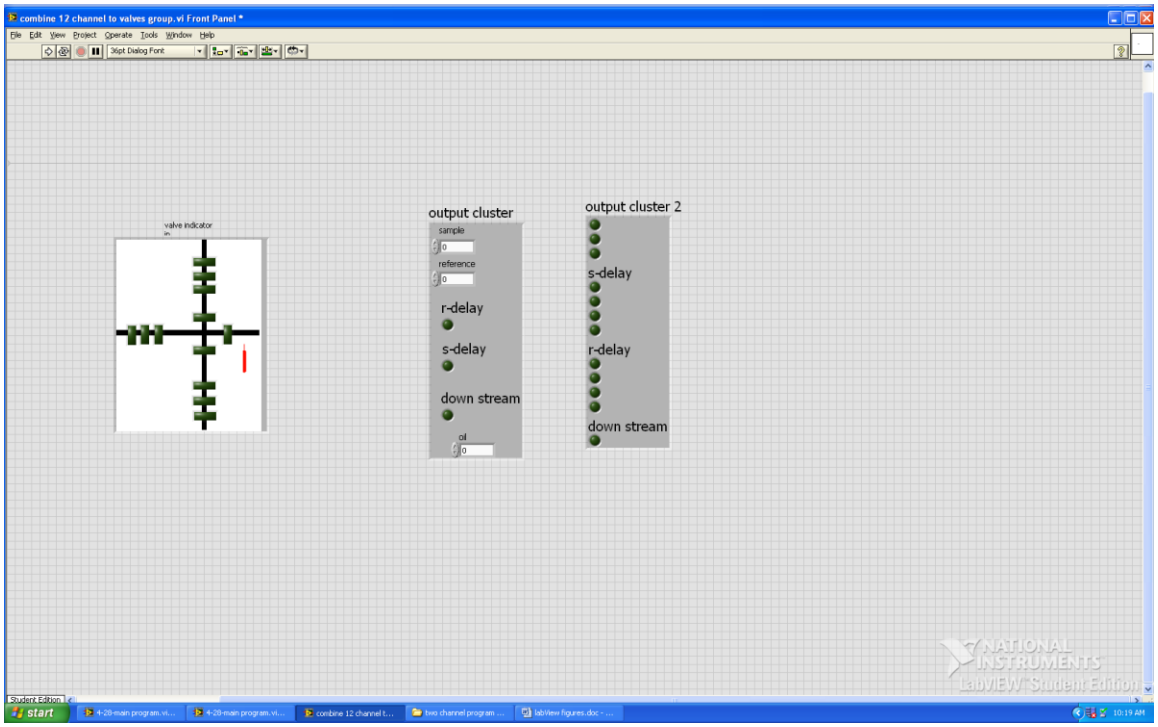

Figure B.9 Sub VI-front panel of arranging valve pumping to channels

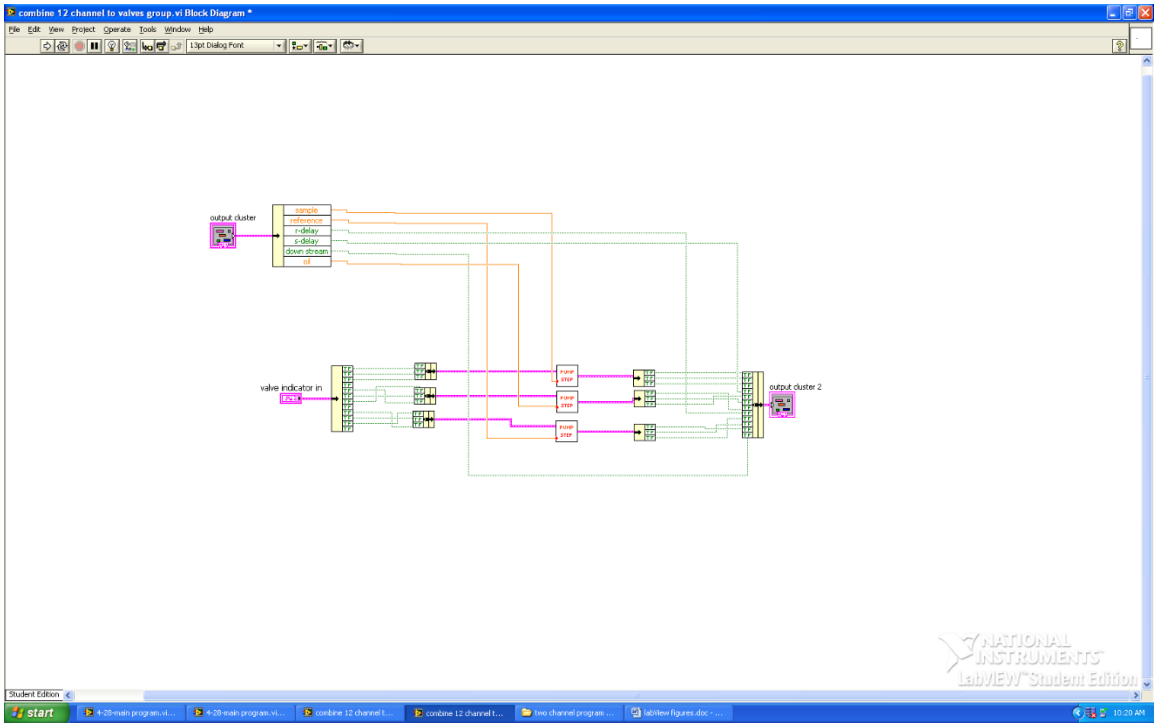

Figure B.10 Sub VI-block diagram of arranging valve pumping to channels

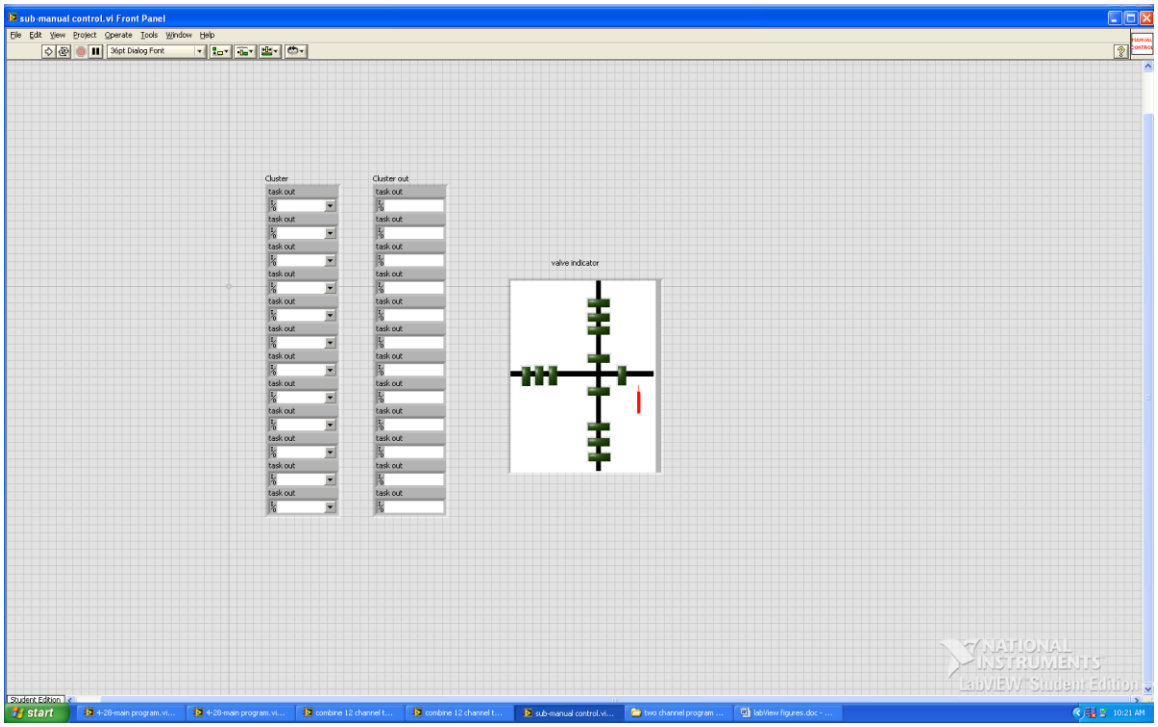

Figure B.11 Sub VI-front panel of Manual control

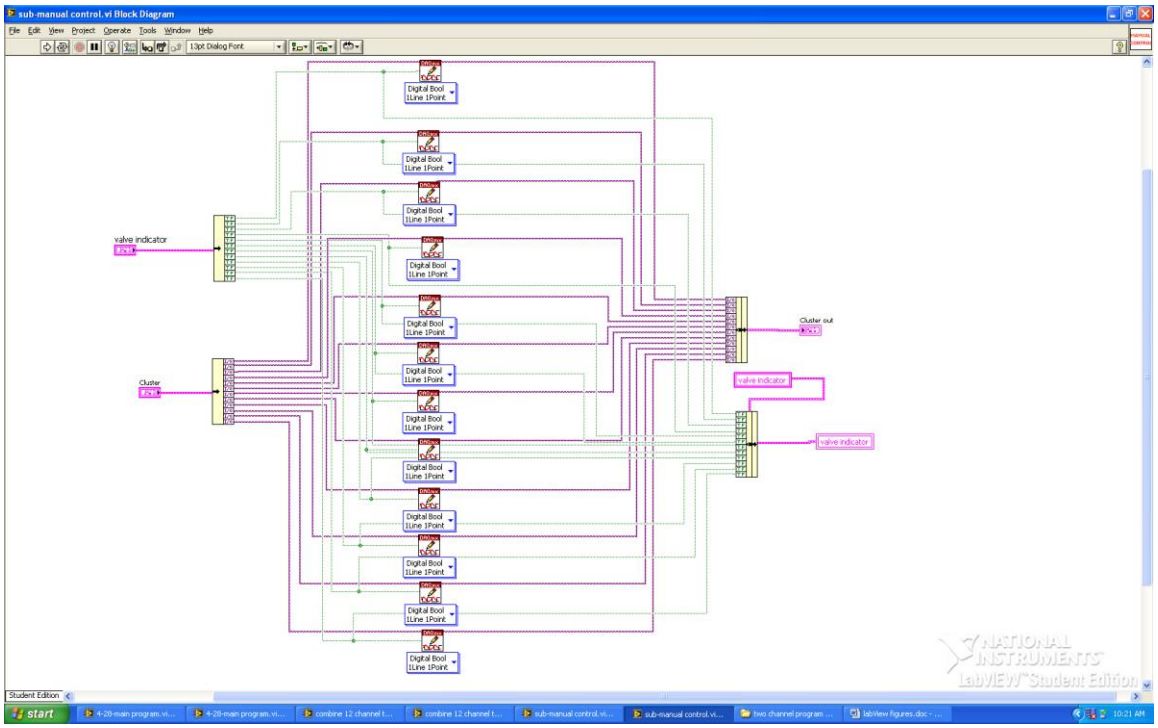

Figure B.12 Sub VI-block diagram of Manual control

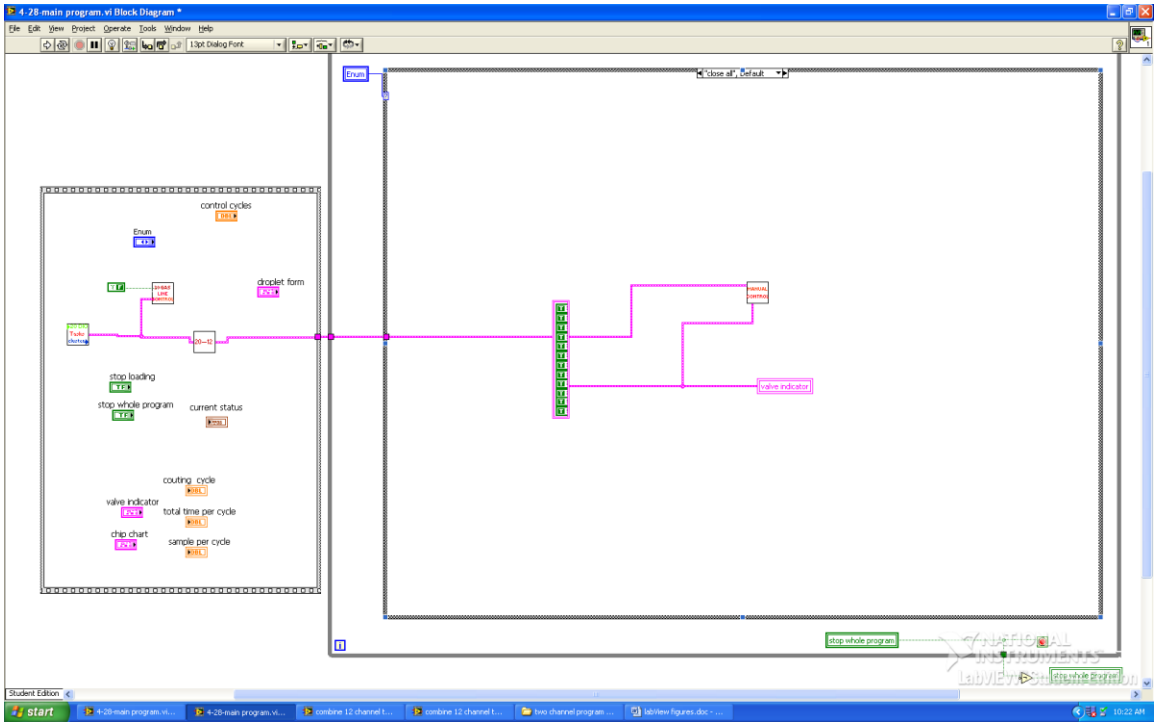

Figure B.13 Sub VI-block diagram of Close all valves

Four-channel microchip program

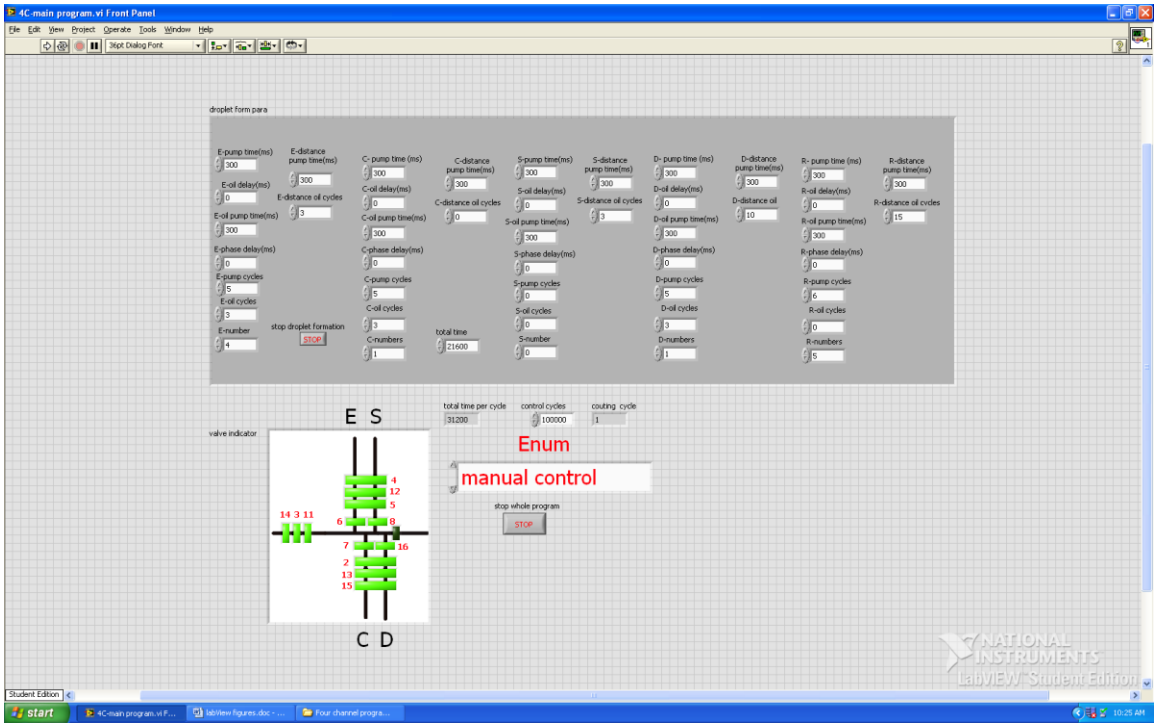

Figure C.1 Front panel of four-channel control

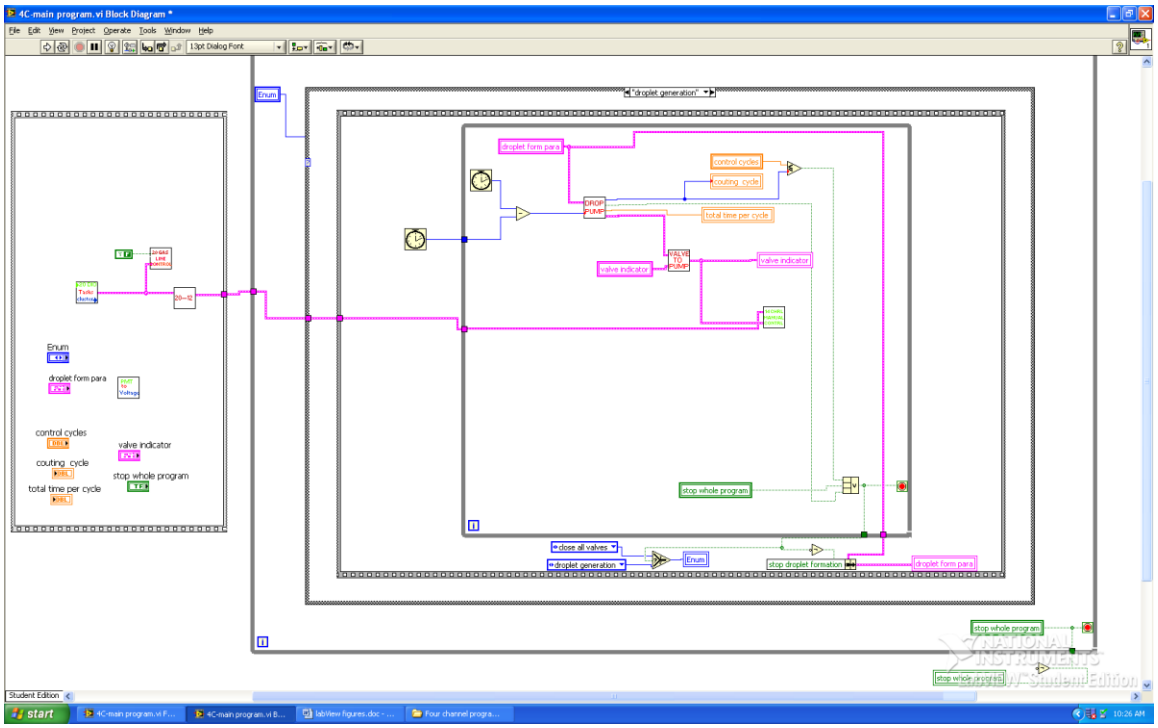

Figure C.2 Block diagram of four-channel control

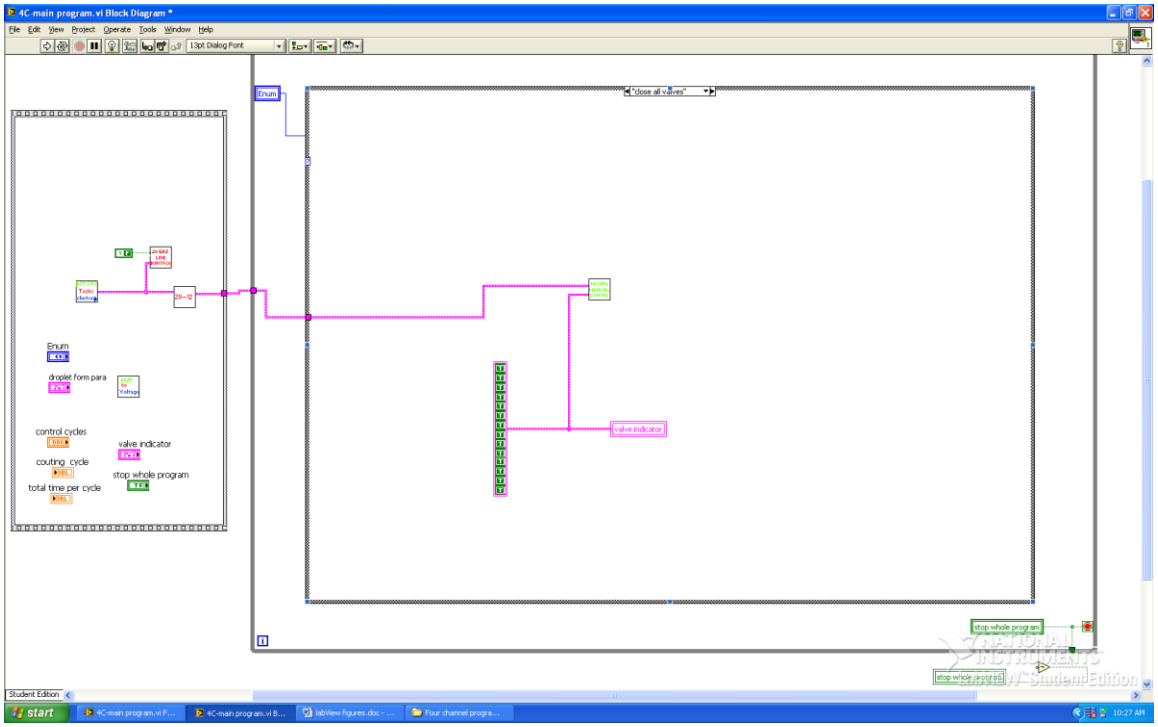

Figure C.3 Sub VI-block diagram of Close all valves

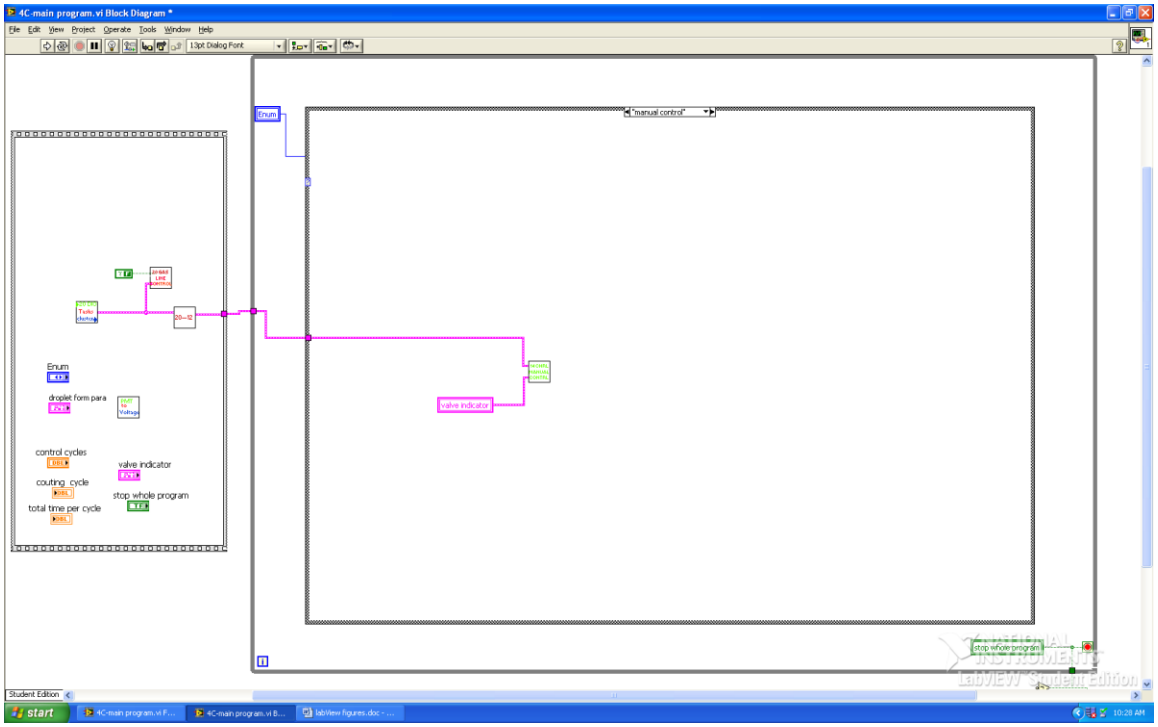

Figure C.4 Sub VI-block diagram of manual control

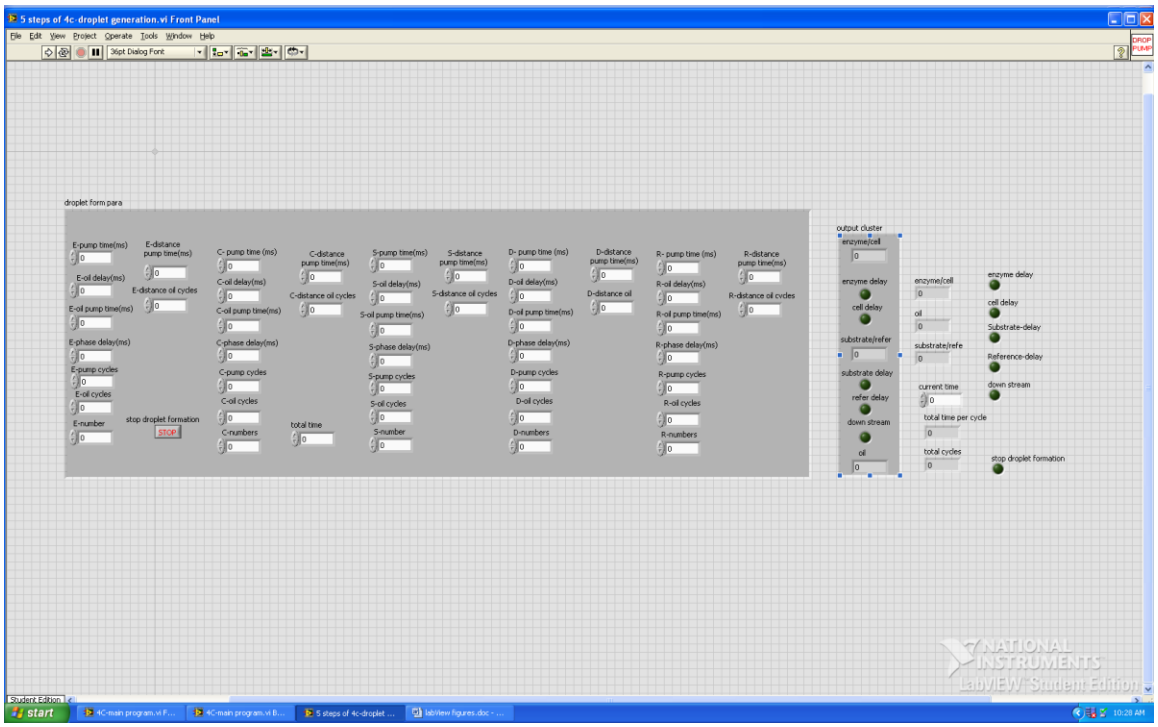

Figure C.5 Sub VI-front panel of droplet generation

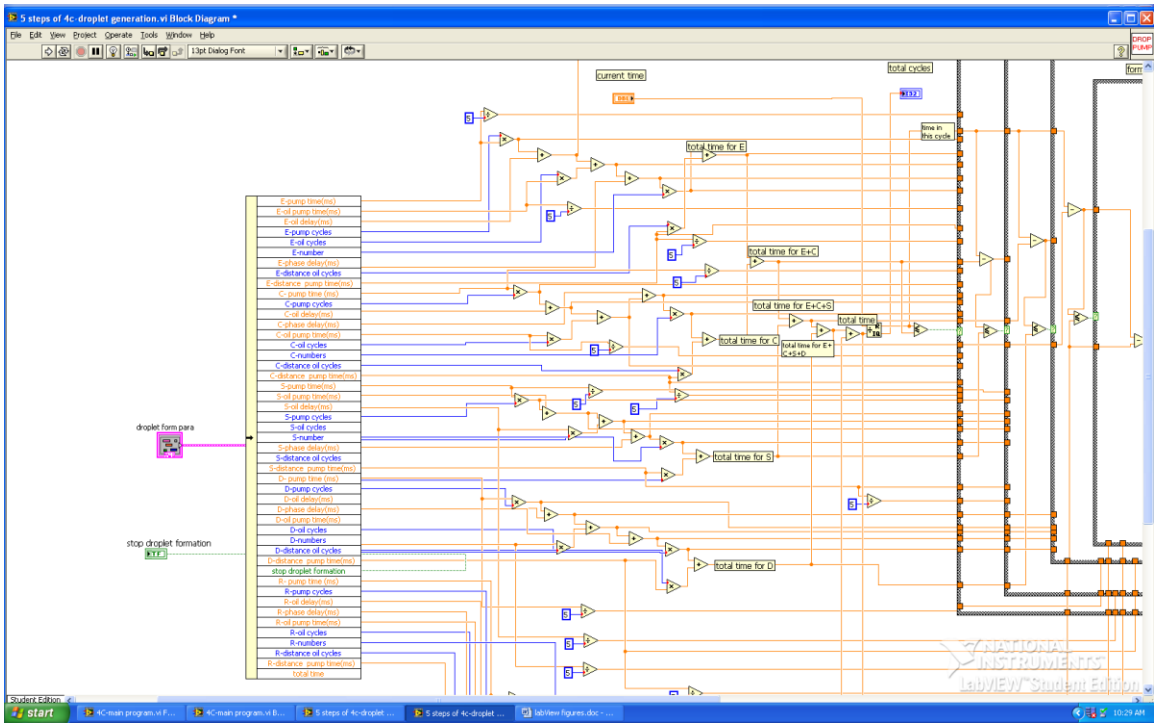

Figure C.6 Sub VI-block diagram of droplet generation-1

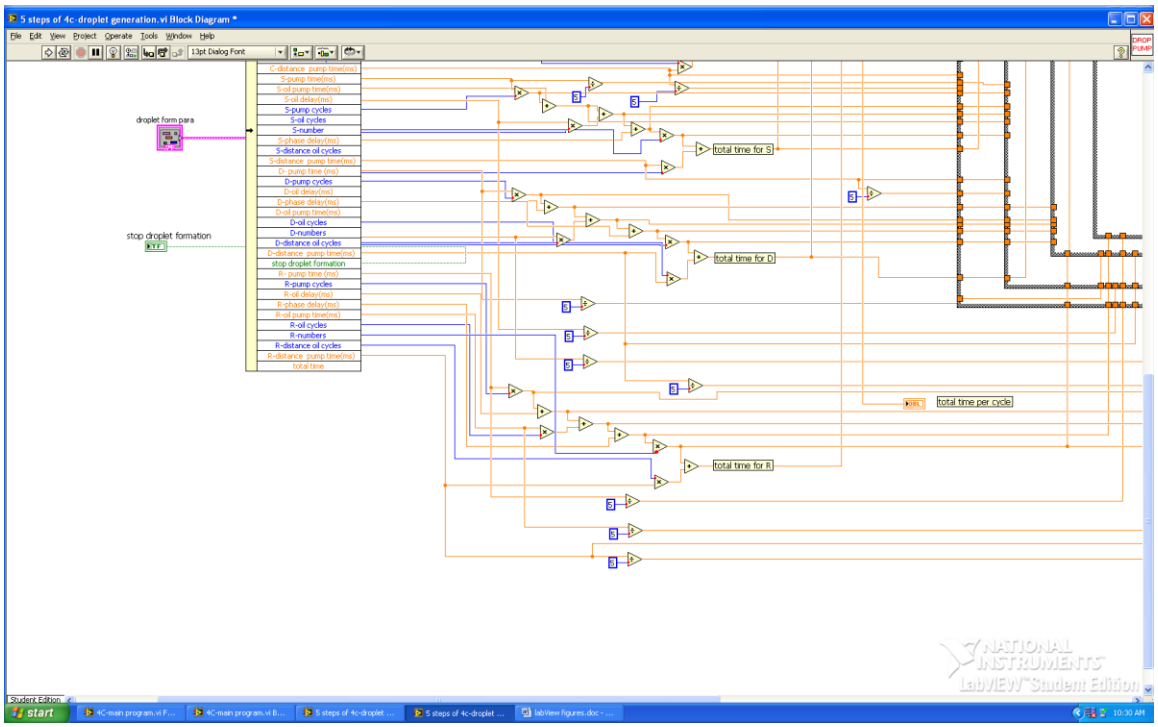

Figure C.7 Sub VI-block diagram of droplet generation-2

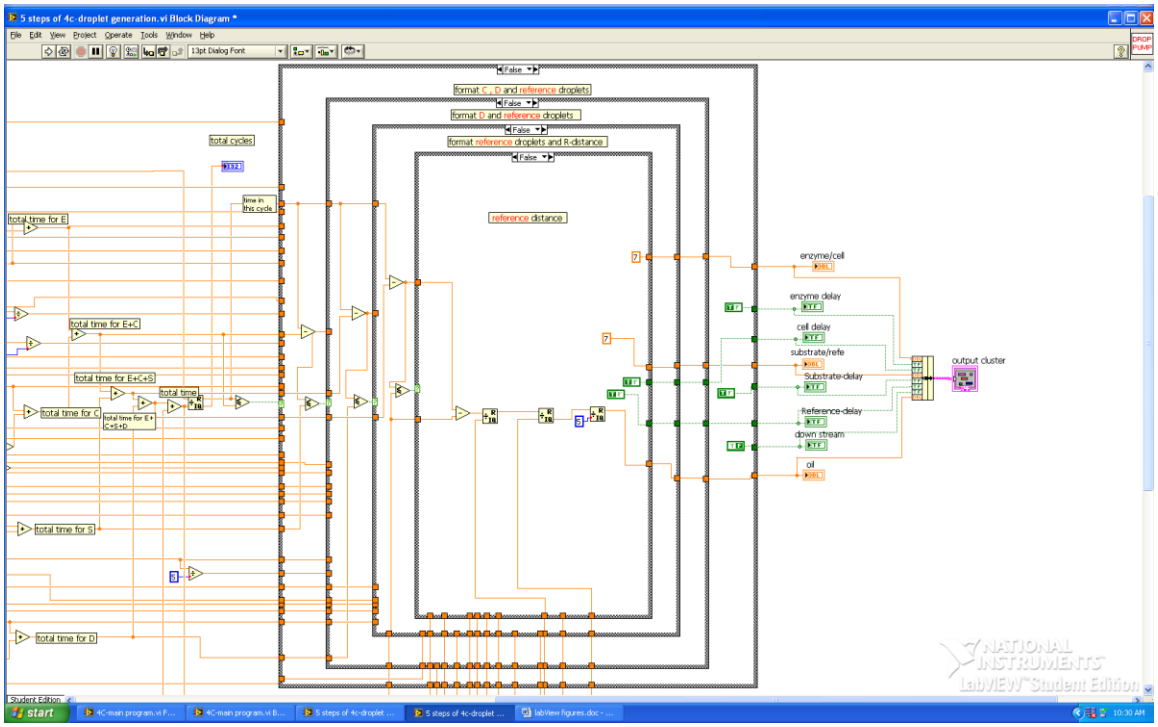

Figure C.8 Sub VI-block diagram of droplet generation-3

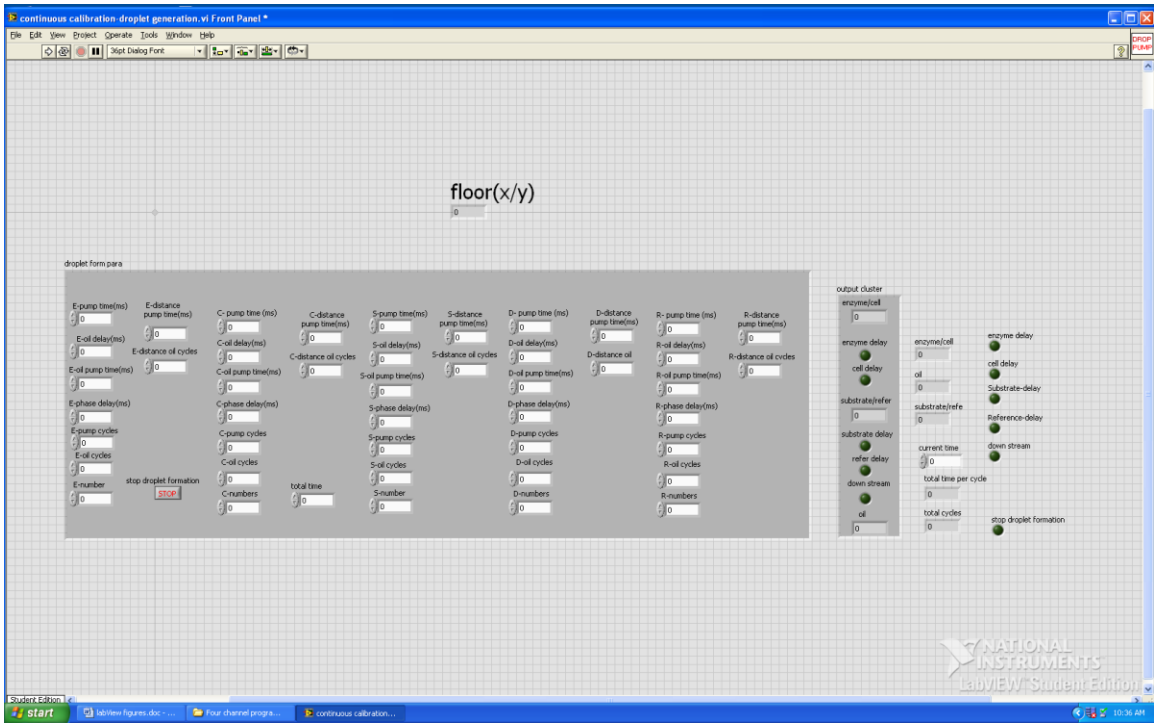

Figure C.9 Sub VI-front panel of continuous calibration generation

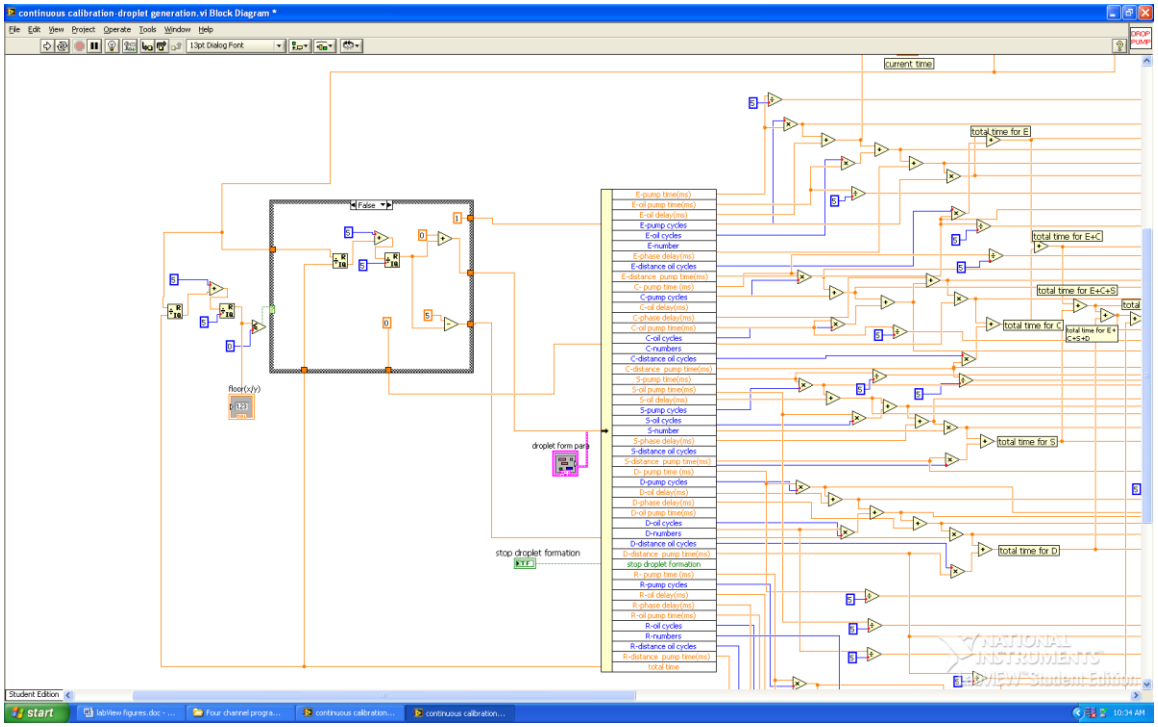

Figure C.10 Sub VI-block diagram of continuous calibration generation-1

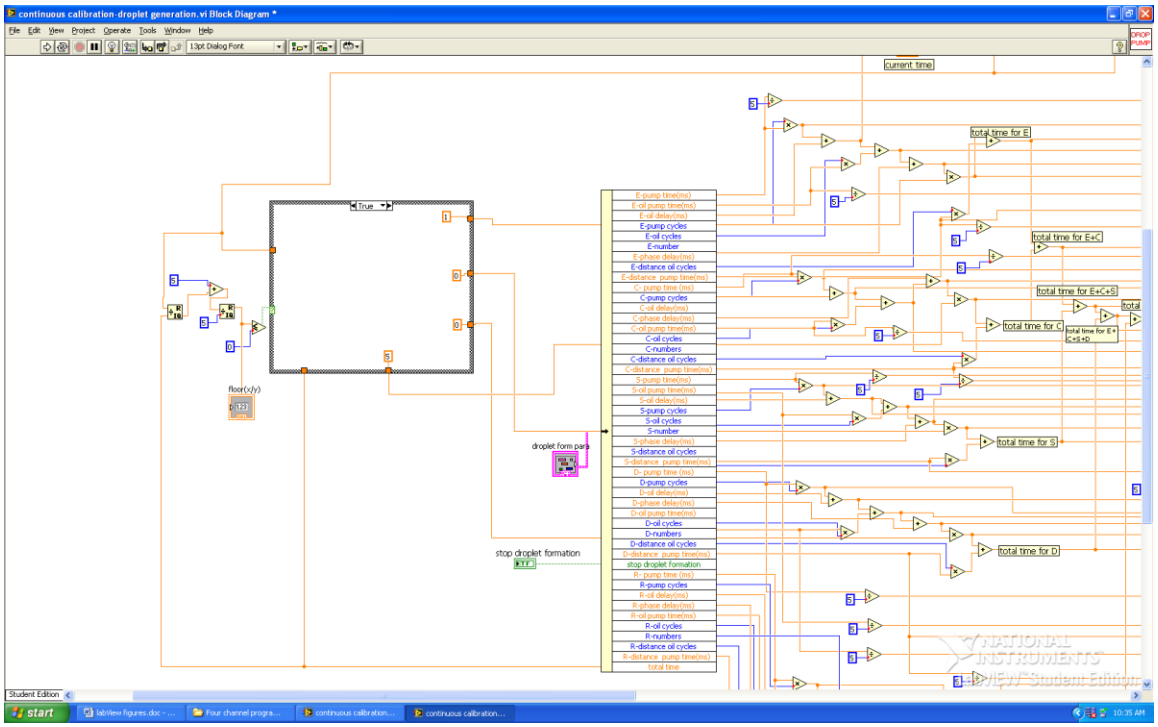

Figure C.11 Sub VI-block diagram of continuous calibration generation-2

(The right part of this sub VI is same as previous 4-channel droplet generation)

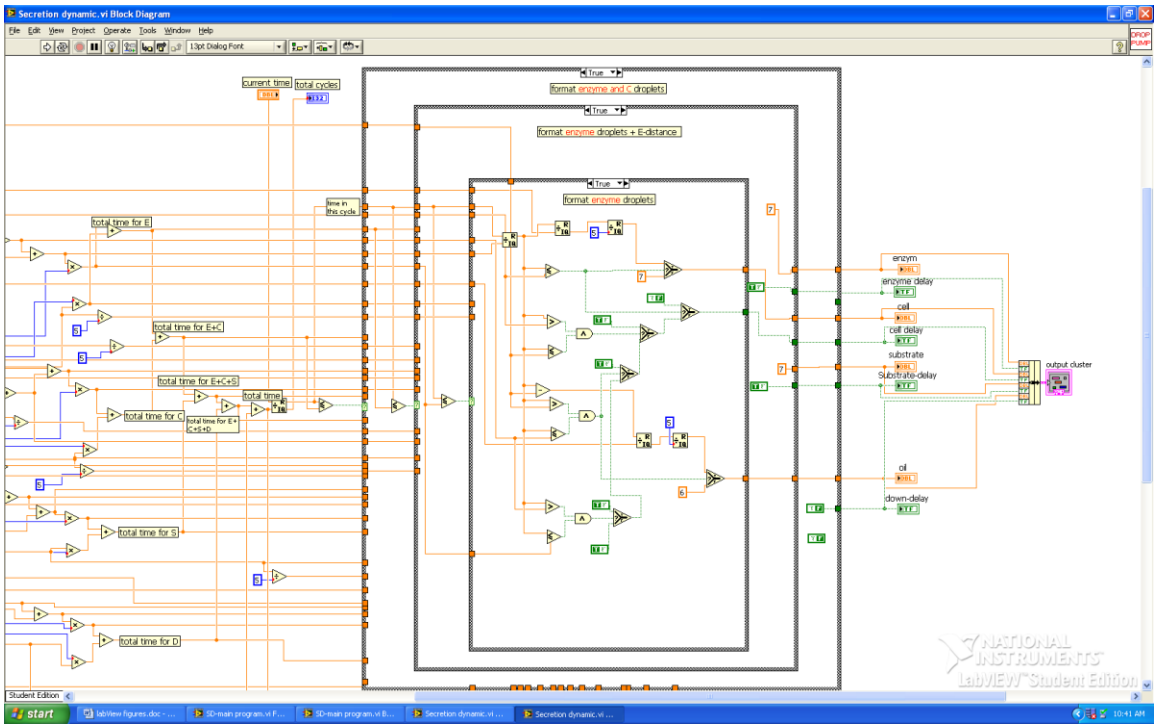

Figure C.12 Sub VI-block diagram of controlling the types of droplet-1

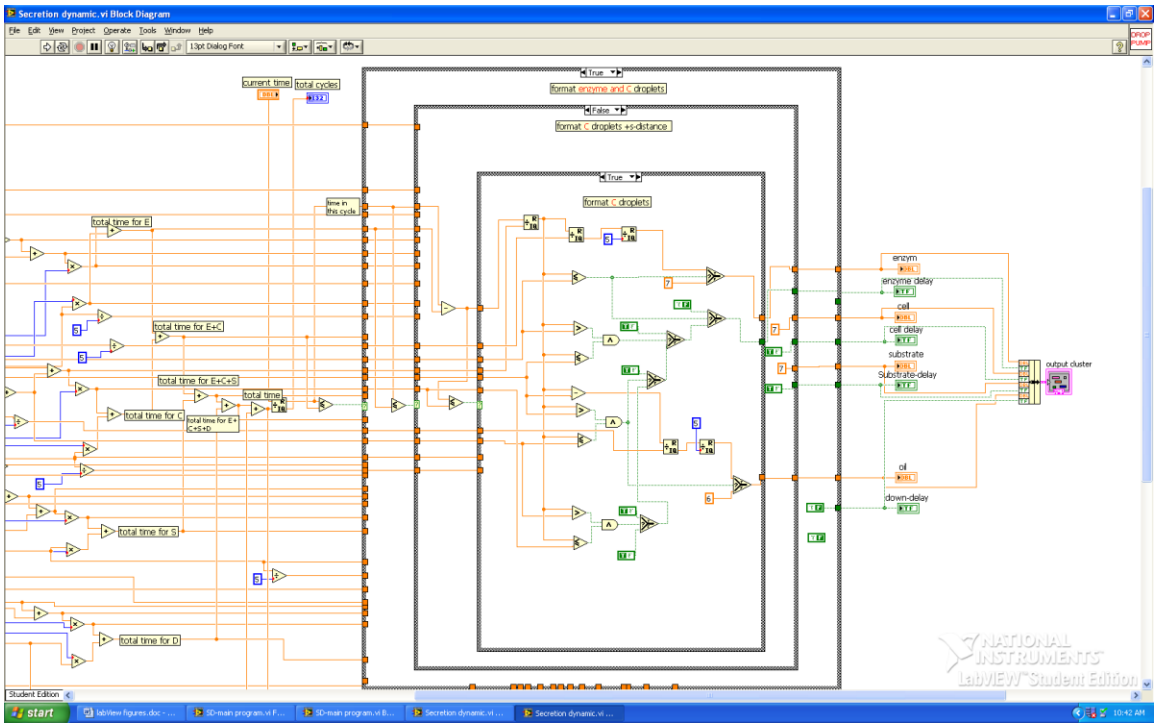

Figure C.13 Sub VI-block diagram of controlling the types of droplet-2

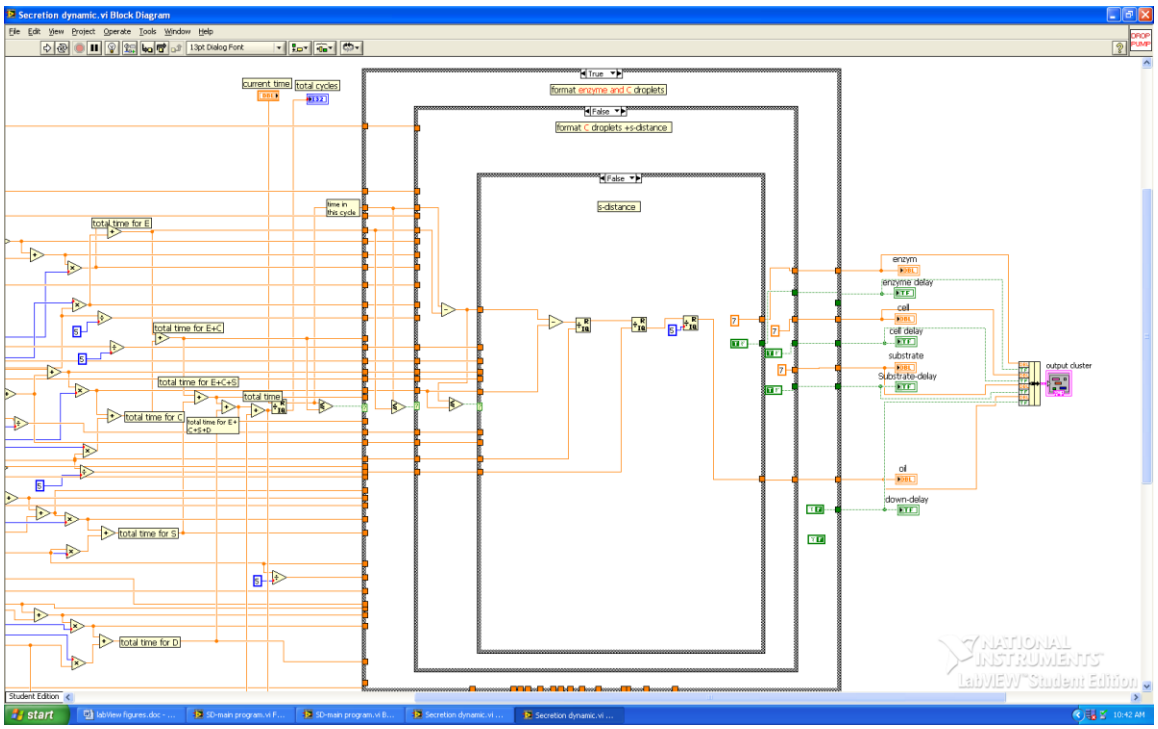

Figure C.14 Sub VI-block diagram of controlling the types of droplet-3